

Aus der Klinik für Strahlentherapie und Radioonkologie  
Geschäftsführende Direktorin: Frau Prof. Dr. Rita Engenhardt-Cabillic  
des Fachbereichs Medizin der Philipps-Universität Marburg

Titel der Dissertation:

**Estimating the effects on the dose distribution through  
the Bragg Peak degradation of lung tissue in proton  
therapy of thoracic tumors**

Inaugural-Dissertation zur Erlangung des Doktorgrades der Medizinwissenschaften

(Dr. rer. med.)

dem Fachbereich Medizin der Philipps-Universität Marburg

vorgelegt von

**Veronika Flatten**

21.09.1990

aus Aachen

Marburg, 2021

Angenommen vom Fachbereich Medizin der Philipps-Universität Marburg am:  
08.12.2021

Gedruckt mit Genehmigung des Fachbereichs Medizin.

Dekan: Prof. Dr. Denise Hilfiker-Kleiner

Referenten: Prof. Dr. Rita Engenhardt-Cabillic & Prof. Dr. Klemens Zink

1. Korreferent: Prof. Dr. Andreas Burchert

---

## In Peer-Review Journalen veröffentlichte oder akzeptierte Artikel

Die vorliegende kumulative Dissertation stellt eine Zusammenfassung der Forschungsergebnisse dar, welche wie folgt in Fachzeitschriften publiziert wurden:

[1] **V. Flatten**, K.-S. Baumann, U. Weber, R. Engenhardt-Cabillic, and K. Zink. Quantification of the dependencies of the Bragg peak degradation due to lung tissue in proton therapy on a CT-based lung tumor phantom. *Physics in Medicine & Biology*, 64(15):155005, 2019.

[2] K.-S. Baumann, **V. Flatten**, U. Weber, S. Lautenschläger, F. Eberle, K. Zink, and R. Engenhardt-Cabillic. Effects of the Bragg peak degradation due to lung tissue in proton therapy of lung cancer patients. *Radiation Oncology*, 14(1):1–15, 2019.

[3] J. M. Burg, **V. Flatten**, U. Weber, R. Engenhardt-Cabillic, H. Vorwerk, K. Zink, and K.-S. Baumann. Experimental determination of modulation power of lung tissue for particle therapy. Accepted by *Physics in Medicine & Biology*, 2021.

[4] **V. Flatten**, J. M. Burg, M. Witt, L. Derksen, P. Fragoso Costa, J. Wulff, C. Bäumer, B. Timmermann, U. Weber, H. Vorwerk, R. Engenhardt-Cabillic, K. Zink, and K.-S. Baumann. Estimating the modulating effect of lung tissue in particle therapy using a clinical CT voxel histogram analysis. *Physics in Medicine & Biology*, 66(18):185002, 2021.

[5] **V. Flatten**, A. Friedrich, R. Engenhardt-Cabillic, and K. Zink. A phantom based evaluation of the dose prediction and effects in treatment plans, when calculating on a direct density CT reconstruction. *Journal of applied clinical medical physics*, 21(3):52–61, 2020.

Die Publikationen werden im Text entsprechend der oben definierten Reihenfolge mit den Nummern 1-5 referenziert. Die aufgelisteten Publikationen verfügen, sofern erforderlich, über eine Abdruckgenehmigung von IOP Publishing im Auftrag des "Instituts for Physics and Engineering in Medicine" (IPEM).

---

## Conference contributions

Im Laufe der Promotion wurden die folgenden relevanten Konferenzbeiträge präsentiert:

- Giersch Symposium 2017, Frankfurt, Deutschland, Postervorstellung
- ESTRO37, 2018, Barcelona, Spanien, Postervorstellung
- PTCOG57 2018, Cincinnati, USA, Postervorstellung
- DEGRO24, 2018, Leipzig, Deutschland, Vortrag
- DGMP 2018, Nürnberg, Deutschland, Vortrag
- ESTRO38, 2019, Mailand, Italien, Postervorstellung
- PTCOG58, 2019, Manchester, Vereinigtes Königreich, Postervorstellung
- DEGRO25, 2019, Münster, Deutschland, Postervorstellung
- DGMP 2019, Stuttgart, Deutschland, Vortrag
- PTCOG59, 2021, online, Postervorstellung
- DEGRO 2021, online, Vortrag
- DGMP 2021, online, Vortrag

---

## Zusammenfassung

Die Partikeltherapie für Tumore in der Lunge z.B. nicht-kleinzellige Bronchialkarzinome stellt eine vielversprechende Therapieoption dar. Zugleich stellt die Bestrahlung von Lungenkarzinomen mit Protonen oder Kohlenstoffionen eine vielseitige Herausforderung dar. Die Bewegung des Tumors, des Herzens und des gesamten Thorax durch die Atmung und den Herzschlag fordern eine zeitlich mit der Atmung und Tumorbewegung gekoppelte Bestrahlungsapplikation. Zusätzlich bringt das Lungengewebe durch seine mikroskopische Struktur weitere Unsicherheiten in die Dosisberechnung.

In klinischen CTs, welche die Grundlage der Bestrahlungsplanung und Dosisberechnung bilden, werden die Mikrometer großen luftgefüllten Alveolen der Lunge nicht aufgelöst, sondern durch eine mittlere Dichte abgebildet. Der Bragg Peak wird bei Durchstrahlen eines solchen heterogenen Gewebes jedoch aufgeweitet, da einzelne Partikel im Strahl eine immer leicht andere Kombination aus Luft und Gewebeszusammensetzung passieren und dies wiederum zu einer leicht unterschiedlichen Reichweite der Teilchen führt.

Wird diese Verbreiterung des Bragg Peaks in der Bestrahlungsplanung nicht berücksichtigt, so kann diese potenziell zu einer Unterdosierung im Zielvolumen und somit dann zu einer schlechteren Tumorkontrolle führen und zusätzlich zu einer höheren Dosis in den Risikoorganen und im Normalgewebe, so dass die Toxizitätsrate den Therapieerfolg gefährdet.

In der vorliegenden Dissertation werden die Auswirkungen der Bragg Peak Verbreiterung auf die Dosisverteilung simuliert und analysiert, so dass eine Abschätzung der Effekte im klinischen Alltag möglich ist. Dafür werden CT Bilder mit Hilfe einer Dichtemodulationsfunktion der Lunge manipuliert, welche die Verbreiterung der mikroskopischen Strukturen auf makroskopische Strukturen überträgt. Somit kann ein direkter Vergleich zwischen den Dosisverteilungen mit und ohne die Verbreiterung gezogen werden. Verschiedene Abhängigkeiten wie die Tumorgöße und -lage, sowie die Tumorform werden systematisch untersucht und die Ergebnisse für fünf Patienten dargestellt, so dass die klinische Relevanz abgeschätzt und beurteilt werden kann.

Zudem werden Messungen vorgestellt, welche die eingeführte Materialeigenschaft der "Modulationsstärke" eines Gewebes für Lungengewebe zeigen. Auf Basis dieser Daten können die offenen Punkte der Analysen angegangen und die Unsicherheiten verringert werden, so dass besser begründete Einschätzungen vorgenommen werden. Zudem wird ein mathematisches

---

Modell präsentiert, welches die Abschätzung der Modulationsstärke auf Basis einer CT-Histogrammanalyse erlaubt.

Zusammen bilden die vorgestellten Arbeiten die Grundlage und Voraussetzung der Integration der Bragg-Peak Verbreiterung des Lungengewebes in die klinische, patientenindividuelle Bestrahlungsplanung.

---

## Summary

Particle therapy offers to be a promising therapeutic option for tumors in the lung like Non-small cell lung cancer (NSCLC). However, the irradiation of NSCLCs with protons or carbon ions poses different challenges. The movement of the tumor, the heart and the entire thorax through breathing and the heartbeat requires a motion mitigated radiation application. In addition, the microscopic structure of the lung tissue holds further uncertainties of the calculation of the optimized dose distribution.

In clinical CTs, on which treatment planning and dose calculation is based, the micrometer-sized air-filled alveoli of the lungs are not fully resolved, but are mapped through a medium density. As each particle of the beam passes a slightly different composition of air and tissue which leads to a slightly different range of the particles, the Bragg peak is degraded when irradiating such a heterogeneous tissue as lung.

If this degradation of the Bragg peak is not taken into account into treatment planning, it can potentially lead to an underdose in the target volume and thus to a loss in tumor control. Additionally, the degradation can also lead to a higher dose in the organs at risk and normal tissue, endangering the success of the therapy by a higher toxicity of the treatment. In this dissertation, the effects of the Bragg Peak degradation on the dose distribution are calculated and analyzed so that an assessment of the effects for the clinical routine is available. For this purpose, CT images are manipulated with the help of a density modulation function, which modulates the density of the macroscopic lung voxel to reproduce the microscopic effect. Thus, a direct comparison between the dose distributions with and without the degrading effect is possible. Various dependencies like the tumor size, position and shape are systematically examined and the results of the degradation on clinical plans are presented for five patients. Hence, the clinical relevance can be estimated and assessed. In addition, measurements are presented which show the introduced material property of the "modulation power" of lung tissue. On the basis of this data, the uncertainties of the presented calculation and analysis can be reduced and estimated better. In addition, a mathematical model is presented which allows to estimate the modulation power on the

---

basis of a clinical CT histogram analysis.

Together, the works presented offer a basis for the patient-specific translation of the Bragg peak degradation of lung tissue into the clinical treatment planning procedure.



# Contents

<b>Zusammenfassung</b>	<b>iii</b>
<b>Summary</b>	<b>v</b>
<b>List of Figures</b>	<b>ix</b>
<b>Abbreviations</b>	<b>xii</b>
<b>1 Introduction</b>	<b>1</b>
1.1 Lung cancer and its treatment . . . . .	1
1.2 Radiotherapy with a focus on particle therapy . . . . .	2
1.3 Computer tomography in radiotherapy . . . . .	4
1.4 Treatment planning in radiotherapy . . . . .	5
1.5 Monte Carlo code TOPAS . . . . .	6
1.6 Particle therapy for lung cancer – benefits against challenges . . . . .	7
1.7 Bragg peak degradation . . . . .	8
1.8 Aim and motivation . . . . .	10
<b>2 Summary of the published results</b>	<b>12</b>
2.1 Publication 1 . . . . .	12
2.1.1 Summary of publication 1 . . . . .	12
2.1.2 Contribution . . . . .	15
2.2 Publication 2 . . . . .	16
2.2.1 Summary of publication 2 . . . . .	16
2.2.2 Contribution . . . . .	20
2.3 Article 3 . . . . .	21
2.3.1 Summary of publication 3 . . . . .	21
2.3.2 Contribution . . . . .	24
2.4 Publication 4 . . . . .	25
2.4.1 Summary of publication 4 . . . . .	25
2.4.2 Contribution . . . . .	29
2.5 Publication 5 . . . . .	30
2.5.1 Summary of publication 5 . . . . .	30
2.5.2 Contribution . . . . .	32
<b>3 Discussion</b>	<b>33</b>
3.1 Dependencies of the effects caused by the lung modulation . . . . .	33
3.2 Effects of the lung modulation for clinical cases . . . . .	34

---

3.3	Measurement of the modulation power . . . . .	35
3.4	Estimation $P_{mod}$ on clinical CT data sets . . . . .	36
3.5	Patient specific uncertainty analysis of the lung modulation effect . . . . .	37
3.6	Uncertainties for lung cancer treatment with PBS . . . . .	37
<b>4</b>	<b>Conclusion &amp; Outlook</b>	<b>40</b>
	<b>References</b>	<b>42</b>
	<b>Published Articles</b>	<b>51</b>
	Verzeichnis der akademischen Lehrerenden . . . . .	147
	Danksagung . . . . .	148

# List of Figures

1.1	Depth dose distributions for different radiotherapy treatment modalities. (a) shows the physical depth dose curves and (b) shows the application of state-of-the-art photon VMAT versus a proton therapy SOBP. The proton plan has two opposing field from left and right, thus there is dose in L-R direction but not outside the field in anterior-posterior direction. The photon VMAT is constantly irradiating while the photon beam rotates around the body. Thus, the dose is accumulated in the center but the shown profile indicates the dose in the irradiated region (valid for both L-R and A-P). Thus, the photon plan deposits dose everywhere in the irradiated body region, while the proton plan deposits only a slightly higher dose in a defined region where the beams enter the body. A proton VMAT would lose this advantage. Exemplarily, the rotationally symmetric photon curve (green) and the proton curve in beam direction (light blue) and parallel to the beam (dark blue) are displayed. . . . .	3	
	a	Integrated depth dose curves for photons in green, protons in blue and carbon ions in red in water from a single direction. . . . .	3
	b	Depth dose curves for an extended tumor positioned in the center of a 30 cm water phantom. . . . .	3
1.2	Exemplary graph showing the Bragg peak degradation. The blue BP in the upper graph shows the reference curve without a modulating material in the beamline. In yellow, the measured degraded BP is shown and the green dashed curve represents the convoluted curve which was obtained by convolution of the reference curve and the normal distribution shown in the lower graph. The mean of the normal distribution shifts the BP, thus this value is obtained by calculating the difference of the range in water for the distal 82% dose value, for both, the reference and the degraded curve. At this point, the BP is minimal affected by range straggling. The width of the normal distribution is then adjusted to minimize the difference between the resulting convoluted curve (green dashed curve) and the measured degraded curve (in yellow) for LN-300. Figure taken from ([Flatten et al., 2021]). © Institute of Physics and Engineering in Medicine. Reproduced with permission. All rights reserved. . . . .	9	
2.1	General effects of the Bragg curve degradation for two modulation power values (450 $\mu\text{m}$ in orange and 800 $\mu\text{m}$ in red) in comparison to the originally planned dose distribution (in black). Figures taken from [Flatten et al., 2019] - Figure 3. © Institute of Physics and Engineering in Medicine. Reproduced with permission. All rights reserved. . . . .	13	
	a	Depth dose curves through the central beam axis. . . . .	13

b	Cumulative dose volume histogram (DVH) corresponding to (a). . .	13
2.2	Differences of the mean PTV dose of the modulated dose distribution in comparison to the original dose distribution in dependence on the distance in lung $d_L$ . Figures taken from [Flatten et al., 2019] - Figure 4 and 6. © Institute of Physics and Engineering in Medicine. Reproduced with permission. All rights reserved. . . . .	14
a	Dose difference of the mean dose in the PTV for different tumor sizes.	14
b	Dose difference of the mean dose in the PTV for different modulation power values. . . . .	14
2.3	Dose difference for the mean PTV dose for all calculated dose distributions. All performed calculations are divided by the three chosen modulation power values of 250 $\mu\text{m}$ (red), 450 $\mu\text{m}$ (green) and 800 $\mu\text{m}$ (yellow). The straight lines are linear regressions to the data sorted by modulation power. Figure taken from [Flatten et al., 2019] - Figure 7. © Institute of Physics and Engineering in Medicine. Reproduced with permission. All rights reserved. .	14
2.4	Axial views on the center of the tumor volume for the optimized proton treatment plans of five exemplary patients. For each patient, a single beam was optimized from 0°, 315° and 270°, respectively. As shown, also the resulting dose distributions with all three beams were evaluated. On the basis of [Baumann et al., 2019] - Figure 1 and 2. © Institute of Physics and Engineering in Medicine. Reproduced with permission. All rights reserved. .	17
2.5	The 95% (left column), 80% (middle column) and 20% (right column) isodose lines for four different patient cases and beam configurations. In purple, the planned dose without the Bragg peak degradation is shown and in green, the corresponding dose distribution when a modulation power of 800 $\mu\text{m}$ is assumed and accounted for. Figure taken from [Baumann et al., 2019] - Figure 6. © Institute of Physics and Engineering in Medicine. Reproduced with permission. All rights reserved. . . . .	19
2.6	CT images of the central slice of the five porcine lung samples. On the right, the high resolution CT image of sample number two acquired with the industrial CT scanner is shown. Figure taken from [Burg et al., 2021] - Figure 3. © Institute of Physics and Engineering in Medicine. Reproduced with permission. All rights reserved. . . . .	22
2.7	Determination of the modulation power $P_{mod}$ for sample number 3 at the central position. In the top graph, the optimization with a single Gaussian distribution is shown and in the bottom plot, the proposed analysis with the double Gaussian optimization is show. Figure taken from [Burg et al., 2021] - Figure 5. © Institute of Physics and Engineering in Medicine. Reproduced with permission. All rights reserved. . . . .	23
2.8	Schematic overview of the basic concept for the CT histogram analysis and the mathematical relations. On the left, images of a homogeneous material are shown. In the middle, the images for the heterogeneous material are shown and on the right, the corresponding histograms. The resolution is decreased from top to bottom from the highest resolution needed to fully resolve the heterogeneous material to the clinical CT image. Additionally, the corresponding proportionalities are given. On the basis of [Flatten et al., 2021] - Figure 2. . . . .	26

2.9	CT histograms for the nine materials under investigation. Each plot shows three different slice thicknesses: 0.1 mm (small animal CT) in green, 0.6 mm in blue and 1.5 mm in red. Note the different scales on the x-axis. Figure taken from [Flatten et al., 2021] - Figure 5. © Institute of Physics and Engineering in Medicine. Reproduced with permission. All rights reserved. .	27
2.10	The modulation power $P_{mod}$ acquired by the BP measurement plotted against $P_{fit}$ ( $P_{mod}$ ) calculated with the CT histogram analysis. The dotted linear regressions are marked by the green and blue line, respectively. The surrounding bands indicate an agreement with the regression line within $\pm 0.04$ mm for (a) and $\pm 0.06$ mm for (b). Figures taken from [Flatten et al., 2021] - Figure 6 and 8. © Institute of Physics and Engineering in Medicine. Reproduced with permission. All rights reserved. . . . .	28
	a Modulation power for the heterogeneous materials. . . . .	28
	b Modulation power for three positions of the five lung samples. . . . .	28
2.11	Calibration curves for the two different reconstruction algorithms for four tube voltages of 80 kVp (blue), 100 kVp (red), 120 kVp (grey) and 140 kVp (yellow). The dotted line shows the fit that was included in the TPS for the typically used 120 kVp curve. Figures taken from [Flatten et al., 2020] - Figure 2. Reproduced with permission. . . . .	31
	a Calibration curve for the standard HU reconstruction. . . . .	31
	b Calibration curve for the DirectDensity reconstruction. . . . .	31
2.12	RED profile through the metal implant and the surrounding tissue for all reconstructions under investigation. Figure taken from [Flatten et al., 2020] - Figure 10. Reproduced with permission. . . . .	32

# Abbreviations

<b>AAA</b>	Anisotrop Analytical Algorithm
<b>ART</b>	Alderson Radiation Therapy phantom
<b>BAMS</b>	Beam Application and Monitoring System
<b>BP</b>	Bragg Peak
<b>CBCT</b>	Cone Beam Computer Tomography
<b>COPD</b>	Chronic Obstructive Pulmonary Disease
<b>CT</b>	Computer Tomography
<b>CTDI</b>	CT Dose Index
<b>CTV</b>	Clinical Target Volume
<b>DD</b>	Direct Density
<b>DICOM</b>	Digital Imaging and COmmunication in Medicine
<b>DNA</b>	DeoxyriboNucleic Acid
<b>DVH</b>	Dose-Volume Histogram
<b>FWHM</b>	Full-Width-Half-Maximum
<b>GEANT4</b>	GEometry ANd Tracking
<b>GTV</b>	Gross Target Volume
<b>HU</b>	Hounsfield Unit
<b>IDD</b>	Integrated Depth Dose curve
<b>iMAR</b>	iterative Metal Artifact Reduction algorithm
<b>IMPT</b>	Intensity Modulated Proton Therapy
<b>ICRU</b>	International Commission on Radiation Units and measurements
<b>ITV</b>	Internal Target Volume
<b>MC</b>	Monte Carlo

---

<b>MD</b>	Mass Density
<b>MIT</b>	Marburg Ion-Beam Therapy Center
<b>MRI</b>	Magnetic Resonance Imaging
<b>MU</b>	Monitor Units
<b>NSCLC</b>	Non-Small Cell Lung Cancer
<b>OAR</b>	Organs At Risk
<b><math>P_{mod}</math></b>	modulation power
<b>PB</b>	Pencil Beam
<b>PBS</b>	Pencil Beam Scanning
<b>PET</b>	Positron Emission Tomography
<b>PTCOG</b>	Particle Therapy Co-Operative Group
<b>PTV</b>	Planning Target Volume
<b>RED</b>	Relative Electron Density
<b>RBE</b>	Relative Biological Effectiveness
<b>SBRT</b>	Stereotactic Body RadioTherapy
<b>SCLC</b>	Small Cell Lung Cancer
<b>TOPAS</b>	TOol for PArticle Simulations
<b>TPS</b>	Treatment Planning System
<b>VMAT</b>	Volumetric Modulated Arc Therapy
<b>WET</b>	Water Equivalent Thickness
<b>WPE</b>	West german Proton therapy center Essen

# 1 | Introduction

## 1.1 | Lung cancer and its treatment

With 19.3 million estimated new cancer cases in 2020 worldwide and almost 10 million cancer related deaths, cancer is one of the world's leading cause of death and its effective treatment an all-embracing issue in every health system [Sung et al., 2021]. Lung cancer as subset has the second highest incidences of the new cancer cases (11.2%) and is the leading cause of cancer related death with roughly 1.8 million deaths in 2020 [Sung et al., 2021]. This shows that the established treatment procedures do not have the high tumor control rates and survival outcomes that are available for other cancer entities.

For cancer, especially lung cancer, the three pillars on which treatment relies on are surgery, chemotherapy and radiotherapy. In most cases, a combination of the treatment modalities is recommended to the patient. Recently, immunotherapy (e.g. immune checkpoint inhibitors or vaccine therapy) for advanced stages of lung cancer has been added to the available treatment options and show promising results [Lemjabbar-Alaoui et al., 2015]. Lung cancer is highly heterogeneous and has to be divided into two main categories: Small cell lung cancers (SCLCs) which are derived from the hormonal cells of the lung and Non-small cell lung cancers (NSCLCs) which are large cell anaplastic carcinomas and make up most of the lung cancer cases with roughly 85% [Lemjabbar-Alaoui et al., 2015]. NSCLCs are staged into one of four categories which mostly define the proposed treatment options and have a major influence on the overall-survival. While five year survival for stage I NSCLC ranges from 80-60% after surgery and for stage II from 50-30%, the overall-survival is drastically reduced for stage III and stage IV NSCLCs to 15-2%. Unfortunately, more than 70% of the diagnosed NSCLCs are stage III or higher [Lemjabbar-Alaoui et al., 2015] and many are unresectable at the point of their diagnosis. Several radiotherapeutic studies [Mehta et al., 2001, Kong et al., 2005, Bradley et al., 2015] show that the local tumor control is improved in dose escalation studies for NSCLCs. However, with an increased dose given to the patients, an increase in dose to the organs at risk (OARs) comes along. In most cases radiation induced pneumonitis is the severely limiting factor to the dose escalation needed to control the tumor growth [Sonke and Belderbos, 2010].



## 1.2 Radiotherapy with a focus on particle therapy

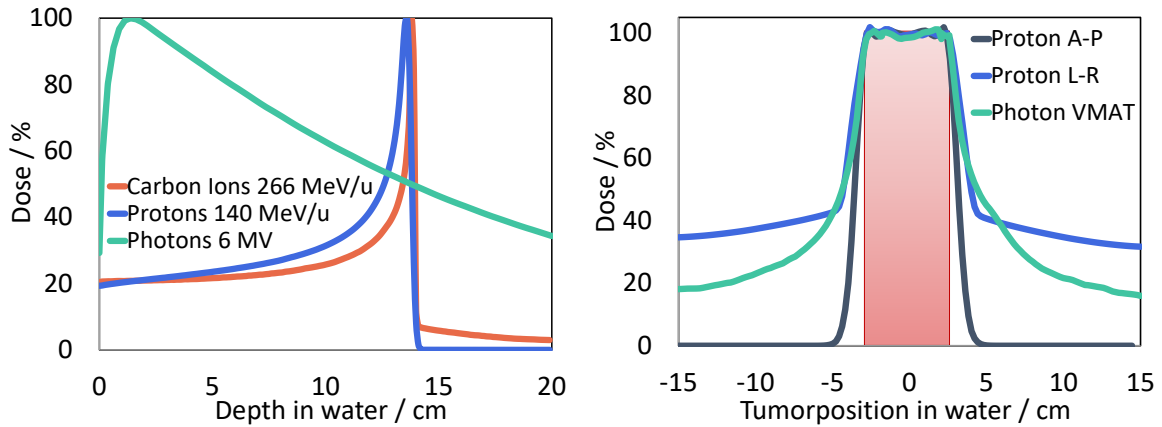
In the conventional external radiotherapy, photon bremsstrahlung (mostly 6 MV) is directed on the tumor to damage the tumor cells. When irradiated with an energy high enough to ionize the atoms in the cells, damage in the deoxyribonucleic acid (DNA) can occur. The probability for an unreparable double-strand break in the DNA is increased with the energy deposited in the cells [Fowler, 1989]. Thus, an increase in the dose applied to the cells decreases the cell survival. As the radiation is applied externally to the patient, also healthy tissue is irradiated and therefore damaged. With fractionating the dose given to the patient and repeating the irradiation after a defined time, the cell repair mechanisms are enabled and some radiation damage is repaired. Fortunately, these fractionation schemes have a greater influence on the normal tissue than on tumor cells, helping to reduce the damage to the surrounding normal tissue [Tubiana, 1988]. To additionally minimize the dose given to specific OARs or the normal tissue, the patient is irradiated under different angles or via a 360° rotation, smearing the exposure outside and concentrating the dose inside the tumor volume. Modern techniques further reduce the dose to critical OARs by modulating the beam fluence [Otto, 2008, Nutting et al., 2000].

However, with a look at figure 1.1a, a major disadvantage of photon beam radiation becomes obvious: The maximum dose deposition is between 1-2 cm under the skin (depending on the photon energy) and even so the fluence is attenuated, the theoretical range is infinite. Therefore, the treatment with heavy ions like protons, helium or carbon ions has a physical advantage: the particles stop after a defined range and the highest energy is deposited nearby (also see figure 1.1a). In 1946, Wilson proposed to use this advantage in clinical radiotherapy with protons [Wilson, 1946]. Roughly ten years later, the first clinical studies were performed at experimental beam sites [Lawrence, 1957]. Figure 1.1b shows the exemplary dose sparing in a clinical set-up with two beams entering from left and right. The sparing of the surrounding normal tissue and organs at risks outside the ion beams allows a higher dose per fraction to increase the tumor control rate. For heavier ions like helium or carbon ions, the benefit is increased by the higher biological effectiveness of this radiation [Kraft, 2000, Paganetti et al., 2002]. Today, over 110 treatment sites worldwide offer a therapy with protons of which 12 also offer carbon ions and more than 30 new centers are planned to be built [PTCOG, 2021a,b].

Figure 1.1a shows the depth dose curve for Protons and Carbon ions, which is also called the Bragg curve. It is described via the Bethe-Bloch equation (without corrections):

$$-\frac{dE}{dx} = \frac{4\pi n z^2}{m_e c^2 \beta^2} \left( \frac{e^2}{4\pi\epsilon_0} \right)^2 \left[ \ln \left( \frac{2m_e c^2 \beta^2}{I(1-\beta^2)} \right) - \beta^2 \right] \quad (1.1)$$

$dE/dx$  describes the energy loss of a charged particle with charge  $z$ , energy  $E$  and speed  $\beta = v/c$  after traveling a distance  $x$  in a material with an electron density  $n$  and a mean



(a) Integrated depth dose curves for photons in green, protons in blue and carbon ions in red in water from a single direction. (b) Depth dose curves for an extended tumor positioned in the center of a 30 cm water phantom.

Figure 1.1: Depth dose distributions for different radiotherapy treatment modalities. (a) shows the physical depth dose curves and (b) shows the application of state-of-the-art photon VMAT versus a proton therapy SOBP. The proton plan has two opposing field from left and right, thus there is dose in L-R direction but not outside the field in anterior-posterior direction. The photon VMAT is constantly irradiating while the photon beam rotates around the body. Thus, the dose is accumulated in the center but the shown profile indicates the dose in the irradiated region (valid for both L-R and A-P). Thus, the photon plan deposits dose everywhere in the irradiated body region, while the proton plan deposits only a slightly higher dose in a defined region where the beams enter the body. Exemplarily, the rotationally symmetric photon curve (green) and the proton curve in beam direction (light blue) and parallel to the beam (dark blue) are displayed.

excitation potential  $I$ . Thus, the energy deposition increases with increasing the atomic number or decreasing the velocity of the particle. Therefore, the highest energy is deposited at the point where the particle is the slowest and comes to a stop.

To reach an extended dose distribution as presented in figure 1.1b, two different application techniques are used in the clinical context. For the passive scattering application, the beam is scattered and the energy is continuously degraded via a modulator wheel. The beam is then collimated and a patient specific range compensator adapts the beam to the distal edge of the target volume. Advantages lie in the fast application and the availability to include organ motion into the target margin. The main disadvantage is due to the fact, that even so the distal edge is optimized to the target extension, tissue proximal to the target is unnecessarily irradiated [Goitein et al., 2002, Kase et al., 2012]. The active raster scanning technique or pencil beam scanning (PBS) on the other hand delivers single energy spots which are overlaid to accumulated in the target volume. This is achieved in the lateral dimension via bending magnets and in beam directions via a change in energy. Thus, this application technique is much slower and has its own time structure that could interfere with internal organ motion [Bert and Durante, 2011, De Ruyscher et al., 2015]. However,

in comparison to the passive application technique, only the target volume is irradiated with the prescribed dose [Zhang et al., 2010].

In general, two different accelerator types are clinically available: synchrotrons or cyclotrons. The passive application can only be performed with a cyclotron, while helium or carbon ions are (at least at the moment) only available in synchrotron sites [PTCOG, 2021a].

### 1.3 | Computer tomography in radiotherapy

In radiotherapy, the patient-specific dose calculation is essential for the success of the treatment. Thus, highly accurate dose calculation algorithms need to be combined with the patient geometry and information about the absorption and stopping power of the specific tissue. For this, computed tomography images are essential to radiotherapy. Before every radiotherapy, a planning CT is acquired underlying strict constraints. In conventional radiotherapy, the Hounsfield units of the CT image are transferred to the property of electron density via a lookup table [Schneider et al., 1996]. The relative electron density (RED) is needed to calculate the absorption of the tissues in the beam path. This calibration curve is depending on the chosen tube voltage. Thus, in most radiotherapy departments, only a single calibration curve for 120 kVp tube voltage is implemented in the treatment planning system (TPS). In particle therapy, the procedure is similar, however in this case, the relative stopping power is of interest [Bourque et al., 2014]. Then, ray-tracing algorithms calculate the accumulated path length through the patient and thus, where the beam comes to a stop [Hong et al., 1996].

The patient is immobilized to reproduce the planning CT image at best. Even so, the imaged patient geometry is always only a snap-reading method, small differences are bound to occur between the planning image and the patient positioning during treatment, especially in the thoracic and abdominal region, where organs are constantly moving through breathing, the heart beat and the muscle constrictions of the digestive tract. In photon therapy, slight differences like e.g. a different filling of the bladder or a different respiration phase have only a minor effect on the dose distribution. In particle therapy, however, this could lead to a completely different beam path length which could potentially lead to the dose being applied to the OAR and not to the target [Jiang, 2006, Bert and Durante, 2011]. To estimate and include the effect of movement into the planning routine, 4D-CTs offer a time resolved imaging [Brandner et al., 2006, Hof et al., 2009]. A 4D-CT includes a set of eight to ten 3D-CT sets, which were only acquired at a specific respiratory state. With these sets, the movement of the OARs and the tumor can be analyzed over a complete breathing cycle.

## 1.4 Treatment planning in radiotherapy

On the planning CT, radiation oncologists delineate the OARs and the target volume with the help of additional information from diagnostic images like magnetic resonance imaging (MRI) or positron emission tomography (PET). The clinical target volume (CTV) includes the clinical delineation and uncertainties of the solid tumor (Gross target volume - GTV) [ICRU, 2016]. In the case of moving targets, the CTV is contoured on every phase of a respiratory-gated 4D-CT. The internal target volume (ITV) is then produced by the accumulation of the outlines of each CTV on every 4D-CT-phase [Muirhead et al., 2008]. Additional margins are applied to the CTV or if existent the ITV to account for the uncertainties in the immobilization, the beam application technique and other inter-fractional changes [ICRU, 2016, Purdy, 2004]. The so obtained planning target volume (PTV) is then the defined volume which is optimized to be irradiated with the prescribed dose.

Then, medical physicists choose the beam application technique (e.g. the beam energy in photon therapy, the beam angles and beam modulation technique) and optimize the dose distribution. This is performed with dedicated treatment planning system (TPS) computers. In clinical routine, the TPS offers fast analytical algorithms to calculate the dose distribution in the patient. In the presented works, treatment planning was performed with the Eclipse TPS (Varian). The base data in Eclipse were measured and simulated with a Monte Carlo code (see section 1.5) to fit the corresponding measurement sites, in this case the Truebeam radiotherapy system [Glide-Hurst et al., 2013] in the clinic for radiotherapy and radiooncology Marburg and the Marburg Ion-Beam Therapy Centre (MIT) Accelerator Facility [Scheeler et al., 2016].

However, the prescribed dose is optimized and calculated for each patient on the planning CT. In general, a typical dose per fraction given to the tumor is between 1.8-2.2 Gy and the fractionation schemes offer between 13 and 33 fractions [ICRU, 2016, Degro, 2021]. In case of small tumor volumes, an increased dose per fraction in 1-5 fractions is applied in photon therapy [ICRU, 2017, Wilke et al., 2019]. The so called stereotactic treatment offers an increased tumor control because of the high dose per fraction. The toxicity is controlled by an increased number of beam directions. As the tumor volume is small, the integral dose given to a patient in a single fraction is comparable to the conventional fractionation schemes of 2 Gy. Thus, the application of the beam has to be even more precise as uncertainties are not washed out by the large number of fractions.

## 1.5 Monte Carlo code TOPAS

However, these clinically used dose algorithms have weaknesses when it comes to high density deviations like the transition from tissue to lung and for very high or low densities in general. In these cases, Monte Carlo (MC) calculations offer a much higher accuracy. In general, Monte Carlo simulations use a stochastic approach to solve a problem by simulating a huge number of random experiments. Via the law of large numbers, the result verges towards the expected mean value. This method introduced by [Metropolis and Ulam \[1949\]](#) is used in many fields of research. In radiation physics, this method is used to simulate the transfer and interactions of particles through and with matter. In specialized toolkits, the basis of radiation physics like particle characteristics, interaction processes and cross sections is implemented. Geant4 is such a toolkit used for various research topics [[Agostinelli et al., 2003](#)]. TOPAS (TOol for PArticle Simulation) is based on Geant4 but specializes on medical applications of ionizing radiation [[Perl et al., 2012](#), [Faddegon et al., 2020](#)].

Due to the nature of Monte Carlo, these calculations are highly accurate if the number of simulated particle tracks is also high. A high number of simulated particles goes inherently with a high calculation capability or a waste amount of time. Thus, in the clinical context, the radiation transport is calculated via analytical algorithms. These are fast and for the main clinical cases accurate. However, in cases deviating from the main clinical set up, the models are not optimized or trained for and thus, less accurate. In these cases, the MC method is highly suggested. With a steady increase in computing power, MC calculations are emerging to be clinically useful [[Pemler et al., 2006](#), [Wagenaar et al., 2020](#)].

All MC simulations that were performed, were conducted with the TOPAS toolkit. To ensure a good agreement between measurement, TPS and MC simulation. The parameters (e.g. the initial beam width and the energy spread) were optimized to best reproduce the measured data before the code was used for the investigation of a specific problem. Therefore, the complete beam application and monitoring system (BAMS) was built and validated in TOPAS.

As TOPAS does not feature an treatment plan optimizer, plans were optimized in Eclipse and then recalculated with TOPAS. For this, a python script was written which automatically converts DICOM RT-Plan files into TOPAS input files, corresponding to the patient and beam set-up from the Eclipse treatment plan.

## 1.6 Particle therapy for lung cancer – benefits against challenges

As radiotherapy for lung cancer benefits from an increased dose per fraction, particle therapy offers a dose distribution with a decreased dose to the OARs like the lungs, the heart or the spinal cord while applying an increased dose to the tumor compared to photon therapy [Widesott et al., 2008, Zhang et al., 2010]. However, the beam application on a moving target surrounded by lung tissue combines the most challenging aspects of particle therapy. This is especially true for active scanning application, where interplay effects of organ or tumor motion with the movement of the beam are likely to occur [De Ruyscher et al., 2015].

In conventional radiotherapy or passive scattering sites, the movement is included in a simple margin concept of the ITV (as described in section 1.4). As the 3D conventional photon therapy and the passive scattering proton therapy irradiate the enlarged tumor volume completely during the beam-on time, the tumor is irradiated independent on the respiratory phase. The downside of this is the large volume that is irradiated with the prescribed dose and hence, the additional dose in the OARs. Therefore in most cases, an additional sparing of the normal tissue is gained via gating techniques: When the beam application is gated, the breathing phase and the beam on signal is correlated. This can be implemented via pressure sensitive belts and other external markers, 3D camera systems, constant x-ray imaging or the tracking of implanted magnetic fiducial markers [Keall et al., 2006]. Another method that gains attraction is the tumor tracking option. In this case, the tumor movement is not only observed but the beam application is following the tumor in its movement [Keall et al., 2006, Desplanques et al., 2013].

In active scanning particle treatment sites, additional techniques are used for motion mitigation. Gating plays also the most important role in active scanning applications. The gating window, however is narrowed down to acquire an almost unmoved target set-up [Lu et al., 2007]. The Particle Therapy Co-Operative Group (PTCOG) advises a maximum tumor movement of 5 mm for active scanning [Chang et al., 2017]. Gating is mostly combined with a fast rescanning beam application [Ebner et al., 2017, Tsunashima, 2012]. Rescanning describes the application, where the dose of each beam spot is reduced while the scanning of the target is repeated. The same dose is applied but the time structure has changed. This reduces the likelihood that a single beam spot is completely missing the moving target which would minimize the dose given to the tumor.

Another idea which would also allow synchrotron treatment facilities to irradiate the tumor faster are the implementation of 3D patient specific range modulators. These are scanned with an iso-energetic pencil beam and optimize the irradiated volume not only to the distal edge of the tumor (as done with passive scattering) but also to the proximal edge [Simeonov

et al., 2017].

Besides the difficulties in implementing these motion mitigation techniques in particle therapy, clinical trials show a good outcome for particle therapy of early-staged and advanced NSCLC. In a meta-analysis by Grutters et al. [2010], the particle therapy studies were found to be as effective as stereotactic body irradiation (SBRT) for early-stage NSCLC. The meta-analysis showed that SBRT and particle therapy with lower doses per fraction offered the same tumor control and survival rates as surgical interventions and were inferior to conventional radiotherapy [Grutters et al., 2010].

In a phase II study, Chang et al. [2011] combined a 74 Gy proton therapy scheme with concurrent chemotherapy for stage III lung tumor patients. The reported overall survival and progression-free survival rates were 86% and 63% after 1 year and a median survival time of 29.4 months. These are promising results, as the mean survival time for conventional radiotherapy with concurrent chemotherapy ranges about 15 months [Zarogoulidis et al., 2013].

This shows that even so particle therapy for lung tumors faces higher uncertainties and challenges than conventional therapy, the results are favoring particle therapy treatment. If the current uncertainties are under control or bypassed, the results should be expected to be even more promising.

## 1.7 | Bragg peak degradation due to heterogeneous materials

This work focuses on the uncertainty caused by the Bragg peak degradation, when irradiating lung tumors with particles. Urie et al. [1986] stated in the eighties that the BP is degraded when it passes inhomogeneities: If particles travel a slightly different composition of materials, they also stop after a slightly different range. Thus, the BP is not as sharp as it would be in a homogeneous material and the BP is degraded [Sawakuchi et al., 2008]. This is shown in figure 1.2. The measured pristine BP (top panel in blue) is degraded when the lung tissue mimicking sample is inserted (top panel in yellow). In the human body, lung is one of the most inhomogeneous organs. On a microscopic scale, lung parenchyma is a mixture of air and tissue. Thus, the BP is broadened and degraded when it passes through lung [Titt et al., 2015]. Measurements verified this degradation effect for lung-equivalent materials [Sell et al., 2012, Titt et al., 2015, Ringbaek et al., 2017]. Due to the micrometer scale of the degrading structures, common clinical CT images do not resolve these inhomogeneities. Instead an average density value is given [España and Paganetti, 2011, Perles et al., 2011]. Hence, the effect is not accounted for in clinical treatment planning.

Baumann et al. [2017] and Ringbaek et al. [2017] found a way to quantify the extend of

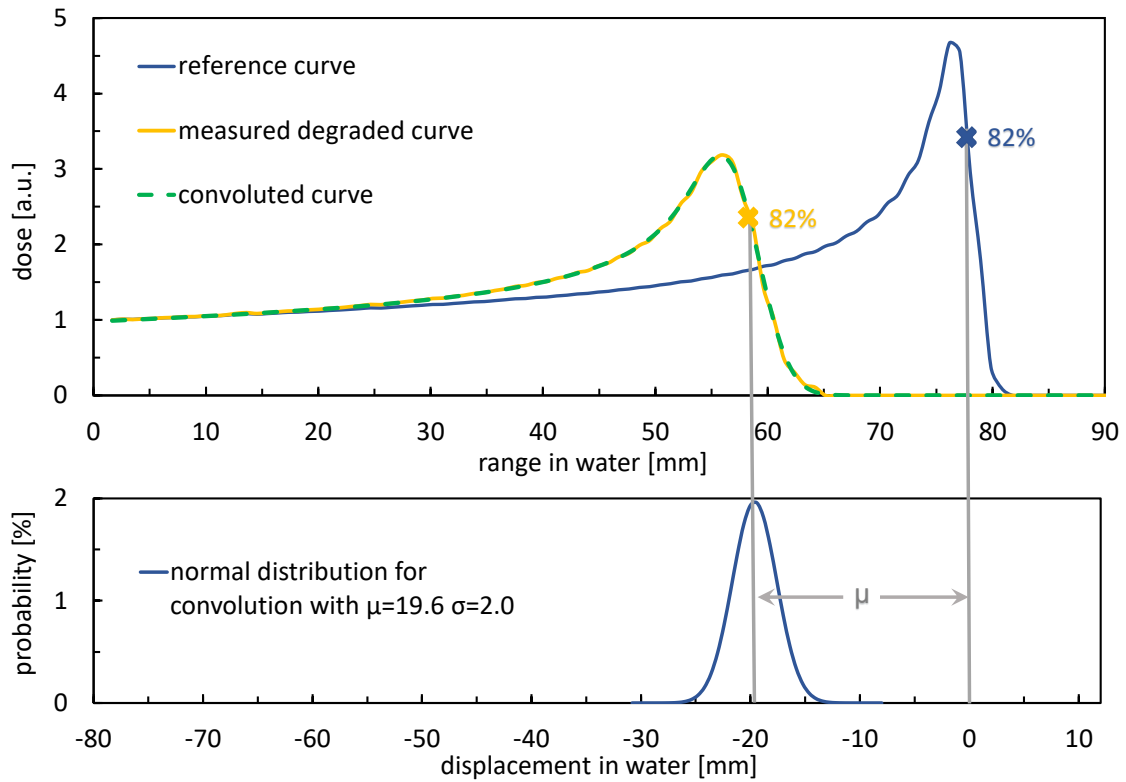


Figure 1.2: Exemplary graph showing the Bragg peak degradation. The blue BP in the upper graph shows the reference curve without a modulating material in the beamline. In yellow, the measured degraded BP is shown and the green dashed curve represents the convoluted curve which was obtained by convolution of the reference curve and the normal distribution shown in the lower graph. The mean of the normal distribution shifts the BP, thus this value is obtained by calculating the difference of the range in water for the distal 82% dose value, for both, the reference and the degraded curve. At this point, the BP is minimal affected by range straggling. The width of the normal distribution is then adjusted to minimize the difference between the resulting convoluted curve (green dashed curve) and the measured degraded curve (in yellow) for LN-300. Figure taken from ([Flatten et al., 2021]). © Institute of Physics and Engineering in Medicine. Reproduced with permission. All rights reserved.

the Bragg peak degradation by introducing a new material characteristic: the modulation power  $P_{\text{mod}}$ . A larger value of the modulation power means a stronger degradation effect. Figure 1.2 illustrates how the modulation power of materials can be calculated: If the unperturbed BP curve (top panel in blue)  $b_0$  is convolved with a normal distribution  $F$  (bottom panel), a convoluted curve  $b_*$  (top panel in green) is obtained. If the parameters of the normal distribution are optimized, the convoluted curve equals the curve degraded by a modulating material. The normal distribution  $F$ , in this case, describes the probability of the water-equivalent thickness a particle accumulates when traversing the modulating material. In the example of figure 1.2, the mean water-equivalent thickness  $\mu$  is 19.6 mm and 68.3% of the particles will stop within  $\pm 2.0$  mm of this mean range.



Equation 1.2 gives the described correlation (from [Baumann et al., 2017]):

$$b_*(z) = (F * b_0)(z) = \int_{-\infty}^{\infty} F(t|\mu, \sigma)b_0(z + t)dt \quad (1.2)$$

The modulation power can then be calculated via the mean water equivalent thickness of the material  $\mu$  and the width of the normal distribution  $\sigma$ :

$$P_{mod} := \frac{\sigma^2}{\mu} \quad (1.3)$$

The ability to quantify the Bragg peak degradation leads to follow up questions: How large is the modulation power for lung tissue and thus, how large is the effect on the dose distribution?

Witt [2014] measured the modulation power at different points of a ventilated porcine lung. The lung was irradiated with a carbon ion BP. The pristine BP and the curve with the lung positioned in the beam path were measured to determine the modulation power as described. The resulting modulation powers ranged from 150  $\mu\text{m}$  up to 750  $\mu\text{m}$ . However, most values centered around 450  $\mu\text{m}$ . This measurement gave a first indication of the modulation power, allowing to estimate the effects on the dose distribution for these modulation power values. However, for a patient specific treatment option, it would be favorable to determine the individual modulation power at the exact beam position.

In his work, Baumann et al. [2017] proofed that the degradation effect can be reproduced on a macroscopic scale by modulating the density values of the CT voxels. He showed that the dose calculated on an image resolution which divides the CT voxel in e.g. 100 equally small voxels equals the dose calculated on CT images where the density of the voxel was changed for  $\sim 100$  times. Depending on the concept of the introduced modulation power, the density value was changed according to a discrete probability density function optimized for a specific  $P_{mod}$ . This work proofed that the concept was valid for two dimensional simple geometries. Thus, the next steps to translate the concept to clinical patient CTs can be approached.

## 1.8 | Aim and motivation

This dissertation focuses on the degradation of the BP when treating lung tumors with proton therapy. It aims to give answers and methods to answer the open questions that need to be addressed for a more profound handling of the degradation in the clinical context. Therefore, the first main objective is to translate the concept of the density modulation of voxel presented by Baumann et al. [2017] to a more clinical set-up and quantify the effect on the dose distribution.

In a CT-based phantom study, the dependencies of different geometrical and anatomical

parameters like the tumor size, shape and position within the lung are analyzed to determine the major influences on the disturbed dose distribution. Thereafter, an estimation of the effects on the dose distribution in dependence of determinable CT parameters can be performed.

In a next step, the model is then transferred to five patient plans. For each patient three single beam plans are optimized and the effects of the BP degradation is analyzed. For the first time, the effects of the Bragg Peak degradation are shown on the dose distribution of proton treatment plans. Additionally to the single beam configuration, the influence of the number of beam directions is addressed. The results are then compared to the phantom study. These calculations of the effect of the BP degradation on the dose distribution for various clinical set-ups show the effect for different values of the modulation power.

As the effects strongly depend on the chosen value for the modulation power, it is crucial to improve the window of the assumable modulation power values. Hence, the next steps focus on the measurement of the modulation power of frozen porcine lung samples as these are the closest to human lung samples. The mean variation of the modulation power of lung tissue is analyzed and gives an estimate of the modulation power for patient cases.

In the final step, a model is derived that allows an estimation of the modulation power from clinical CT images, even so the modulating structures are not fully resolved by the clinical CT resolution. The model is calibrated with modulation power values acquired via the in-beam measurement of these heterogeneous materials. To confirm and test the model in the set-up closest to the patient anatomy, the results of the frozen porcine lung samples are also analyzed and compared to the model.

## 2 | Summary of the published results

### 2.1 | Publication 1

#### Quantification of the dependencies of the Bragg peak degradation due to lung tissue in proton therapy on a CT-based lung tumor phantom

##### 2.1.1 | Summary of publication 1

In Publication 1 [Flatten et al., 2019], the work by Baumann et al. [2017] is transferred and continued on CT-based phantoms. The aim of this work is to show the effect of the Bragg peak degradation on the dose distribution and to answer the questions of which parameters influence the strength of the effect on the dose distribution. Furthermore, the influence of the parameters under investigation was quantified.

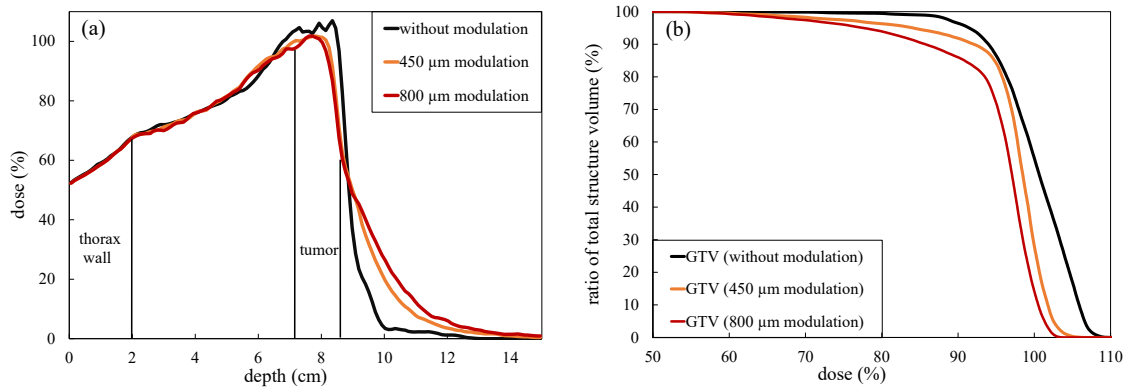
In a first step, CT based phantoms were produced that allowed to investigate the parameters of interest, mainly: the tumor size, the position within the lung and the tumor shape (see figure 2 in Publication 1). Each CT phantom had a voxel size of  $1.5 \times 1.5 \times 1.5 \text{ mm}^3$  and was built with a 2 cm water slab to mimic the thorax wall. A spherical water volume positioned within the lung mimicked the tumor. All voxels within the lung were set to have a density of  $0.26 \text{ g/cm}^3$  corresponding to an inhaled lung [Schneider et al., 1996].

Six different spherical tumor volumes were investigated:  $1 \text{ cm}^3$ ,  $2 \text{ cm}^3$ ,  $6 \text{ cm}^3$ ,  $14 \text{ cm}^3$ ,  $25 \text{ cm}^3$  and  $43 \text{ cm}^3$ .

For each of the six tumor sizes, six positions within the lung were evaluated. The distance between lung entry and tumor center was 2 cm, 4 cm, 6 cm, 10 cm, 15 cm, and 20 cm, respectively.

To investigate the tumor shape, which is not always spherical in the patient, two differently sized ellipsoids were investigated.

As proposed by Baumann et al. [2017], the modulation was reproduced by performing a density modulation on the lung voxels for a specific modulation power. For each CT phantom set, 100 differently modulated data sets were produced for a modulation power of  $250 \mu\text{m}$ ,  $450 \mu\text{m}$  and  $800 \mu\text{m}$ . A single proton beam was optimized on the original CT set in



(a) Depth dose curves through the central beam axis. (b) Cumulative dose volume histogram (DVH) corresponding to (a).

Figure 2.1: General effects of the Bragg curve degradation for two modulation power values (450  $\mu\text{m}$  in orange and 800  $\mu\text{m}$  in red) in comparison to the originally planned dose distribution (in black). Figures taken from [Flatten et al., 2019] - Figure 3. © Institute of Physics and Engineering in Medicine. Reproduced with permission. All rights reserved.

the TPS Eclipse (Varian). The plan was then recalculated on all modulated CT sets with the Monte Carlo code TOPAS. For this, a tool was developed that transformed DICOM RT plans into TOPAS input files. To obtain the final modulated dose distribution, the 100 dose cubes were superposed. The non-modulated plan was also recalculated in TOPAS to allow a distinct evaluation of the differences caused by the modulation and not the difference of the calculation methods.

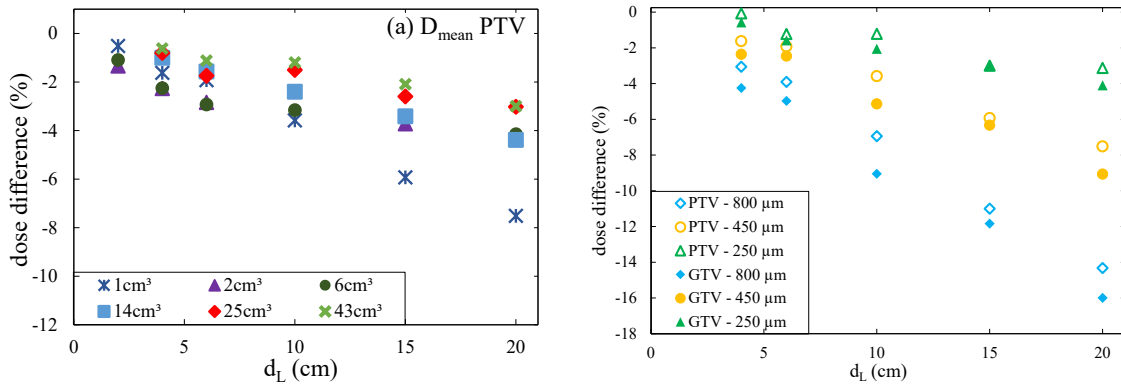
The general effects of the Bragg peak degradation on the dose distribution are shown in figure 2.1 (also see Publication 1, figure 3). The depth dose curves show that the dose is smoothed and degraded, leading to a decreased dose in the tumor and an increased dose distal to the tumor volume. The decrease in dose is also observable in the DVH. As to be expected, the effect increases with increasing modulation power.

Figure 2.2 (see also Publication 1, figure 4-6) shows the main dependencies of the resulting underdose in the PTV: The mean dose in the PTV decreases with increasing depth in lung ( $d_L$ ) and increasing modulation power. However, it decreases with increasing tumor volume.

The tumor volume was further investigated by means of tumor shape: It was found that rather than the tumor volume, the tumor length in beam direction is the parameter of interest. An empirically found parameter was introduced to better describe the geometrical dependency:

$$L_S = 2 \cdot \frac{a^2}{\sqrt{b \cdot c}} \quad (2.1)$$

In equation 2.1 (also see Publication 1, equation 1),  $a$  is the tumor length in beam direction while  $b$  and  $c$  describe the lateral tumor extension. With the help of this so-called scaled



(a) Dose difference of the mean dose in the PTV for different tumor sizes.

(b) Dose difference of the mean dose in the PTV for different modulation power values.

Figure 2.2: Differences of the mean PTV dose of the modulated dose distribution in comparison to the original dose distribution in dependence on the distance in lung  $d_L$ . Figures taken from [Flatten et al., 2019] - Figure 4 and 6. © Institute of Physics and Engineering in Medicine. Reproduced with permission. All rights reserved.

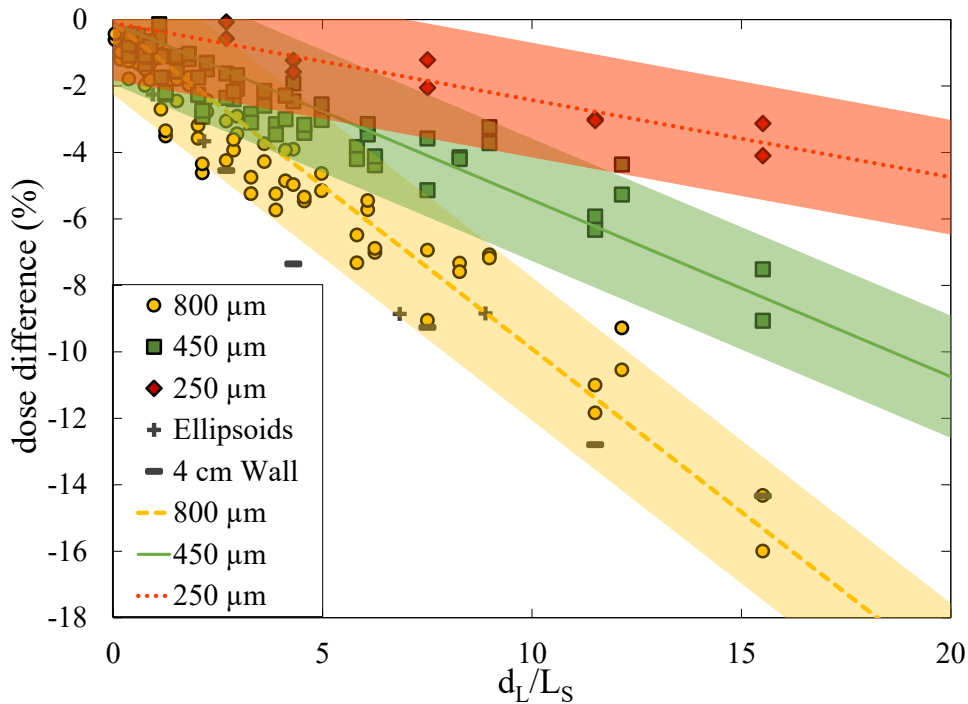


Figure 2.3: Dose difference for the mean PTV dose for all calculated dose distributions. All performed calculations are divided by the three chosen modulation power values of 250  $\mu\text{m}$  (red), 450  $\mu\text{m}$  (green) and 800  $\mu\text{m}$  (yellow). The straight lines are linear regressions to the data sorted by modulation power. Figure taken from [Flatten et al., 2019] - Figure 7. © Institute of Physics and Engineering in Medicine. Reproduced with permission. All rights reserved.

tumor length, a universal presentation of the results can be given, as shown in figure 2.3 (also see Publication 1, figure 7).

Figure 2.3 allows an estimation of the underdose of the PTV in dependence on the scaled tumor length  $L_S$  and the distance in lung  $d_L$  for three different modulation power values. Additional investigations, which examine the effect of the thickness of the thorax wall and the dependency on planning parameters such as the lateral and longitudinal spot spacing showed only a minor effect and were included in figure 2.3.

Publication 1 is the first publication that measures the effect of the Bragg peak degradation on a 3-dimensional dose distribution and identifies the extent and the important parameters that influence the dose disturbance. As visible from figure 2.3, for small tumor volumes and the maximum modulation power, a decrease in the mean dose up to -16% was found. The more probable values (in terms of tumor volume and distance in lung, as well as modulation power) identify dose differences between -5% and smaller than -1%. This work allows an estimation of the underdose in the PTV in dependence on the specific situation.

However, figure 2.3 also shows that the main unknown parameter that strongly influences the dose distribution is the modulation power, as all other parameters can be obtained from the treatment planning CT and thus be included correctly in possible calculations of the effect. Thus, Article 3 and Publication 4 will tackle the task to give a better estimation of the modulation power of lung tissue.

## 2.1.2 | Contribution

V. Flatten wrote the manuscript and executed most the study. She set up the treatment plans and converted the DICOM plans into TOPAS input files. V. Flatten analyzed the simulation results. K.-S. Baumann aided with the design of the study. He created all CT-based phantoms and applied the density modulation. The MC calculations were performed with the beam monitor system of the Marburg Ion-beam therapy center, which was commissioned by K.-S. Baumann beforehand. U. Weber had the original idea for the density modulation and the mathematical model. The tool to optimize the density probability functions was created by U. Weber. R. Engenhart-Cabillic supported the clinical assessment with her expertise. K. Zink supervised the work and helped with the physical assessment. All authors revised this manuscript, substantively.

## 2.2 | Publication 2

### Effects of the Bragg peak degradation due to lung tissue in proton therapy of lung cancer patients

#### 2.2.1 | Summary of publication 2

Publication 2 [Baumann et al., 2019] aims to transfer the method and findings of Publication 1 to clinical patient data and thus, evaluate the effects of the BP degradation in potential lung treatment cases. Therefore, five lung cancer patient CTs were chosen. The patients were originally treated with hypofractionated stereotactic body radiotherapy (SBRT) with photons at the clinic for radiotherapy and radiooncology in Marburg and replanned for this study with protons giving 30 Gy in one fraction. The tumor volume of the five exemplary patients ranged between  $2.7\text{ cm}^3$  and  $46.4\text{ cm}^3$ . For particle therapy of lung tumors, most published studies treat larger tumor volumes, as the movement is smaller in these cases. However, also smaller volumes would benefit from proton therapy and have been treated with [Hata et al., 2007, Bush et al., 2004, Chen et al., 2019].

The tumor volumes were positioned at different parts of the right lung, not directly attached to the thorax wall or the mediastinum, as Publication 1 showed that distal tissue has an impact in the spot optimization. The different patients are shown in figure 2.4 (also see Publication 2, figure 1 and 2). To systematically review the effect of the Bragg peak degradation, a single beam was optimized in the Eclipse TPS (Varian) from a gantry angle of either  $0^\circ$ ,  $270^\circ$  and  $315^\circ$  for all patients. In the clinical routine, some of these configurations would be neglected (e.g. see figure 2.4, patient 3, beam from  $0^\circ$ ) as the beam would penetrate most of the body. This would result in unnecessary dose to the patient and additionally increase range uncertainties. Similar to Publication 1, constraints were only given to the PTV to ensure the dose to be within 95% to 110% and organs at risk (OAR) were not close to the tumor volumes. The PTV was produced by expanding the clinically contoured CTV by a 3 mm margin. The beams were analyzed separately as well as three-field proton plan. As with active scanning, a modulation of the beam can be achieved quite easily, two intensity modulated proton therapy (IMPT) plans were additionally optimized and analyzed (see Publication 2, figure 3). An overview of the volumes and the tumor position is given in Publication 2, table 1.

Corresponding to Publication 1 and the method described by Baumann et al. [2017], voxel that were assigned to the lung contour were modulated with a  $P_{mod}$  specific density function. The modulation power values under investigation were chosen to be  $100\ \mu\text{m}$ ,  $250\ \mu\text{m}$ ,  $450\ \mu\text{m}$  and  $800\ \mu\text{m}$ . Again, the values were orientated on the measurements by

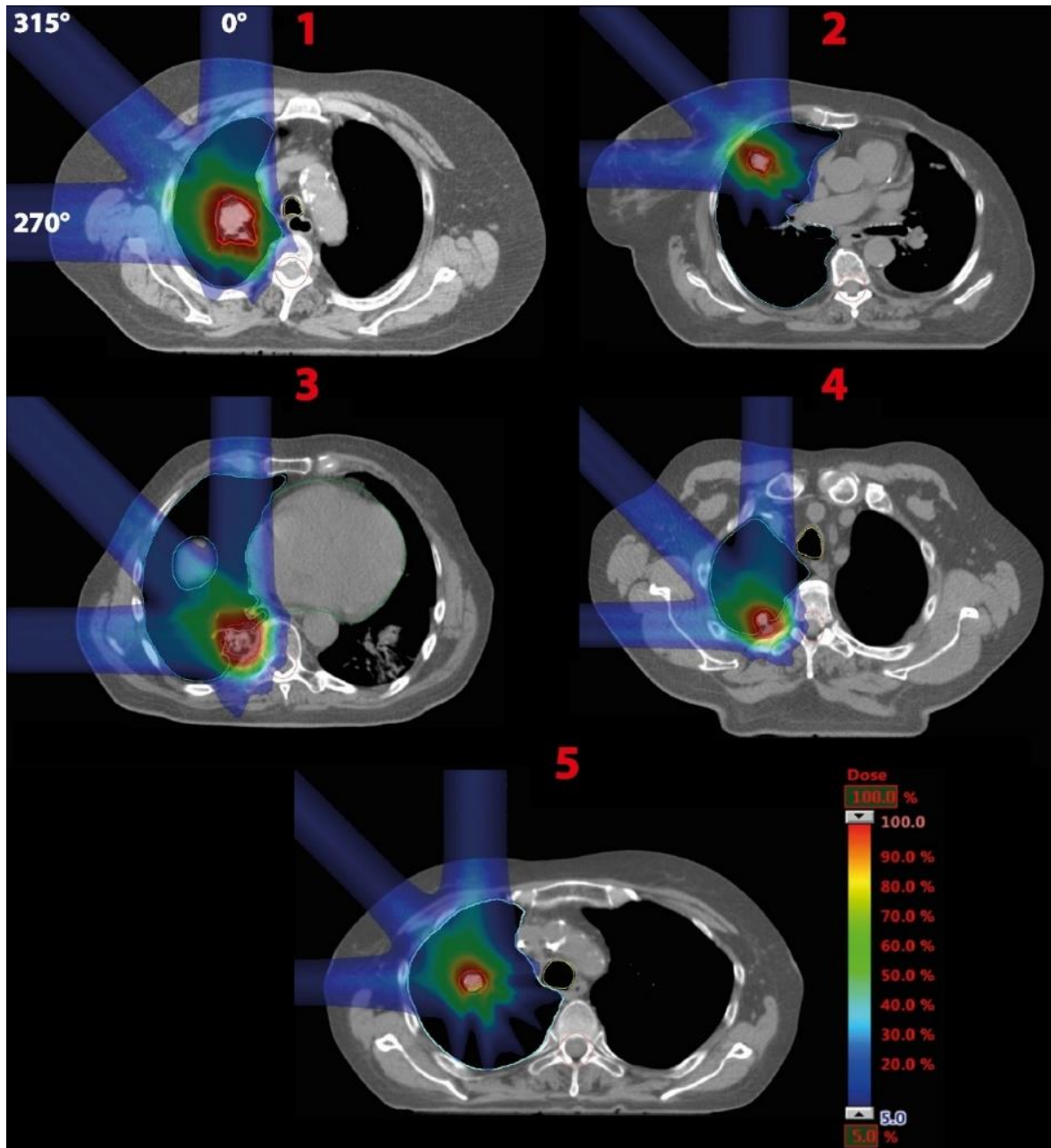


Figure 2.4: Axial views on the center of the tumor volume for the optimized proton treatment plans of five exemplary patients. For each patient, a single beam was optimized from 0°, 315° and 270°, respectively. As shown, also the resulting dose distributions with all three beams were evaluated. On the basis of [Baumann et al., 2019] - Figure 1 and 2. © Institute of Physics and Engineering in Medicine. Reproduced with permission. All rights reserved.



Witt [2014]. As before, all modulated and the original plans were calculated with the Monte Carlo code TOPAS.

The resulting dose distributions were compared by means of the mean dose of the CTV ( $D_{mean}$ ), the  $D_{98\%}$  and the  $D_{2\%}$  of the CTV. The  $D_{98\%}$  and the  $D_{2\%}$  describe the dose given to at least 98% (2%) of the volume. Thus, these values are the robust equivalents of the minimum and maximum dose.

In general, the dose distributions showed the same behavior when comparing the modulated dose with the originally planned dose as presented in Publication 1. This is shown in Publication 2, figure 5: The dose in the tumor is smoothed and decreased and the dose distal to the tumor is increased. As the distances in lung are small, the effect on the dose is not as profound as assumable from figure 2.3.

Table 3 and 4 in Publication 2 give the evaluated parameters for the CTV as well as for the OARs (for patient 1 only) that might be affected. Figure 2.5 (also see Publication 2, figure 6) shows the effects graphically: The degradation transports more dose distally. Thus, the high doses presented by the 95% and 80% isodose lines are decreased in its extension and volume but the low dose represented by the 20% isodose line is increased in its distal extension and volume in all cases. It is also visible, that the effect is more developed in the lung (figure 2.5, patient 1-2,5) than in normal tissue (patients 3-4). This is quantified as range uncertainty in table 2 (Publication 2): In normal tissue the range uncertainty for the 800  $\mu\text{m}$  modulation power is about  $\pm 3$  mm and in lung roughly  $\pm 8$  mm. In all fifteen patient plans, a decrease in the mean dose of up to 5% was found.

However, these results are a very conservative approximation, as the modulation power is more likely to be below 450  $\mu\text{m}$ . In this case, the decrease in  $D_{mean}$  is reduced to 3% at maximum and more likely to be around 1%. The range uncertainty is reduced to be approximately within  $\pm 2$  mm in normal tissue.

To transfer the results of the single beam plans to more clinical plans, the three field plans and the IMPT plans were also evaluated. The results showed for both, the single beam optimized plans and the IMPT plans the same reductions in the mean dose as for the single field plans. In most cases, the decrease in the mean dose correlated with the decrease of the mean dose of the beam with the longest path in the lung. Thus, the maximum decrease found for the single field set-up defines the decrease of the whole plan.

Hence, the resulting effects on the mean dose are in an order of magnitude that is clinically acceptable at the current state of accuracy for lung tumor treatment as the likely deviation in the mean dose is roughly -1% (up to -3% for a  $P_{mod}$  of 450  $\mu\text{m}$ ). Nevertheless, the results are strongly depending on the modulation power and a better knowledge of the modulation power of lung tissue would reinforce the drawn estimations and conclusions.

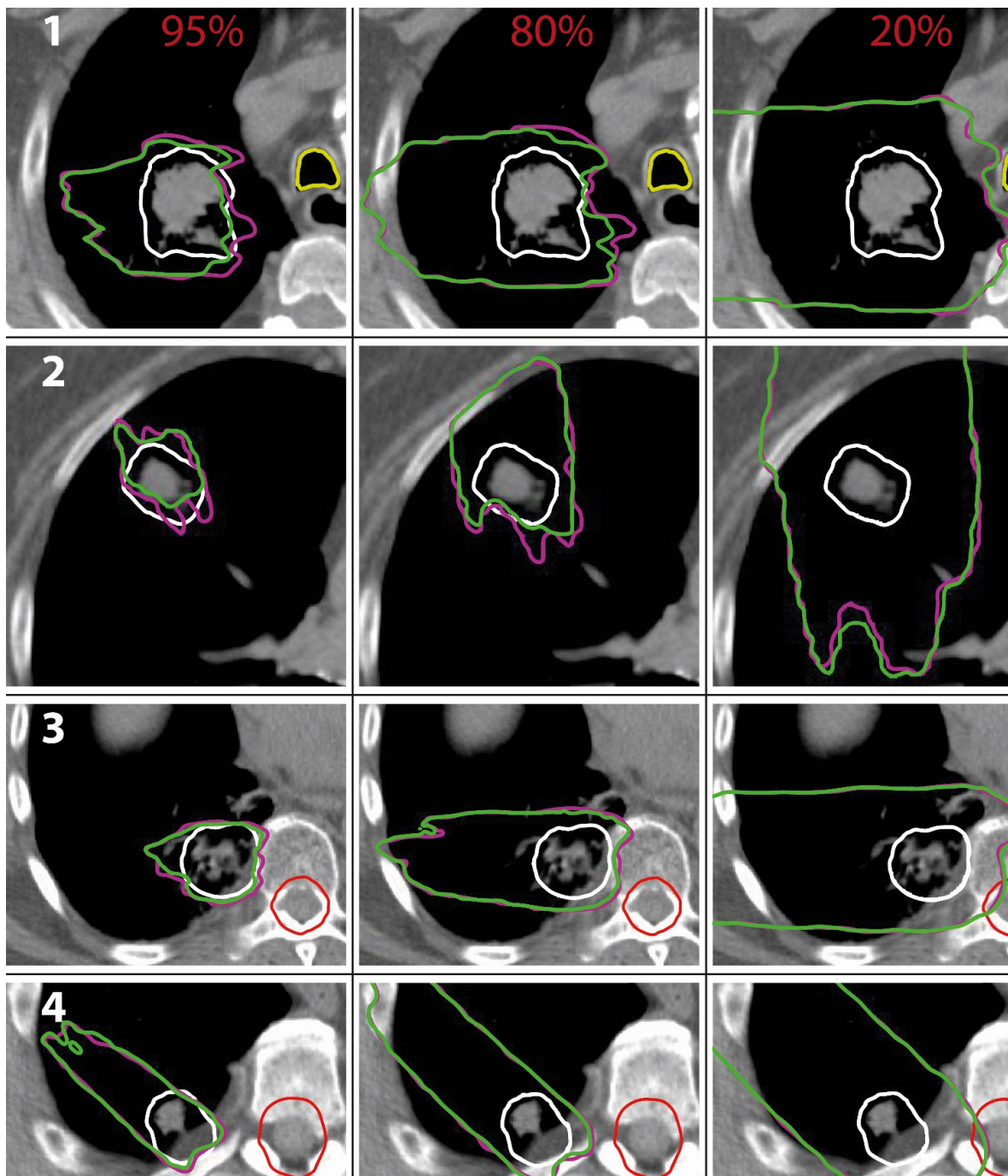


Figure 2.5: The 95% (left column), 80% (middle column) and 20% (right column) isodose lines for four different patient cases and beam configurations. In purple, the planned dose without the Bragg peak degradation is shown and in green, the corresponding dose distribution when a modulation power of  $800\ \mu\text{m}$  is assumed and accounted for. Figure taken from [Baumann et al., 2019] - Figure 6. © Institute of Physics and Engineering in Medicine. Reproduced with permission. All rights reserved.

### 2.2.2 | Contribution

K.-S. Baumann designed the study and prepared the manuscript. He produced the density modulated DICOM sets. The MC calculations were performed with the beam monitor system of the Marburg Ion-beam therapy center, which was commissioned by K.-S. Baumann beforehand. He analyzed the DVHs and produced all figures. V. Flatten optimized the treatment plans and converted the DICOM plans into TOPAS input files. She subsequently generated the DVHs and supported the analysis. U. Weber had the original idea for the density modulation and the mathematical model. The tool to optimize the density probability functions was created by U. Weber. S. Lautenschläger and F. Eberle contributed to this work by contouring the DICOM sets and helped with clinical information on treatment plans. K. Zink supervised the work and helped with the physical assessment. R. Engenhardt-Cabillic helped with the clinical assessment and supervised the work. All authors revised this manuscript, substantively.

## 2.3 | Article 3 - submitted to be published

### Experimental determination of modulation power of lung tissue for particle therapy

#### 2.3.1 | Summary of publication 3

Publication 1 and Publication 2 use values for the modulation power that are based on the measurements by Witt [2014], which covered a range of  $P_{mod}$  from 100 up to 750  $\mu\text{m}$ . This measurement was performed with a complete, ventilated porcine lung. However, the results were not published and adequate image material to estimate the beam path through the lung and to describe the ventilated state of the lung is missing. The only other publication which gives results for ex-vivo lung measurements features plastinated lung samples [Titt et al., 2015]. The effect of the plastination, however, might affect the modulation power. Thus no reliable values for the modulation power of human lung in its physiological state can be estimated.

The aim of this publication [Burg et al., 2021] was to produce citable data for the modulation power of lung and to narrow the range of the values for  $P_{mod}$  as the results from Publication 1 and Publication 2 strongly depended on the chosen modulation power.

Two porcine lungs from domestic pigs and one lung from wild boar were chosen, as porcine lung offers the closest approximation to human lung [Judge et al., 2014]. To extend the data not only by reproducible in-beam measurements but also by additional and CT imaging, the porcine lungs were deep frozen during ventilation and cut into 5 samples (Sample 1-3 from domestic pig, 4-5 from wild boar). Each sample had a size of  $4 \times 4 \times 10 \text{ cm}^3$ , as this size and the frozen state offered the possibility to perform CT imaging with a conventional (resolution of 1 mm) and an industrial CT scanner (resolution up to 50  $\mu\text{m}$ ). A 3D printed sample holder was designed to allow careful handling and distinct positioning of the samples in the beamline (also see Article 3, figure 1).

Figure 2.6 shows a CT scan of the five samples after cutting. The industrial CT scan on the right shows the clearly increased resolution. The high resolution CT indicates that the lung sample consists of larger structures which are mainly due to the larger bronchial structure in the lung. These are also blurrily visible in the conventional CT scan. Additionally, the high resolution image shows also the fine substructure of the alveoli filled with air.

Each sample was irradiated with a 140 MeV carbon ion beam at three different positions within the sample at the Marburg Ion-Beam Therapy Center. The resulting Bragg curve was measured with the peakfinder watercolumn (PTW) with and without the sample placed in the beam line (also see Article 3, figure 2).

Analog to the described determination of the modulation power  $P_{mod}$  in figure 1.2, figure 2.7 shows exemplarily the resulting modulation power for one sample: The measured reference

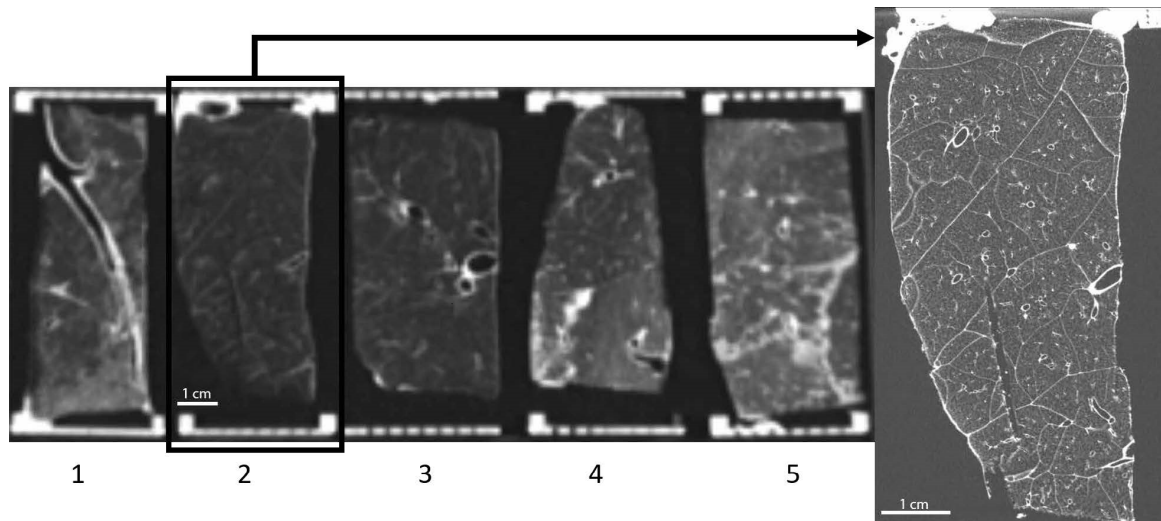


Figure 2.6: CT images of the central slice of the five porcine lung samples. On the right, the high resolution CT image of sample number two acquired with the industrial CT scanner is shown. Figure taken from [Burg et al., 2021] - Figure 3. © Institute of Physics and Engineering in Medicine. Reproduced with permission. All rights reserved.

curve is convolved with an optimized normal distribution to fit the measured degraded curve. The given values for the width of the normal distribution  $\sigma$  and the displacement in water  $\mu$  allow the calculation of the modulation power via equation 1.3.

As also illustrated in the top part of figure 2.7, the optimization with a single Gaussian distribution does not always result in a complete agreement between the measured modulated curve and the convolved curve in all cases. These discrepancies mainly occur when larger structures are visible in the beam path as indicated by the black arrow on the left side of figure 2.7. In these cases, the measured modulation power and thus the measured structure size is a cumulative structure size consisting of two or more different structure sizes: the larger bronchial structure size and the fine alveoli structure size. Thus, we introduced an optimized method to better estimate the modulation power and achieve a higher agreement between the measured and convolved curve: Instead of a single Gaussian distribution, a double Gaussian was optimized. This is shown in the bottom part of figure 2.7. In this case, two different modulation power values are obtained, which describe the smaller structures as well as the possible larger structures in the lung. With the normalization factors (also see Article 3, equation 4), a cumulative modulation power can be derived. All resulting modulation power values for the 3 positions at the five samples are given in Article 3, table 1.

Additionally, the energy independence was confirmed, which was postulated by the definition of the modulation power [Baumann et al., 2017, Ringbaek et al., 2017] but never tested for lung measurements (see Article 3, figure 6).

Finally, to give an estimate of the uncertainty and the range of fluctuation of the modulation power for adjacent lung tissue, repositioning measurements were performed. As shown in

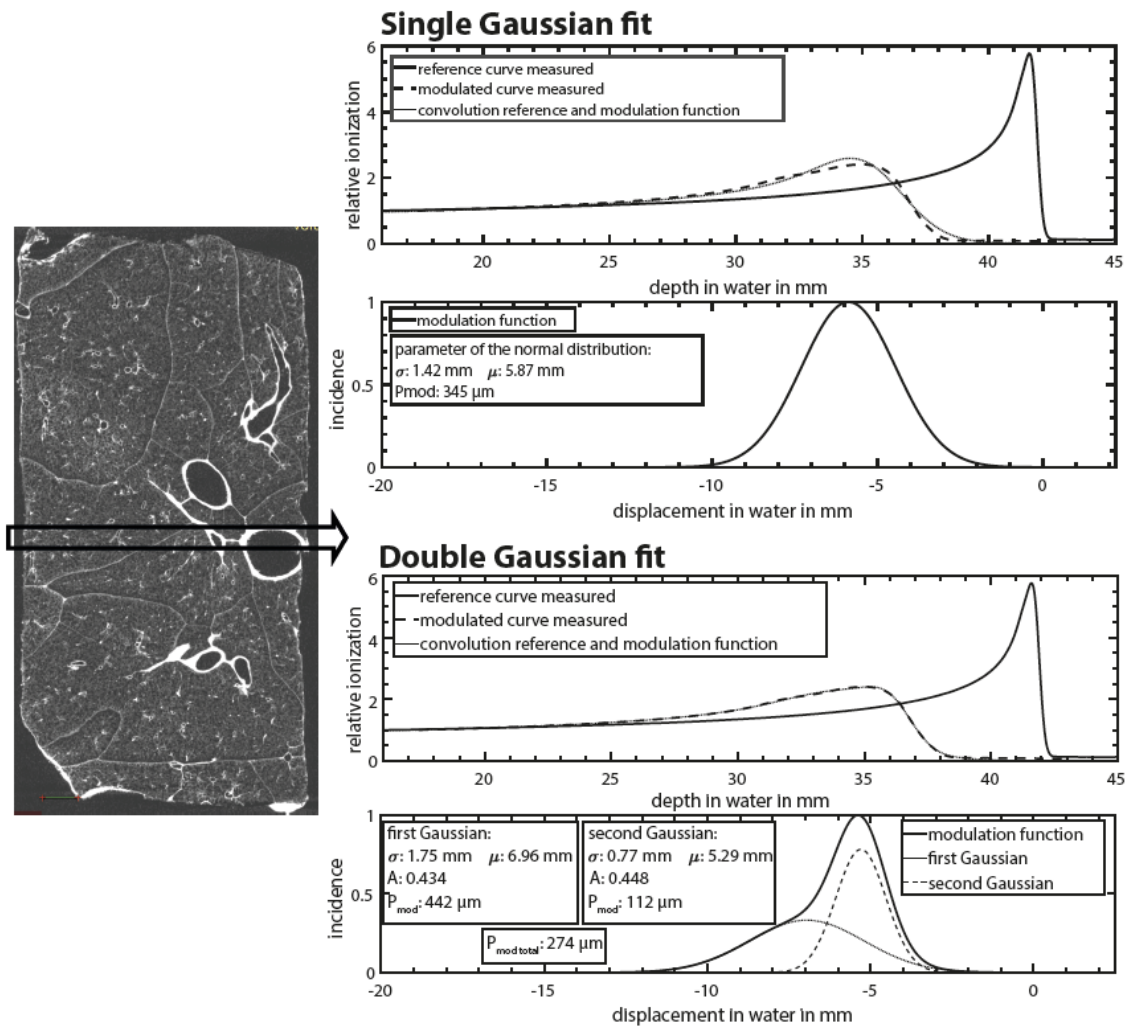


Figure 2.7: Determination of the modulation power  $P_{mod}$  for sample number 3 at the central position. In the top graph, the optimization with a single Gaussian distribution is shown and in the bottom plot, the proposed analysis with the double Gaussian optimization is shown. Figure taken from [Burg et al., 2021] - Figure 5. © Institute of Physics and Engineering in Medicine. Reproduced with permission. All rights reserved.

Article 3, table 1, the center position of sample number one was repositioned twice to estimate the measurement uncertainty. It was also shifted by 2 mm or rotated by  $2^\circ$  to estimate the fluctuation of the modulation power over a small area of lung tissue.

With the systematic freezing of the samples, we were able to produce reproducible results for the modulation power of lung tissue. The probable values for the modulation power are in average around  $220 \mu\text{m}$  with a measured minimum of  $62 \mu\text{m}$  and a maximum of  $583 \mu\text{m}$ . This drastically reduces the range of probable modulation power values, as the old values proposed  $100 \mu\text{m}$ - $800 \mu\text{m}$ . The larger values were measured in lung sample number five, which was not ventilated probably. So, for a healthy lung, the range can even be reduced to  $62 \mu\text{m}$ - $367 \mu\text{m}$ . In cases where patients have a collapsed lung, COPD or severe pneumonia,

the higher modulation power measured in the not probably ventilated lung sample cloud be a better estimate.

The repositioning showed deviations of roughly 10% and the rotation and shift a deviation up to 30%. This, however, indicates that the modulation power strongly depends on the exact position where the beam passes the lung and can change by almost 30% within the normal setup accuracy of the clinical routine. Nevertheless, as shown in Publication 1 and Publication 2 the effect on the dose distribution does not drastically change between an assumed modulation power of 200  $\mu\text{m}$  or 250  $\mu\text{m}$ . However, it might be of interest if the modulation power of the region of interest in the lung is tending more towards the 60  $\mu\text{m}$  or the 600  $\mu\text{m}$ . Therefore, the acquired data was further used in Publication 4 to validate a model to estimate the modulation power calculated with a clinical CT histogram analysis.

### 2.3.2 | Contribution

J. Burg wrote the manuscript and performed all measurements. He designed and executed the freezing process as well as the sample acquisition and cutting. V. Flatten helped with the BP measurements and documented the sample cutting. U. Weber helped design the experimental set up and the freezing process. H. Vorwerk and R. Engenhardt-Cabillic contributed to the clinical interpretation of the collected data. K. Zink helped with the physical assessment. He established the contact to the industrial micro CT site. K.-S. Baumann supervised this work and supported designing the study. He helped with the freezing and cutting procedure and the BP measurements. K.-S. Baumann performed parts of the analysis of the modulation power. All authors revised this manuscript, substantively.

## 2.4 | Publication 4

### Estimating the modulating effect of lung tissue in particle therapy using a clinical CT voxel histogram analysis

#### 2.4.1 | Summary of publication 4

In Publication 4 [Flatten et al., 2021], the topic of an estimation of the modulation power via a clinical CT histogram is addressed. Even so Article 3 [Burg et al., 2021] narrowed the range of probable modulation power values for lung, a patient specific high precision lung cancer treatment with protons or carbon ions should include the effect of the Bragg peak degradation. Thus, a patient specific evaluation and estimation of the modulation power is needed.

The mathematical derivation given in Publication 4 is based on a basic assumption: Even in the case, where the resolution of the image is not sufficient, the microscopic structure of heterogeneous tissue spreads around a mean value and thus, broadens the width of an histogram. This is shown in the summarizing figure 2.8:

With the assumption that the heterogeneous material consist of two materials (tissue and air in the case of lung), a high resolution CT image would result in a histogram, which clearly identifies each voxel as either air or tissue. Mathematically, this would equal a binominal distribution. A decrease in the resolution would lead to intermediate density values and a further decrease would center around the mean density without displaying the original materials. For a low resolution, the binomial distribution can be approximated by a normal distribution. However, the modulation power  $P_{mod}$  correlates with the structure size  $d$  [Baumann et al., 2017] and the structure size correlates with the high resolution  $r_0$  needed to clearly identify all voxel as one of either original material. The width of the clinical CT histogram correlates with the ratio  $n$  of the clinical image resolution  $r$  and the original resolution  $r_0$ . Thus, the modulation power  $P_{mod}$  can be correlated with the width  $\sigma$  and the mean  $\mu$  of a normal distributed CT histogram of a clinical CT image. The exact mathematical derivation is given in Publication 4 equations 2-7 and 10-15 and results in the proportionality under investigation:

$$P_{mod} \propto \sqrt[3]{\frac{\sigma^2}{-1000HU \cdot \mu - \mu^2}} \equiv P_{fit} \quad (2.2)$$

Two measurement series were performed and analyzed. First, eight differently heterogeneous materials were measured in a proton beam at the West German Proton Therapy center Essen (WPE) and scanned with a conventional CT scanner (Somatom Definition,



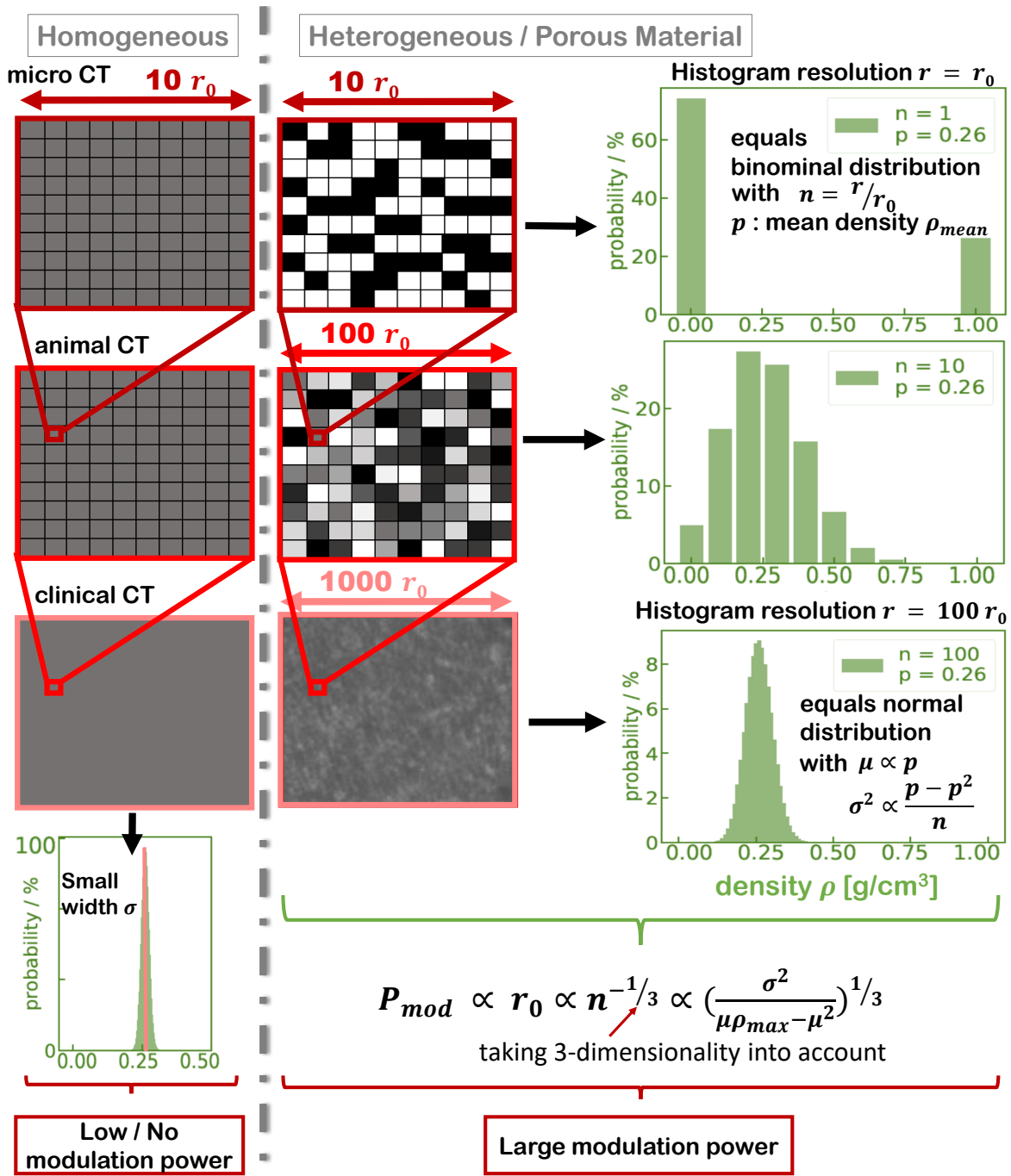


Figure 2.8: Schematic overview of the basic concept for the CT histogram analysis and the mathematical relations. On the left, images of a homogeneous material are shown. In the middle, the images for the heterogeneous material are shown and on the right, the corresponding histograms. The resolution is decreased from top to bottom from the highest resolution needed to fully resolve the heterogeneous material to the clinical CT image. Additionally, the corresponding proportionalities are given. On the basis of [Flatten et al., 2021] - Figure 2.

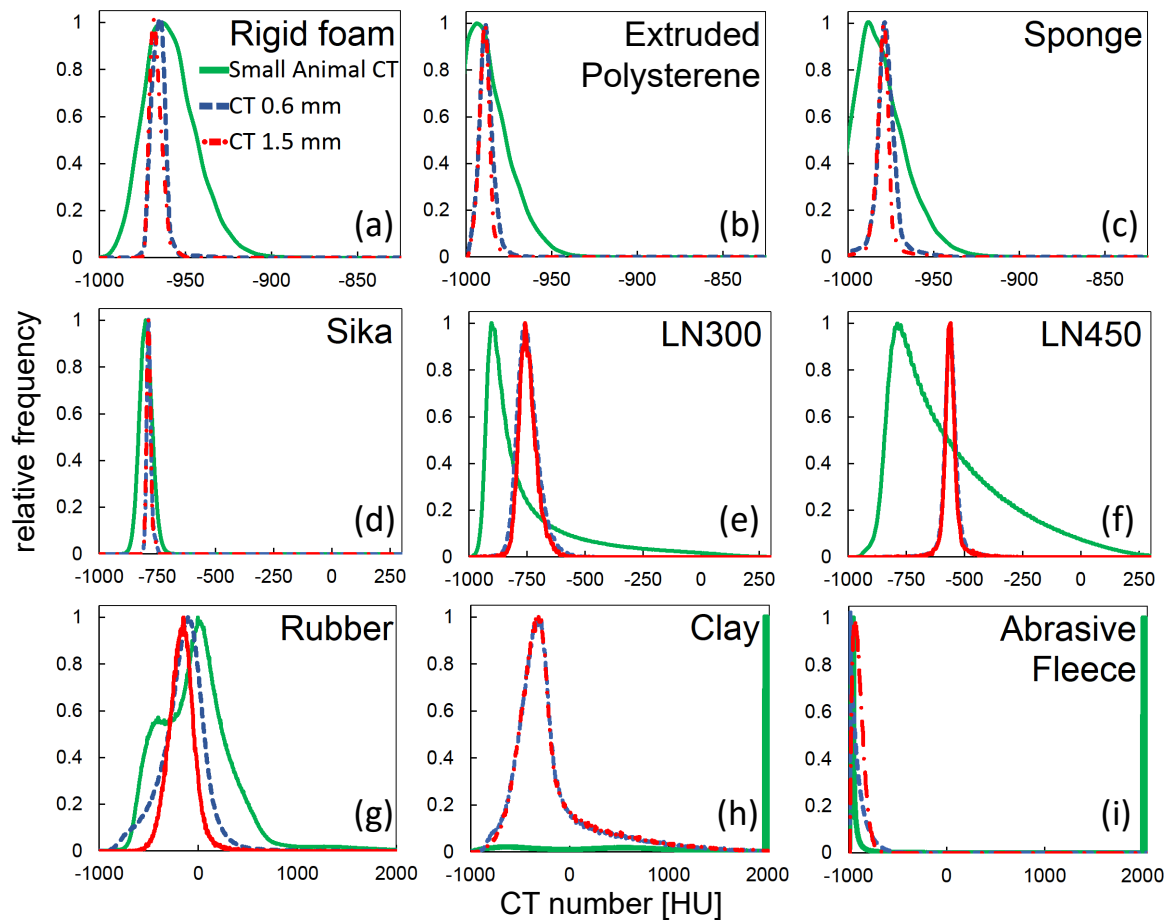


Figure 2.9: CT histograms for the nine materials under investigation. Each plot shows three different slice thicknesses: 0.1 mm (small animal CT) in green, 0.6 mm in blue and 1.5 mm in red. Note the different scales on the x-axis. Figure taken from [Flatten et al., 2021] - Figure 5. © Institute of Physics and Engineering in Medicine. Reproduced with permission. All rights reserved.

Siemens Healthineers) with a resolution of  $1.0 \times 1.0 \times 0.6 \text{ mm}^3$ . Second, the lung sample measurements performed for Article 3 were used in combination with CT images of the same CT scanner and parameters. The measurement procedure in both series was the same as already described in Article 3.

Before analyzing the resulting CT histograms, measurements to determine the influence of various set-up and CT parameters on the width of the histogram were performed and analyzed. It was found, that the effective exposure, defined as the applied exposure per slice and the surrounding attenuating material had a significant influence on the width of the histogram (see Publication 4, figure 3 and 4). Therefore, a reference material was placed next to the sample under investigation and was always scanned in the same scan to allow an estimation of the set-up-specific attenuation.

Figure 2.9 shows the resulting CT histograms for the heterogeneous materials. The influence of the CT resolution is shown with the additional curves for a high resolution small animal CT (X-Cube, Molecubes) with a resolution  $0.1 \times 0.1 \times 0.1 \text{ mm}^3$  and a lower resolution of

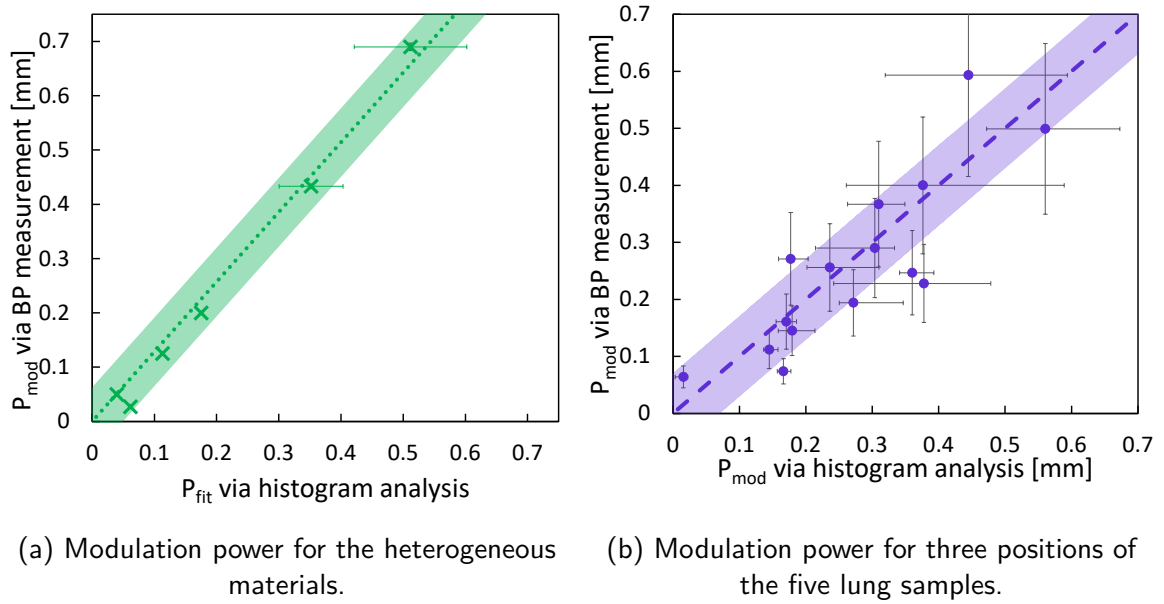


Figure 2.10: The modulation power  $P_{mod}$  acquired by the BP measurement plotted against  $P_{fit}$  ( $P_{mod}$ ) calculated with the CT histogram analysis. The dotted linear regressions are marked by the green and blue line, respectively. The surrounding bands indicate an agreement with the regression line within  $\pm 0.04$  mm for (a) and  $\pm 0.06$  mm for (b). Figures taken from [Flatten et al., 2021] - Figure 6 and 8. © Institute of Physics and Engineering in Medicine. Reproduced with permission. All rights reserved.

$1.0 \times 1.0 \times 1.5 \text{ mm}^3$  (also see Publication 4, figure 5). From left to right the histograms in figure 2.9 are roughly increasing in their modulation power that was measured in the particle beam. This is underlined by the increasing discrepancies between the three curves for each material. In general, the more the small animal CT features a binomial distribution and not a normal distribution, the higher is the probable modulation power. The measurement results are given in Publication 4, table 1.

As equation 2.2 only shows a proportionality, the first step was to prove this relation and the second step was to derive the proportionality factor. Figure 2.10a shows the values of the modulation power  $P_{mod}$ , measured in-beam, plotted against the calculated values for  $P_{fit}$  which were derived via equation 2.2 from the fitted mean and width of the normal distribution. The dotted line shows the fitted normal regression. The band indicates a good agreement within  $\pm 0.04$  mm. The obtained proportionality factor for the 0.6 mm slice thickness was 1.28 mm.

In a final step this proportionality factor was taken and multiplied with the  $P_{fit}$  values for the lung sample CT histograms. The results are given in figure 2.10b. Again, the modulation power acquired via the in-beam measurement described in Article 3 and the ones obtained with the CT histogram analysis are in good agreement.

The uncertainties shown in figure 2.10a mark the deviation of the analyzed clinical CT histograms from a normal distribution, especially for higher values of  $P_{mod}$ . However, the accuracy in x-direction in figure 2.10b is highly influenced by the exact position of

the analyzed CT region. Thus, the uncertainty was estimated by slightly shifting the contour within 2 mm as a more exact matching between scan and in-beam measurement position could not be performed. This corresponds to the discussion and uncertainty measurements of Article 3: In y-direction, the 30% uncertainty caused by the 2 mm shift or 2° rotation was chosen as uncertainty even so this is probably a very conservative assumption. The error bars underline the discussion in Article 3: The higher modulation power values mostly correspond to two or more structure sizes, therefore, a single Gaussian distribution might not completely describe the CT histogram.

Nevertheless, this model enables a patient individual or even regional analysis of the modulation power of a distinct region in a clinical CT. This is the basis to incorporate the effects of the Bragg peak degradation into the planning procedure to estimate and hopefully compensate the underdose in the tumor volume.

### 2.4.2 | Contribution

V. Flatten wrote the manuscript and executed most of the measurements of the study. She designed the study and performed the analysis of the data. J. Burg supported this work by providing the lung samples and the results of their in-beam measurement. Beforehand, he designed the freezing, cutting and sample handling process. M. Witt and L. Derksen helped with the estimation of the modulation power via the BP measurement. P. Fragoso Costa performed the measurements with the small animal CT. J. Wulff and C. Bäumer supported the original idea and helped design the study. They helped perform the BP measurements of the heterogeneous surrogates and gave input for the data analysis, continuously. B. Timmermann supported the idea and allowed a clinical assessment. U. Weber helped with the lung sample acquisition, handling and measurement. H. Vorwerk and R. Engenhardt-Cabillic contributed to the clinical interpretation of the collected data. K. Zink helped with the physical assessment and supported the taken measurements. K.-S. Baumann supervised the work and the design of the study. He helped with all the BP measurements. K.-S. Baumann performed parts of the analysis of the modulation power. All authors revised this manuscript, substantively.

## 2.5 | Publication 5 - side project

### **A phantom based evaluation of the dose prediction and effects in treatment plans, when calculating on a direct density CT reconstruction**

#### 2.5.1 | Summary of publication 5

The last Publication 5 [Flatten et al., 2020] is labeled as side project as it has no direct attachments to the topic of the Bragg peak degradation. Nevertheless, for the measurements and dependencies discussed in Publication 4, a serious engagement with the topic of clinical CT imaging in radiation therapy was essential. Thus, this publication deals with the implementation of CT imaging in the clinical workflow for photon radiotherapy with a focus on a commercial algorithm that directly converts the measured Hounsfield units (HU) to density values.

The commercially available 'DirectDensity' reconstruction algorithm (Siemens Healthineers) uses a threshold to divide the acquired CT image into a 'bone image' (see Publication 5, figure 1). As bone is describing the highest natural density values and is present in every clinical CT image, it offers a good reference. In projection space, this bone sinogram is combined with a physical attenuation model and the original sinogram. Put together, a relative electron density (RED) sinogram and thus, a RED CT image can be reconstructed. Figure 2.11 (also see Publication 5, figure 2) shows the benefit of the implementation of the DD algorithm: The standard HU reconstruction is strongly depending on the chosen tube voltage. Whereas the DD reconstruction features the same calibration curve for all tube voltages. Additionally, it features just one regression curve which is needed to be implemented over the range of image values, while the HU reconstruction is divided in at least two curves.

The DD reconstruction was evaluated for different photon radiation techniques (single field, 3D conformal radiotherapy and VMAT) and for different phantoms evaluating basic geometries as well as anthropomorphic set-ups (see Publication 5, figure 3). To test the limits of the manufacturer recommendation, the algorithm was tested at the presence of metal implants, as these feature a higher density as bone. Thus, the algorithm with its simple threshold will assign the metal implants to the bone image, which could lead to distortion and errors. Additionally, the combination with an iterative Metal Artifact Reduction (iMAR) algorithm was evaluated.

The calculated dose distribution were evaluated by means of dose profiles (see Publication 5, figure 4-6), DVHs (see Publication 5, figure 7 and 8) and mean doses (see Publication 5, table 2). As visible from the dose profiles, the highest discrepancy was found in air with

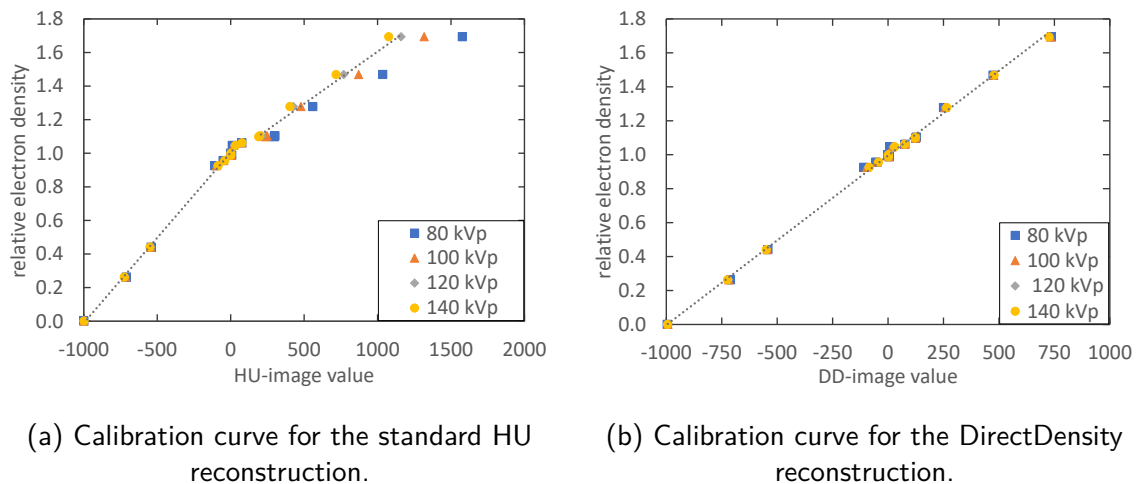


Figure 2.11: Calibration curves for the two different reconstruction algorithms for four tube voltages of 80 kVp (blue), 100 kVp (red), 120 kVp (grey) and 140 kVp (yellow). The dotted line shows the fit that was included in the TPS for the typically used 120 kVp curve. Figures taken from [Flatten et al., 2020] - Figure 2. Reproduced with permission.

a deviation of +3.3% locally compared to the HU dose calculation. However, in clinical cases the deviations are reduced as the number of beam direction is increased. The results agree with Van der Heyden et al. [2017]: The maximum dose difference for clinical plans was found to be within 1% (0.7% in the trachea) and more likely in the order of 0.4%. The DVHs showed no visible differences.

The estimated RED values were also evaluated (see Publication 5, table 1 and 3): Again, difference occur for the low densities like air or lung tissue and for the evaluated metal implants. However, in case of metal, the use of a higher tube voltage (in this case 140 kVp) which can be used with the DD algorithm shows a significantly better estimation of the RED for metals than the standard HU reconstruction. Therefore, the DD implementation shows deviations in regions where the uncertainties in the clinical routine are high in the first place (e.g. in regions like air and metal) and gives even better results for the metal reconstruction.

This is also visible in figure 2.12 (also see Publication 5, figure 9 and 10). The ideal RED value should be around seven. This means, that the RED value is underestimated in all cases but better represented by the high tube voltage DD images. Additionally, the DD image show less image artifacts surrounding the metal implant. This would severely increase the accuracy of the calculated dose.

Being restricted to only one calibrated tube voltage is a disadvantage in radiotherapy as the patient could clearly benefit from an optimized tube voltage. The implementation of such an algorithm would allow to scan children with the 80 kVp and adipose patients with 140 kVp. For both patient groups, this would result in a higher image quality and thus less dose given to the patient for a constant image quality. The found differences in RED and dose are neglectable for most clinical situations. Even in the regions where differences are higher,

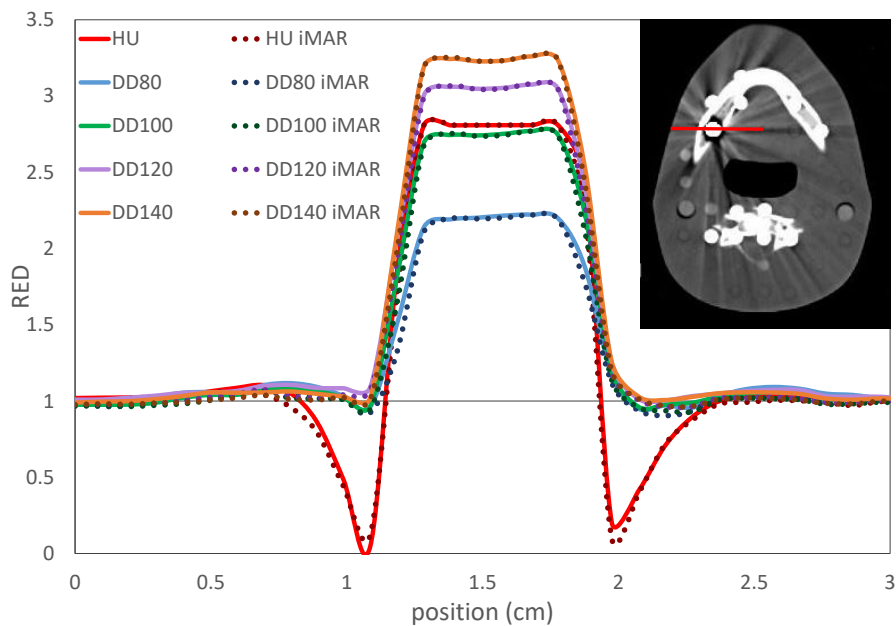


Figure 2.12: RED profile through the metal implant and the surrounding tissue for all reconstructions under investigation. Figure taken from [Flatten et al., 2020] - Figure 10. Reproduced with permission.

a change of the patient geometry is likely and more severe. Additionally, the implemented algorithms for the dose calculations have also high uncertainties in the problematic region. For particle therapy, such an algorithm would be very beneficial. However, as the stopping power and not the electron density is needed, this cannot be easily implemented in particle therapy.

## 2.5.2 Contribution

V. Flatten prepared the manuscript and executed the measurement series with metal. She coordinated and supported the study design and all measurements. The figures and the analysis of the metal effects were performed by V. Flatten. A. Friedrich executed the measurements without metal and produced most of the figures. She performed the general analysis. R. Engenhardt-Cabillic supported the clinical assessment with her expertise. K. Zink supervised the work and helped with the physical assessment. All authors revised this manuscript, substantively.

## 3 | Discussion

### 3.1 | Dependencies of the effects caused by the lung modulation

The dependencies of the Bragg peak degradation on the dose distribution were analyzed in Publication 1 [Flatten et al., 2019]. In this phantom study, we showed that the effect increases with an increasing path through the lung, a decreasing volume (more precisely: the scaled tumor length in beam direction as defined in equation 2.1) and the modulation power. These results were confirmed in Publication 2 [Baumann et al., 2019] and the publication by Winter et al. [2020], where both include the degradation effect in the calculation of lung cancer treatment plans. In both publications, the resulting differences between the non-modulated plan and the modulated plan increase for a small volume after a large beam through lung. For example, Publication 2, table 3 shows that for the same tumor volume, the effect increases from a difference in  $D_{mean}$  of -0.9% (270°) to -2.1% (0°) for an increasing depth in lung. And comparing two different volumes with the same mean depth in lung (see Publication 2, table 3 and 4, Patient 1 and 5 for the 315° beam configuration) a decrease in the underdose from -4.9% to -1.5% is observable for an increased volume (3 cm<sup>3</sup> to 47 cm<sup>3</sup>).

Other effects like the spot spacing in longitudinal direction also influenced the strength of the effect but depended strongly on the optimized spot weights. For the plans optimized with the open-source software tool matRad [Wieser et al., 2017], this was also identified as critical parameters [Winter et al., 2020].

The results of Article 3 show a mean modulation power of 220 μm. Therefore, the red band ( $P_{mod} = 250 \mu\text{m}$ ) in figure 2.3 gives the most probable dose difference that can be assumed for the patient specific configuration. For a worst-case scenario, the results shown in green ( $P_{mod} = 450 \mu\text{m}$ ) should be consulted.



## 3.2 Effects of the lung modulation for clinical cases

Publication 2 gives the first published results of the degradation effect on lung cancer patients. In 2020, [Winter et al.](#) implemented the degradation by convolving the pristine Bragg peak with a normal distribution. The width of the normal distribution depends on the distance in lung which was calculated via ray-tracing. Thereafter, the analytical dose calculation is used to sum the dose of the degraded BPs. This method was then performed on 10 patients for a representative modulation power of 256  $\mu\text{m}$  and a worst-case scenario of 750  $\mu\text{m}$ . This study focuses on the effects in IMPT plans consisting mostly of three beams. Thus, the results cannot be directly compared, however, the two IMPT plans under investigation in Publication 2 showed that the results of the mean dose is in the same order of magnitude as for the most degraded single beam. Nevertheless, effects on the minimum and maximum dose as evaluated by [Winter et al.](#) are not comparable as this is highly influenced by the spot weights and additionally, we investigated the  $D_{2\%}$  and the  $D_{98\%}$  because of the high uncertainties on such single voxel values like the minimum and maximum dose.

Comparing the mean doses shows that the reported differences compared to the non-modulated cases are of the same magnitude: a maximum deviation of the mean dose of -4.9% ( $P_{mod} = 750 \mu\text{m}$ ) is decreased to -1.6% ( $P_{mod} = 256 \mu\text{m}$ ) [[Winter et al., 2020](#)]. These results are stated for the patient with the highest effects. However, the tumor volume and dimensions are not given. Therefore, no deeper comparison can be made. Because the author states that the effect is reduced for larger tumor volumes, it is presumably a small tumor volume.

As the influence on the dose distribution are small in the clinical context of moving targets, the effects can be easily compensated for in clinical treatment planning. Publication 2, figure 7 proposes two different options to acknowledge the effects of the BP degradation: the first option, that is clinical already in use, is the extension of the PTV margins in proximal but mainly in distal beam direction. The application of such beam specific targets feature a severe increase of target coverage for range uncertainties [[Park et al., 2012](#)] and are implemented in commercial TPS (e.g. Eclipse, Varian). Especially for thoracic tumors, including all parameters of uncertainties resulting from stopping power, set-up and motion in a beam specific target increases target coverage and dose sparing at pencil beam scanning facilities [[Lin et al., 2015](#)].

The second option displayed in Publication 2, figure 7 proposes a slightly increased dose in the PTV margin (not the CTV) to compensate the effect of the degradation. As the guideline of the ICRU [[ICRU, 2016, 2017](#)] proposes the dose of the target to be within 95% to 107%, a minimal increase of 3% in the target margin would be feasible for proton therapy. However, this implementation would increasingly benefit from the exact calculation of the patient and plan specific disturbed dose calculation. Hence, this method is not likely to be

integrated into the clinical routine. Especially, since the publication of [Winter et al. \[2020\]](#) is a step further to the implementation of the effects of the Bragg peak degradation in a clinical TPS. Then, the effect can be directly integrated into the optimization process. Nevertheless, this concept should demonstrate that hotspots (points exceeding 105% of the prescribed dose) are not critical as these points are smoothed by the lung degradation. Points that are underdosed however, will most likely be further reduced in dose, especially at the proximal or distal end of the PTV.

### 3.3 Measurement of the modulation power

The results for the degradation effect on the dose [[Flatten et al., 2019](#), [Baumann et al., 2019](#), [Winter et al., 2020](#)] indicate that the knowledge of the modulation power is essential. Some publications have measured the modulation power and effect for heterogeneous lung substitutes: [Titt et al. \[2015\]](#) used substitutes and a plastinated lung to evaluate the modulation effect. He estimates the uncertainties in the distal fall-off up to 3 mm. As the plastinated lungs probably differ from physiological lungs, plastinated lungs are more a substitute than a precise measurement of data for physiological lung. [Hranek et al. \[2020\]](#) presents measurements of seven different lung mimicking substitutes. The measured modulation power values ranged between 0.1 mm and 1.1 mm. This demonstrates the broad range of the modulation power for materials with similar densities to lung (0.03-0.51 g/cm<sup>3</sup>). [Dal Bello \[2017\]](#) also presents measurements and simulations for lung substitutes and a 3D printed phantom which center around a mean modulation power of 250  $\mu\text{m}$ . Publication 4 [[Flatten et al., 2021](#)] also presents new values for the modulation power of eight different heterogeneous materials, ranging from 0.03 mm to 0.69 mm with a mean modulation power of 0.20 mm.

Measurements in lung were performed in a master thesis [[Witt, 2014](#)] and recently, in a publication which facilitates proton radiography [[Meijers et al., 2020](#)]. Unfortunately, the work by [Meijers et al.](#) does not present values of the modulation power but compares measurements of the water-equivalent thickness (WET) to TPS calculations. Nevertheless, the thesis by [Witt](#), which presents measurements with a carbon ion beam, gives a first indication of the range of the modulation power of lung tissue. The mean modulation power measured was 0.44 mm and the minimum and maximum values were 0.15 mm and 0.75 mm, respectively.

The results presented in Article 3 narrow down the range of probable values for the modulation power in lung to 0.06 mm-0.59 mm with most values in the range of  $0.25 \pm 0.15$  mm. An advantage compared to the other results is clearly the handling of the frozen samples. In the unfrozen case, the lung degenerates over the measurement session of 4 hours or more and thus, reproducibility is not given and matching of image and measurement results need to be considered with special care. The newly presented method to optimize two Gaussian

distribution offers a higher conformity between measurement and extracted modulation power. Additionally, these results agree with the assumable mixture of structure sizes: One of the two fitted Gaussian distributions represents the structure size of the alveoli in the range of roughly 0.2 mm [Ochs et al., 2004] and the larger one (if present) represents the structure size of the bronchi of 0.8 mm [Seneterre et al., 1994].

For the treatment planning, the larger structures of the bronchi are probably accounted for as these are visible in the clinical CT. Hence, for the additional effect of the Bragg peak degradation by the alveoli a smaller modulation power of 0.2 mm should be assumed.

### 3.4 | Estimation $P_{mod}$ on clinical CT data sets

Implementing the estimation of the effect of the Bragg peak degradation in the clinical routine requires in total three points: First, a valid method to calculate the degradation effects is needed. This is given with the MC method established in Publication 1 and even more in Publication 2 or with the integration into an analytical PB calculation engine as it is done by Winter et al. [2020]. Second, as for every patient plan, the information about the exact geometrical conditions and the estimated stopping power of the anatomy in the beam path are needed to be known. Hence, a clinical CT and stopping power lookup-table are the essential basics. And third, the modulation power of the patient lung is needed for the exact calculation of the degradation.

As a first approximation for the modulation power of lung, the results presented in Article 3 can be used. For a rough estimate of the degradation effect on the basis of a plan recalculation, this will be sufficient, as Publication 1 and Publication 2 show only small deviations for modulation power values  $\pm 100 \mu\text{m}$ .

However, the next step would be to optimize the plan with acknowledging the modulating effect of the lung tissue. Hence, a rough estimate of the modulation power in general is not sufficient. In this case, a patient and even lung region specific analysis is essential, which is possible with the method presented in Publication 4.

The results published in Publication 4 show that the modulation power of heterogeneous materials and the frozen lung samples could be well estimated with the derived mathematical relation. For the clinical implementation, a CT and program specific calibration is needed to be performed with a lung substitute (e.g. LN-300) and a reference material that is present during the patient scan (e.g. the vacuum mat). Then, all patient scans with the calibrated CT program and the reference material can be used to estimate the modulation power for a specific region in the lung. As soon as the region of interest is contoured, a CT voxel histogram can be generated and scaled to the width of the reference material histogram. The resulting mean and width of the lung histogram enable the calculation of the modulation power via the calibration factor gained from the LN-300 measurement. This workflow can be established easily and economically in every clinic.

As particle therapy claims for itself to be a high precision therapy modality, an implementation of the degradation effects for the treatment of lung cancer patients is consequential for the long-term perspective.

### 3.5 Patient specific uncertainty analysis of the lung modulation effect

If we have now estimated the modulation power of the patient via the described method, the next step is to obtain an estimate for the dose uncertainties. As the optimization with degraded curves is a current topic of research, the integration into the clinics is on the verge but not yet realizable. In clinics where a MC tool with the density modulation as presented in Publication 1 and Publication 2 is established, the step is straight-forward. However, also other clinics can estimate the effects for each patient with the presented publications. As an example: Table 1 in Publication 2 states the tumor characteristics needed to evaluate the estimation proposed in Publication 1. Thus, the configurations with the maximum and minimum dose difference are investigated (see Publication 2, tables 3 and 4: minimum found for patient 1 at  $270^\circ$ ; maximum for *patient 5* at  $315^\circ$ ). The length in lung is measured to be 3.3 cm ( $3.6\text{ cm}$ ) for Patient 1 ( $5$ ) and the tumor length in beam direct is given as 4.2 cm ( $0.6\text{ cm}$ ). Including the volume, this results in values for  $L_S$  of 3.8 cm ( $0.7\text{ cm}$ ) and thus for  $d_L/L_S = 0.86$  ( $5.13$ ). Hence, figure 2.3 enables the estimation of decrease of the mean dose for the modulation power of  $450\ \mu\text{m}$  of roughly  $-0.5\%$  ( $-2.7\%$ ). This correlates well with the calculated values of  $-0.5\%$  for patient 1 and  $-3\%$  for *patient 5* as published in table 3 and 4 (see Publication 1).

The uncertainties on the presented values are still high but the presented works are the only published results that fulfill the aim to allow a patient-specific estimation of the effect of the Bragg peak degradation on the dose distribution.

### 3.6 Uncertainties for lung cancer treatment with PBS

There is one important point of criticism when it comes to evaluate the uncertainties of particle therapy for lung cancer patients that all presented results have in common: The investigated set-ups assume no movement of any kind. Besides every day set-up uncertainties, movement caused by breathing is the major source of uncertainty in the thoracic region. There are techniques like high frequency jet ventilation which hold the patient in a defined respiratory status [Santiago et al., 2013]. The downside of the method is that the patient has to be put under anesthesia over the whole course of treatment. Recent studies propose the utilization of deep-inspiration breath-hold in combination with

a breath-hold training for patients [Emert et al., 2021]. However, in most cases the aim to stop the motion caused by breathing is neglected and shifted towards control of the motion. Mostly, this is done by gating techniques [Lu et al., 2007, Ebner et al., 2017], where the respiratory phase is monitored and the beam-on time is synchronized with the breathing cycle. In a consensus statement from 2017, the PTCOG thoracic and lymphoma subcommittee defines the main requirements that need to be met to treat thoracic tumors with PBS [Chang et al., 2017]. As an upper limit, a movement of 5 mm is defined as reasonable for PBS. In comparison, for passive scatter techniques a movement up to 10 mm is acceptable. The main argument is the interplay effect between the different motions: the tumor movement caused by breathing and the beam movement due to the application technique [Tsunashima, 2012]. Hence, fast rescanning is recommended [Phillips et al., 1992, Knopf et al., 2011, Chang et al., 2017] so that the complete dose of a spot is not deposited at once, where the tumor might be not at the targeted position.

Gating only reduces the amplitude of motion to an acceptable value. Without gating, up to 20% decrease in dose for a 20 mm amplitude can be estimated [Tsunashima, 2012]. Rescanning on the other hand increases a homogeneous dose application in the target leading to a 7% decrease in dose if only rescanning and no gating is applied and a reduced decrease in dose of only 2-5% if both is used [Tsunashima, 2012].

Additionally, uncertainties resulting from the dose calculation algorithms and the HU to stopping power conversion are present for all particle plan calculations. Paganetti [2012] summarizes these uncertainties to uncertainties in the commission of the beam data and the beam application accuracy to  $\pm 5$  mm, uncertainties related to the dose calculation method with  $\pm 4.6\%$  for analytical PB algorithms and  $\pm 2.6\%$  for MC dose engines and uncertainties due to the biological models by  $+0.8\%$ .

These are the uncertainties specific to particle therapy, however, uncertainties that are also existent in photon therapy have been simply translated to particle therapy but the outcome might have more impact: Set-up errors in photon therapy are compensated by an additional margin to the CTV forming the PTV. In particle therapy however, a simple margin does not lead to a reliable coverage of the target as range changing material might displace the beamspot position in the target. In the mediastinum and abdomen, a 6 mm margin is typical (in dependence on the in room imaging option). Park et al. [2012] calculated a decrease of 4% of the minimum dose in the CTV for a 6 mm set-up error. Including a 8 mm motion amplitude, this would lead to a decrease of 11% (in agreement with [Tsunashima, 2012]). Hence, only a margin does not sufficiently account for the uncertainties as it does in photon therapy. The described method of beam specific targets in combination with robust planning, which calculates and optimizes the dose distribution for different scenarios effectively reduces the uncertainties to 4% for both, the set-up and motion uncertainty [Park et al., 2012].

Even with all these uncertainties, the interfractional changes in the anatomy are not jet

accounted for which could potentially result in an even more severely disturbed dose. This is mainly addressed via frequent imaging and recalculations. Promising steps to integrate the cone-beam CT (CBCT) and establish fast and reliable workflows for online adaptive replanning are being incorporated in the first clinics [[Thummerer et al., 2020](#), [Albertini et al., 2020](#)].

With all these sources of uncertainties in mind, at the current situation in the clinical routine, the uncertainties in dose calculation and application due to the Bragg peak degradation in lung tissue are neglectable with a realistic estimation of a decrease in dose by 1-3% [[Baumann et al., 2019](#)]. Nevertheless, a lot of the uncertainties can already be minimized by the application and integration of new techniques and workflows. Hence, the uncertainties are steadily better under control and further minimized. For a high precision patient specific treatment, the consideration of the effects of the Bragg peak degradation should be a future step. In cases of interest, the presented results offer the possibility to estimate the effects.

## 4 | Conclusion & Outlook

The presented works address the topic of the degradation of the Bragg peak through lung tissue for proton therapy of lung tumors. In four publications, the concept of a density modulation of the lung voxels was transferred to clinical CT data sets [Flatten et al., 2019, Baumann et al., 2019], different parameters and their effect on the disturbed dose distribution were evaluated [Flatten et al., 2019] and the effect was estimated for clinical patient plans [Baumann et al., 2019]. As the material characteristic of the modulation power is of interest, measurements were performed to evaluate the modulation power for lung tissue [Burg et al., 2021] and a model was derived and validated that allows to estimate the modulation power from clinical CT images [Flatten et al., 2021]. The combination and spectrum of these publications shed a light into the topic of the degradation effect which has been known for quite some time [Urie et al., 1986].

The effects on the dose distribution were found to be with a 1-3% decrease in dose and an additional uncertainty of roughly 2 mm WET in a clinical acceptable range - at least at the moment.

Even though these uncertainties are not the leading and defining uncertainties, they should be minimized. The presented works offer a great opportunity and lay the foundation for further steps towards a translation into the clinic. The next step of Publication 1 and Publication 2 would be the implementation of the degradation into a treatment planning system and consequently to not only calculate but also to optimize the dose distribution with the degradation accounted for. This goes hand in hand with further testing and analyzing of the method to estimate the modulation power from Publication 4. It would be of interest to analyze the modulation power for different respiratory states for which 4D-CT data sets could be examined. The results in Article 3 show that the lung is mostly a mixture of two structure sizes. Hence, the topic of structures already considered by the TPS needs to be evaluated, e.g. larger bronchial structures in the order of millimeter are probably visible in the CT and thus accounted for by the TPS. All together, the effects of movement and degradation could be combined via dose calculation on 4D-CTs with different modulation power values depending on the breathing phase.

The consideration of the Bragg peak degradation and the modulation power in the optimization process would decrease the uncertainties in treatment planning. If it is implemented in a robust optimization method, where additionally to the degradation of the BP, patient

set-up uncertainties, stopping power uncertainties and movement would be calculated for different scenarios, the robustness and safe application of proton therapy for lung tumors would strongly enhance and reach the uncertainties of photon therapy. With this, the higher tumor control rates combined with the lower toxicities of proton therapy for lung cancer would be even better as the benefits outweigh by far the challenges and uncertainties.



# References

- S. Agostinelli et al. Geant4 - a simulation toolkit. *Nucl. Instrum. Methods Phys. Res. A*, 506:250–303, 2003. doi: [http://dx.doi.org/10.1016/S0168-9002\(03\)01368-8](http://dx.doi.org/10.1016/S0168-9002(03)01368-8).
- F. Albertini, M. Matter, L. Nenoff, Y. Zhang, and A. Lomax. Online daily adaptive proton therapy. *The British journal of radiology*, 93(1107):20190594, 2020.
- K.-S. Baumann, M. Witt, U. Weber, R. Engenhart-Cabillic, and K. Zink. An efficient method to predict and include Bragg curve degradation due to lung-equivalent materials in Monte Carlo codes by applying a density modulation. *Physics in Medicine & Biology*, 62(10):3997, 2017.
- K.-S. Baumann, V. Flatten, U. Weber, S. Lautenschläger, F. Eberle, K. Zink, and R. Engenhart-Cabillic. Effects of the Bragg peak degradation due to lung tissue in proton therapy of lung cancer patients. *Radiation Oncology*, 14(1):1–15, 2019.
- C. Bert and M. Durante. Motion in radiotherapy: particle therapy. *Physics in Medicine & Biology*, 56(16):R113, 2011.
- A. E. Bourque, J.-F. Carrier, and H. Bouchard. A stoichiometric calibration method for dual energy computed tomography. *Physics in Medicine & Biology*, 59(8):2059, 2014.
- J. D. Bradley, R. Paulus, R. Komaki, G. Masters, G. Blumenschein, S. Schild, J. Bogart, C. Hu, K. Forster, A. Magliocco, et al. Standard-dose versus high-dose conformal radiotherapy with concurrent and consolidation carboplatin plus paclitaxel with or without cetuximab for patients with stage IIIA or IIIB non-small-cell lung cancer (RTOG 0617): a randomised, two-by-two factorial phase 3 study. *The lancet oncology*, 16(2):187–199, 2015.
- E. D. Brandner, A. Wu, H. Chen, D. Heron, S. Kalnicki, K. Komanduri, K. Gerszten, S. Burton, I. Ahmed, and Z. Shou. Abdominal organ motion measured using 4D CT. *International Journal of Radiation Oncology\* Biology\* Physics*, 65(2):554–560, 2006.
- J. M. Burg, V. Flatten, M. Witt, L. Derksen, U. Weber, R. Engenhart-Cabillic, H. Vorwerk, K. Zink, and K.-S. Baumann. Experimental determination of modulation power of lung tissue for particle therapy. *Physics in Medicine & Biology*, 2021.

- D. A. Bush, J. D. Slater, B. B. Shin, G. Cheek, D. W. Miller, and J. M. Slater. Hypofractionated proton beam radiotherapy for stage I lung cancer. *Chest*, 126(4): 1198–1203, 2004.
- J. Y. Chang, R. Komaki, C. Lu, H. Y. Wen, P. K. Allen, A. Tsao, M. Gillin, R. Mohan, and J. D. Cox. Phase 2 study of high-dose proton therapy with concurrent chemotherapy for unresectable stage III nonsmall cell lung cancer. *Cancer*, 117(20):4707–4713, 2011.
- J. Y. Chang, X. Zhang, A. Knopf, H. Li, S. Mori, L. Dong, H.-M. Lu, W. Liu, S. N. Badiyan, S. Both, et al. Consensus guidelines for implementing pencil-beam scanning proton therapy for thoracic malignancies on behalf of the PTCOG thoracic and lymphoma subcommittee. *International Journal of Radiation Oncology\* Biology\* Physics*, 99(1): 41–50, 2017.
- J. Chen, J. J. Lu, N. Ma, J. Zhao, C. Chen, M. Fan, G. Jiang, and J. Mao. Early stage non-small cell lung cancer treated with pencil beam scanning particle therapy: retrospective analysis of early results on safety and efficacy. *Radiation Oncology*, 14(1):1–9, 2019.
- R. Dal Bello. Degradation of proton and carbon Bragg peaks due to density inhomogeneities . *Master thesis, Department of Physics and Astronomy, University of Heidelberg, Germany*, 2017. URL <http://www.ub.uni-heidelberg.de/archiv/22822>. [last accessed: June 2021].
- D. De Ruyscher, E. Sterpin, K. Haustermans, and T. Depuydt. Tumour movement in proton therapy: solutions and remaining questions: a review. *Cancers*, 7(3):1143–1153, 2015.
- Degro. Übersicht der Leitlinien der Deutschen Gesellschaft für Radioonkologie e.V. <https://www.awmf.org/fachgesellschaften/mitgliedsgesellschaften/visitenkarte/fg/deutsche-gesellschaft-fuer-radioonkologie.html>, 2021. last accessed: July 2021.
- M. Desplanques, B. Tagaste, G. Fontana, A. Pella, M. Riboldi, G. Fattori, A. Donno, G. Baroni, and R. Orecchia. A comparative study between the imaging system and the optical tracking system in proton therapy at CNAO. *Journal of radiation research*, 54 (suppl\_1):i129–i135, 2013.
- D. K. Ebner, H. Tsuji, S. Yasuda, N. Yamamoto, S. Mori, and T. Kamada. Respiration-gated fast-rescanning carbon-ion radiotherapy. *Japanese journal of clinical oncology*, 47 (1):80–83, 2017.
- F. Emert, J. Missimer, P. A. Eichenberger, M. Walser, C. Gmür, A. J. Lomax, D. C. Weber, and C. M. Spengler. Enhanced deep-inspiration breath hold superior to high-frequency

- percussive ventilation for respiratory motion mitigation: A physiology-driven, mri-guided assessment toward optimized lung cancer treatment with proton therapy. *Frontiers in oncology*, 11, 2021.
- S. España and H. Paganetti. Uncertainties in planned dose due to the limited voxel size of the planning CT when treating lung tumors with proton therapy. *Physics in Medicine & Biology*, 56(13):3843, 2011.
- B. Faddegon, J. Ramos-Méndez, J. Schuemann, A. McNamara, J. Shin, J. Perl, and H. Paganetti. The TOPAS tool for particle simulation, a Monte Carlo simulation tool for physics, biology and clinical research. *Physica Medica*, 72:114–121, 2020.
- V. Flatten, K.-S. Baumann, U. Weber, R. Engenhart-Cabillic, and K. Zink. Quantification of the dependencies of the Bragg peak degradation due to lung tissue in proton therapy on a CT-based lung tumor phantom. *Physics in Medicine & Biology*, 64(15):155005, 2019.
- V. Flatten, A. Friedrich, R. Engenhart-Cabillic, and K. Zink. A phantom based evaluation of the dose prediction and effects in treatment plans, when calculating on a direct density CT reconstruction. *Journal of applied clinical medical physics*, 21(3):52–61, 2020.
- V. Flatten, J. M. Burg, M. Witt, L. Derksen, P. F. Costa, J. Wulff, C. Bäumer, B. Timmermann, U. Weber, H. Vorwerk, et al. Estimating the modulating effect of lung tissue in particle therapy using a clinical ct voxel histogram analysis. *Physics in Medicine & Biology*, 66(18):185002, 2021.
- J. F. Fowler. The linear-quadratic formula and progress in fractionated radiotherapy. *The British journal of radiology*, 62(740):679–694, 1989.
- C. Glide-Hurst, M. Bellon, R. Foster, C. Altunbas, M. Speiser, M. Altman, D. Westerly, N. Wen, B. Zhao, M. Miften, et al. Commissioning of the Varian TrueBeam linear accelerator: a multi-institutional study. *Medical physics*, 40(3):031719, 2013.
- M. Goitein, A. J. Lomax, and E. S. Pedroni. Treating cancer with protons. *Physics Today*, 55(0):45–51, 2002.
- J. P. Grutters, A. G. Kessels, M. Pijls-Johannesma, D. De Ruyscher, M. A. Joore, and P. Lambin. Comparison of the effectiveness of radiotherapy with photons, protons and carbon-ions for non-small cell lung cancer: a meta-analysis. *Radiotherapy and Oncology*, 95(1):32–40, 2010.
- M. Hata, K. Tokuyue, K. Kagei, S. Sugahara, H. Nakayama, N. Fukumitsu, T. Hashimoto, M. Mizumoto, K. Ohara, and Y. Akine. Hypofractionated high-dose proton beam therapy

- for stage I non-small-cell lung cancer: preliminary results of a phase I/II clinical study. *International Journal of Radiation Oncology\* Biology\* Physics*, 68(3):786–793, 2007.
- H. Hof, B. Rhein, P. Haering, A. Kopp-Schneider, J. Debus, and K. Herfarth. 4D-CT-based target volume definition in stereotactic radiotherapy of lung tumours: comparison with a conventional technique using individual margins. *Radiotherapy and Oncology*, 93(3): 419–423, 2009.
- L. Hong, M. Goitein, M. Bucciolini, R. Comiskey, B. Gottschalk, S. Rosenthal, C. Serago, and M. Urie. A pencil beam algorithm for proton dose calculations. *Physics in Medicine & Biology*, 41(8):1305, 1996.
- A. Hranek, A. F. Resch, D. Georg, and B. Knaeusl. Investigation of the Bragg peak degradation caused by homogeneous and heterogeneous lung tissue substitutes: proton beam experiments and comparison to current clinical dose calculation. *Physics in Medicine & Biology*, 65(24):245036, 2020.
- ICRU. Report 62. *Journal of the International Commission on Radiation Units and Measurements*, os32(1):NP–NP, 04 2016. ISSN 1473-6691.
- ICRU. Report 91. *Journal of the International Commission on Radiation Units and Measurements*, 14(2):1–160, 07 2017. ISSN 1473-6691.
- S. B. Jiang. Radiotherapy of mobile tumors. In *Seminars in radiation oncology*, volume 16, pages 239–248. Elsevier, 2006.
- E. P. Judge, J. L. Hughes, J. J. Egan, M. Maguire, E. L. Molloy, and S. O’Dea. Anatomy and bronchoscopy of the porcine lung. A model for translational respiratory medicine. *American journal of respiratory cell and molecular biology*, 51(3):334–343, 2014.
- Y. Kase, H. Yamashita, H. Fuji, Y. Yamamoto, Y. Pu, C. Tsukishima, and S. Murayama. A treatment planning comparison of passive-scattering and intensity-modulated proton therapy for typical tumor sites. *Journal of radiation research*, 53(2):272–280, 2012.
- P. J. Keall, G. S. Mageras, J. M. Balter, R. S. Emery, K. M. Forster, S. B. Jiang, J. M. Kapatoes, D. A. Low, M. J. Murphy, B. R. Murray, et al. The management of respiratory motion in radiation oncology report of AAPM Task Group 76 a. *Medical physics*, 33(10): 3874–3900, 2006.
- A.-C. Knopf, T. S. Hong, and A. Lomax. Scanned proton radiotherapy for mobile targets—the effectiveness of re-scanning in the context of different treatment planning approaches and for different motion characteristics. *Physics in Medicine & Biology*, 56 (22):7257, 2011.

- F.-M. Kong, R. K. Ten Haken, M. J. Schipper, M. A. Sullivan, M. Chen, C. Lopez, G. P. Kalemkerian, and J. A. Hayman. High-dose radiation improved local tumor control and overall survival in patients with inoperable/unresectable non-small-cell lung cancer: Long-term results of a radiation dose escalation study. *International Journal of Radiation Oncology\* Biology\* Physics*, 63(2):324–333, 2005.
- G. Kraft. Tumor therapy with heavy charged particles. *Progress in particle and Nuclear Physics*, 45:S473–S544, 2000.
- J. H. Lawrence. Proton irradiation of the pituitary. *Cancer*, 10(4):795–798, 1957.
- H. Lemjabbar-Alaoui, O. U. Hassan, Y.-W. Yang, and P. Buchanan. Lung cancer: Biology and treatment options. *Biochimica et Biophysica Acta (BBA)-Reviews on Cancer*, 1856(2):189–210, 2015.
- L. Lin, M. Kang, S. Huang, R. Mayer, A. Thomas, T. D. Solberg, J. E. McDonough, and C. B. Simone. Beam-specific planning target volumes incorporating 4D CT for pencil beam scanning proton therapy of thoracic tumors. *Journal of applied clinical medical physics*, 16(6):281–292, 2015.
- H.-M. Lu, R. Brett, G. Sharp, S. Safai, S. Jiang, J. Flanz, and H. Kooy. A respiratory-gated treatment system for proton therapy. *Medical physics*, 34(8):3273–3278, 2007.
- M. Mehta, R. Scrimger, R. Mackie, B. Paliwal, R. Chappell, and J. Fowler. A new approach to dose escalation in non-small-cell lung cancer. *International Journal of Radiation Oncology\* Biology\* Physics*, 49(1):23–33, 2001.
- A. Meijers, O. C. Seller, J. Free, D. Bondesson, C. S. Oria, M. Rabe, K. Parodi, G. Landry, J. Langendijk, S. Both, et al. Assessment of range uncertainty in lung-like tissue using a porcine lung phantom and proton radiography. *Physics in Medicine & Biology*, 65(15):155014, 2020.
- N. Metropolis and S. Ulam. The monte carlo method. *Journal of the American statistical association*, 44(247):335–341, 1949.
- R. Muirhead, S. G. McNee, C. Featherstone, K. Moore, and S. Muscat. Use of maximum intensity projections (MIPs) for target outlining in 4DCT radiotherapy planning. *Journal of Thoracic Oncology*, 3(12):1433–1438, 2008.
- C. Nutting, D. Dearnaley, and S. Webb. Intensity modulated radiation therapy: a clinical review. *The British journal of radiology*, 73(869):459–469, 2000.
- M. Ochs, J. R. Nyengaard, A. Jung, L. Knudsen, M. Voigt, T. Wahlers, J. Richter, and H. J. G. Gundersen. The number of alveoli in the human lung. *American journal of respiratory and critical care medicine*, 169(1):120–124, 2004.

- K. Otto. Volumetric modulated arc therapy: IMRT in a single gantry arc. *Medical physics*, 35(1):310–317, 2008.
- H. Paganetti. Range uncertainties in proton therapy and the role of Monte Carlo simulations. *Physics in Medicine & Biology*, 57(11):R99, 2012.
- H. Paganetti, A. Niemierko, M. Ancukiewicz, L. E. Gerweck, M. Goitein, J. S. Loeffler, and H. D. Suit. Relative biological effectiveness (RBE) values for proton beam therapy. *International Journal of Radiation Oncology\* Biology\* Physics*, 53(2):407–421, 2002.
- P. C. Park, X. R. Zhu, A. K. Lee, N. Sahoo, A. D. Melancon, L. Zhang, and L. Dong. A beam-specific planning target volume (PTV) design for proton therapy to account for setup and range uncertainties. *International Journal of Radiation Oncology\* Biology\* Physics*, 82(2):e329–e336, 2012.
- P. Pemler, J. Besserer, U. Schneider, and H. Neuenschwander. Evaluation of a commercial electron treatment planning system based on Monte Carlo techniques (eMC). *Zeitschrift für medizinische Physik*, 16(4):313–329, 2006.
- J. Perl, J. Shin, J. Schuemann, B. Faddegon, and H. Paganetti. TOPAS: an innovative proton Monte Carlo platform for research and clinical applications. *Medical Physics*, 39(11):6818–6837, 2012. doi: <http://dx.doi.org/10.1118/1.4758060>.
- L. Perles, D. Mirkovic, G. Sawakuchi, and U. Titt. Monte Carlo Investigation of Rebinning Material Density Distributions of Lung Parenchyma Phantoms in Proton Therapy. *Nuclear Technology*, 175(1):22–26, 2011. doi: <http://stacks.iop.org/0031-9155/56/i=13/a=007>.
- M. H. Phillips, E. Pedroni, H. Blattmann, T. Boehringer, A. Coray, and S. Scheib. Effects of respiratory motion on dose uniformity with a charged particle scanning method. *Physics in Medicine & Biology*, 37(1):223, 1992.
- PTCOG. <https://www.ptcog.ch/index.php/facilities-in-operation>, 2021a. last accessed: March 2021.
- PTCOG. <https://www.ptcog.ch/index.php/facilities-under-construction>, 2021b. last accessed: March 2021.
- J. A. Purdy. Current ICRU definitions of volumes: limitations and future directions. In *Seminars in radiation oncology*, volume 14, pages 27–40. Elsevier, 2004.
- T. P. Ringbaek, Y. Simeonov, M. Witt, R. Engenhardt-Cabillic, G. Kraft, K. Zink, and U. Weber. Modulation power of porous materials and usage as ripple filter in particle therapy. *Physics in Medicine and Biology*, 2017. doi: 10.3109/0284186X.2013.832834.

- A. Santiago, U. Jelen, F. Ammazalorso, R. Engenhardt-Cabillic, P. Fritz, W. Mühlnickel, W. Enghardt, M. Baumann, and A. Wittig. Reproducibility of target coverage in stereotactic spot scanning proton lung irradiation under high frequency jet ventilation. *Radiotherapy and Oncology*, 109(1):45–50, 2013.
- G. Sawakuchi, U. Titt, D. Mirkovic, and R. Mohan. Density heterogeneities and the influence of multiple Coulomb and nuclear scatterings on the Bragg peak distal edge of proton therapy beams. *Physics in Medicine and Biology*, 53(17):4605–19, 2008. doi: <http://stacks.iop.org/0031-9155/53/i=17/a=010>.
- U. Scheeler, T. Haberer, C. Krantz, S. Sievers, M. Strohmeier, R. Cee, E. Feldmeier, M. Galonska, K. Höppner, J. Mosthaf, et al. Recommissioning of the Marburg Ion-Beam Therapy Centre (MIT) Accelerator Facility. In *Proc. 7th Intl. Particle Accelerator Conf.(IPAC'16)*, pages 1908–1910, 2016.
- U. Schneider, E. Pedroni, and A. Lomax. The calibration of CT Hounsfield units for radiotherapy treatment planning. *Physics in Medicine and Biology*, 41(1):111, 1996.
- M. Sell, U. Titt, L. Perles, D. Mirkovic, R. Mohan, M. Babert, and U. Oelfke. WE-E-BRB-02: Evaluation of Analytical Proton Dose Predictions with a Lung-Like Plastic Phantom. *Medical Physics*, 39(6):3956–3956, 2012. doi: <http://dx.doi.org/10.1118/1.4736144>.
- E. Seneterre, F. Paganin, J. Bruel, F. Michel, and J. Bousquet. Measurement of the internal size of bronchi using high resolution computed tomography (HRCT). *European Respiratory Journal*, 7(3):596–600, 1994.
- Y. Simeonov, U. Weber, P. Penchev, T. P. Ringbæk, C. Schuy, S. Brons, R. Engenhardt-Cabillic, J. Bliedtner, and K. Zink. 3D range-modulator for scanned particle therapy: development, Monte Carlo simulations and experimental evaluation. *Physics in Medicine & Biology*, 62(17):7075, 2017.
- J.-J. Sonke and J. Belderbos. Adaptive radiotherapy for lung cancer. In *Seminars in radiation oncology*, volume 20, pages 94–106. Elsevier, 2010.
- H. Sung, J. Ferlay, R. L. Siegel, M. Laversanne, I. Soerjomataram, A. Jemal, and F. Bray. Global cancer statistics 2020: GLOBOCAN estimates of incidence and mortality worldwide for 36 cancers in 185 countries. *CA: a cancer journal for clinicians*, 2021.
- A. Thummerer, P. Zaffino, A. Meijers, G. G. Marmitt, J. Seco, R. J. Steenbakkens, J. A. Langendijk, S. Both, M. F. Spadea, and A. C. Knopf. Comparison of CBCT based synthetic CT methods suitable for proton dose calculations in adaptive proton therapy. *Physics in Medicine & Biology*, 65(9):095002, 2020.

- U. Titt, M. Sell, J. Unkelbach, M. Bangert, D. Mirkovic, U. Oelfke, and R. Mohan. Degradation of proton depth dose distribution attributable to microstructures in lung-equivalent material. *Medical Physics*, 42(11):6425, 2015. doi: <http://dx.doi.org/10.1118/1.4932625>.
- Y. Tsunashima. Verification of the clinical implementation of the respiratory gated beam delivery technique with synchrotron-based proton irradiation. *UT GSBS Dissertation and Theses (Open Access). The University of Texas Graduate School of Biomedical Sciences, Houston, TX2012*, 2012.
- M. Tubiana. Repopulation in Human Tumors: A Biological Back-Ground for Fractionation in Radiotherapy. *Acta oncologica*, 27(2):83–88, 1988.
- M. Urie, M. Goitein, W. Holley, and G. Chen. Degradation of the Bragg peak due to inhomogeneities. *Physics in Medicine and Biology*, 31(1), 1986. doi: <http://stacks.iop.org/0031-9155/31/i=1/a=001>.
- B. Van der Heyden, M. Öllers, A. Ritter, F. Verhaegen, and W. van Elmpt. Clinical evaluation of a novel CT image reconstruction algorithm for direct dose calculations. *Physics and Imaging in Radiation Oncology*, 2:11–16, 2017.
- D. Wagenaar, L. T. Tran, A. Meijers, G. G. Marmitt, K. Souris, D. Bolst, B. James, G. Biasi, M. Povoli, A. Kok, et al. Validation of linear energy transfer computed in a Monte Carlo dose engine of a commercial treatment planning system. *Physics in Medicine & Biology*, 65(2):025006, 2020.
- L. Widesott, M. Amichetti, and M. Schwarz. Proton therapy in lung cancer: Clinical outcomes and technical issues. a systematic review. *Radiotherapy and Oncology*, 86(2): 154 – 164, 2008. ISSN 0167-8140. doi: <https://doi.org/10.1016/j.radonc.2008.01.003>.
- H.-P. Wieser, E. Cisternas, N. Wahl, S. Ulrich, A. Stadler, H. Mescher, L.-R. Müller, T. Klinge, H. Gabrys, L. Burigo, et al. Development of the open-source dose calculation and optimization toolkit matRad. *Medical physics*, 44(6):2556–2568, 2017.
- L. Wilke, N. Andratschke, O. Blanck, T. B. Brunner, S. E. Combs, A.-L. Grosu, C. Moustakis, D. Schmitt, W. W. Baus, and M. Guckenberger. ICRU report 91 on prescribing, recording, and reporting of stereotactic treatments with small photon beams. *Strahlentherapie und Onkologie*, 195(3):193–198, 2019.
- R. Wilson. Radiological use of fast protons . *Radiology*, 47:487–491, 1946. doi: <http://dx.doi.org/10.1148/47.5.487>.



- J. Winter, M. Ellerbrock, O. Jäkel, S. Greilich, and M. Bangert. Analytical modeling of depth-dose degradation in heterogeneous lung tissue for intensity-modulated proton therapy planning. *Physics and Imaging in Radiation Oncology*, 14:32–38, 2020.
- M. Witt. Modulationseffekte von Kohlenstoffionen bei der Bestrahlung von Lungen. *master thesis, Technische Hochschule Mittelhessen - University of applied sciences, Giessen, Germany*, 2014. URL [https://www.thm.de/lse/images/user/KZink-105/Abschlussarbeiten/Masterarbeit\\_Matthias\\_Witt\\_2014.pdf](https://www.thm.de/lse/images/user/KZink-105/Abschlussarbeiten/Masterarbeit_Matthias_Witt_2014.pdf). [last accessed: May 2021].
- K. Zarogoulidis, P. Zarogoulidis, K. Darwiche, E. Boutsikou, N. Machairiotis, K. Tsakiridis, N. Katsikogiannis, I. Kougioumtzi, I. Karapantzos, H. Huang, et al. Treatment of non-small cell lung cancer (NSCLC). *Journal of thoracic disease*, 5(Suppl 4):S389, 2013.
- X. Zhang, Y. Li, X. Pan, L. Xiaoqiang, R. Mohan, R. Komaki, J. D. Cox, and J. Y. Chang. Intensity-modulated proton therapy reduces the dose to normal tissue compared with intensity-modulated radiation therapy or passive scattering proton therapy and enables individualized radical radiotherapy for extensive stage IIIB non-small-cell lung cancer: a virtual clinical study. *International Journal of Radiation Oncology\* Biology\* Physics*, 77(2):357–366, 2010.

# Published Articles

In the following, the original articles are presented.

**[1]** Quantification of the dependencies of the Bragg peak degradation due to lung tissue in proton therapy on a CT-based lung tumor phantom

page 52

**[2]** Effects of the Bragg peak degradation due to lung tissue in proton therapy of lung cancer patients

page 63

**[3]** Experimental determination of modulation power of lung tissue for particle therapy

page 78

**[4]** Estimating the modulating effect of lung tissue in particle therapy using a clinical CT voxel histogram analysis

page 106

**[5]** A phantom based evaluation of the dose prediction and effects in treatment plans, when calculating on a direct density CT reconstruction

page 137



## PAPER

# Quantification of the dependencies of the Bragg peak degradation due to lung tissue in proton therapy on a CT-based lung tumor phantom

RECEIVED  
1 February 2019REVISED  
6 May 2019ACCEPTED FOR PUBLICATION  
31 May 2019PUBLISHED  
1 August 2019Veronika Flatten<sup>1,2,4</sup>, Kilian-Simon Baumann<sup>1,2</sup>, Uli Weber<sup>3</sup>, Rita Engenhardt-Cabillic<sup>1</sup> and Klemens Zink<sup>1,2</sup><sup>1</sup> Department of Radiotherapy and Radiooncology, University Medical Center Giessen–Marburg, Marburg, Germany<sup>2</sup> Institute of Medical Physics and Radiation Protection, University of Applied Sciences, Giessen, Germany<sup>3</sup> Biophysics Department, GSI Helmholtzzentrum für Schwerionenforschung, Darmstadt, Germany<sup>4</sup> Author to whom any correspondence should be addressed.E-mail: [flatten@staff.uni-marburg.de](mailto:flatten@staff.uni-marburg.de)

Keywords: Monte Carlo, Bragg peak degradation, proton therapy, lung modulation, lung tissue

## Abstract

The fine, sub-millimeter sized structure of lung tissue causes a degradation of the Bragg peak curve in particle therapy. The Bragg peak is degraded because particles of the same energy traverse lung tissue of different compositions of high and low density materials. Hence, they experience different energy losses resulting in variable ranges and a broadened Bragg peak.

Since this fine structure of lung tissue is not resolved in standard treatment-planning CTs, current state-of-the-art dose calculation procedures used in the clinical routine are unable to account for this degradation. Neglecting this Bragg peak degradation in treatment planning can lead to an underdose in the target volume and an overdose distal to the target.

Aim of this work is to systematically investigate the potential effects of the Bragg peak degradation on the dose distribution in dependence of different parameters like the tumor volume and its depth in lung.

Proton plans were optimized on CT based phantoms without considering the Bragg peak degradation and afterwards recalculated with the Monte Carlo toolkit TOPAS: first, without consideration of the degradation and second, with the Bragg peak degradation accounted for. The direct comparison of these two dose distributions enables a quantification of the degradation effect. To carve out the dependencies of various parameters that could influence the Bragg peak degradation and thus the target dose, the simulations were performed for a variety of tumor sizes and shapes, as well as different positions within the lung.

The results show that due to the Bragg peak degradation the mean dose in the target volume can be reduced by a few percent up to 14% (for extreme cases) depending on the geometry. It was shown that this effect increases with a decreasing tumor volume and increasing depth of the tumor.

For the first time, a tumor specific estimation of the effect on the dose distribution due to the Bragg peak degradation in lung tissue is presented.

## 1. Introduction

Since first proposed by Wilson (1946), proton irradiation to treat cancer has evolved from an experimental treatment in research facilities to a routine treatment option in specialized cancer centers. In scanned proton beam facilities, each tumor is irradiated with an optimized combination of proton beams of different energies and positions, concentrating the Bragg peaks in a plateau which encloses the tumor. The low dose in the entrance channel and the high energy deposition at a finite range qualify for a good tumor control with a low toxicity in the surrounding tissue and organs (Schulz-Ertner and Tsujii 2007, Zhang *et al* 2010). As in all common radiation therapy treatments, treatment plans nowadays are optimized for the specific anatomy of the patient by calculating the specific dose distributions on the acquired CT images. Eventhough CT resolution allows a macroscopic

visualization and delineation of the organs in combination with additional dose calculation information, no information about microscopic tissue characteristics can be obtained with a conventional CT scanner. The CT resolution results in an averaged representation of the lung as homogenous medium in CTs while on a microscopic scale it consists of pulmonary alveoli with a density close to water filled with air having a much smaller density. For ion therapy this is challenging as heterogeneous materials on a microscopic scale cause the Bragg peak to smear out (Urie *et al* 1986, Sawakuchi *et al* 2008). The smearing-out arises because some particles might pass through more lung tissue with a high density and others through more air cavities with a low density. Hence, these particles are slowed down unevenly resulting in different ranges and the degradation of the Bragg peak. Even though the Bragg peak degradation when traversing heterogeneous media has been known for some time and it was shown that this could have a significant impact on the target dose (Goitein 1977, Espana and Paganetti 2011), state-of-the-art treatment planning systems and routines do not account for this Bragg peak degradation, ignoring the potential of an underdose in the target volume and an overdose distal to the target (Goitein 1977, Sawakuchi *et al* 2008).

Nevertheless, first steps to include the Bragg peak degradation in treatment planning have been performed. To quantify the effect of the Bragg peak degradation on a depth dose curve, measurements in waterphantoms positioned downstream from 3D-printed and other porous lung substitutes (Sell *et al* 2012, Titt *et al* 2015, Ringbaek *et al* 2017) have been performed. With the help of Monte Carlo simulations, the concept of the ‘modulation power’ based on a mathematical model was introduced to describe and quantify the effects of the Bragg peak degradation on a mono-energetic Bragg peak (Witt *et al* 2015, Ringbaek *et al* 2017). Baumann *et al* (2017) introduced and extensively tested a mathematical model to reproduce this artificial Bragg peak degradation on rougher structures like CT voxels with dimensions in the millimeter range: by sequentially modulating the density of the CT voxels within the lung, the Bragg peak degradation can be reproduced. Hence, it is possible to reproduce the Bragg peak degradation due to lung tissue on the basis of clinically acquired CT images, although they do not resolve the fine structure of the lung tissue.

In this study, the effects of the Bragg peak degradation on various target volumes in dependence on their depth in lung were analyzed. As the individual anatomy of each patient and thus the tumor shape and its position in the lung differs, the comparison and analysis of the degradation effect is more evident and systematic when performing the calculation of this effect on geometrical, CT-based phantoms. For each of these dicom-based CT slab phantoms a treatment plan was optimized without considering the degradation. These plans were subsequently recalculated with TOPAS in two scenarios: with and without the density modulation reproducing the Bragg peak degradation. Therefore, we were able to perform Monte Carlo simulations for different tumor sizes and distances in lung on the regular CT, as well as on the modulated CTs as proposed by Baumann *et al* (2017). This allows the analysis of the effects of the Bragg peak degradation dependent on tumor size and the depth in lung and thus enabling an uncertainty estimation for proton therapy treatments for lung carcinomas in clinical cases. The effects of other parameters like the tumor shape, the energy and the planning setup on the Bragg peak degradation were also evaluated.

## 2. Materials and methods

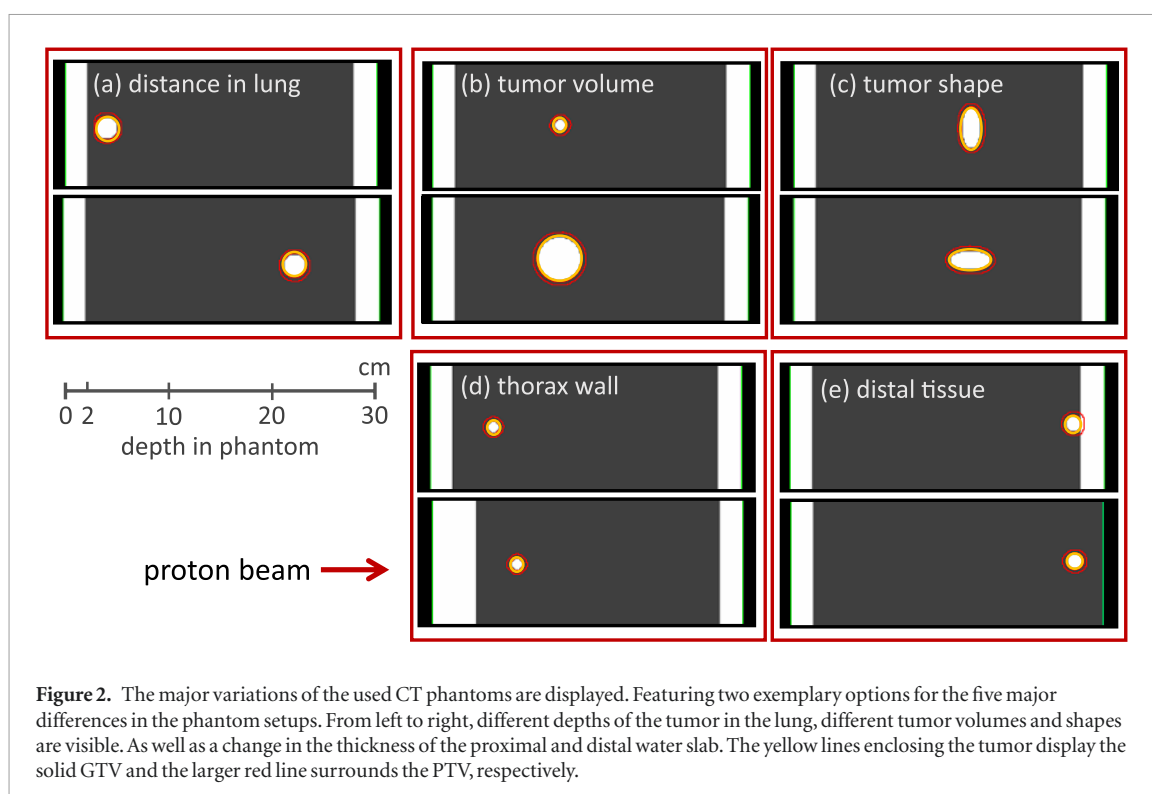
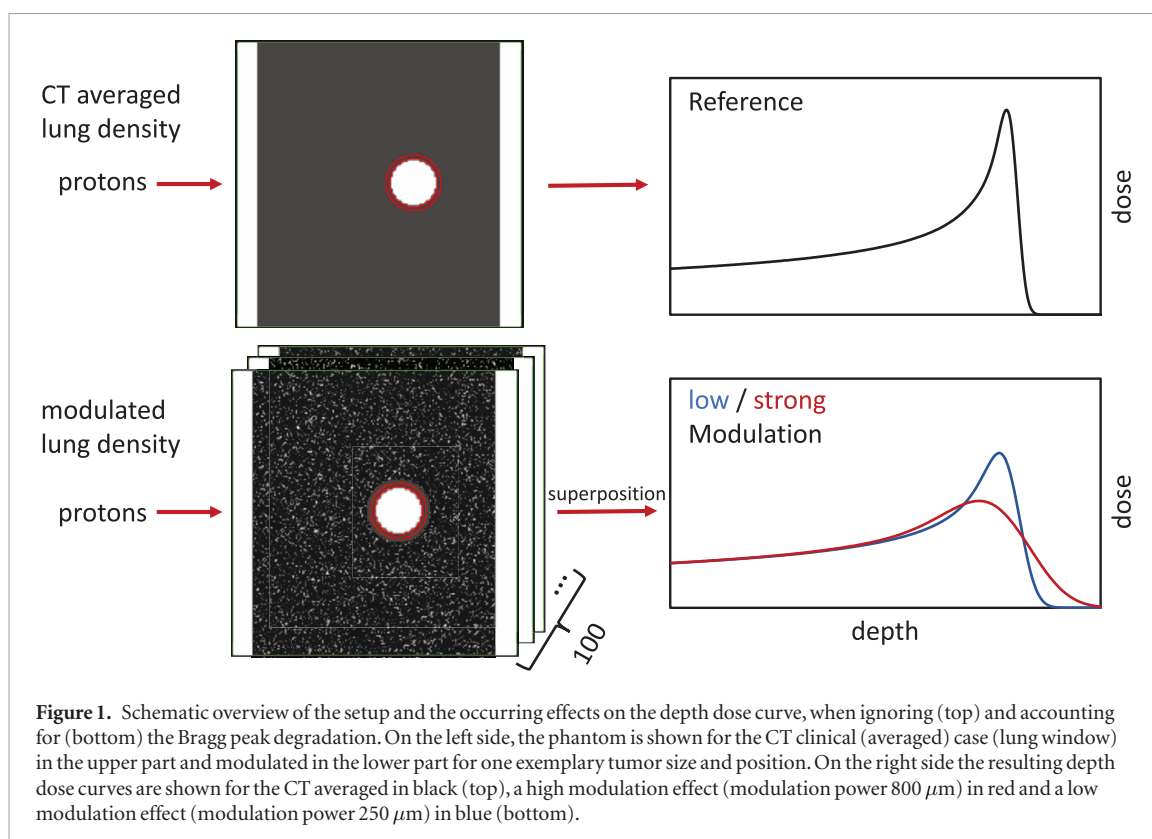
### 2.1. CT modulation

As shown by Baumann *et al* (2017), on a macroscopic level the Bragg peak degradation can be reproduced by alternating the density of the voxel that the particle passes through between either the density of air or tissue. To reproduce the effect of the Bragg peak degradation a sequence of 100 CTs with differently randomized lung density voxels was implemented in the Monte Carlo simulations, as displayed in figure 1. The expectation value of the density of each voxel is  $0.26 \text{ g cm}^{-3}$  corresponding to the average density of an inflated lung (Schneider *et al* 1996). The superposition of the dose distributions from each of the 100 randomized CTs modulates the density and hence the Bragg peak degradation is reproduced. A more detailed description of the mathematical model and the modulation process is described by Baumann *et al* (2017).

Measurements indicated that the modulation power for lung tissue ranges between  $100 \mu\text{m}$  and  $800 \mu\text{m}$  (Witt 2014). To be able to conduct an approximation for the effect of the Bragg peak degradation, a modulation of  $450 \mu\text{m}$  was chosen for most setups in this study. Some simulations were repeated with a more probable modulation power of  $250 \mu\text{m}$  and an extreme modulation power of  $800 \mu\text{m}$ , to allow an estimation of the influence of the modulation power.

### 2.2. Phantoms

To fulfill the objective of the pure assessment of the differences in the dose distribution especially in the target due to the Bragg peak degradation in lung tissue, a phantom study was conducted in a static setup so that organ motion was ignored. Reducing the phantom to the most simplistic case as shown in figure 2, each CT consisted of two water slabs of 2 cm thickness separated by 25 cm of lung tissue, representing the lung enclosed by the thorax wall and the mediastinum or other distal tissue. The density of the water slabs was  $1.00 \text{ g cm}^{-3}$ . The lung was set to have a density of  $0.26 \text{ g cm}^{-3}$  corresponding to the density of an inflated lung (Schneider *et al* 1996). The



CT voxels had a size of  $1.5 \times 1.5 \times 1.5 \text{ mm}^3$ . The artificial tumors were represented by spheres or ellipsoids of different sizes with a density of  $1.00 \text{ g cm}^{-3}$  that were positioned at various depths within the lung.

Various phantoms and thus treatment plans were produced to allow an extensive evaluation of the dependencies of the Bragg Peak degradation. In the following, a brief description of the varied parameters is given (compare figure 2):

### 2.2.1. (a) Distance traveled in lung tissue

Six different depths in lung were investigated ranging from 2 cm to 20 cm (2 cm, 4 cm, 6 cm, 10 cm, 15 cm, 20 cm) for the distance ( $d_L$ ) between the beginning of the lung and the tumor center. The smallest and largest distance are displayed in figure 2.

### 2.2.2. (b) Size of tumor volume

Six different spherical volumes ( $1\text{ cm}^3$ ,  $2\text{ cm}^3$ ,  $6\text{ cm}^3$ ,  $14\text{ cm}^3$ ,  $25\text{ cm}^3$ ,  $43\text{ cm}^3$ ) were chosen to be evaluated, the smallest, with a volume of  $1\text{ cm}^3$ , and largest, which has a volume of  $43\text{ cm}^3$ , are shown in figure 2.

### 2.2.3. (c) Shape of tumor volume

As tumor volumes in patients are not always shaped spherically, two different ellipsoids were investigated. The parameters  $a, b$  and  $c$  denote semi-axes of the ellipsoid. Length  $a$  always describes the axis parallel to the beam direction and  $b$  and  $c$  the axis perpendicular to the beam. Two axis had always the same length for both ellipsoids. The smaller ellipsoid ( $9\text{ cm}^3$ ) features the short axis ( $a = b = 2\text{ cm}$ ) twice and the long axis ( $c = 4\text{ cm}$ ) once while the larger one ( $19\text{ cm}^3$ ) features the short axis only once and thus the long axis twice ( $a = 2\text{ cm}, b = c = 4\text{ cm}$ ). Both ellipsoids were irradiated with the short axis (as just described) and the long axis (by switching  $a \leftrightarrow c$ ) in beam direction.

### 2.2.4. (d) Thickness of thorax wall

The simulations for the smallest tumor volume ( $1\text{ cm}^3$ ) were also performed with a thicker wall as displayed in figure 2.

### 2.2.5. (e) Tissue distal to the tumor volume

The simulations for the longest distance in lung were performed with and without the wall distal to the tumor. This represents tumors close to the mediastinum in comparison to tumors only surrounded by lung.

## 2.3. Planning setup and Monte Carlo simulations

Treatment plans for spot scanning protons were optimized using the commercially available treatment planning system Eclipse version 13.7 (Varian). One single field from the left side was optimized with a lateral spot spacing of 60% of the FWHM in air and an energy spacing of 3 MeV or 1 MeV for larger or smaller volumes, respectively. The volume optimized for was the PTV, which encloses the voxels identified as tumor (GTV) with a margin of 3 mm lung tissue. 30 Gy RBE were planned to be applied in a single fraction.

All simulations were conducted with the Monte Carlo code TOPAS (TOOl for PArTicle Simulations) version 3.1.p1 (Perl *et al* 2012) which is a Geant4 (GEometry AND Tracking) (Agostinelli *et al* 2003) based toolkit focused on proton therapy applications. Each optimized RTplan was recalculated with TOPAS in two scenarios: with and without the Bragg Peak modulation model.

The dose distributions of both scenarios were scored as dose-to-water and compared by evaluating the mean dose ( $D_{mean}$ ), the dose in at least 20% of the volume ( $D_{20}$ ) and 95% of the volume ( $D_{95}$ ), respectively. These three dose values were determined for both, the GTV and the PTV. To evaluate also small dependencies, the modulation effects for the setups shown in figures 2(c)–(e) are presented with the strong modulation power of  $800\ \mu\text{m}$ . All other results are presented with a modulation power of  $450\ \mu\text{m}$  to give a more reasonable estimation of the effect.

## 3. Results

### 3.1. General effect of the Bragg peak degradation

Figures 3(a) and (c) show two exemplary depth-dose curves along the beam axis. For the first 2 cm the particles travel through the water slab and thus no modulation is observed. From depth 2 cm on, small discrepancies in dose can be observed as the particles traverse the lung. Reaching the Bragg peak plateau, the differences between the non-modulated scenario giving the dose distribution as predicted by the TPS and the modulated scenario giving the dose distribution, as it would be in the patient, increase and show the systematic effect of the degradation: on the one hand less dose at the beginning and the end of the spread out Bragg peak and on the other hand an higher dose distal to the Bragg peaks induced due to a broader fall off.

The dose curve for the modulated cases is smoother in the high-dose region showing that the Bragg peak degradation leads to a smoothing effect on the dose in beam direction similar to a ripple filter (Ringbaek *et al* 2017).

The dose-volume histogram (DVH) presented in figures 3(b) and (d) show the influence of the Bragg peak degradation on the GTV. It can be observed, that the mean dose in the GTV is reduced in the modulated case in comparison to the predicted dose. In general, the dose coverage is significantly deteriorated.

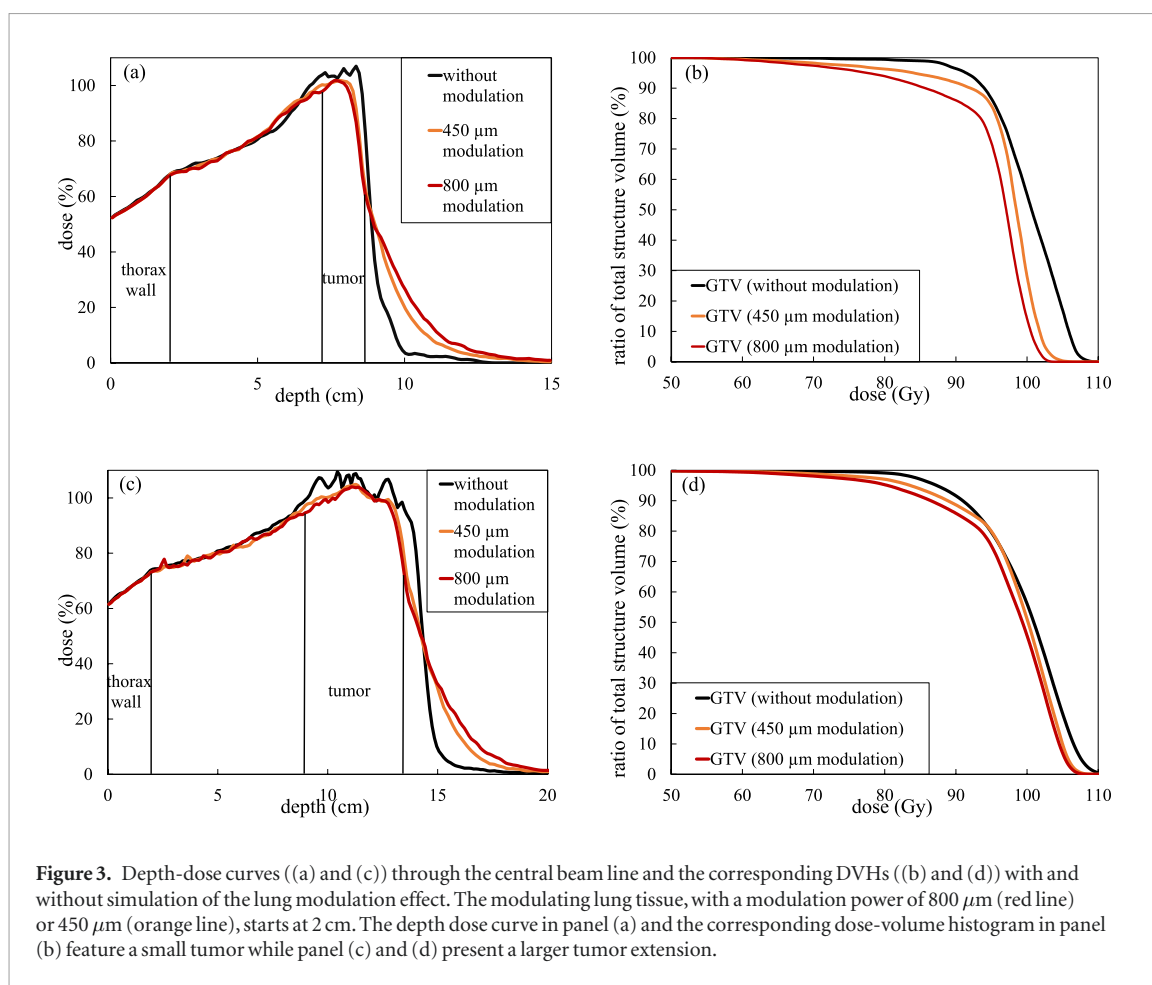


**Figure 3.** Depth-dose curves ((a) and (c)) through the central beam line and the corresponding DVHs ((b) and (d)) with and without simulation of the lung modulation effect. The modulating lung tissue, with a modulation power of  $800\ \mu\text{m}$  (red line) or  $450\ \mu\text{m}$  (orange line), starts at 2 cm. The depth dose curve in panel (a) and the corresponding dose-volume histogram in panel (b) feature a small tumor while panel (c) and (d) present a larger tumor extension.

### 3.2. Dependency on depth in lung tissue and the tumor volume

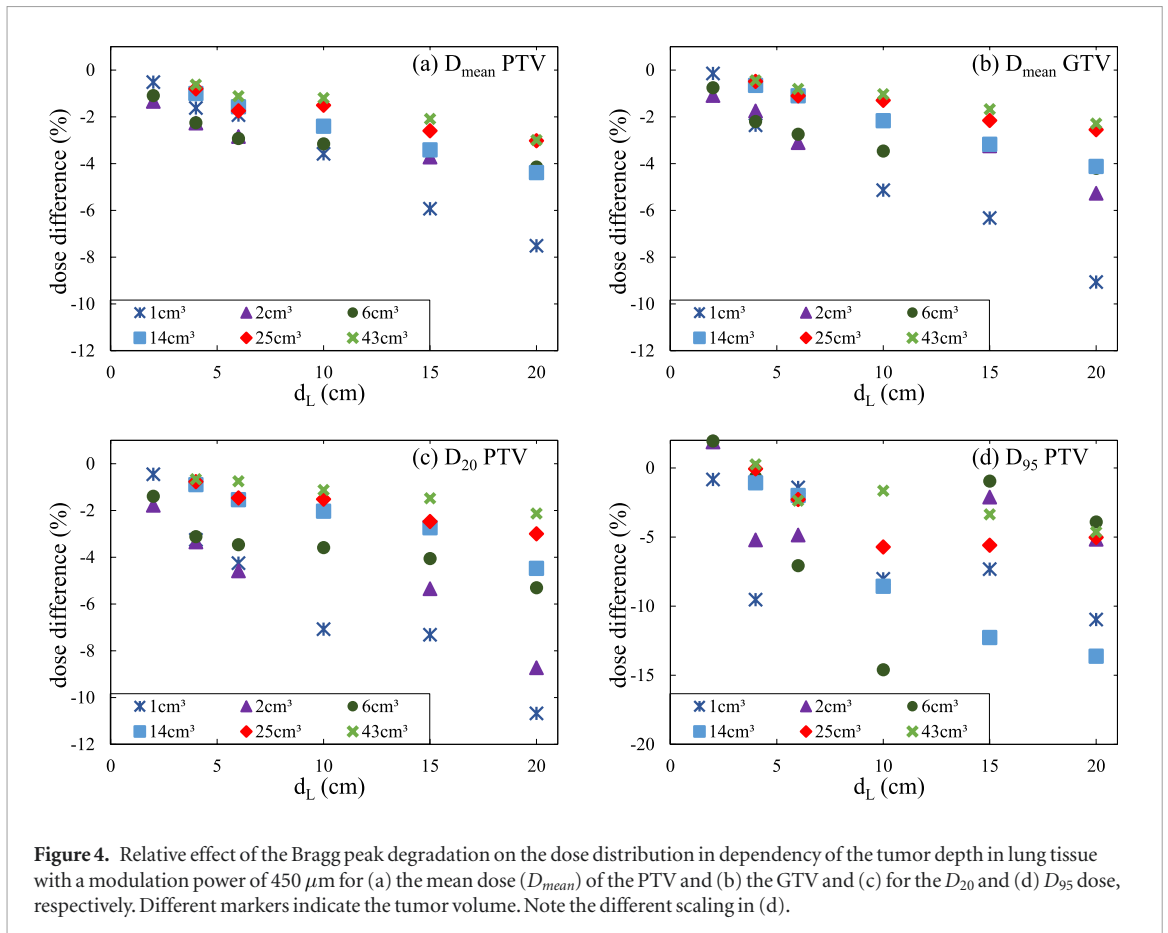
Figure 4 shows the evaluated dose parameters ( $D_{mean}$ ,  $D_{95}$  and  $D_{20}$ ) for the modulated and non-modulated cases in dependency on the depth of the tumor in lung and different tumor volumes. All results are presented as a relative difference of the modulated and TPS calculated dose, which is used as reference dose. To make an estimate of the statistical error done with the Monte Carlo simulation, several plans were recalculated with different random number seeds. The reference mean dose without the modulation effect was found to have an uncertainty of about 0.05% for the presented values, nevertheless as the modulation is produced by the sum of 100 dose plans with each one-hundredth of the total number of particles, the uncertainty is increased to roughly 0.5%. Thus all presented values have to be reviewed with an uncertainty of 0.5%, which corresponds in most cases to the marker size. For single voxel values such as the maximum and minimum dose the uncertainty is slightly, as only a minor part of the simulated particles contribute to the dose value of this voxel.

In the upper part of figure 4, the mean dose is evaluated for the PTV (a) and the GTV (b), respectively. A clear correlation between the tumor depth and the dose reduction can be observed: the greater the distance traveled in lung, the higher the dose difference. Additionally, a clear dependence on the tumor volume is visible: the smaller the tumor size, the larger the dose difference. Figures 4(a) and (b) show a almost linear relationship between tumor depth and the dose difference.

The highest deviation from the expected value of  $D_{mean}$  is found to be  $-8\%$  for the largest distance of 20 cm in combination with the smallest volume of  $1\ \text{cm}^3$ . With decreasing distance in the lung it decreases below  $-1\%$ . The smallest differences occur for the largest sphere with a volume of  $43\ \text{cm}^3$ .  $D_{mean}$  rises from  $-1\%$  at a 4 cm distance between the beginning of the lung and the sphere center to  $-3\%$  at 20 cm distance.

Even though both upper plots look quite similar, differences can be noted. On the one hand, the effect for the smallest tumor is higher when only the GTV is evaluated, while on the other hand the effect for the larger sized tumors is reduced for the GTV in larger distances, broadening the range covered in figure 4(b). For the GTV, the smallest tumor shows differences from a 0% difference at 2 cm lung distance up to  $-9\%$  at 20 cm, while differences for the largest tumor are between  $-1\%$  and  $-2\%$  for 4 cm and 20 cm, respectively.

In the bottom panel of figure 4 the relative differences of the dose values enclosing 95% ( $D_{95}$ ) and 20% ( $D_{20}$ ) of the volume, respectively, are shown. The  $D_{20}$  show more scatter but the trend of more passed lung resulting in a higher dose reduction is still valid. For the largest distance, a  $D_{20}$  dose difference between  $-2\%$  and  $-11\%$  is observed.



For the  $D_{95}$ , the data points scatter more randomly. Some points show even a positive discrepancy between the modulated and original calculation. Thus no clear correlation can be found.

The lung modulation influences the dose at the distal end of the tumor the most. Thus, plans optimized in a way that all the high dose area coincides with the distal region of the PTV show more effect on the  $D_{20}$ . On the other hands plans barely surrounding the distal region with the proposed 95% of the planned dose, will show a significant reduction of the  $D_{95}$ . For example, two identical volumes positioned in the dose distribution presented in figure 3(c) at depths 10–11.5 cm and 11–12.5 cm show a similar behavior in their decrease of the mean dose (around 1%). The  $D_{20}$  is decreased by 2% for the proximal volume and by only 1% for the distal volume. The big difference is observed for the  $D_{95}$ : while the coverage for the proximal volume is even increased by 2% due to the smoothing effect of the Bragg peak degradation, the  $D_{95}$  for the distal volume is decreased by  $-5\%$  because of the strong impact of the degradation effect at the distal end. Thus, small variation in the optimized plan, which are not observable from the DVH but only from the actual dose distribution have a great influence on parameters like the  $D_{95}$ .

In the further analysis only the mean dose is evaluated as (accounting to figure 4) it is a good indicator for the effects of the modulation.

### 3.3. Dependency on the shape of the radiated volume

It was found that the underdosage of the ellipsoid-shaped PTV depends on its orientation rather than on its volume: if the short axis was orientated in beam direction, the underdosage was about  $-9\%$  for both volumes. For the long axis in beam direction the underdose was around  $-3\%$ .

To be able to approximate the decrease of the mean dose not only for different positions in lung but also for different tumor sizes and shapes, an empirically found parameter is presented, which well describes the geometrical dependencies:

$$L_S = 2 \cdot \frac{a^2}{\sqrt{b \cdot c}} \quad (1)$$

$a$  denotes the axis in beam direction (as described in section 2.2(d)).  $L_S$ , which can be described as the scaled tumor length in beam direction, offers the possibility to normalize the different orientations of the tested ellipsoids with the spherical setups. This means if the  $x$ -axis in figure 4(a) is transformed from  $d_L$  to  $d_L/L_S$ , the different slopes for the different tumor sizes are leveled into one and thus a simple approximation for all cases can be made.



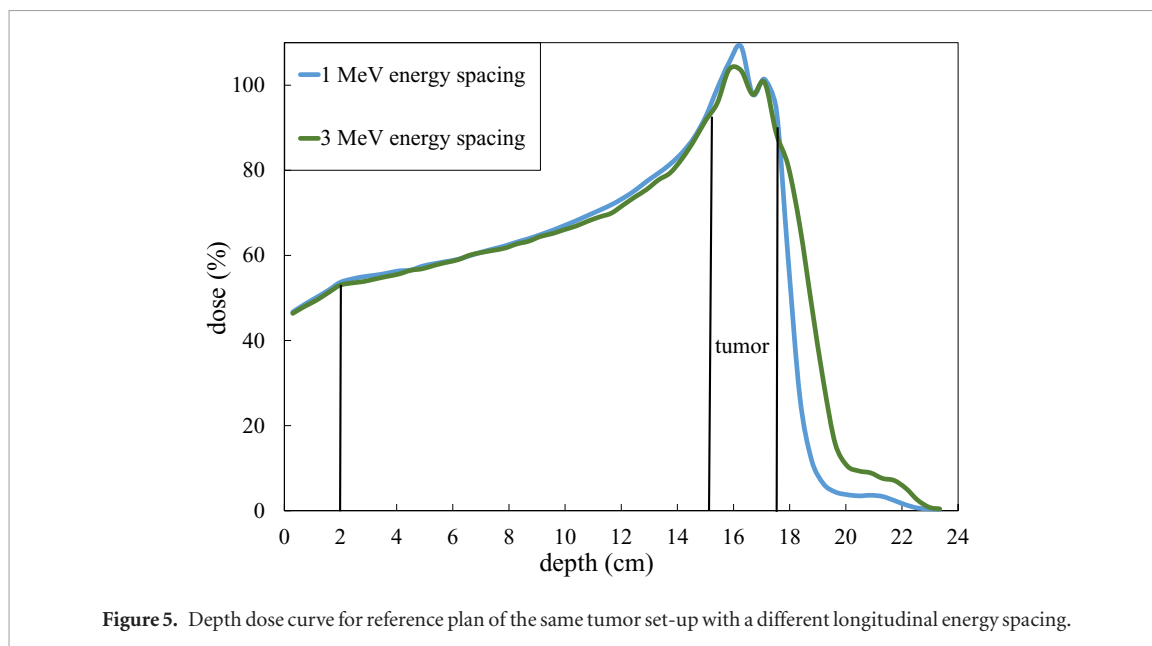


Figure 5. Depth dose curve for reference plan of the same tumor set-up with a different longitudinal energy spacing.

### 3.4. Dependency on the lateral and longitudinal spot spacing

As the Bragg peak degradation changes the width of each Bragg peak in beam direction, differences in the energy spacing may have an influence on the outcome of the Bragg peak degradation effects.

For the simulations redone with a different energy (longitudinal) spacing, a higher dose difference was observed in the cases where a more narrow spot spacing was optimized. For the 1 MeV energy spacing, the underdosage showed an about 40% higher dose difference in comparison to the 3 MeV energy spacing. Plans with a wider energy spacing have often a lower conformity and the smoothing effect of the Bragg peak degradation flattens the profile but does not reduce the mean dose significantly. For a high conformity plan, the smoothing leads to a more decreased mean dose. A higher conformity also allows the optimizer to spare dose in the surrounding normal tissue, which leads to a steeper dose fall-off which is also closer to the PTV. Figure 5 shows two different reference plans, which show the steeper gradient for the closer energy spacing. Of course, this can be accounted for during the planning procedure.

Regarding the lateral spot spacing, no difference within the uncertainties of the simulation with a lower lateral spot spacing was observed.

### 3.5. Energy dependency

To analyze the dependency of the Bragg peak degradation on the energy, the plans for the  $1\text{ cm}^3$  spherical tumor were also calculated with a thicker entrance wall (4 cm instead of 2 cm) leading to higher proton energies to enclose the tumor volume. Because this effect is expected to be smaller, the highest modulation power was chosen. The results are displayed in table 1. While for the GTV, only the small distances in lung show some discrepancies when the energy is increased, all dose differences for the mean PTV dose increase when applying a thicker wall. Higher proton energies have a smaller peak to plateau ratio as well as smaller lateral FWHM. Thus, lower energy plans might show less conformity than higher energy plans. As presented in section 3.4, a plan with higher conformity is more affected by the Bragg peak degradation. In general, applying higher proton energies increases the dose differences about additional  $-2\%$  for the PTV.

### 3.6. Effect of distal tissue

If the tumor is placed in the vicinity to the mediastinum, tissue follows distal to the tumor. Simulations for the  $2\text{ cm}^3$  tumor were performed to analyze the effects of the Bragg peak degradation with and without distal tissue. Again, the highest modulation power of  $800\ \mu\text{m}$  was used, to give a very conservative approximation. The results are presented in table 2. The mean dose was reduced by 19%, if the plan was optimized with no tissue distal to the tumor. However, with the optimization performed with distal tissue, the mean dose was only decreased by 10%, independent on the presence of distal tissue during the dose calculation. This outlines that the effect caused in the presence of distal tissue is solely caused by the optimized spot setting, as plans optimized with distal tissue feature more energy layers behind the tumor volume and thus leading to a smoother distal fall-off.

For a smaller distance of 6 cm and a larger distance between the PTV and the distal tissue, the effect is significantly reduced as the case in brackets in table 2 shows. The closer the tumor lays to distal tissue and the more the

**Table 1.** Dose differences for the mean dose of the GTV and the PTV, for a wall of 2 cm and a wall of 4 cm thickness (see figure 2). The tumor volume was 1 cm<sup>3</sup> and the modulation power 800  $\mu\text{m}$ .

GTV <sub>mean</sub> dose difference (%)				
Depth	4 cm	6 cm	10 cm	15 cm
2 cm wall	−4	−5	−9	−12
4 cm wall	−3	−7	−9	−12

PTV <sub>mean</sub> dose difference (%)				
Depth	4 cm	6 cm	10 cm	15 cm
2 cm wall	−3	−4	−7	−11
4 cm wall	−5	−7	−9	−13

**Table 2.** Dose differences for the PTV mean dose when calculated and optimized on a CT with or without tissue distal to the tumor. The distance in lung was 25 cm (6 cm) for all settings and the modulation power 800  $\mu\text{m}$ .

	PTV <sub>mean</sub> dose difference (%)	
	Calculated on CT with distal tissue	Calculated on CT without distal tissue
Optimized on CT with distal tissue	−10 [−4]	−10 [−4]
Optimized on CT without distal tissue	−19 [−5]	−19 [−5]

of PTV overlaps with the mediastinal wall, the smaller is the effect of the lung modulation. The occurrence of this effect depends on the settings of the machine in the treatment planning system.

### 3.7. Modulation power

As described in section 2.1 and by Baumann *et al* (2017), the modulation power is a parameter in the mathematical model used to reproduce the Bragg peak degradation, indicating the strength of the modulation effect. Measurements indicate a modulation power between 100  $\mu\text{m}$  and 800  $\mu\text{m}$  (Witt 2014). The modulation power in the simulations presented was chosen to be mostly 450  $\mu\text{m}$  but also 800  $\mu\text{m}$  to make a conservative approximation for clinical cases. As the modulation power has a great influence on the modulation effect, some of the simulations were redone with a modulation power of 250  $\mu\text{m}$  as presented in figure 6 to also give a less conservative approximation of the Bragg peak degradation. As expected, a lower modulation power decreases the dose differences occurring due to the Bragg peak degradation. For a linear approximation a lower slope would be assigned. Still, the increase of the dose difference for both, the GTV and the PTV in dependency of the distance in lung is clearly visible. A lower modulation power of 250  $\mu\text{m}$  reduces the effect further to 0% for a depth of 4 cm and to −3% for the 20 cm depth.

### 3.8. Combined approximation of the degradation

As the aim was to allow an estimation of the change in the dose distribution for clinical cases, all data were combined in figure 7. To connect all different setups and results, the dose difference was plotted against the ratio of the penetration depth in lung and the scaled tumor length in beam direction as proposed in equation (1). This condenses all data allowing a linear approximation and thus enabling a prediction of the reduction of the mean dose in the tumor.

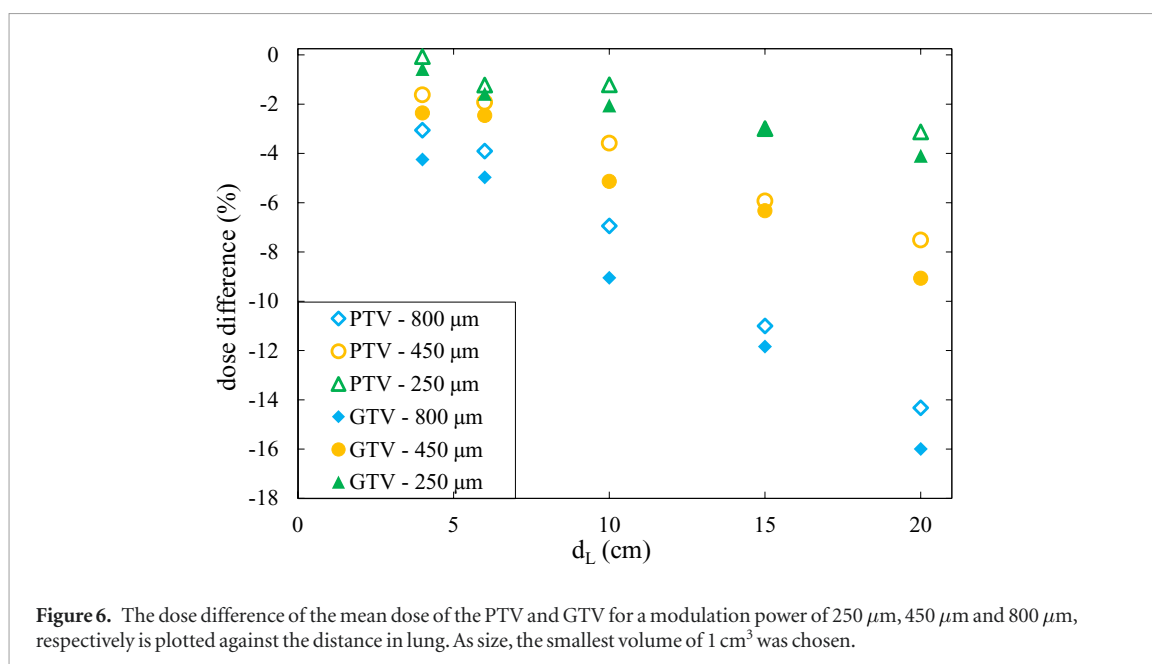
The GTV volumes and the depths in lung were chosen to represent a realistic variety over all possible lung tumor scenarios.

For a less conservative approach, figure 7 also gives the approximation for a modulation power of 250  $\mu\text{m}$ , which seems to be clinically more likely. The slope was gained by a fit through all data calculated with 250  $\mu\text{m}$  whereas the width of the uncertainty band was taken from the 800  $\mu\text{m}$  fit.

## 4. Discussion

The presence of the Bragg peak degradation due to microscopic inhomogeneities is well known, however its effects are not accounted for in any TPS, hence the impact of the patient dose is not known.

In this phantom based study, the impact of the Bragg peak degradation on the dose of lung tumors was estimated in dependence on different clinical treatment parameters such as the tumor depth in lung, the tumor volume and its shape, the proton energy and the energy spacing. All in all, the results show that the longer the



distance the particles travel through lung and the smaller the tumor volume, the higher is the difference between planned mean dose and actual mean dose of the target volume. In all cases an underdosage of the tumor volume was found. The most extreme case investigated in this work showed an underestimation of the mean dose of  $-14\%$  (800 μm). But more clinical relevant setups (distance of 6 cm, modulation power of 250 μm, see figure 6) result in an underestimation of about 2%.

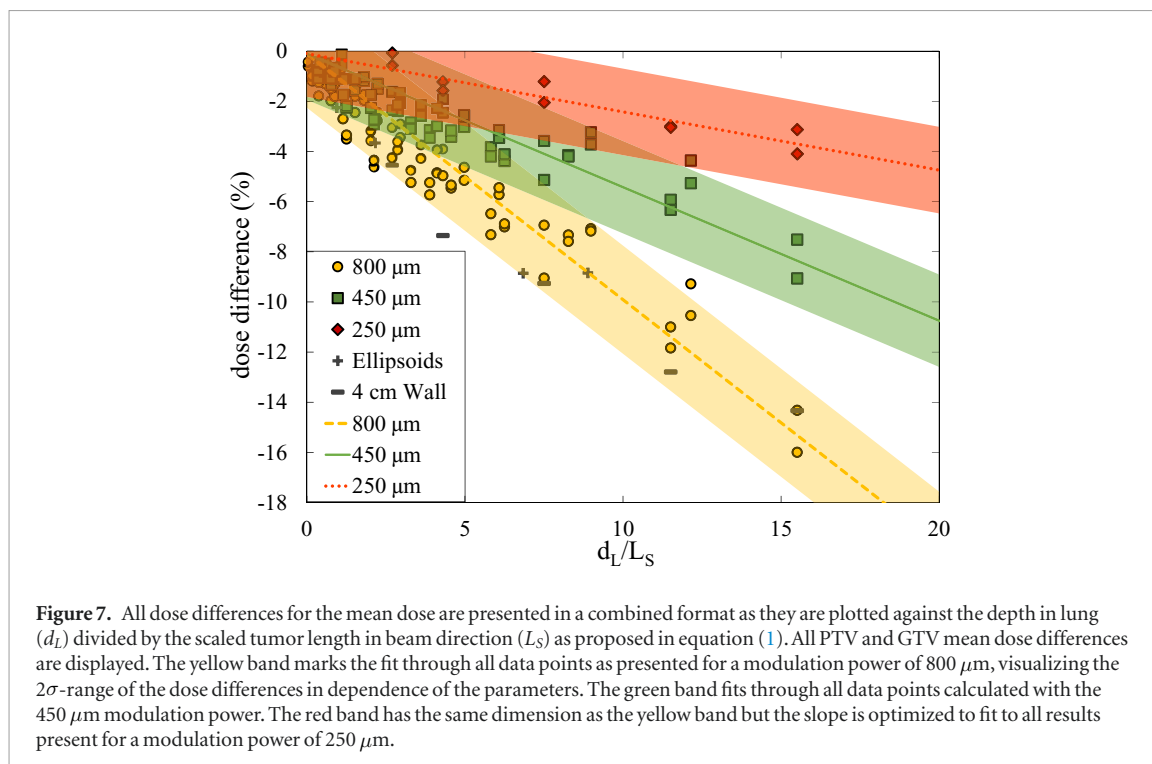
In general, it was found that the Bragg peak modulation smooths the dose distribution: hot spots are reduced leading to a steeper gradient in the DVH around a reduced mean value in comparison to the DVH predicted by the TPS.

Another dependency that was investigated was the energy selection by the TPS, which was found to have an influence on the dose distribution. All plans calculated with a thicker thorax wall and thus higher energy selection showed an increased dose difference. This correlates with the results obtained for the spot spacing as parameter under investigation: energy spacing has a relevant impact on the dose when the Bragg peak degradation is accounted for. An increased number of energy layers throughout the tumor (and not distal to the tumor) leads to a decrease of the weight of each spot. With the Bragg peak degradation the peak dose is decreased and as the missing dose is only distributed in the distal region, more spots result in a decreased peak dose thus a decreased mean dose.

At last, the effect of tissue distal to the tumor was investigated as it is the case when the tumor is attached to the mediastinum. It was found that this has no direct influence on the dose calculated with and without the Bragg peak degradation accounted for. However, for the given TPS settings, the plan optimization process was highly influenced by distal tissue. When a plan is optimized with tissue distal to the tumor with the same margin around the tumor more energy layers have spots within this margin because a spot spacing of e.g. 1 MeV results in about 1 mm distance in water but a far higher distance in air. Therefore, plans optimized with distal tissue feature a higher dose behind the tumor, resulting in a decreased dose reduction when accounting for the Bragg peak degradation. For small tumor volumes, the dose difference could be decreased by a half.

It was possible to include most results in the dose difference band in figure 7. This band allows an estimation of the uncertainty when not including the Bragg peak degradation in lung tissue for many clinical cases. If an approximation of the effect on the dose distribution for clinical case is of interest, the average distance in lung needs to be estimated and the tumor length in beam direction needs to be measured and evaluated. With these information and the results presented in figure 7 the reduction of the mean dose can be estimated in a conservative approach or a more probable approach.

In comparison to the intra- and interfractional motion in proton treatment of lung cancer (Widesott *et al* 2008, De Ruysscher *et al* 2015), the underestimation of 2% in the best case seems negligible, but differences around 10% that were also observed should rather not be neglected. Nevertheless, as tumor movement is more and more accounted for by robust planning, gating, tracking and plan-of-the-day concepts thus reducing the effect on the dose distribution to a minimum, future treatment concepts should aim for an incorporation of the Bragg peak degradation.



As the measurements of the modulation power covers a broad range and the change in the modulation power shows the most severe changes in the dose effects, more data for the modulation power in human lungs are needed.

## 5. Conclusion

A detailed 3D systematic analysis of the effect of the Bragg peak degradation was performed. The results were presented in dependency of the distance through lung tissue, the size and shape of the treatment volume, as well as plan specific parameters as particle energy and spot distance. The effects were estimated for different modulation powers, giving a worst-case scenario and more likely scenarios. The results allow for the first time an approximation of the uncertainty on the mean dose for a clinical scanned proton treatment plan. Even though tumor movement affects the treatment outcome more than the Bragg peak degradation, an inclusion of the dose changes due to the Bragg peak degradation is bringing proton therapy for lung carcinomas closer to a high precision therapy.

## References

- Agostinelli S et al 2003 Geant4—a simulation toolkit *Nucl. Instrum. Methods Phys. Res. A* **506** 250–303
- Baumann K-S, Witt M, Weber U, Engenhart-Cabillic R and Zink K 2017 An efficient method to predict and include Bragg curve degradation due to lung-equivalent materials in Monte Carlo codes by applying a density modulation *Phys. Med. Biol.* **62** 3997
- De Ruyscher D, Sterpin E, Haustermans K and Depuydt T 2015 Tumour movement in proton therapy: solutions and remaining questions: a review *Cancers* **7** 1143–53
- Espana S and Paganetti H 2011 Uncertainties in planned dose due to the limited voxel size of the planning CT when treating lung tumors with proton therapy *Phys. Med. Biol.* **56** 3843
- Goitein M 1977 The measurement of tissue heterodensity to guide charged particle radiotherapy *Int. J. Radiat. Oncol. Biol. Phys.* **3** 27–33
- Perl J, Shin J, Schuemann J, Faddegon B and Paganetti H 2012 TOPAS: an innovative proton Monte Carlo platform for research and clinical applications *Med. Phys.* **39** 6818–37
- Ringbaek T P, Simeonov Y, Witt M, Engenhart-Cabillic R, Kraft G, Zink K and Weber U 2017 Modulation power of porous materials and usage as ripple filter in particle therapy *Phys. Med. Biol.* **62** 2892
- Sawakuchi G, Titt U, Mirkovic D and Mohan R 2008 Density heterogeneities and the influence of multiple Coulomb and nuclear scatterings on the Bragg peak distal edge of proton therapy beams *Phys. Med. Biol.* **53** 4605–19
- Schneider U, Pedroni E and Lomax A 1996 The calibration of CT Hounsfield units for radiotherapy treatment planning *Phys. Med. Biol.* **41** 111
- Schulz-Ertner D and Tsjuii H 2007 Particle radiation therapy using proton and heavier ion beams *J. Clin. Oncol.* **25** 953–64
- Sell M, Titt U, Perles L, Mirkovic D, Mohan R, Babert M and Oelfke U 2012 WE-E-BRB-02: evaluation of analytical proton dose predictions with a lunglike plastic phantom *Med. Phys.* **39** 3956
- Titt U, Sell M, Unkelbach J, Bangert M, Mirkovic D, Oelfke U and Mohan R 2015 Degradation of proton depth dose distribution attributable to microstructures in lung-equivalent material *Med. Phys.* **42** 6425
- Urie M, Goitein M, Holley W and Chen G 1986 Degradation of the Bragg peak due to inhomogeneities *Phys. Med. Biol.* **31** 1


- Widesott L, Amichetti M and Schwarz M 2008 Proton therapy in lung cancer: clinical outcomes and technical issues a systematic review *Radiother. Oncol.* **86** 154–64
- Wilson R 1946 Radiological use of fast protons *Radiology* **47** 487–91
- Witt M 2014 Modulationseffekte von Kohlenstoffionen bei der Bestrahlung von Lungen *Master's Thesis* Technische Hochschule Mittelhessen—University of Applied Sciences, Giessen, Germany
- Witt M, Weber U, Simeonov Y and Zink K 2015 SU-E-T-671: range-modulation effects of carbon ion beams in lung tissue *Med. Phys.* **42** 3491
- Zhang X, Li Y, Pan X, Xiaoqiang L, Mohan R, Komaki R, Cox J D and Chang J Y 2010 Intensity-modulated proton therapy reduces the dose to normal tissue compared with intensity-modulated radiation therapy or passive scattering proton therapy and enables individualized radical radiotherapy for extensive stage iiib non-small-cell lung cancer: a virtual clinical study *Int. J. Radiat. Oncol. Biol. Phys.* **77** 357–66

RESEARCH

Open Access

# Effects of the Bragg peak degradation due to lung tissue in proton therapy of lung cancer patients



Kilian-Simon Baumann<sup>1,2\*</sup> , Veronika Flatten<sup>1,2</sup>, Uli Weber<sup>3</sup>, Stefan Lautenschläger<sup>1,4</sup>, Fabian Eberle<sup>1,4</sup>, Klemens Zink<sup>1,2,5</sup> and Rita Engenhardt-Cabillic<sup>1,4</sup>

## Abstract

**Purpose:** To quantify the effects of the Bragg peak degradation due to lung tissue on treatment plans of lung cancer patients with spot scanning proton therapy and to give a conservative approximation of these effects.

**Methods and materials:** Treatment plans of five lung cancer patients (tumors of sizes 2.7–46.4 cm<sup>3</sup> at different depths in the lung) were optimized without consideration of the Bragg peak degradation. These treatment plans were recalculated with the Monte Carlo code TOPAS in two scenarios: in a first scenario, the treatment plans were calculated without including the Bragg peak degradation to reproduce the dose distribution predicted by the treatment-planning system (TPS). In a second scenario, the treatment plans were calculated while including the Bragg peak degradation. Subsequently, the plans were compared by means of  $D_{\text{mean}}$ ,  $D_{98\%}$  and  $D_{2\%}$  in the clinical target volume (CTV) and organs at risk (OAR). Furthermore, isodose lines were investigated and a gamma index analysis was performed.

**Results:** The Bragg peak degradation leads to a lower dose in the CTV and higher doses in OARs distal to the CTV compared to the prediction from the TPS. The reduction of the mean dose in the CTV was – 5% at maximum and – 2% on average. The deeper a tumor was located in the lung and the smaller its volume the bigger was the effect on the CTV. The enhancement of the mean dose in OARs distal to the CTV was negligible for the cases investigated.

**Conclusions:** Effects of the Bragg peak degradation due to lung tissue were investigated for lung cancer treatment plans in proton therapy. This study confirms that these effects are clinically tolerable to a certain degree in the current clinical context considering the various more critical dose uncertainties due to motion and range uncertainties in proton therapy.

**Keywords:** Proton therapy, Lung modulation, Bragg peak degradation, Treatment planning

## Background

Since proposed for radiation therapy, ion beams are of increasing interest in radiation oncology [1, 2]. In homogeneous materials the dose profile of heavy charged particles such as protons consists of a low dose plateau at small depths followed by the so-called Bragg peak where most of the dose is deposited. The Bragg peak is

followed by a sharp distal fall-off. This finite range and sharp distal fall-off of the dose deposition as well as the comparable low entrance dose lead to a reduction in the integral dose. These advantages of protons in radiation therapy lead to the possibility of a conformal dose distribution in the target while sparing surrounding healthy tissue [3]. Mainly two approaches for the use of proton therapy have evolved [4]: 1) to escalate the dose in the tumor while allowing the same dose to organs at risk (OAR) compared to conventional photon therapy and 2) keeping the target dose constant compared to conventional photon therapy and reducing the dose deposited

\* Correspondence: [kilian-simon.baumann@staff.uni-marburg.de](mailto:kilian-simon.baumann@staff.uni-marburg.de)

<sup>1</sup>University Medical Center Giessen-Marburg, Department of Radiotherapy and Radiooncology, Marburg, Germany

<sup>2</sup>University of Applied Sciences, Institute of Medical Physics and Radiation Protection, Giessen, Germany

Full list of author information is available at the end of the article



© The Author(s). 2019 **Open Access** This article is distributed under the terms of the Creative Commons Attribution 4.0 International License (<http://creativecommons.org/licenses/by/4.0/>), which permits unrestricted use, distribution, and reproduction in any medium, provided you give appropriate credit to the original author(s) and the source, provide a link to the Creative Commons license, and indicate if changes were made. The Creative Commons Public Domain Dedication waiver (<http://creativecommons.org/publicdomain/zero/1.0/>) applies to the data made available in this article, unless otherwise stated.

to OARs as much as possible. Both approaches can be considered for the treatment of lung cancer patients with protons. On the one hand, it has been shown in some studies that a dose escalation in the tumor improves local control and survival in non-small cell lung cancer (NSCLC) patients [4]. On the other hand, the sparing of healthy tissue is of interest for tumors in difficult anatomies where the tumor is located near to sensitive structures or even enclosed by OARs. This is often the case for lung cancer patients due to the possible proximity of OARs like the heart, esophagus, trachea, large blood vessels and the spinal cord [4].

For early-stage NSCLC patients the outcomes achieved with proton therapy are similar to those achieved with stereotactic body radiotherapy (SBRT) [4] despite excellent dose distributions and sparing of OARs. This holds especially for small peripheral lesions, since these are mostly located far from critical structures (except for ribs and chest wall) and hence a sparing of OARs is well achievable with SBRT. However, for larger tumors, especially those located near to OARS, proton therapy might be superior to SBRT.

For locally advanced (stage III) lung cancer patients, virtual clinical studies showed that in proton plans it is possible to reduce the dose deposition in normal tissue, especially in the heart, compared to photon plans [3–5]. Additionally, a phase II study with 44 patients showed an enhanced median survival in a combined radio-chemotherapy when irradiating with protons compared to photons. The patients treated with protons showed minimal grade 3 toxicities [4, 6].

In addition to the debatable benefits of proton therapy compared to SBRT in lung cancers, some difficulties in treating lung cancers with protons arise due to the underlying physics as well as the technical application of the proton beam. One of the main issues is the range of protons that depends on the material in the beam path: in case that the patient's anatomy changes and hence is different during the treatment compared to the treatment-planning process, the range and hence the dose deposition can be different to that predicted by the TPS. Hence, the outcome of the treatment is vulnerable to changes in the anatomy of the patient as the patient moves, is not optimally positioned or the anatomy of the patient changes between fractions, e.g. due to a shrinkage of the tumor or weight loss [7–10]. Especially the change in the anatomy between fractions causes a need in plan adaption strategies for proton therapy [11].

Another issue is that the range of protons is predicted based on X-ray CT images while the conversion of stopping powers from X-ray CT images is inaccurate [12, 13]. Furthermore, uncertainties in the dose deposited arise from uncertainties in biological effectiveness models [7, 14].

A crucial topic in the proton therapy of lung cancer patients is motion management since interplay effects due to respiratory motion or motion of the heart combined with the precise application of actively scanned proton beams can lead to a severe underdosage of the target volume [15–20].

Another uncertainty in proton therapy of lung cancer patients arises from the characteristics of the lung tissue itself: The heterogeneous structure of the lung tissue leads to a degradation of the Bragg peak and to a wider distal fall-off [21, 22]. If this degradation is not considered correctly during the treatment planning of lung cancer patients, it might lead to an underdosage of the target volume and an overdosage of normal tissue distal to the target volume [22, 23]. Although this degradation has been described in numerous works [24–29], it cannot be considered in the clinical treatment-planning process and dose calculation on treatment-planning CT images. The reason is that due to the restricted resolution of treatment-planning CTs, the microscopic structure of lung tissue is not resolved sufficiently and a more homogeneous tissue distribution is predicted [26, 30].

Baumann et al. [29] introduced and extensively tested an efficient method to consider the Bragg peak degradation on the base of typically used treatment-planning CT data in Monte Carlo codes by applying a density modulation to voxels associated with the lung. Flatten et al. [31] used this model to estimate the effects of the Bragg peak degradation based on a phantom study where spherical tumors of different sizes were placed at different depths in the lung and the underdosage of the target volume was quantified. The result showed that the underdosage of the target volume increases with an increasing depth of the tumor in lung and a decreasing tumor volume. The maximum underdosage in terms of the mean dose was –15% compared to the dose distribution predicted by the treatment-planning system that did not consider the Bragg peak degradation.

In this study the effects of the Bragg peak degradation were investigated on clinical cases for various anatomical locations of the tumor in the lung and different treatment plans. We chose simple field configurations so that the results can be used by a large variety of proton centers. The goal is to give upwards estimations for the dose uncertainty in the target volume and OARs. For that, we included also extreme cases (e.g. small tumor volumes and large depths in lung) to quantify the maximum degradation effect in realistic patient anatomies.

## Methods and materials

### Selection of patients

We investigated five exemplary clinical cases with tumor volumes between 2.7 cm<sup>3</sup> and 46.4 cm<sup>3</sup>. The tumors were located in the right lung in the upper lobe (two

cases) or the central lobe (three cases). We chose the clinical cases to have tumors located in the center of the lung as well as tumors that are located near to soft tissue or OARs. In doing so we are able to investigate different depth of the tumor in the lung as well as the effects of the Bragg peak degradation on surrounding normal tissue and OARs. For two cases the tumor was located near to the spinal cord. No tumor was located directly at the thorax wall in order to always have lung tissue between the thorax wall and the tumor and hence in the beam path. The patients were originally treated with photons and retrospectively re-planned with protons for this study. We used different beam directions in the proton plans to generate different path lengths in the lung (see Fig. 1 and Table 1).

As described in the introduction, small tumor volumes as investigated in this study might not benefit from proton therapy compared to SBRT and hence tend to be less relevant for proton therapy. Yet, small tumor volumes have been treated with protons at different centers [32–34], with volumes going down to only 1 cm<sup>3</sup>. Furthermore, Flatten et al. [31] showed that the effects of the Bragg peak degradation increase with a decreasing tumor volume. Thus, we investigated these small tumors

as well, in particular to derive an upwards estimation for larger and thus clinically more relevant tumor volumes.

**Treatment planning**

All treatment plans were optimized with Eclipse v.13.7 (VARIAN) using the non-linear universal proton optimizer, v.13.7.15. The total prescribed dose was 30 Gy (RBE) and the only planning objective was to deliver at least 95% of the prescription dose to at least 98% of the planning target volume (PTV). For small tumor volumes we accepted hot spots (up to 115% of the prescribed dose) in the PTV. The PTV was the clinical target volume (CTV) plus an isotropic margin of 3 mm, although most PTV concepts proposed in the literature [7, 34–36] are field specific and account for uncertainties of the proton’s range or the positioning of the patient. However, in the majority of clinical situations, an isotropic margin around the CTV is used for treatment planning as done in this study. Additionally, we planned on static CT data, ignoring movements of the anatomy due to respiration in both the planning and dose calculation. By excluding any effects due to motion, positioning of the patient or range uncertainties, we are able to extract the pure effects of the Bragg peak degradation. We analyzed these effects on the CTV and not the PTV, since the CTV

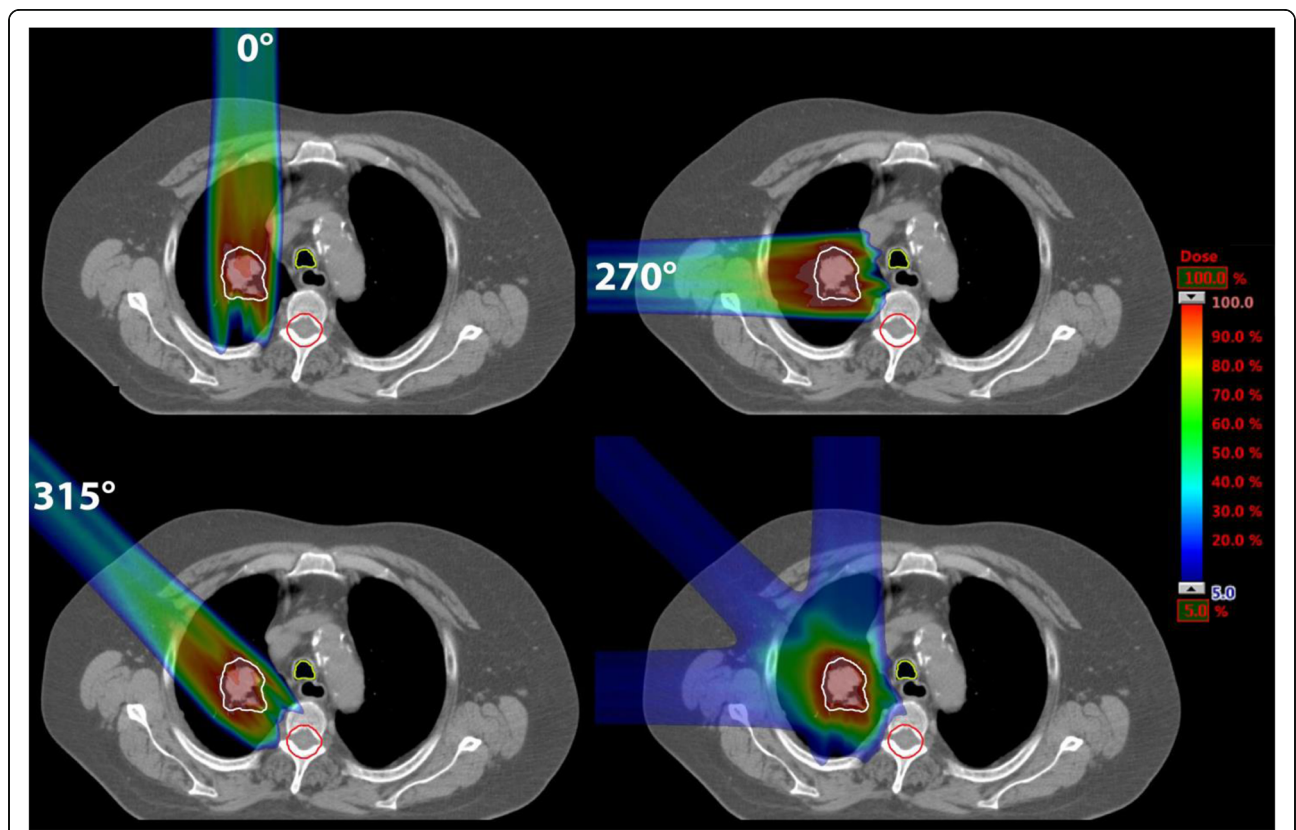


**Fig. 1** CT slices of one exemplary patient (patient 1): for the beam directions 0°, 270° and 315° plans were optimized individually consisting of one single field. On the bottom right the sum of these plans is shown. The CTV is marked in white, trachea in light green and spinal cord in red. On the right a color bar is given indicating the relative dose



**Table 1** Volumes of the CTVs and lungs for the five patients and minimum and maximum diameter of the CTVs as well as depths in lung of the CTVs for each beam direction. The depth of the CTV corresponds to the path length through lung tissue for the spot at the isocenter

Patient	Lung volume in cm <sup>3</sup>	Volume of CTV in cm <sup>3</sup>	min./max. diameter of CTV in cm	Depth of CTV in cm for different beam directions		
				0°	270°	315°
1	2294	46.4	2.9/4.2	6.2	3.3	3.6
2	1882	4.2	1.8/2.3	1.8	2.1	1.5
3	1705	32.1	3.5/5.2	12.2	9.2	9.2
4	1780	6.2	2.2/2.4	6.9	2.7	5.3
5	1600	2.7	1.6/2.0	4.5	3.8	3.6

is the clinically relevant structure. Since for each optimized plan the dose deposited in the OARs was below any critical value we did not include any constraints for OARs in the treatment-plan optimization.

We decided to investigate simple treatment plans consisting of only one single field coming from either 0°, 270° or 315°. We used different beam directions to generate different depths of the CTV in the lung. The distal spot spacing was 3 mm, the lateral spot spacing was 0.45 times the full-width-half-maximum (FWHM) in air. The FWHM for 70 MeV protons was 32.5 mm and for 221 MeV protons it was 8.1 mm.

The different beam directions are shown in Fig. 1 for one exemplary patient. As described later in the text, we also made a sum plan of the three single field plans for each patient as shown in Fig. 1 bottom right. In Fig. 2 the remaining four patients are shown with one exemplary treatment plan each.

Although some of these beams may not be the best choice from a clinical point of view (e.g. OARs distal to the PTV, large depth of the tumor in the lung), we decided to investigate these cases anyway to give an upwards estimation for the effects of the Bragg peak degradation also for worst-case scenarios.

The motivation for using simple treatment plans is to highlight the effects of the Bragg peak degradation. Furthermore, there is no gold standard in plan design for lung cancer patients, especially concerning the choice of number of fields and beam directions, although several proton centers have already treated lung cancer patients with protons [6, 32–34]. Thus, in keeping the treatment plans simple, we can assure that the results from this study are usable for as many different proton centers as possible since the dependencies of the Bragg peak degradation (e.g. on the depth of tumor in lung) can be assessed more easily using simple treatment plans compared to complex IMPT plans.

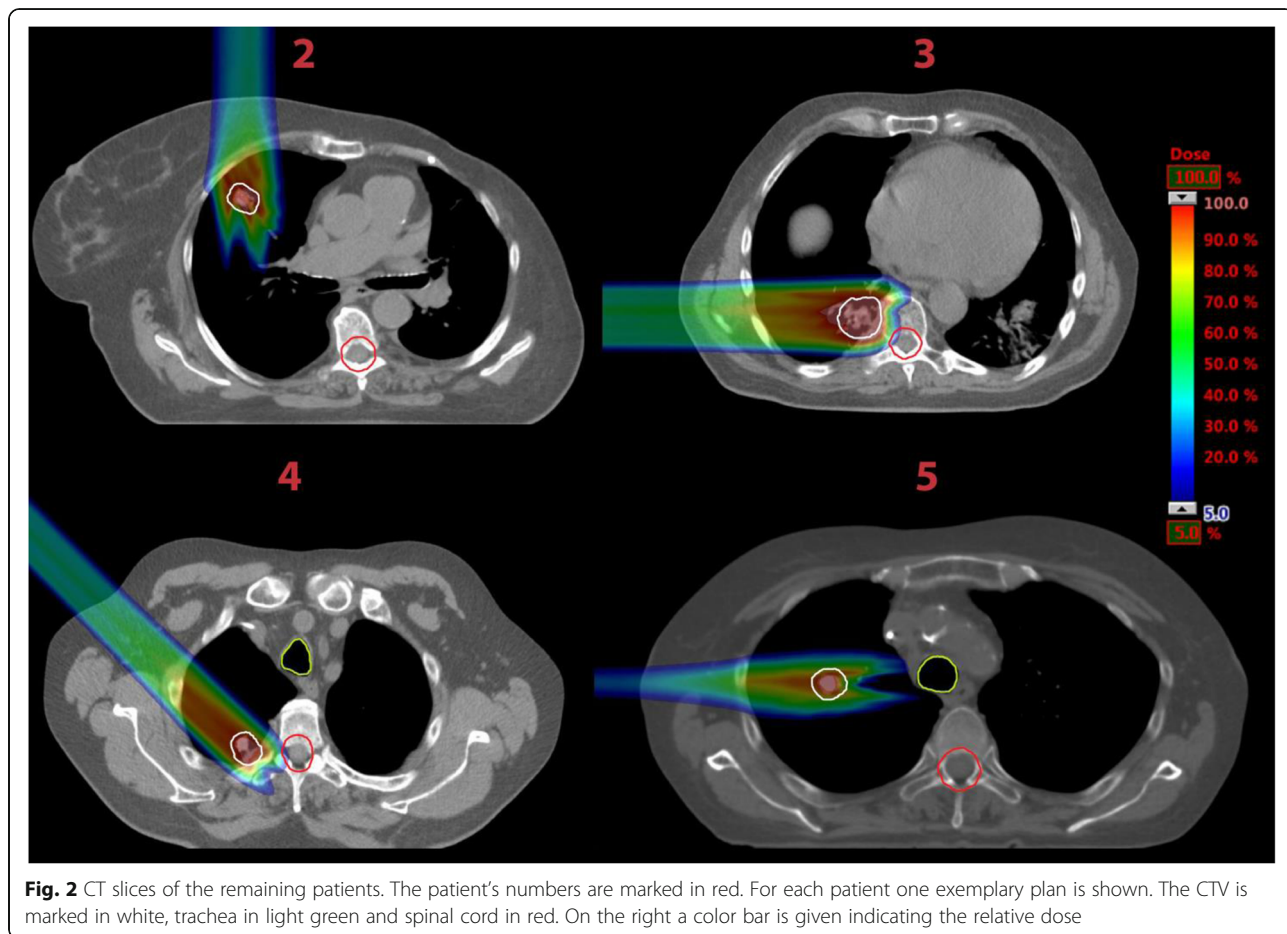
In order to assess whether the results from this study can be used to estimate the effects of the Bragg peak

degradation for more complex plans, we investigated two IMPT plans, one each for patient 1 and 5 as shown in Fig. 3. The choice fell on these two patients since they have the largest and smallest tumor volume (compare Table 1). Multi-field optimization was enabled to optimize three fields for each plan. The same PTV concept and planning objectives were used as for the simple plans. For patient 1 the beam directions were 180°, 270° and 330°. For patient 5 the beam directions 10°, 180° and 270° were used.

#### Simulations

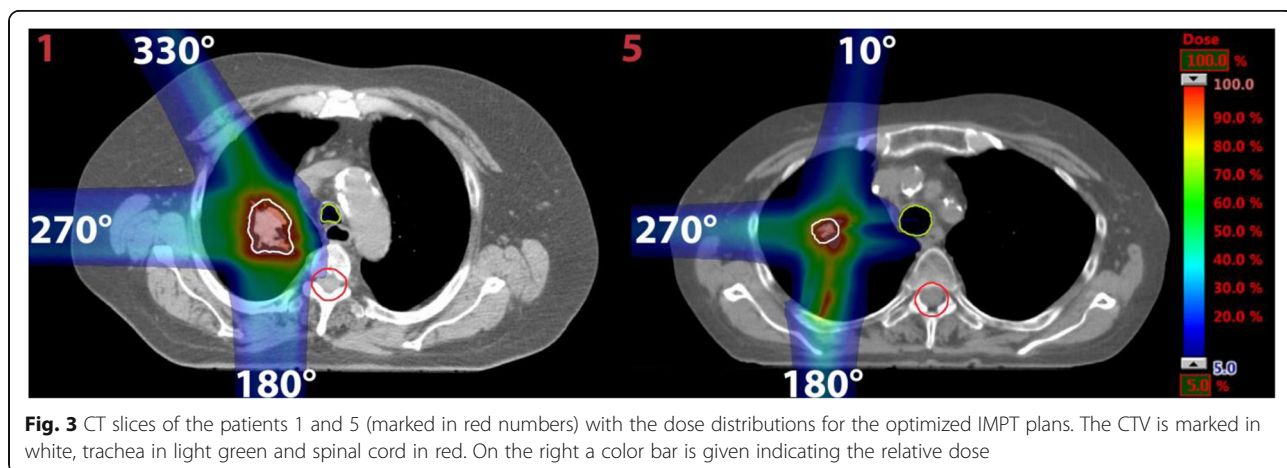
Simulations were performed using the Monte Carlo code TOPAS (Tool for Particle Simulations) version 3.1.p1 [37], a toolkit based on Geant4 (Geometry And Tracking) version geant4–10-03-patch-01 [38]. We used the same beam data in both TOPAS and Eclipse and commissioned these data to match the beam delivery system at the Ion-Beam Therapy Center Marburg. Dose calculation results in water between TOPAS and Eclipse agreed well. The passing rate of the gamma index 1%/1 mm for voxels with dose values greater than 20% of the maximum dose was larger than 98% for single spots. It is known that differences between dose calculation algorithms as used in Eclipse and Monte Carlo codes such as TOPAS exist especially for dose calculations in the lung [39]. Hence, all dose calculations were performed with TOPAS so that differences in the dose calculation between TOPAS and Eclipse do not falsify the results.

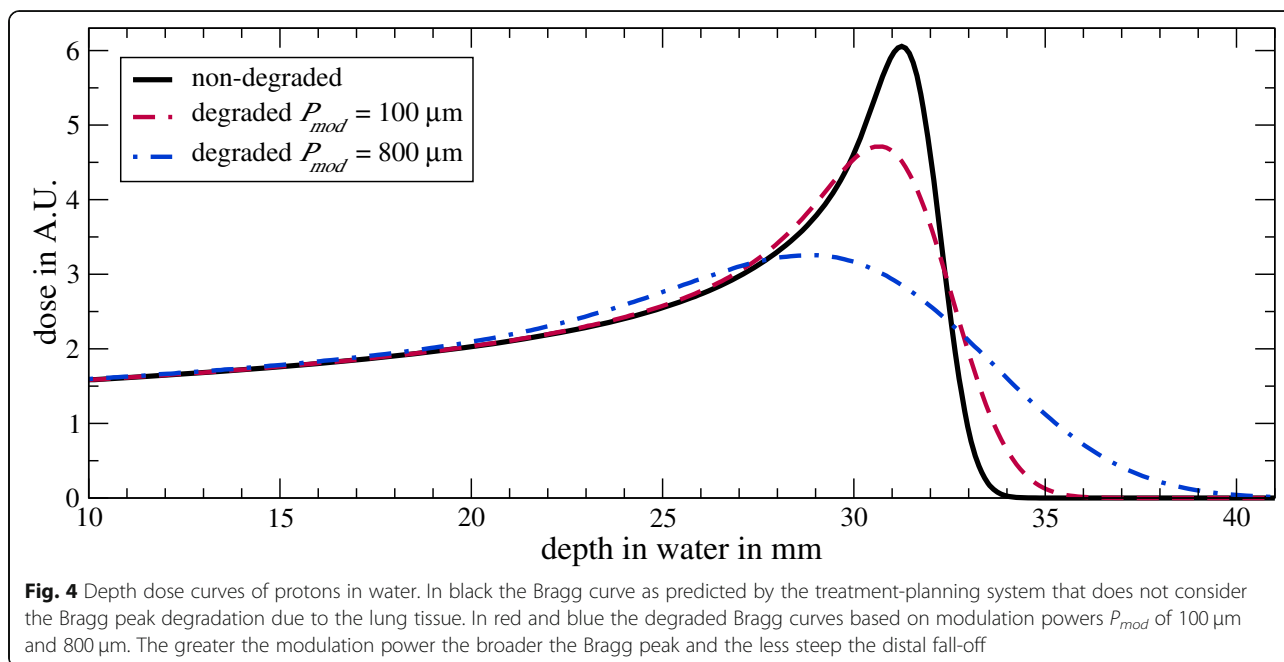
Each treatment plan optimized with Eclipse was recalculated in TOPAS in two scenarios: In the first scenario, each optimized treatment plan was calculated on the original CT data. Hence, this calculation corresponds to the prediction from the treatment-planning system. In a second scenario, the plans were recalculated while considering the Bragg Peak degradation. To do so, we used the mathematical model presented by Baumann et al. [29]. The strength of the Bragg peak degradation is quantified by the material characteristic “modulation power”  $P_{mod}$ . The greater the modulation power of a heterogeneous material like lung tissue the broader the



Bragg peak and the less steep the distal fall-off as shown in Fig. 4. Based on the modulation power a density distribution can be derived. When modulating the density of each voxel associated with the lung within the patient following this density distribution, the Bragg peak degradation due to the lung tissue is being reproduced [29]. The dose distributions for each plan obtained from using

the original CT data (non-modulated case) and when applying the density modulation (modulated case) were compared in means of cumulative dose volume histograms (DVH), mean doses  $D_{mean}$ ,  $D_{98\%}$  and  $D_{2\%}$  in the CTV and OARs. Additionally, we investigated the differences in the dose distribution when combining the dose distributions from the single plans (beam directions 0°,





270° and 315°) for each patient to an added-up dose distribution to investigate the influence of the number of irradiated fields on the degradation effects.

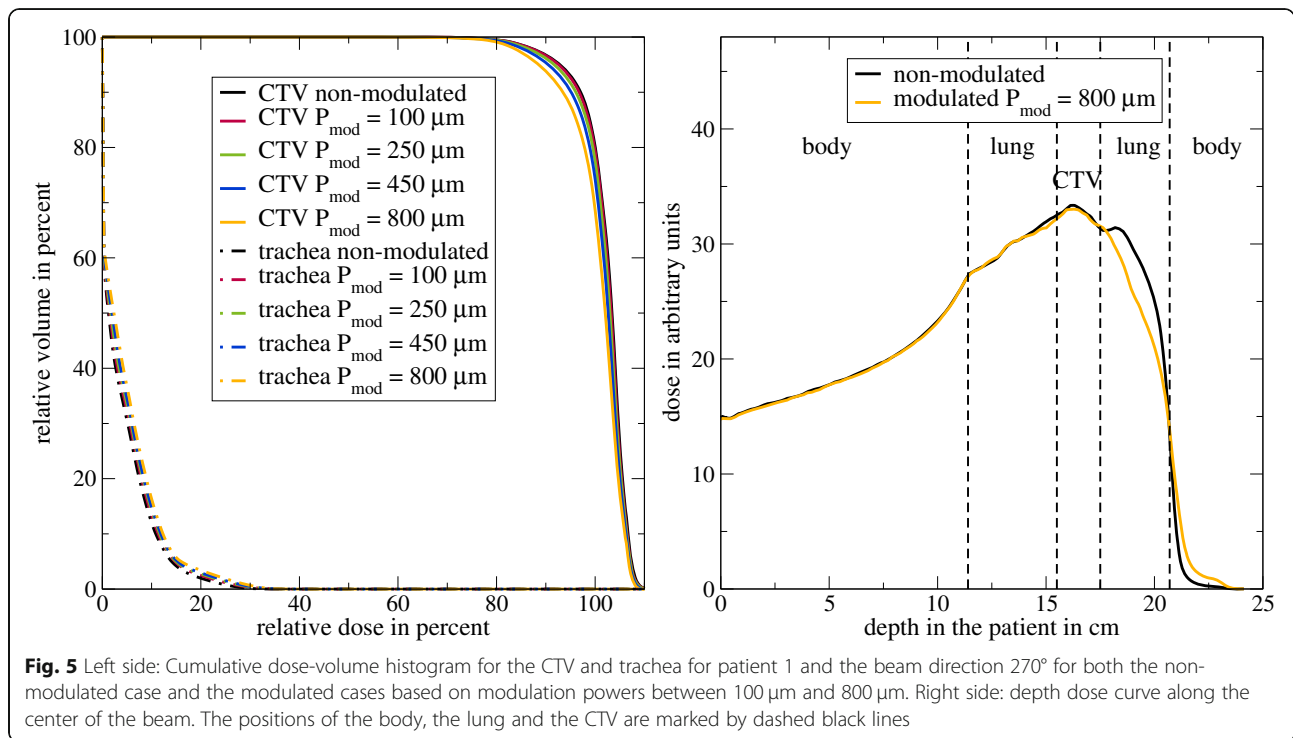
In a study by Witt [40] the modulation powers of porcine lungs were measured in proton beams to be in the range from 300  $\mu\text{m}$  to 750  $\mu\text{m}$ . Since the measurements were performed with complete lungs, the measured modulation powers correspond to integrated modulation powers of all the structures of the lung being arranged in the beam that cannot be identified in CT images. The modulation power increases with increasing structure sizes [29]. Thus, the modulation power varies with the position in the lung. In the peripheral region of the lung the modulation power tends to be smaller compared to the central lung where the size of the structures is greater. For almost each measurement the modulation power was in the range from 300  $\mu\text{m}$  to 500  $\mu\text{m}$  with an average of 450  $\mu\text{m}$ . For one measurement the modulation power was 750  $\mu\text{m}$ . However, for this measurement the lung was positioned in a way that a large bronchial structure was in the beam line.

To clarify whether these results obtained with porcine lungs are applicable for human lung tissue, high-resolution CT images with a resolution of 4  $\mu\text{m}$  of human lung tissue samples were investigated by Witt [40] and Baumann et al. [29]. The so-gained modulation powers were in the range from 50  $\mu\text{m}$  to 250  $\mu\text{m}$ . The authors discussed that the preparation of the tissue samples resulted in a noticeable loss of water of up to 37% and hence in a reduction of the sizes of the lung structures. Therefore, the modulation powers gained in this investigation are lower compared to the measurements with porcine lungs.

Both the measurements with porcine lungs and the investigation of human lung tissue samples indicate that the modulation power of lung tissue is in the order of some hundred micrometers. However, until now there is no possibility to determine a patient-specific modulation power for each region of the lung. Therefore, in this study we investigated the effects of the Bragg peak degradation based on modulation powers of 100  $\mu\text{m}$ , 250  $\mu\text{m}$ , 450  $\mu\text{m}$  and 800  $\mu\text{m}$ , covering the whole range of modulation powers found in the measurements of porcine lungs and the investigation of human lung tissue samples with some additional buffer to determine the minimum and maximum degradation effects in exemplary clinical cases. For the IMPT plans we only used a modulation power of 450  $\mu\text{m}$ .

## Results

In Fig. 5 on the left side the DVH for patient 1 and the beam direction 270° is shown for the CTV and the OAR trachea. The Monte Carlo calculated DVH for each volume is shown for the non-modulated case representing the dose distribution predicted by the treatment-planning system and the modulated cases where the Bragg peak degradation based on modulation powers between 100  $\mu\text{m}$  and 800  $\mu\text{m}$  is considered. The dose coverage of the CTV decreases with an increasing modulation power. The dose deposited in the trachea increases with an increasing modulation power. On the right side the depth dose curves along the center of the beam for the non-modulated scenario and the modulated one based on the maximum modulation power of 800  $\mu\text{m}$  are shown. The positions of the body, the lung and the CTV are marked by dashed black lines. We



decided to show the results for the extreme modulation power of 800  $\mu\text{m}$  since for a smaller modulation power the effects are not visible as clearly: when entering the body both dose distributions are the same. In the lung the effects of the degradation can be seen resulting in a broader dose curve and a less steep fall-off for the modulated case. Within the CTV there is a slightly higher dose for the non-modulated case. In the lung distal to the CTV there is a significantly higher dose for the non-modulated case. The background is that in this case a spot is used by the TPS where the Bragg peak is located distal to the CTV in order to achieve a sufficient dose coverage within the CTV. This peak is smoothed in the modulated case as described by Flatten et al. [31]. In the body distal to the lung the dose for the modulated case is higher due to the broader fall-off resulting in a larger range and hence a higher dose deposition.

In Fig. 6 exemplary isodose lines [41, 42] for 95, 80 and 20% of the prescribed dose are shown for the non-modulated case (pink) and the modulated case based on a modulation power of 800  $\mu\text{m}$  (green). Additionally, the CTV is marked in white, the trachea in light green and the spinal cord in red. Again, we decided to show the results for the extreme modulation power of 800  $\mu\text{m}$ . The 95% isodose lines are shown in the left column, the 80% in the middle column and the 20% in the right column. In the first line the isodose lines for patient 1 (marked with a white number) are shown for the beam direction 270°. The regions enclosed by the 95 and 80% isodose lines are larger for the non-modulated cases

indicating the underdosage of the CTV due to the Bragg peak degradation (compare DVH and depth dose in Fig. 5). The 20% isodose line for the modulated case reaches farther compared to the non-modulated case. The same effects can be seen for all patients.

The greater range of the 20% isodose lines shows the potential risk of an overdosage in OARs distal to the target volume. Especially for patient 3 and 4 in Fig. 6 the isodose lines for 20% of the prescribed dose reach into the spinal cord. However, the additional range of the 20% isodose lines is 2 mm at maximum for these two patients. The maximum shift of each isodose line for the modulated case compared to the non-modulated case for the patients as shown in Fig. 6 are listed in Table 2. A negative sign marks a shorter range compared to the non-modulated case. The range uncertainties of the isodose lines in lung (patient 1 and patient 2 except for the 20% isodose line) are larger compared to those in tissue (patient 3 and 4 all isodose lines and 20% isodose line of patient 1).

To quantify the effects shown in Figs. 5 and 6 in terms of dose, the absolute dose values for the non-modulated case and the differences in percent of the mean dose  $D_{\text{mean}}$ ,  $D_{98\%}$  (the dose that is received by 98% percent of the volume) and  $D_{2\%}$  between the modulated cases and the non-modulated case for patient 1 are reported in Table 3 for the CTV, the trachea and the spinal cord. The  $D_{98\%}$  is taken to quantify the minimum dose received by a volume while the  $D_{2\%}$  is taken to quantify the maximum dose received by a volume. For the OARs

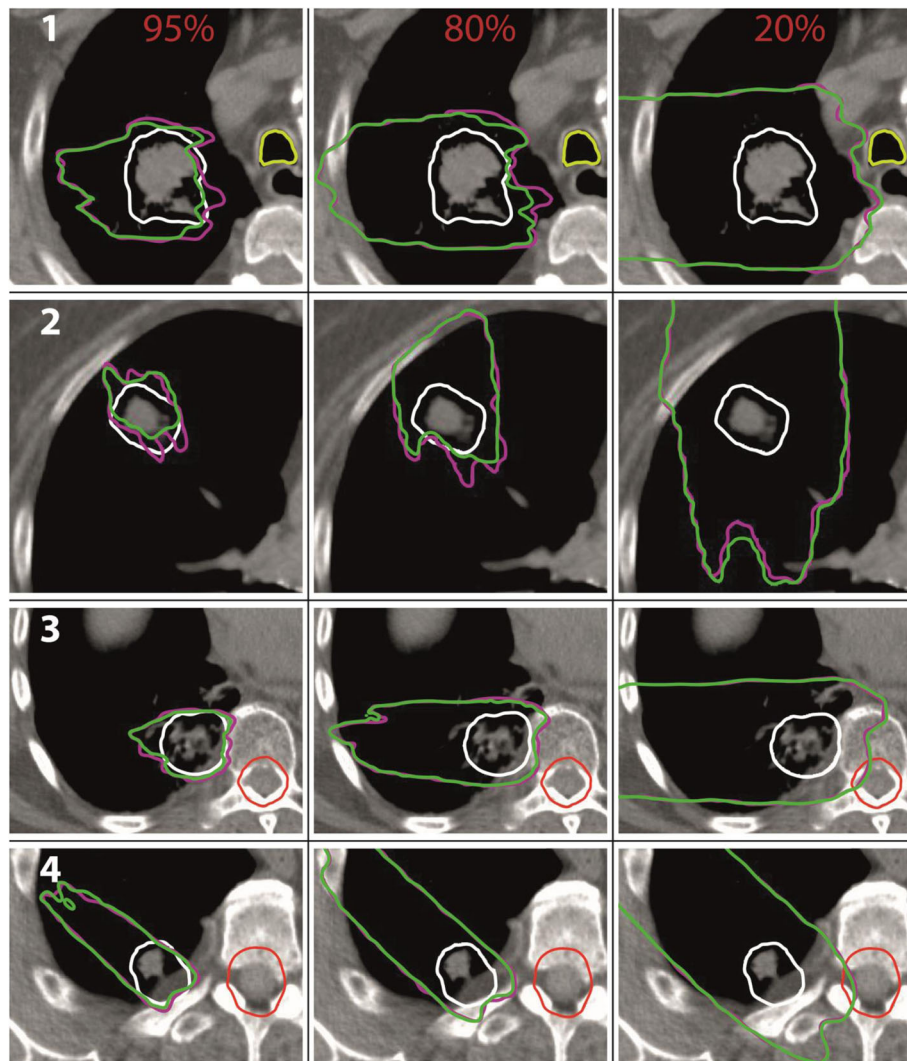


**Fig. 6** Isodose lines for 95, 80 and 20% of the prescribed dose. In pink for the non-modulated case, in green for the modulated case based on a modulation power of 800  $\mu\text{m}$ . In the first column the 95%, in the middle column the 80% and in the right column the 20% isodose lines. Different patient cases are marked in white numbers. The CTV is marked in white, the trachea in light green and the spinal cord in red

the mean dose  $D_{\text{mean}}$  and the  $D_{2\%}$  as a quantification of the maximum dose are shown.

The mean dose  $D_{\text{mean}}$ ,  $D_{98\%}$  and  $D_{2\%}$  in the CTV are smaller for the modulated cases compared to the non-modulated case and hence the prediction from the treatment-planning system. The differences increase with an increasing modulation power. The largest differences can be seen for the beam direction  $0^\circ$  (corresponding to the largest depth in lung) and the maximum modulation power of 800  $\mu\text{m}$ . Concerning the OARs trachea and spinal cord, the doses deposited in the modulated cases are greater compared to the non-modulated case for the beam directions  $270^\circ$  and  $315^\circ$ . The differences increase with an increasing modulation power. The maximum difference in the mean dose  $D_{\text{mean}}$  is +24% for the trachea as well as the spinal cord.

However, these relative deviations correspond to low absolute deviations of 0.3 Gy and <0.1 Gy, respectively. The largest difference for the  $D_{2\%}$  value for the trachea is +24% and +21% for the spinal cord. These deviations correspond to 1.5 Gy and 0.2 Gy, respectively. It can be seen, that the effects of the Bragg peak degradation on the OARs are almost non-existent for a beam direction  $0^\circ$  since in this case no OAR is positioned distal to the PTV. The effects on the trachea are largest for the beam direction  $270^\circ$ . For the spinal cord the effects are largest for the beam direction  $315^\circ$ .

In Table 4 the absolute dose values and the differences in percent of the mean dose  $D_{\text{mean}}$ ,  $D_{98\%}$  and  $D_{2\%}$  for the CTV between the modulated cases and the non-modulated case are shown for the patients 2 to 5. The results are given for a modulation power of 800  $\mu\text{m}$  to

**Table 2** Maximum shift in mm of the isodose lines for the modulated case based on a modulation power of 800 μm compared to the non-modulated case for the patients and beam directions as shown in Fig. 6. A negative sign stands for a shorter range

Patient/beam direction	Maximum range uncertainty in mm for isodose lines		
	95%	80%	20%
1 / 270°	-8	-5	3
2 / 0°	-8	-10	5
3 / 270°	-4	-3	2
4 / 315°	-2	-2	2

give an estimation of the maximum effects. Additionally, the results for a more realistic modulation power of 450 μm are given. The deviations between the modulated cases and the non-modulated case for the OARs are as small and negligible as for patient 1 and hence not shown for the other patients. As it is the case with patient 1, the dose coverage of the CTV in the modulated cases is lower compared to the non-modulated case.

For a modulation power of 800 μm the maximum differences in the mean dose  $D_{mean}$  as well as the  $D_{98\%}$  are

roughly - 5%. For the  $D_{2\%}$  it is about - 4%. The average difference in the mean dose  $D_{mean}$  is in the order of - 2%, for  $D_{98\%}$  it is - 3% and for  $D_{2\%}$  it is about - 2%.

For a more realistic modulation power of 450 μm the maximum differences in the mean dose  $D_{mean}$ , the  $D_{98\%}$  as well as the  $D_{2\%}$  are roughly - 3%. The average difference in the mean dose  $D_{mean}$  is in the order of - 1%, for  $D_{98\%}$  it is roughly - 2% and for  $D_{2\%}$  it is - 1%.

Additionally, we looked at the differences in the mean dose  $D_{mean}$ ,  $D_{98\%}$  and  $D_{2\%}$  for the CTV between the modulated cases and the non-modulated case when all three plans from the beam directions 0°, 270° and 315° are combined. As for the irradiation with one single field, in the combined scenario with three fields, the differences between the modulated cases and the non-modulated case are at maximum about - 5% for a modulation power of 800 μm. For a modulation power of 450 μm the maximum difference is about - 3%.

In Table 5 the passing rates for the gamma index 3%/1 mm (local) are shown for each patient and the dose distributions based on modulation powers of 450 μm and 800 μm. All voxels with at least 20% of the maximum dose were included in the analysis. We chose to set a small

**Table 3** Absolute dose values for the non-modulated case and differences in percent of the mean dose  $D_{mean}$ ,  $D_{98\%}$  (only for the CTV) and  $D_{2\%}$  for the CTV and OARs between the modulated and the non-modulated cases for patient 1

Modulation	CTV			Trachea		Spinal cord	
	$D_{mean}$	$D_{98\%}$	$D_{2\%}$	$D_{mean}$	$D_{2\%}$	$D_{mean}$	$D_{2\%}$
beam direction: 0° (depth in lung: 6.2 cm)							
$D_{non-mod}$ in Gy (RBE)	29.9	25.7	32.2	0.1	0.5	< 0.1	0.1
100 μm	-0.3%	-0.4%	-0.4%	-1%	+ 1%	0%	- 1%
200 μm	-0.7%	- 1.2%	- 0.8%	0%	+ 1%	0%	- 1%
450 μm	- 1.3%	- 3.0%	- 1.2%	0%	+ 2%	0%	- 1%
800 μm	-2.1%	-4.9%	- 1.8%	0%	+ 2%	+ 1%	- 1%
beam direction: 270° (depth in lung: 3.3 cm)							
$D_{non-mod}$ in Gy (RBE)	30.1	27.3	30.4	1.1	5.6	0.1	0.7
100 μm	-0.2%	-0.1%	-0.2%	+ 7%	+ 9%	+ 2%	+ 6%
200 μm	-0.5%	-1.0%	- 0.3%	+ 12%	+ 13%	+ 2%	+ 9%
450 μm	- 0.5%	-2.2%	- 0.5%	+ 16%	+ 17%	+ 7%	+ 14%
800 μm	- 0.9%	-4.1%	-0.6%	+ 24%	+ 24%	+ 9%	+ 21%
beam direction: 315° (depth in lung: 3.6 cm)							
$D_{non-mod}$ in Gy (RBE)	29.8	26.6	41.6	0.2	1.0	0.1	0.7
100 μm	0.0%	0.0%	+ 0.1%	+ 3%	+ 2%	+ 6%	+ 7%
200 μm	-0.4%	-1.5%	-0.2%	+ 2%	+ 1%	+ 11%	+ 11%
450 μm	-0.8%	-1.5%	- 0.4%	+ 2%	+ 2%	+ 15%	+ 14%
800 μm	- 1.5%	-3.0%	- 0.6%	+ 5%	+ 5%	+ 24%	+ 21%

**Table 4** Absolute dose values for the non-modulated case and differences in percent of the mean dose  $D_{\text{mean}}$ ,  $D_{98\%}$  and  $D_{2\%}$  between the modulated and the non-modulated cases for the CTV and the patients 2 to 5. The modulation powers used in these cases are 450  $\mu\text{m}$  and 800  $\mu\text{m}$ 

Patient	Modulation	Beam direction: 0°			Beam direction: 270°			Beam direction: 315°		
		$D_{\text{mean}}$	$D_{98\%}$	$D_{2\%}$	$D_{\text{mean}}$	$D_{98\%}$	$D_{2\%}$	$D_{\text{mean}}$	$D_{98\%}$	$D_{2\%}$
2	$D_{\text{non-mod}}$ in Gy (RBE)	29.9	23.4	32.0	30.1	25.2	31.1	30.0	22.1	32.3
	450 $\mu\text{m}$	-1.8%	-0.7%	-0.2%	-1.1%	-0.8%	-0.7%	-1.1%	-1.5%	-0.7%
	800 $\mu\text{m}$	-3.1%	-2.9%	-3.8%	-1.9%	-1.4%	-1.1%	-2.0%	-2.5%	-1.2%
3	$D_{\text{non-mod}}$ in Gy (RBE)	30.0	25.8	32.2	30.1	28.3	31.5	30.0	27.0	31.9
	450 $\mu\text{m}$	-1.1%	-1.4%	-0.9%	-0.6%	-2.9%	-0.5%	-0.8%	-2.2%	-0.8%
	800 $\mu\text{m}$	-1.8%	-2.8%	-1.5%	-1.1%	-5.1%	-0.8%	-1.4%	-4.2%	-1.1%
4	$D_{\text{non-mod}}$ in Gy (RBE)	30.0	25.7	31.0	30.0	24.2	32.2	30.0	26.8	30.8
	450 $\mu\text{m}$	-1.3%	-2.5%	-0.8%	-0.6%	-1.2%	-0.3%	-0.6%	-1.1%	-0.4%
	800 $\mu\text{m}$	-2.2%	-4.2%	-1.2%	-1.0%	-2.0%	-0.5%	-1.0%	-2.0%	-0.7%
5	$D_{\text{non-mod}}$ in Gy (RBE)	30.1	27.2	32.8	30.0	23.7	31.6	30.1	27.9	33.8
	450 $\mu\text{m}$	-2.6%	-0.5%	-1.1%	-2.0%	-3.0%	-2.1%	-3.0%	-1.5%	-3.2%
	800 $\mu\text{m}$	-4.7%	-2.8%	-2.1%	-3.1%	-4.6%	-3.2%	-4.9%	-2.5%	-4.3%

distance-to-agreement since the effect of the Bragg peak degradation leads to a broadening of the Bragg peak and hence a small shift in the dose (compare Figs. 5 and 6). The allowed dose difference was set to 3% since this is roughly the average effect on the mean dose in the CTV for a modulation power of 800  $\mu\text{m}$ . For a modulation power of 800  $\mu\text{m}$ , the minimal passing rate is 90.4% for patient 5 and the beam direction 315° corresponding to the maximum difference in the mean dose (compare Table 3). The average passing rate is 96.8%. For a modulation power of 450  $\mu\text{m}$  the minimum passing rate is 93.1% and the average passing rate is 98.5%. We also investigated

**Table 5** Passing rates in percent of the gamma index 3%/1 mm including all voxels with at least 20% of the maximum dose for all patients depending on the modulation power and beam direction

Patient	Modulation power	Beam direction		
		0°	270°	315°
1	450 $\mu\text{m}$	98.5	97.2	99.0
	800 $\mu\text{m}$	96.4	95.4	97.3
2	450 $\mu\text{m}$	97.3	99.3	99.9
	800 $\mu\text{m}$	94.7	95.5	99.2
3	450 $\mu\text{m}$	99.5	99.8	99.6
	800 $\mu\text{m}$	98.8	99.0	99.0
4	450 $\mu\text{m}$	99.9	100	99.9
	800 $\mu\text{m}$	99.6	100	99.9
5	450 $\mu\text{m}$	96.0	98.2	93.1
	800 $\mu\text{m}$	91.7	95.6	90.4

the gamma index when including only those voxels with at least 80% of the maximum dose. For this gamma index the minimum passing rate is 84.0% with an average passing rate of 94.6% for a modulation power of 800  $\mu\text{m}$ .

In order to assess whether the results from this study being derived using simple treatment plans can be used to estimate the dose uncertainty due to the Bragg peak degradation on more complex plans like IMPT plans, we investigated two IMPT plans - one each for patient 1 and 5. The reduction of the mean dose  $D_{\text{mean}}$  of the CTV was -1% for patient 1 and a modulation power of 450  $\mu\text{m}$ . For patient 5 it was about -3%. For patient 1, the reduction of the mean dose of the CTV approximately corresponds to the average dose reduction for the simple treatments plans with beam directions 0°, 270° and 315° (compare Table 3). For patient 5 the dose reduction for the IMPT plan is in the order of the maximum effect for the simple treatment plans.

## Discussion

The influence of the Bragg peak degradation due to lung tissue on treatment plans of lung cancer patients was investigated. For all cases the treatment-planning system overestimated the dose delivered to the CTV and in some cases underestimated the dose delivered to distal OARs. This effect increases with an increasing modulation power. The maximum underestimation of the mean dose  $D_{\text{mean}}$  is -5% for the CTV and an extreme modulation power of 800  $\mu\text{m}$ . The average underestimation is in the order -2%. This extreme modulation power of

800  $\mu\text{m}$  can occur in cases where a larger bronchial structure in the lung is positioned in the proton beam. However, for a more realistic modulation power of 450  $\mu\text{m}$ , the underestimation of the mean dose  $D_{\text{mean}}$  is only about  $-3\%$  at maximum. The average underestimation is roughly  $-1\%$ .

Concerning the effects on OARs, it was shown that the effects are dependent on the beam direction which defines the relative position between the target volume and OAR for a given anatomy: As shown in Fig. 5 on the right side, the Bragg peak degradation results in a higher dose distal to the Bragg peak. Hence, only OARs distal to the PTV can receive a higher dose than predicted by the treatment-planning system. Due to range uncertainties in proton therapy it would typically be avoided to arrange fields in a way that an OAR is located directly distal to the PTV. Nevertheless, in some cases this is inevitable for example when the patient has been previously irradiated in this region or due to technical limitations of the beam delivery system. Additionally, anatomical characteristics could enforce an irradiation where an OAR is positioned distal to the PTV as it is the case with patient 3 as shown in Fig. 2: for the beam directions  $315^\circ$  and  $270^\circ$  the spinal cord is positioned distal to the PTV. However, for the beam direction  $0^\circ$  the beam crosses the heart and the distance in lung is quite large. Since a patient's anatomy can oblige to use beams where an OAR is positioned distal to the PTV, we also investigated these cases. The underestimation of the mean dose  $D_{\text{mean}}$  in the OARs trachea and spinal cord was 0.3 Gy at maximum. For the  $D_{2\%}$  quantifying the maximum dose deposited in these OARs it was 1.5 Gy at maximum. The resulting enhanced dose deposited to OARs is far from any dose constraints used in the conventional treatment planning. Thus, the effects of the Bragg Peak degradation on OARs distal to the PTV are negligible for the cases investigated. However, in cases where the OAR is located directly distal to the PTV the effects might be larger and significant.

We were able to reproduce the findings from Flatten et al. [31] that the effects of the Bragg peak degradation increase with an increasing depth of the tumor in the lung and a decreasing tumor volume: for example, for patient 1 the underdosage of the CTV increases from  $-0.5\%$  to  $-1\%$  (for a modulation power of 450  $\mu\text{m}$ ) between the beam direction  $270^\circ$  where the tumor depth is 3.3 cm and the beam direction  $0^\circ$  where the depth is 4.6 cm.

When comparing the results from patient 1 for the beam direction  $315^\circ$  with the results from patient 5 for the beam direction  $315^\circ$  one can see that in both cases the tumor is at a depth of 3.6 cm (see Table 1). However, the CTV of patient 1 is with  $46.4\text{ cm}^3$  much larger compared to patient 5 with a volume of  $2.7\text{ cm}^3$ . The effect of the Bragg peak degradation on the mean dose

in the CTV for patient 1 is with  $-1\%$  much smaller compared to patient 5 with  $-3\%$  (for a modulation power of 450  $\mu\text{m}$ ).

Regarding the number of fields used to irradiate the CTV, it was shown that as expected, the effect of the Bragg peak degradation is independent on the number of fields as long as these fields are optimized individually.

Concerning the complexity of the irradiation plans, we decided to investigate simple plans with only one single field as described in the [Methods & materials](#) section. By investigating different beam directions, a large variety of scenarios (depth of tumor in lung, OAR distal to the PTV) has been covered and even for the worst cases the underdosage of the CTV was  $-5\%$  at maximum for an extreme modulation power of 800  $\mu\text{m}$  and only about  $-3\%$  for a more realistic modulation power of 450  $\mu\text{m}$ . To assess whether these results can be applied to more complex treatment plans, we investigated two IMPT plans for a realistic modulation power of 450  $\mu\text{m}$ . For both patients the reduction of the mean dose of the CTV was in the same order compared to the simple treatment plans. This supports the statement that the results found in this study – although being derived using simple treatment plans – can be used to estimate the dose uncertainties due to the Bragg peak degradation for more complex plans.

The passing rate of the gamma index was on average 96.8% for a modulation power of 800  $\mu\text{m}$  and 98.5% for a modulation power of 450  $\mu\text{m}$ . The minimum passing rate for a realistic modulation power of 450  $\mu\text{m}$  was 93.1%. The high passing rate of the gamma index is reasonable because as shown in Figs. 5 and 6 the Bragg peak degradation leads to a shift of the isodose lines. This shift is on average very small and hence covered by the distance-to-agreement in the gamma index. For all cases investigated in this study the passing rate was clinically acceptable. In addition to the finding that the reduction of the mean dose is on average only in the order of  $-1\%$  and at maximum  $-3\%$  for a realistic modulation power of 450  $\mu\text{m}$ , this supports that the effects of the Bragg peak degradation are clinically tolerable.

What is more, it is well-known in the literature that the relative biological effectiveness (RBE) of protons is larger than 1.1 at the distal part of the Bragg peak [43]. At the moment, this change in RBE is not considered in commonly used treatment-planning systems, hence, this larger biological effect might partially balance out the physical underdosage of the target volume due to the Bragg peak degradation which mainly occurs at the distal end of the Bragg peak and hence the target volume (compare Fig. 5). However, this change in RBE could also



potentially increase the effects of the larger dose deposited in normal tissue distal to the Bragg peak.

The Bragg peak degradation due to lung tissue is only one of various issues in proton therapy in general and in proton therapy of lung cancer patients in particular as mentioned in the introduction. Thus, the dose and range uncertainties due to this degradation shall be compared to these other uncertainties in order to quantify its importance in the current clinical context. In a study by Paganetti [7] an overview of range uncertainties is given. Range uncertainties in proton therapy arise – among other things – from measurement uncertainties in water for commissioning ( $\pm 0.3$  mm), patient setup ( $\pm 0.7$  mm) or differences in the dose calculation between the treatment-planning system and Monte Carlo codes as a gold standard for dose calculation ( $\pm 2$  mm). Other reasons for range uncertainties are due to the conversion of x-ray HU to stopping powers ( $\pm 1\%$  of the range) or biological effects ( $\sim 0.8\%$  of the range or  $\sim 3$  mm [14]). These range uncertainties refer to the range of the 80% distal dose and correspond to average values. Furthermore, these uncertainties might be bigger in lung treatments [7]. The maximum range uncertainties for the 80% isodose lines due to the Bragg peak degradation based on an extreme modulation power of  $800\ \mu\text{m}$  found in this study (see Table 2) are 10 mm in lung and 4 mm in tissue and hence are in the order of the mentioned average range uncertainties. Note that the values given by Paganetti [7] are average values while the range uncertainties investigated in this study are maximum values.

Additionally, range and dose uncertainties arise when changes of the anatomy due to weight loss or a shrinkage of the tumor are not accounted for. Szeto et al. [10] analyzed robust intensity modulated treatment plans of 16 patients with locally advanced NSCLC. The treatment dose was recalculated based on daily anatomy variations. Eight patients had an undercoverage of the target volume larger than 2 GyE with a maximum of 12 GyE in terms of the  $D_{99}$  (dose that is received by 99% of the target volume). With a prescribed dose of 66 GyE this corresponds to relative deviations in the  $D_{99\%}$  of 3% to 18%. The maximum difference in the  $D_{98\%}$  found in this study was 3% for a realistic modulation power of  $450\ \mu\text{m}$ .

Another crucial issue in proton therapy of lung cancer patients is motion. Dowdell et al. [20] investigated treatment plans for 5 lung cancer patients. Due to the interplay effects caused by the patient's motion, the mean dose in the target volume was only 88% to 92% of the prescribed dose. These interplay effects are however highly patient specific.

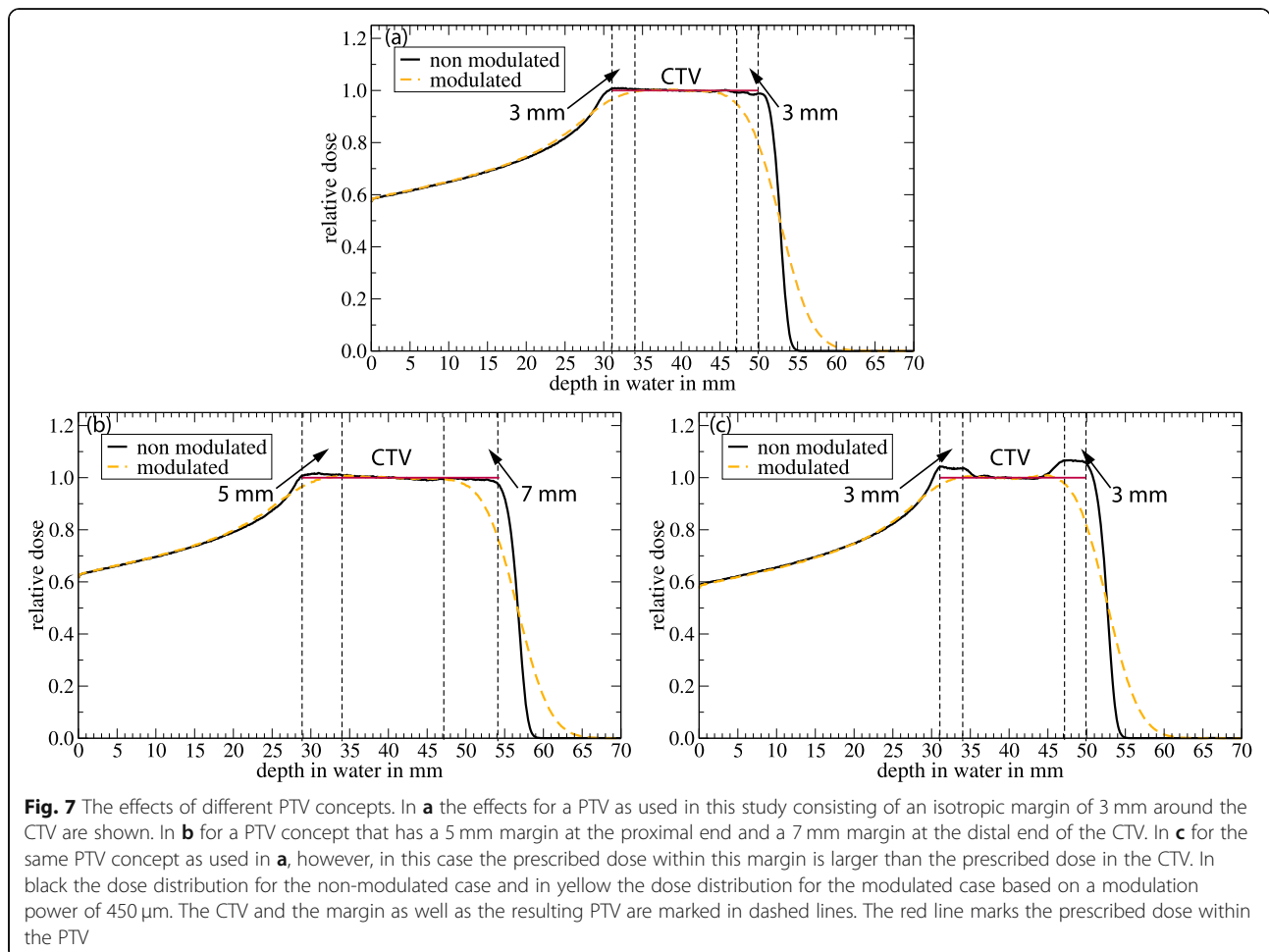
At last, we want to introduce and discuss two possible PTV concepts to account for and to avoid an underdosage of the target volume due to the Bragg peak

degradation: following the range shifts as shown in Fig. 6, one possible PTV concept could be to increase the margin around the CTV at both the distal and proximal end. The effects of such a PTV concept are depicted in Fig. 7: the dose distributions in a water phantom downstream from 80 mm of lung tissue with a modulation power of  $450\ \mu\text{m}$  are shown for the non-modulated (black) and the modulated case (yellow). The CTV marked with dashed lines is at depths between 34 mm and 47 mm. In (a) the dose distributions can be seen for a PTV concept as used in this study with an isotropic margin of 3 mm around the CTV. The red line marks the prescribed dose within the CTV and PTV. In (b) the dose distributions are shown for the case where the PTV is the CTV plus a margin of 5 mm at the proximal end and a margin of 7 mm at the distal end. The dose coverage within the CTV and PTV is better compared to (a). The disadvantage of such a PTV concept is that the dose distribution reaches farther and hence leads to a higher integral dose in the normal tissue and maybe OARs distal to the PTV.

To avoid this larger range and additional dose deposited in normal tissue, another PTV concept might be used as depicted in Fig. 7c: in this case the same PTV concept as in (a) is used (isotropic margin of 3 mm around the CTV), however, during the treatment-planning process a larger dose is prescribed within the margin at both the proximal as well as the distal end. In this case we used a 3% larger dose in the proximal and a 6% larger dose in the distal margin. By doing so a comparable dose distribution in the CTV as in Fig. 7b can be achieved, however, the dose deposited in normal tissue is smaller due to the shorter range. Note that such a PTV concept is connected to challenges since it is hard to guarantee a dose homogeneity in such a small volume. Furthermore, a difference of only 3% in dose in such a small volume is in the order of the uncertainties in proton therapy as discussed above, hence, it would hardly be possible to measure this difference in dose (e.g. as part of quality assurance).

For both PTV concepts an exact knowledge of the anatomy (depth of tumor in lung, tumor volume, location of tumor relative to soft tissue) is important to choose the appropriate values for the additional margin (case b) or the additional dose (case c). Furthermore, the knowledge of the modulation power within the lung tissue is important, since this defines the range and dose uncertainties connected to the Bragg peak degradation. Unfortunately, there is currently no solution to determine the modulation power in patients in-vivo. This is a critical issue still to be solved.

Altogether, the effects of the Bragg peak degradation are at maximum about 5% concerning the



underestimation of the mean dose  $D_{\text{mean}}$  in the CTV when optimizing the treatment plan without considering the degradation due to the lung tissue. Compared to the range and dose uncertainties in proton therapy of lung cancer patients due to the addressed reasons, the effects of the Bragg peak degradation are clinically tolerable to a certain degree in the current clinical context. However, these mentioned dose uncertainties are constantly being reduced which might change this clinical context. Hence, a consideration of the Bragg peak degradation could become more relevant in the future and would bring proton therapy for lung cancer patients closer to a high-precision therapy. The effects of the degradation might be accounted for in the treatment-planning process by applying a corresponding PTV concept as suggested in this study. What is more, this PTV concept and hence the dose deposition in the patient could be optimized when having a detailed knowledge of the lung tissue's modulation power. In our opinion, the exact determination of this modulation power is one crucial issue still to be solved.

## Conclusion

The effects of the Bragg peak degradation due to lung tissue on lung cancer patients were investigated. The maximum effect on the mean dose  $D_{\text{mean}}$  in the CTV according to this study was about 5% at maximum for an extreme modulation power of 800  $\mu\text{m}$ , a long distance travelled through lung and a small tumor volume. For a more realistic modulation power of 450  $\mu\text{m}$  the maximum effect was only about 3% in terms of  $D_{\text{mean}}$ . For OARs the effect was negligible for the cases investigated. This study confirms that the effects of the Bragg peak degradation are clinically tolerable to a certain degree in the current clinical context considering the various more critical dose uncertainties due to motion and range uncertainties in proton therapy. Furthermore, these effects might be accounted for by using corresponding PTV concepts as suggested in this study.

## Abbreviations

CTV: Clinical target volume;  $D_{2\%}$ : Dose that is received by 2% of a structure's volume;  $D_{98\%}$ : Dose that is received by 98% of a structure's volume;  $D_{\text{mean}}$ : Average dose within a structure; IMPT: Intensity modulated proton

therapy; OAR: Organ at risk; PTV: Planning target volume; RBE: Relative biological effectiveness; SBRT: Stereotactic body radiation therapy

#### Acknowledgements

We would like to thank the reviewers which helped to improve this manuscript.

#### Authors' contributions

K-SB used the mathematical model to generate the density modulation functions needed for the density modulation to reproduce the Bragg peak degradation in the Monte Carlo simulations. K-SB created the density-modulated DICOM sets and executed the Monte Carlo simulations as well as analyzed the DVHs produced with Eclipse. K-SB wrote the manuscript. VF optimized the treatment plans and transferred these optimized plans to the Monte Carlo code TOPAS and subsequently generated the DVHs. UW contributed to the mathematical model to consider the Bragg peak degradation in Monte Carlo codes underlying to this study. SL and FE contributed to this work by contouring the DICOM sets and helped with clinical information on treatment plans. KZ substantively revised this work and was supervising the work. RE-C substantively revised this work and was supervising the work.

#### Funding

We did not receive any funding for this work.

#### Availability of data and materials

The datasets generated during and/or analyzed during the current study are available from the corresponding author on reasonable request.

#### Ethics approval and consent to participate

Not applicable.

#### Consent for publication

Not applicable.

#### Competing interests

The authors declare that they have no competing interests.

#### Author details

<sup>1</sup>University Medical Center Giessen-Marburg, Department of Radiotherapy and Radiooncology, Marburg, Germany. <sup>2</sup>University of Applied Sciences, Institute of Medical Physics and Radiation Protection, Giessen, Germany. <sup>3</sup>GSI Helmholtzzentrum für Schwerionenforschung, Biophysics Division, Darmstadt, Germany. <sup>4</sup>Marburg Ion-Beam Therapy Center (MIT), Marburg, Germany. <sup>5</sup>Frankfurt Institute of Advanced Studies – FIAS, Frankfurt, Germany.

Received: 19 February 2019 Accepted: 6 September 2019

Published online: 25 October 2019

#### References

- Wilson RR. Radiological use of fast protons. *Radiology*. 1946;47:487–91.
- Smith AR. Proton therapy. *Phys Med Biol*. 2006;51(13):R491.
- Chang JY, Zhang X, Wang X, et al. Significant reduction of normal tissue dose by proton radiotherapy compared with three-dimensional conformal or intensity-modulated radiation therapy in stage I or stage III non-small-cell lung cancer. *Int J Radiat Oncol Biol Phys*. 2006;65(4):1087–96.
- Chang JY, Jabbour SK, de RD, et al. Consensus statement on proton therapy in early-stage and locally advanced non-small cell lung cancer. *Int J Radiat Oncol Biol Phys*. 2016;95(1):505–16.
- Nichols RC, Huh SN, Henderson RH, et al. Proton radiation therapy offers reduced normal lung and bone marrow exposure for patients receiving dose-escalated radiation therapy for unresectable stage III non-small-cell lung cancer: a dosimetric study. *Clin Lung Cancer*. 2011;12(4):252–7.
- Chang JY, Komaki R, Lu C, et al. Phase 2 study of high-dose proton therapy with concurrent chemotherapy for unresectable stage III nonsmall cell lung cancer. *Cancer*. 2011;117(20):4707–13.
- Paganetti H. Range uncertainties in proton therapy and the role of Monte Carlo simulations. *Phys Med Biol*. 2012;57(11):R99–117.
- Unkelbach J, Chan TCY, Bortfeld T. Accounting for range uncertainties in the optimization of intensity modulated proton therapy. *Phys Med Biol*. 2007;52(10):2755–73.
- Hui Z, Zhang X, Starkschall G, et al. Effects of interfractional motion and anatomic changes on proton therapy dose distribution in lung cancer. *Int J Radiat Oncol Biol Phys*. 2008;72(5):1385–95.
- Szeto YZ, Witte MG, van Kranen SR, et al. Effects of anatomical changes on pencil beam scanning proton plans in locally advanced NSCLC patients. *Radiother Oncol J Eur Soc Ther Radiol Oncol*. 2016;120(2):286–92.
- Hoffmann L, Alber M, Jensen MF, et al. Adaptation is mandatory for intensity modulated proton therapy of advanced lung cancer to ensure target coverage. *Radiother Oncol J Eur Soc Ther Radiol Oncol*. 2017;122(3):400–5.
- España S, Paganetti H. The impact of uncertainties in the CT conversion algorithm when predicting proton beam ranges in patients from dose and PET-activity distributions. *Phys Med Biol*. 2010;55(24):7557–71.
- Arbor N, Dauvergne D, Dedes G, et al. Monte Carlo comparison of x-ray and proton CT for range calculations of proton therapy beams. *Phys Med Biol*. 2015;60(19):7585–99.
- Carabe A, Moteabbed M, Depauw N, et al. Range uncertainty in proton therapy due to variable biological effectiveness. *Phys Med Biol*. 2012;57(5):1159–72.
- Bert C, Grözinger SV, Rietzel E. Quantification of interplay effects of scanned particle beams and moving targets. *Phys Med Biol*. 2008;53:2253–65.
- Bert C, Durante M. Motion in radiotherapy: particle therapy. *Phys Med Biol*. 2011;56:R113.
- Grassberger C, Dowdell S, Lomax A, et al. Motion interplay as a function of patient parameters and spot size in spot scanning proton therapy for lung cancer. *Int J Radiat Oncol Biol Phys*. 2013;86(2):380–6.
- Moyers MF, Miller DW, Bush DA, et al. Methodologies and tools for proton beam design for lung tumors. *Int J Radiat Oncol Biol Phys*. 2001;49(5):1429–38.
- Bert C, Saito N, Schmidt A, et al. Target motion tracking with a scanned particle beam. *Med Phys*. 2007;34(12):4768–71.
- Dowdell S, Grassberger C, Sharp GC, et al. Interplay effects in proton scanning for lung: a 4D Monte Carlo study assessing the impact of tumor and beam delivery parameters. *Phys Med Biol*. 2013;58(12):4137–56.
- Urie M, Goitein M, Holley WR, et al. Degradation of the Bragg peak due to inhomogeneities. *Phys Med Biol*. 1986;31:1.
- Sawakuchi GO, Titt U, Mirkovic D, et al. Density heterogeneities and the influence of multiple coulomb and nuclear scatterings on the Bragg peak distal edge of proton therapy beams. *Phys Med Biol*. 2008;53(17):4605–19.
- Goitein M. The measurement of tissue heterogeneity to guide charged particle radiotherapy. *Int J Radiat Oncol Biol Phys*. 1977;3:27–33.
- Perles LA, Mirkovic D, Sawakuchi GO, et al. Monte Carlo investigation of rebinning material density distributions of lung parenchyma phantoms in proton therapy. *Nucl Technol*. 2011;175(1):22–6.
- Sell M, Titt U, Perles L, et al. WE-E-BRB-02: evaluation of analytical proton dose predictions with a lung-like plastic phantom. *Med Phys*. 2012;39(6):3956.
- Titt U, Sell M, Unkelbach J, et al. Degradation of proton depth dose distribution attributable to microstructures in lung-equivalent material. *Med Phys*. 2015;42(11):6425.
- Ringbaek TP, Simeonov Y, Witt M, et al. Modulation power of porous materials and usage as ripple filter in particle therapy. *Phys Med Biol*. 2017;62:2892.
- Witt M, Weber U, Simeonov Y, et al. SU-E-T-671: range-modulation effects of carbon ion beams in lung tissue. *Med Phys*. 2015;42(6):3491.
- Baumann K-S, Witt W, Weber U, et al. An efficient method to predict and include Bragg curve degradation due to lung-equivalent materials in Monte Carlo codes by applying a density modulation. *Phys Med Biol*. 2017;62:3997–4016.
- España S, Paganetti H. Uncertainties in planned dose due to the limited voxel size of the planning CT when treating lung tumors with proton therapy. *Phys Med Biol*. 2011;56(13):3843.
- Flatten V, Baumann K-S, Weber U, et al. Quantification of the dependencies of the Bragg peak degradation due to lung tissue in proton therapy on a CT-based lung tumor phantom. *Phys Med Biol*. 2019;64:155005.
- Hata M, Tokuyue K, Kagei K, et al. Hypofractionated high-dose proton beam therapy for stage I non-small-cell lung cancer: preliminary results of a phase I/II clinical study. *Int J Radiat Oncol Biol Phys*. 2007;68(3):786–93.
- Bush DA, Slater JD, Shin BB, et al. Hypofractionated proton beam radiotherapy for stage I lung cancer. *Chest*. 2004;126(4):1198–203.
- Chen J, Lu JJ, Ma N, et al. Early stage non-small cell lung cancer treated with pencil beam scanning particle therapy: retrospective analysis of early results on safety and efficacy. *Radiat Oncol (London, England)*. 2019;14(1):16.

35. Góra J, Stock M, Lütgendorf-Caucig C, et al. Is there an advantage in designing adapted, patient-specific PTV margins in intensity modulated proton beam therapy for prostate cancer? *Int J Radiat Oncol Biol Phys.* 2013;85(3):881–8.
36. Park PC, Zhu XR, Lee AK, et al. A beam-specific planning target volume (PTV) design for proton therapy to account for setup and range uncertainties. *Int J Radiat Oncol Biol Phys.* 2012;82(2):e329–36.
37. Perl J, Shin J, Schuemann J, et al. TOPAS: an innovative proton Monte Carlo platform for research and clinical applications. *Med Phys.* 2012;39(11):6818–37.
38. Agostinelli S, et al. Geant4 - a simulation toolkit. *Nucl Instrum Methods Phys Res A.* 2003;506:250–303.
39. Taylor PA, Kry SF, Followill DS. Pencil beam algorithms are unsuitable for proton dose calculations in lung. *Int J Radiat Oncol Biol Phys.* 2017;99(3):750–6.
40. Witt M. Modulationseffekte von Kohlenstoffionen bei der Bestrahlung von Lungen, master thesis, University of Applied Sciences, Giessen, Germany. URL: [https://www.thm.de/lse/images/user/KZink-105/Abschlussarbeiten/Masterarbeit\\_Matthias\\_Witt\\_2014.pdf](https://www.thm.de/lse/images/user/KZink-105/Abschlussarbeiten/Masterarbeit_Matthias_Witt_2014.pdf) (last called: 11/09/2019).
41. International Commission on Radiation Units and Measurements (ICRU). ICRU report volume 50: prescribing, recording, and reporting photon beam therapy. 1993.
42. International Commission on Radiation Units and Measurements (ICRU). ICRU report volume 62: prescribing, recording and reporting photon beam therapy (supplement to ICRU report 50). 1999.
43. Paganetti H, Blakely E, Carabe-Fernandez A, et al. Report of the AAPM TG-256 on the relative biological effectiveness of proton beams in radiation therapy. *Med Phys.* 2019;46(3):e53–78.

## Publisher's Note

Springer Nature remains neutral with regard to jurisdictional claims in published maps and institutional affiliations.

**Ready to submit your research? Choose BMC and benefit from:**

- fast, convenient online submission
- thorough peer review by experienced researchers in your field
- rapid publication on acceptance
- support for research data, including large and complex data types
- gold Open Access which fosters wider collaboration and increased citations
- maximum visibility for your research: over 100M website views per year

**At BMC, research is always in progress.**

Learn more [biomedcentral.com/submissions](https://biomedcentral.com/submissions)



ACCEPTED MANUSCRIPT • OPEN ACCESS

## Experimental determination of modulation power of lung tissue for particle therapy

To cite this article before publication: Jan Michael Burg *et al* 2021 *Phys. Med. Biol.* in press <https://doi.org/10.1088/1361-6560/ac3e0d>

### Manuscript version: Accepted Manuscript

Accepted Manuscript is “the version of the article accepted for publication including all changes made as a result of the peer review process, and which may also include the addition to the article by IOP Publishing of a header, an article ID, a cover sheet and/or an ‘Accepted Manuscript’ watermark, but excluding any other editing, typesetting or other changes made by IOP Publishing and/or its licensors”

This Accepted Manuscript is © 2021 The Author(s). Published by IOP Publishing Ltd..

As the Version of Record of this article is going to be / has been published on a gold open access basis under a CC BY 3.0 licence, this Accepted Manuscript is available for reuse under a CC BY 3.0 licence immediately.

Everyone is permitted to use all or part of the original content in this article, provided that they adhere to all the terms of the licence <https://creativecommons.org/licenses/by/3.0>

Although reasonable endeavours have been taken to obtain all necessary permissions from third parties to include their copyrighted content within this article, their full citation and copyright line may not be present in this Accepted Manuscript version. Before using any content from this article, please refer to the Version of Record on IOPscience once published for full citation and copyright details, as permissions may be required. All third party content is fully copyright protected and is not published on a gold open access basis under a CC BY licence, unless that is specifically stated in the figure caption in the Version of Record.

View the [article online](#) for updates and enhancements.

# Experimental determination of modulation power of lung tissue for particle therapy

Jan Michael Burg<sup>1,2</sup>, Veronika Flatten<sup>1,2,3</sup>, Matthias Witt<sup>1,2,3</sup>,  
Larissa Derksen<sup>1</sup>, Uli Weber<sup>4</sup>, Rita Engenhardt-Cabillic<sup>2,3</sup>,  
Hilke Vorwerk<sup>2,3</sup>, Klemens Zink<sup>1,2,3</sup>, Kilian-Simon Baumann<sup>1,2,3</sup>

<sup>1</sup> University of Applied Sciences Giessen, Institute of Medical Physics and Radiation Protection, Germany

<sup>2</sup> University Medical Center Giessen and Marburg, Department of Radiotherapy and Radiation Oncology, Germany

<sup>3</sup> Marburg Ion-Beam Therapy Center, Marburg, Germany

<sup>4</sup> GSI Helmholtzzentrum für Schwerionenforschung, Biophysics Department, Darmstadt, Germany

E-mail: jan.michael.burg@lse.thm.de

jun. 2021

**Abstract.** In particle therapy of lung tumors, modulating effects on the particle beam may occur due to the microscopic structure of the lung tissue. These effects are caused by the heterogeneous nature of the lung tissue and cannot be completely taken into account during treatment planning, because these micro structures are too small to be fully resolved in the planning CT. In several publications, a new material parameter called modulation power ( $P_{mod}$ ) was introduced to characterize the effect. For various artificial lung surrogates, this parameter was measured and published by other groups and ranges up to approximately 1000  $\mu\text{m}$ . Studies investigating the influence of the modulation power on the dose distribution during irradiation are using this parameter in the range of 100 to 800  $\mu\text{m}$ . More precise measurements for  $P_{mod}$  on real lung tissue have not yet been published. In this work, the modulation power of real lung tissue was measured using porcine lungs in order to produce more reliable data of  $P_{mod}$  for real lung tissue. For this purpose, ex-vivo porcine lungs were frozen in a ventilated state and measurements in a carbon ion beam were performed. Due to the way the lungs were prepared and transferred to a solid state, the lung structures that modulate the beam could also be examined in detail using micro CT imaging. An optimization of the established methods of measuring the modulation power, which takes better account of the typical structures within lung tissue, was developed as well.

*Keywords:* lung tissue, Bragg peak degradation, modulation power, porous material

Submitted to: *Phys. Med. Biol.*

*Bragg peak degradation due to lung tissue***1. Introduction**

Particle therapy with protons and carbon-ions is increasingly used as a treatment modality for cancer patients (Kraft; 2000; Schulz-Ertner and Tsujii; 2007; Grutters et al.; 2010), since the method was first presented in 1946 (Wilson; 1946). The advantage of particle therapy is, besides an increased biological effect for carbon-ions, the physically induced inverse depth dose profile of heavy charged particles in matter, which results in the so-called Bragg peak (Schardt et al.; 2010). Due to the low applied dose in the entrance channel and the significant decrease of the dose distal to the Bragg peak, a high-conformal irradiation with better sparing of the healthy surrounding tissue can be achieved (Chang et al.; 2006).

The described sharp distal dose fall-off is particularly pronounced for homogeneous material. In particle therapy using the raster scanning technique, particles are being applied in pencil beams with beam widths perpendicular to the beam axis in the order of 1 cm (FWHM). If such a beam traverses heterogeneous materials, different particles within the pencil beam will experience different compositions of material or density, respectively, resulting in various ranges of the individual particles. As a result, the width of the Bragg peak increases. This effect is referred to as Bragg peak degradation. (Urie et al.; 1986; Weber and Kraft; 1999; Sawakuchi et al.; 2008). Note that this effect decreases with a decreasing width of the pencil beams since the smaller the extension of the beam the fewer different pathways the particles can take through the heterogeneous material. In the borderline case where the pencil beam is infinitely small, no Bragg peak degradation would be observed, since all particles would take the same pathway (disregarding lateral scattering). The modulation power which is used to describe the Bragg peak degradation is a property of the heterogeneous material. Hence, the modulation power does - in first proximity - not depend on the particle type, energy or

1  
2 *Bragg peak degradation due to lung tissue* 3  
3

4 beam width.  
5

6  
7 With regard to clinical use, especially for the irradiation of lung cancer, this effect should  
8 be taken into account. Due to its anatomy, the lung is particularly heterogeneous and  
9 therefore the effect described has an influence on the dose distribution, especially in  
10 the treatment of lung cancer (Sell et al.; 2012; Titt et al.; 2015; Baumann et al.; 2017,  
11 2019; Flatten et al.; 2019). Since the heterogeneous micro-structures of the lung are  
12 smaller than the typical voxel size of a clinical planning CT, these structures are not  
13 fully resolved in the image and therefore cannot be completely taken into account during  
14 treatment planning. In particular, this can lead to an underdosage of the target volume  
15 and an overdosage of distal normal tissue in comparison to the planned dose and can  
16 thus influence the success of therapy (España and Paganetti; 2011).  
17  
18

19  
20 In order to investigate and describe the effect of microstructures on the Bragg peak,  
21 several studies have been carried out on lung-like plastic phantoms as well as other  
22 porous materials (Sell et al.; 2012; Ringbæk et al.; 2017; Hranek et al.; 2020).  
23 Furthermore, there is a publication that uses plastinated lung samples to study the  
24 effect (Titt et al.; 2015). However, it is unclear how the plastination process affects the  
25 modulation effect compared to physiological lung tissue. In addition to investigating  
26 the effect with the help of surrogates, a mathematical model to predict and quantify  
27 the effect was developed in earlier studies, leading to a new material property called  
28 'modulation power' ( $P_{mod}$ ) (Witt; 2014; Witt et al.; 2015; Ringbæk et al.; 2017). In  
29 the work of Baumann et al. (2017), the mathematical model was verified by means  
30 of Monte Carlo simulations. The calculation of  $P_{mod}$  provides a representative and  
31 efficient method for describing Bragg curve degradation due to porous material and  
32 is independent of the material thickness. The model allows to directly determine the  
33 modulated dose distribution by convoluting a normal distribution with the pristine  
34  
35  
36  
37  
38  
39  
40  
41  
42  
43  
44  
45  
46  
47  
48  
49  
50  
51  
52  
53  
54  
55  
56  
57  
58  
59  
60



### *Bragg peak degradation due to lung tissue*

Bragg curve. By optimizing the parameter  $\sigma$  and  $\mu$  of a normal distribution on the basis of the modulated curves, the modulation power of a certain material can be determined. For treatment planning, this means that if the modulation power of a porous material is known, the degradation of the Bragg peak can be predicted. For a given modulation power, the corresponding normal distribution can be determined by  $\mu$  (which corresponds to the water equivalent thickness of the traversed heterogeneous material) and  $\sigma$  ( $\sigma = \sqrt{P_{mod} * \mu}$ ). Subsequently, the depth dose distributions from the base data are being convolved with this normal distribution. These so-modified base data then include the Bragg peak degradation effects minimizing dose uncertainties. (Paz et al.; 2021) The material property  $P_{mod}$  is used in several publications to study the influence of modulating material on the dose distribution during irradiation for lung cancer treatment (Baumann et al.; 2017, 2019; Flatten et al.; 2019). The assumed values of  $P_{mod}$  in these publications range between approximately 100  $\mu\text{m}$  and 800  $\mu\text{m}$  and are mainly based on a measurement by Witt et al. (2014). The results of the measurements of modulation power on lung surrogates by Harnek et al. (2020) are in the same order of magnitude. This wide range of values for the modulation power is also reflected in a wide range of results in publications that use this parameter to calculate the effect on the dose distribution. In order to obtain a reliable statement for real lung tissue, the actual modulation power of lung tissue is of major importance. However, due to the challenging nature of measuring  $P_{mod}$  on real lungs, published data on this topic is rarely available. In this work, reliable values for  $P_{mod}$  were determined in physiological lung tissue to reduce the range of assumed values. A more accurate value for  $P_{mod}$  of lung tissue is the basis for more accurate calculations when using the parameter.

When physiological lung tissue is considered as the modulating material, its structure differs significantly from the structure in the mathematical model as well as in

*Bragg peak degradation due to lung tissue*

measurements on surrogates. The basic approach in both, the measurements on surrogates and the mathematical model, is the assumption that the material which is modulating the beam is equally heterogeneous over its entire extension. This means that for the porous material under consideration, an almost homogeneous and uniform micro structure with approximate equal size is to be expected. However, this assumption is not valid for physiological lung tissue. Within physiological lung tissue, there are different structure sizes that influence the beam. In addition to these different micro structures within the lungs, there are also larger structures such as bronchial tubes and blood vessels. Besides the determination of reliable values for  $P_{mod}$ , the influence of physiological structures within a lung and their effect on modulation power were studied in detail in this work. The already published model for calculating the modulation power was adapted to better describe the influences of different structure sizes within lung tissue.

For the measurement focused on in this work, this means that depth dose distribution with and without lung samples in the beam were measured and the modulation power for lung tissue was calculated. Using porcine lungs as a model for human lungs, the modulation power for lung tissue was measured and compared with measurements on surrogates. Furthermore, the results were related to the assumed values of the publications that use the mathematical model to study the impact of the modulation effect on the dose distribution. For this purpose, samples of porcine and wild boar lungs were prepared to get as close as possible to the physiological ventilated state of a human lung. By freezing five samples in ventilated states, they were preserved for a certain period of time. The samples preserved this way allow measurements in a particle beam as well as imaging with a CT at different times without changing the structure of the lung samples. This enables a detailed examination of the structures of the lung samples

### *Bragg peak degradation due to lung tissue*

at the exact same position at which the sample was measured in the particle beam. The influence of macroscopic structures within the lung such as bronchial tubes and blood vessels were examined using high-resolution CT-imaging and were considered for the calculation of the modulation power. In addition, measurements were performed to determine whether the effect of the modulation of the Bragg peak is energy-independent as expected.

## **2. Materials and methods**

To get as close to physiological lungs as possible, the sample preparation is essential for measuring the degradation of the Bragg curve, caused by lung tissue during particle beam irradiation. In its physiological form, the lung as an organ for efficient gas exchange with the blood, is mostly filled with air. During respiration, the volume of the lung changes significantly depending on the respiratory state. Due to a variable negative pressure in the thorax, the lung is inflated and filled with air while breathing. Even when fully exhaled, the lung inside the thorax still has a residual filling, caused by the pressure difference between inside and outside the thorax. If the lung is removed from this physiological environment within the thorax, the lung collapses completely and is no longer in a physiological state. Therefore, the main challenge in the preparation of the test samples was to bring the lung into a physiological ventilated state and to preserve it over the measurement period. In this work this was achieved by shock freezing the lungs during ventilation, using positive pressure inside the lungs.

### *2.1. Selection of the sample material*

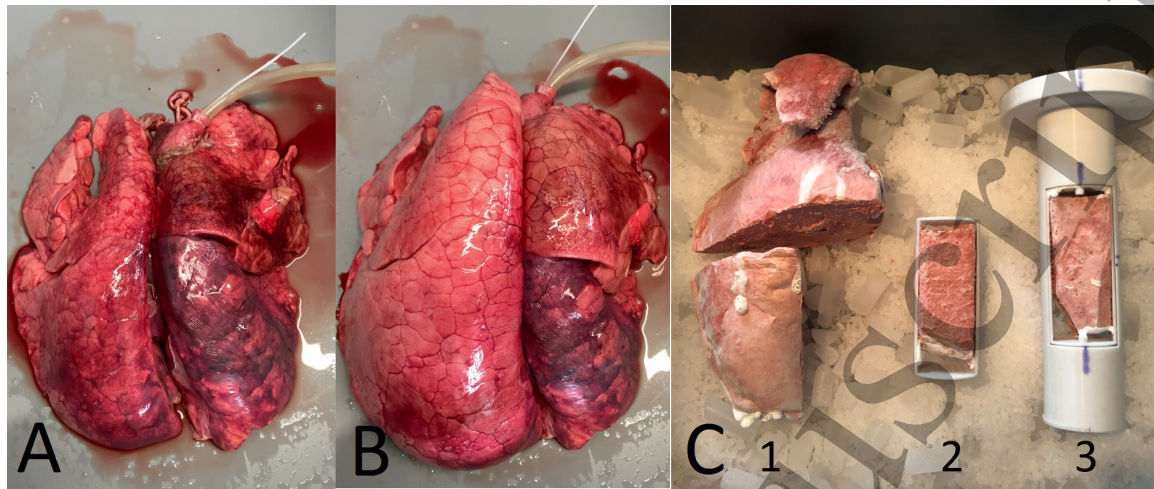
For the experiment, porcine lungs were selected as they are a well suited model due to their similarity to human lungs in size and structure (Judge et al.; 2014). We

### *Bragg peak degradation due to lung tissue*

used two different types of lungs. On the one hand, those were porcine lungs from slaughterhouse waste and on the other hand, we used wild boar lungs provided by a hunter. The difference between these two lungs, relevant for this paper, is the different amount of residual blood in the lungs due to the method of slaughter. When slaughtering domestic pigs in a slaughterhouse, special attention is paid to the bleeding of the animal, which results in a lower quantity of residual blood in the animal compared to hunting, where controlled bleeding of the animal cannot be guaranteed. The increased amount of residual blood within wild boar lungs can affect the density distribution of the lungs and thereby the modulation power. Lungs with more residual blood seem to be more similar to an in-vivo lung which is also heavily perfused. When selecting the lungs, special attention has to be paid to their integrity. As already mentioned, the lungs need to be placed in a physiological condition by means of ventilation. To achieve this, the lungs have to be undamaged and airtight and should have an undamaged trachea for ventilation.

### *2.2. Ventilation and freezing*

To bring collapsed lungs into a ventilated state as close as possible to a physiological lung, the sample lung was inflated using pressured air. For this purpose we inserted a plastic tube into the trachea or a main bronchus of the lung and sealed the connection point with a cable tie. The lungs prepared in this way were connected to the laboratory compressed air system with a hose and an adjustable pressure regulator. The pressure regulator was used to create a constant pressure in the lungs which led to a constant state of ventilation during the entire freezing period. To avoid damage to the lungs, the pressure in the lungs was increased only until there was no visible change in volume. Air loss caused by possible damage to the sample lungs could also be compensated for with this method. Due to the fact that the lungs collapse completely during the

*Bragg peak degradation due to lung tissue*

**Figure 1.** Part A shows a lung before and picture B after ventilation. On the right side in B, it can be seen that the lower part of the left lung could not be ventilated correctly. Part C shows the cutting process from the frozen lung to the final lung sample for the measurements. C1: Cutting the lung to sample size. C2: Fixation in the sample frame. C3: Final lung sample within the sample holder for measurements.

collection process, adhesions of the individual lung structures may occur. In order to remove any possible adhesions that may have formed, the lungs were first fully inflated. Subsequently, the lungs were visually inflated to approximately half of their maximum volume. Since, in contrast to physiological conditions in the thorax, the starting point for ex-vivo ventilation is a completely collapsed lung, ventilation to half the maximum volume corresponds to a rather low to moderate respiratory state. Low respiratory states seem to be more suitable for therapy in the context of tumor motion. (Plathow et al.; 2006) A lung sample before and after ventilation is displayed in Figure 1A and 1B. When inspecting the ventilated lung in Figure 1B, it becomes apparent that the lower part of the left lung could not be ventilated properly. Nevertheless, a sample was prepared from this part to investigate the effect on the modulation power for non-ventilated lung tissue. In the following, this sample will be referred to as sample No. 5. In order to avoid the formation of ice crystals which could potentially damage the microstructure of the lung tissue, the freezing process had to be as quick as possible. Therefore, the

### *Bragg peak degradation due to lung tissue*

lungs were pre-cooled after ventilation using ice water in order to bring them as close to the freezing temperature as possible. The positive pressure inside the ventilated lungs prevented water from entering the lungs through possible leaks. The ventilated and pre-cooled lung samples were then placed in an insulated box filled with dry ice pellets. Special care was taken to ensure that the lungs would not touch the wall of the box or the dry ice inside. To optimize the heat exchange between the lung sample and the environment, a fan was installed in the lower part of the box to circulate the cold air towards the lungs. The temperature measured in the box was held to a maximum of  $-25^{\circ}\text{C}$  throughout the whole period. To ensure complete freezing, a freezing time of at least one hour was chosen.

### *2.3. Preparation of the samples for measurements*

The entire lungs could not be used for further measurements, as the high-resolution CT technically limits the maximum sample size. Therefore, a size of  $4 \times 4 \times 10 \text{ cm}^3$  was defined for all lung samples. The frozen lungs were cut to the sample size with a oscillation saw inside a cold environment to prevent thawing. The saw blade was also cooled with dry ice before each cut. Due to the very low heat capacity of the lung tissue, the samples are particularly vulnerable to thawing. Even a short contact to non cooled material or the skin while handling the samples can cause thawing and structural damage to the samples. To avoid any direct contact to the lung sample and to simplify the handling of the samples, 3D printing was used to create plastic frames in which the samples were fixed. These frames could be mounted in a sample holder, also produced by 3D printing, which can be seen in Figure 1C. The sample holder has additional space above and below the sample that can be filled with dry ice pellets to constantly cool the samples during the measurement procedure. With the help of this setup, the frozen samples could be positioned with repeatable accuracy in all further experiments. A total

### *Bragg peak degradation due to lung tissue*

of 5 ventilated and frozen lung samples were prepared from 3 existing porcine lungs with a size of about  $4 \times 4 \times 10 \text{ cm}^3$  seen in Figure 3. Samples No. 1 to 3 are porcine lungs, samples No. 4 and 5 are wild boar lungs. To avoid the accumulation of ice on the samples due to freezing moisture from the ambient air, it is important to protect the samples from the ambient air. In the setup used in this work, the evaporating dry ice creates a moisture-free protective atmosphere inside the sample box. The storage of the final samples between the measurements was realized in a standard deep freezer at  $-18^\circ\text{C}$ .

### *2.4. CT imaging*

In order to obtain information about the structure of the lung samples and to investigate the influence on the modulation power caused by the lung tissue or by the bronchial tubes and/or blood vessels, CT scans were performed. On the one hand, a conventional CT scanner (Somaton Confidence, Siemens Healthineers, Erlangen Germany) was used to produce CT scans with a resulting pixel size of 0,97 mm at 120 kV for all samples. In addition, further CT images with a significantly higher resolution were produced to examine the microstructures of the lungs. For this purpose CT scans were made on an industrial CT scanner (Werth TomoScope® XL NC) at 102 kV with a resulting pixel size of  $50 \mu\text{m}$ . Due to the time-consuming measurements especially for the industrial CT scanner, the samples needed to be cooled throughout the measurement. For this purpose, the above described sample holder was used in combination with dry ice pellets.

### *2.5. In-beam experiment*

All measurements for the in-beam experiment were performed at the Marburger Ion-Beam Therapy Center (MIT). The MIT facility is operating with a synchrotron accelerator designed by Siemens Healthcare/Danfysik which allows to accelerate both

## Bragg peak degradation due to lung tissue

11

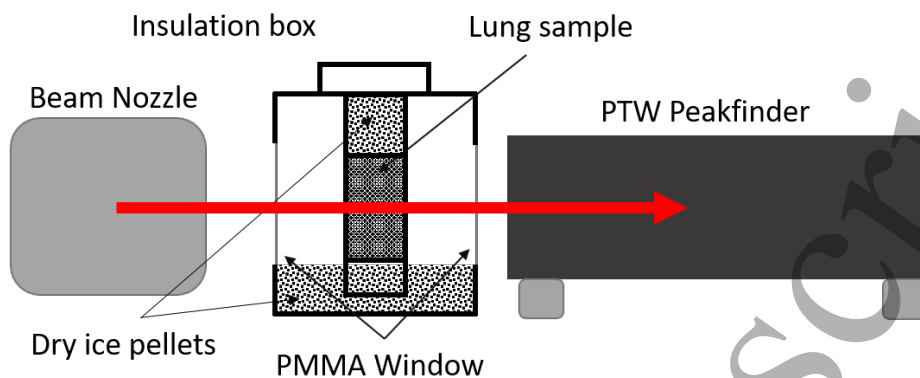


**Figure 2.** Sketch of the measurement setup for the in-beam experiment. The isolated box for positioning the lung samples and the PTW Peakfinder for measuring the depth dose distributions are located on the patient table. Inside the isolating box, dry ice pellets are placed both above and below the lung sample to cool the sample during the measurements. In beam direction, the box has windows made of PMMA for beam entry and exit.

protons and carbon-ions with a maximum energy of 220 MeV for protons and 430 MeV/u for carbon-ions. The facility uses pencil beam scanning technology for the treatment application. We used an isocentric beam application without any deflection of the pencil beam. Carbon-ions with an energy of 140,01 MeV/u and a spot size FWHM of 6,9 mm were used for all measurements, due to the sharper Bragg Peak compared to protons. This energy proved to be suitable for measuring all samples with the same settings in an acceptable time. Since the modulation power exclusively depends on the material properties and not on the ion type, the results from this study gained with C-12 beams is applicable for proton beams, as well. We conducted Monte Carlo simulations with voxelised, heterogeneous geometries as used by Baumann et al (2017) to verify this assumption for a large range of  $P_{mod}$  (100  $\mu\text{m}$  to 800  $\mu\text{m}$ ) and all clinical proton and carbon ion energies. For the measurement of the energy dependence of the modulation power, carbon-ions with an energy of 190,17 MeV/u were also used together with the same measurement setup. The setup for the experimental determination of the range modulation of the carbon ions consisted of two main components as shown in Figure



1  
2  
3 *Bragg peak degradation due to lung tissue* 12

4 2. The first component was the peakfinder water column (PTW, Freiburg Germany)  
5 to measure the integral depth dose distribution for the carbon-ion beam. The second  
6 component was an insulating box with an integrated sample holder to position the  
7 prepared lung samples with repeated accuracy. In order to prevent thawing of the lung  
8 samples during measurement, the sample box was mainly made of polystyrene and was  
9 filled with dry ice pellets to about 5 cm. In the direction of the beam, the walls of the  
10 box were made of 5 mm PMMA in order to prevent any possible modulation effects due  
11 to the heterogeneous polystyrene wall. The resolution for the measurement of the depth  
12 dose distribution was set to 20  $\mu\text{m}$  between each measuring point for the Bragg peak  
13 region. For the entrance channel no fast significant signal changes were to be expected,  
14 therefore the resolution was reduced to save measuring time. All samples were first  
15 irradiated at the center and then 2 cm above (top) and below (bottom) the center by  
16 using different spacers underneath the sample box. Thus, we obtained measured values  
17 for 3 positions from all samples (top, center, bottom) as seen in Figure 4. For the  
18 measurement of the reference curve, the same setup was used, but without the lung  
19 sample in the sample holder.  
20  
21  
22  
23  
24  
25  
26  
27  
28  
29  
30  
31  
32  
33  
34  
35  
36  
37  
38  
39  
40

41 *2.6. Calculation of the modulation power*

42  
43 Based on the in-beam experiment for each lung sample we obtained a modulated depth  
44 dose distribution in water and a corresponding reference measurement without a lung  
45 sample in the beam. From these data, we calculated the modulation power according to  
46 the method described by Baumann et al. (2017). The modulated depth dose distribution  
47  $b_*(z)$  as a function of depth  $z$  in water can be mathematically described by a convolution:  
48  
49  
50  
51  
52  
53

$$54 \quad b_*(z) = (F * b_0)(z) = \int_{-\infty}^{\infty} F(x'|\mu, \sigma) \cdot b_0(z + x') dx' \quad (1)$$

55  
56 According to Equation 1, a modulated depth dose distribution can be calculated by a  
57  
58  
59  
60

1  
2  
3 *Bragg peak degradation due to lung tissue* 13

4 convolution of a Gaussian distribution  $F(x|\mu, \sigma)$  with the reference curve  $b_0(z)$ .

5  
6 To fit the measured modulated depth dose distribution  $b_*(z)$ , the mean  $\mu$  and the width  $\sigma$   
7  
8 of the Gaussian distribution were optimized to achieve high coverage by the convolution  
9  
10 of the Gaussian distribution with the reference curve. Here,  $\mu$  represents the shift of  
11  
12 the center of the distribution in relation to the position of the 82% distal dose fall-off  
13  
14 (Bichsel et al.; 2000) and  $\sigma$  represents the width of the distribution, as seen in Figure 4.  
15  
16 From the parameters of the Gaussian function, the modulation power can be calculated  
17  
18 using Equation 2:  
19  
20

$$21 \quad P_{mod} = \frac{\sigma^2}{\mu} \quad (2)$$

22  
23 Since in this work the modulation power was determined for real lung tissue, a further  
24  
25 approach to calculate the modulation power is introduced. For lung samples with  
26  
27 different structures, the fit as described above does not represent the modulated depth  
28  
29 dose distribution well. To better take into account different modulating effects within  
30  
31 the lung, in a further approach, two Gaussian distributions  $F_1$  and  $F_2$  (seen in Figure  
32  
33 5) were optimized, analogue to the procedure described above resulting in:  
34  
35  
36  
37

$$38 \quad b_*(z) = ((F_1 + F_2) * b_0)(z) = \int_{-\infty}^{\infty} (F_1(x') + F_2(x')) \cdot b_0(z + x') dx' \quad (3)$$

39  
40 For both Gaussian distributions,  $\mu$  and  $\sigma$  were optimized and the modulation power  
41  
42 was calculated. Assuming that  $F_1 + F_2$  are normalized to 1, the total modulation power  
43  
44  $P_{mod, tot}$  was obtained by taking into account the respective fraction  $A_1$  and  $A_2$  for each  
45  
46 Gaussian function to the total modulation function resulting in:  
47  
48  
49

$$50 \quad P_{mod, tot} = \frac{(A_1 \cdot P_{mod1}) + (A_2 \cdot P_{mod2})}{A_1 + A_2} \quad (4)$$

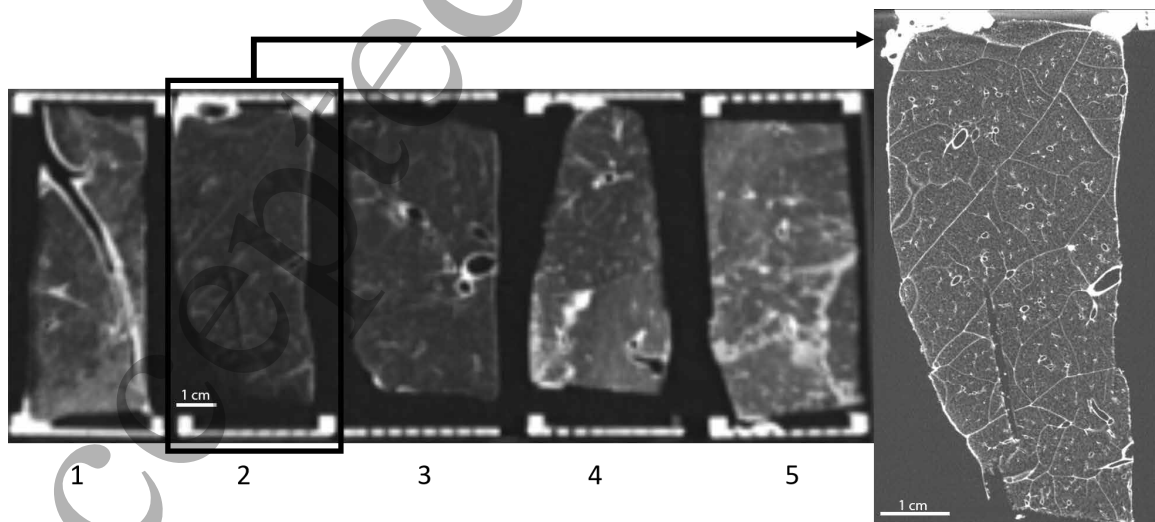
1  
2  
3 *Bragg peak degradation due to lung tissue*  
4  
5

14

### 6 **3. Results**

#### 7 *3.1. Sample preparation*

8  
9  
10 From 3 different lungs a total of 5 samples were prepared. The central slice of the  
11 CT scan of all prepared lung samples and an image of sample No. 2 obtained with  
12 the industrial CT scanner are shown in Figure 3. Due to the pre-cooling of the lungs  
13 and the resulting fast freezing process with a high temperature gradient, no visible ice  
14 crystals were formed within the lung samples. In contrast to artificial lung surrogates,  
15 which consist of a completely homogeneous porous structure, the lung samples which  
16 were prepared in this work differ significantly. It can be seen that the lung samples  
17 have macroscopic structures within the porous lung tissue. These structures are mainly  
18 blood vessels and bronchial tubes that are present in various sizes throughout the whole  
19 lung due to the physiology of lungs. As mentioned above, sample No. 5 could not  
20 be ventilated properly, which results in higher gray values in the CT for this sample  
21 compared to the ventilated samples.  
22  
23  
24  
25  
26  
27  
28  
29  
30  
31  
32  
33  
34  
35  
36



55 **Figure 3.** Left: Central slice of the CT scans for all lung samples obtained using a  
56 clinical CT scanner. Right: CT scan of sample No. 2 using an industrial CT scanner  
57 with a pixel size of 50  $\mu\text{m}$ .  
58  
59  
60

1  
2  
3 *Bragg peak degradation due to lung tissue*

15

4  
5 *3.2. In-beam experiment single Gaussian fit*

6  
7  
8 Figure 4 shows an analysis of the results for the in-beam experiment on sample No. 2  
9 as a representative for all 5 lung samples. The CT image shows the central layer of the  
10 lung sample which also corresponds to the center of the applied beam. The three beam  
11 positions (top, center, bottom) for all samples are represented by the black arrows.  
12  
13  
14  
15  
16  
17  
18  
19  
20  
21  
22  
23  
24  
25  
26  
27  
28  
29  
30  
31  
32  
33  
34  
35  
36  
37  
38  
39  
40  
41  
42  
43  
44  
45  
46  
47  
48  
49  
50  
51  
52  
53  
54  
55  
56  
57  
58  
59  
60

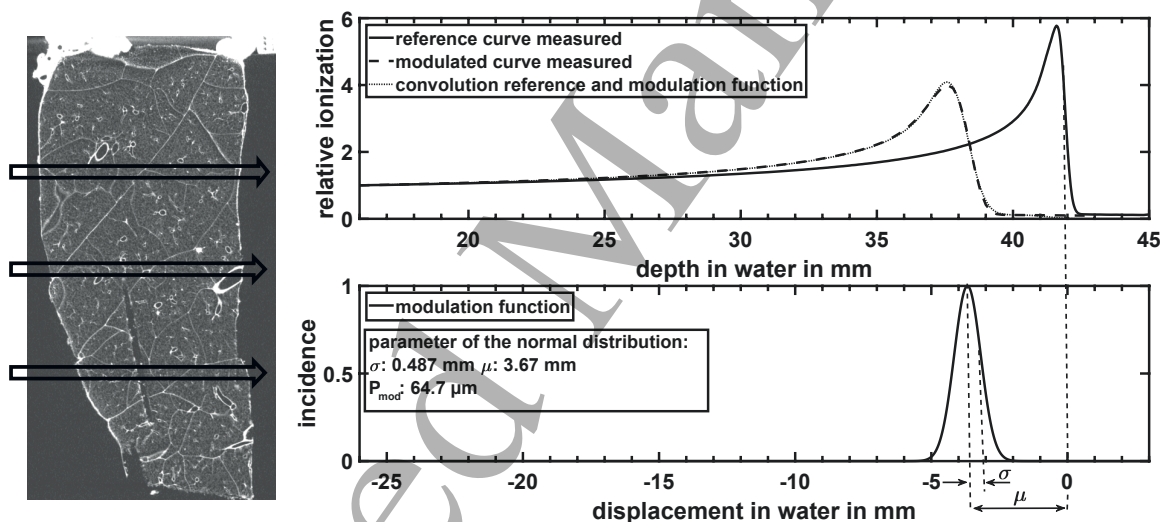


**Figure 4.** Results of the in-beam experiment for sample No. 2. Left: Micro-CT image of the center of the sample. The beam positions (top, center, bottom) are indicated by the black arrows. Right: The upper graph shows the reference curve measured without a sample in the beam and the modulated curve measured with a sample in the beam. The dashed line represents the convolution of the reference curve with the calculated modulation function for the top beam position. The lower part shows the optimized modulation function with the two parameters  $\sigma$  and  $\mu$  from which  $P_{mod}$  was calculated. The y axis is normalized to the maximum.

reference curve with an optimized single Gaussian distribution reproduces the measured modulated depth-dose distribution with high accuracy. Using the parameters  $\sigma$  and  $\mu$  from the Gaussian distribution obtained in this way, the modulation power  $P_{mod}$  was calculated. This procedure was repeated to calculate the modulation power for all 5

Bragg peak degradation due to lung tissue

16

samples at all 3 positions. The results of the modulation power for all samples and beam positions, using single Gaussian optimization, are summarized in Table 1.

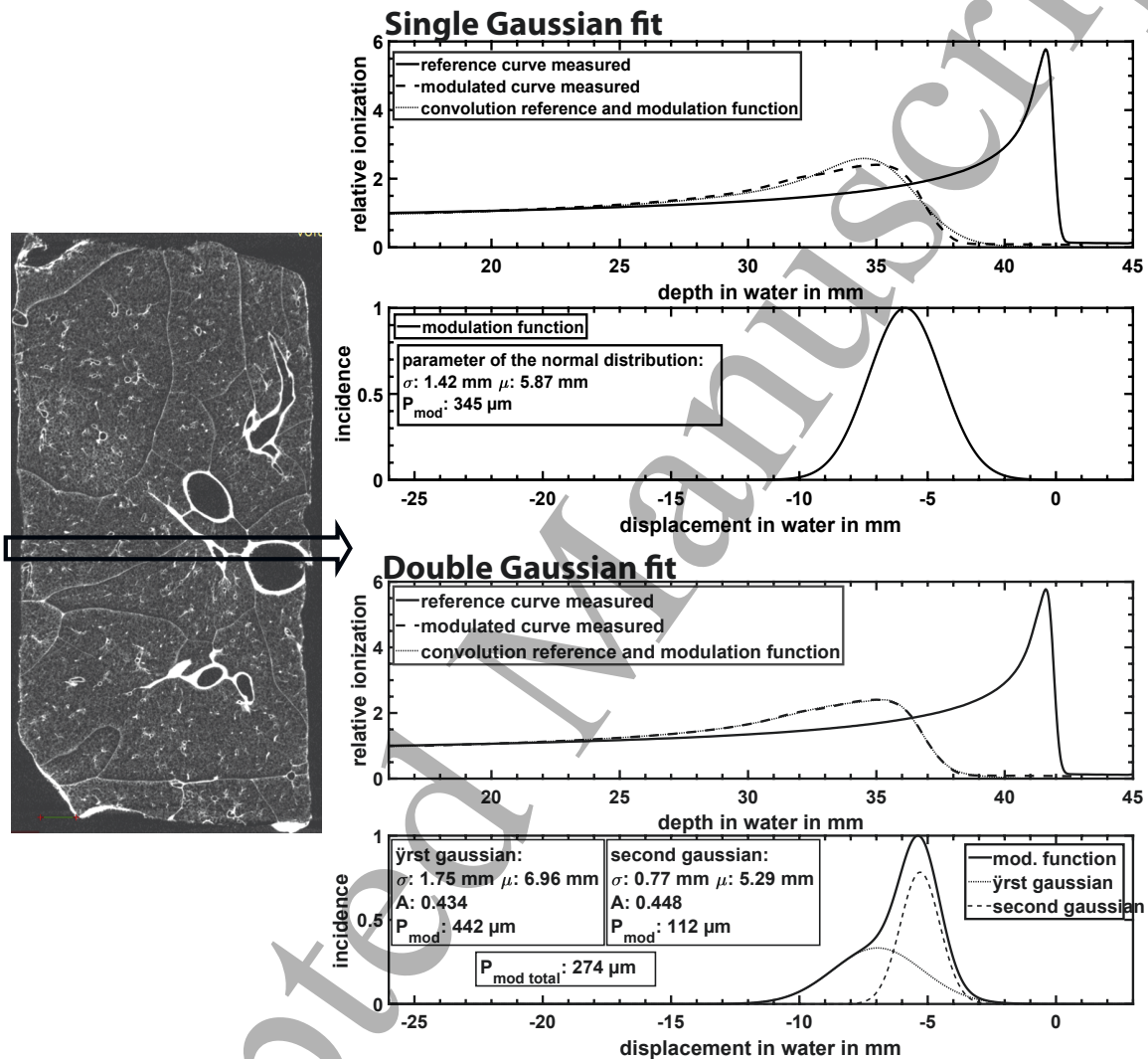


**Figure 5.** The influence of macroscopic structures is shown on sample No. 3. For the central beam position, a larger structure is visible. The beam, indicated by the black arrow, partially penetrates the macroscopic structure which leads to a smearing of the modulated curve in the proximal direction. On the right, the single and the double Gaussian fit methods are displayed. It can be seen that the double Gaussian method represents the modulated curve more accurately.

1  
2  
3 *Bragg peak degradation due to lung tissue* 17

4  
5 *3.3. In-beam experiment double Gaussian fit*

6  
7  
8 The evaluation of the results by means of a single Gaussian fit showed a deviation  
9  
10 between the fit and the measured modulated curve, especially for samples with more  
11  
12 macroscopic structures in the CT (see Figure 5). Therefore, we optimized the fit method  
13  
14 and extended it by performing a double Gaussian fit. The fitting by means of two  
15  
16 gaussian distributions also reflects the two main structures within the lungs, alveoli and  
17  
18 bronchi, with their associated sizes. A continuous size progression from large to small,  
19  
20 which would require a fitting with several Gaussian functions, is not observed. In  
21  
22 detail, the influence of macroscopic structures on the modulation of the Bragg peak  
23  
24 and a comparison of the single Gaussian fit with the optimized double Gaussian fit  
25  
26 method is shown in Figure 5. Using the example of sample No. 3 at the central beam  
27  
28 position, it can be seen that both the microscopic heterogeneous structure as well as  
29  
30 larger bronchial structure are being penetrated by the beam. Due to the heterogeneity  
31  
32 within the sample, the Bragg peak is clearly changed in shape compared to a more  
33  
34 homogeneous sample like sample No. 2 in Figure 4. When looking at the single Gaussian  
35  
36 fit (Figure 5) to determine the modulation power, it becomes apparent that it does  
37  
38 not represent the actual modulation well. The structures within this sample create a  
39  
40 superposition of different modulation effects, which leads to a smearing of the peak in  
41  
42 the proximal direction. To better account for this modulating effect, an optimization  
43  
44 of the existing method was made. Instead of optimizing a single Gaussian distribution  
45  
46 to fit the curve, we optimized two Gaussian distributions. The addition of the two  
47  
48 distributions results in the modulation function with which the curve was fitted. Taking  
49  
50 into account the fraction of each of the individual Gaussian distributions to the overall  
51  
52 modulation function, the modulation power was calculated according to Equation 4.  
53  
54  
55  
56 A direct comparison of the single Gaussian fit and double Gaussian fit for the same  
57  
58  
59  
60

1  
2  
3 *Bragg peak degradation due to lung tissue* 18

4 location in the sample is shown in Figure 5. It can be seen that for this sample the  
5 double Gaussian method has a significantly higher coverage of the curve than the single  
6 Gaussian method. Using this method, all 5 samples were evaluated at all 3 positions.  
7  
8 The results for  $P_{mod}$  can also be seen in Table 1.  
9  
10

11  
12 In summary, we measured values for  $P_{mod}$  in the range of 62 to 583  $\mu\text{m}$ . However, the  
13 values measured on sample No. 5 are significantly higher than the values measured on  
14 the other samples. As mentioned earlier, sample No. 5 was taken from a not properly  
15 ventilated part of the lung and was not suitable for evaluation. The comparison of single  
16 Gaussian fit with double Gaussian fit varied depending on the sample. For samples where  
17 different structures could be seen at the beam position in the CT image, a large deviation  
18 between the two methods was observed. For samples without visible structural changes  
19 in the beam, the single Gaussian and double Gaussian methods give almost identical  
20 results for  $P_{mod}$ . Samples that can already sufficiently be analyzed using the single  
21 Gaussian method can also be analyzed using the double Gaussian method. In this case,  
22 the fraction of the second Gaussian distribution is reduced to an insignificantly small  
23 fraction in relation to the total modulation function. Thus, this method can be used for  
24 all samples and is superior in cases where different structure sizes are present.  
25  
26  
27  
28  
29  
30  
31  
32  
33  
34  
35  
36  
37  
38  
39  
40  
41

42 In order to validate the accuracy of the measurement system with regard to the geometric  
43 misalignment, several measurements were carried out for the central beam position on  
44 sample No. 1. The results for  $P_{mod}$  after repositioning the sample on the same position  
45 as well as with offset and rotation can be seen in Table 1. Repeated repositioning to  
46 the same position in the sample results in a standard deviation of the measured value  
47  $P_{mod}$  of approximately 10%. Taking into account the measured value for rotation and  
48 displacement of the sample, the standard deviation increases to a value of approximately  
49 30%.  
50  
51  
52  
53  
54  
55  
56  
57  
58  
59  
60

*Bragg peak degradation due to lung tissue*

19

**Table 1.** Results of measured modulation powers ( $P_{mod}$ ) for all lung samples. The modulation power was calculated using single Gaussian fit as well as double Gaussian fit. The last column of the table shows the results of the repeat measurements and measurements with displacement and rotation of sample 1. These measurements were made to estimate the measurement errors.

Sample (No.)	Beam Position	$P_{mod}$ ( $\mu\text{m}$ ) single Gaussian fit	$P_{mod}$ ( $\mu\text{m}$ ) double Gaussian fit	$P_{mod}$ ( $\mu\text{m}$ ) diff 1-2
porcine lungs				
1	top	355	367	-12
	center	225	225	0
	bottom	228	171	57
2	top	64	62	2
	center	161	137	24
	bottom	74	73	1
3	top	145	119	26
	center	345	274	71
	bottom	151	112	39
wild boar lungs				
4	top	348	256	92
	center	194	143	51
	bottom	290	288	2
5	top	586	550	36
	center	531	583	-52
	bottom	499	497	2
sample 1 center				
	repositioned 1	225	225	0
	repositioned 2	191	175	16
	repositioned 3	217	209	8
	displaced +2 mm	218	277	-59
	rotation 2°	387	285	102
	rotation -2°	142	169	-27

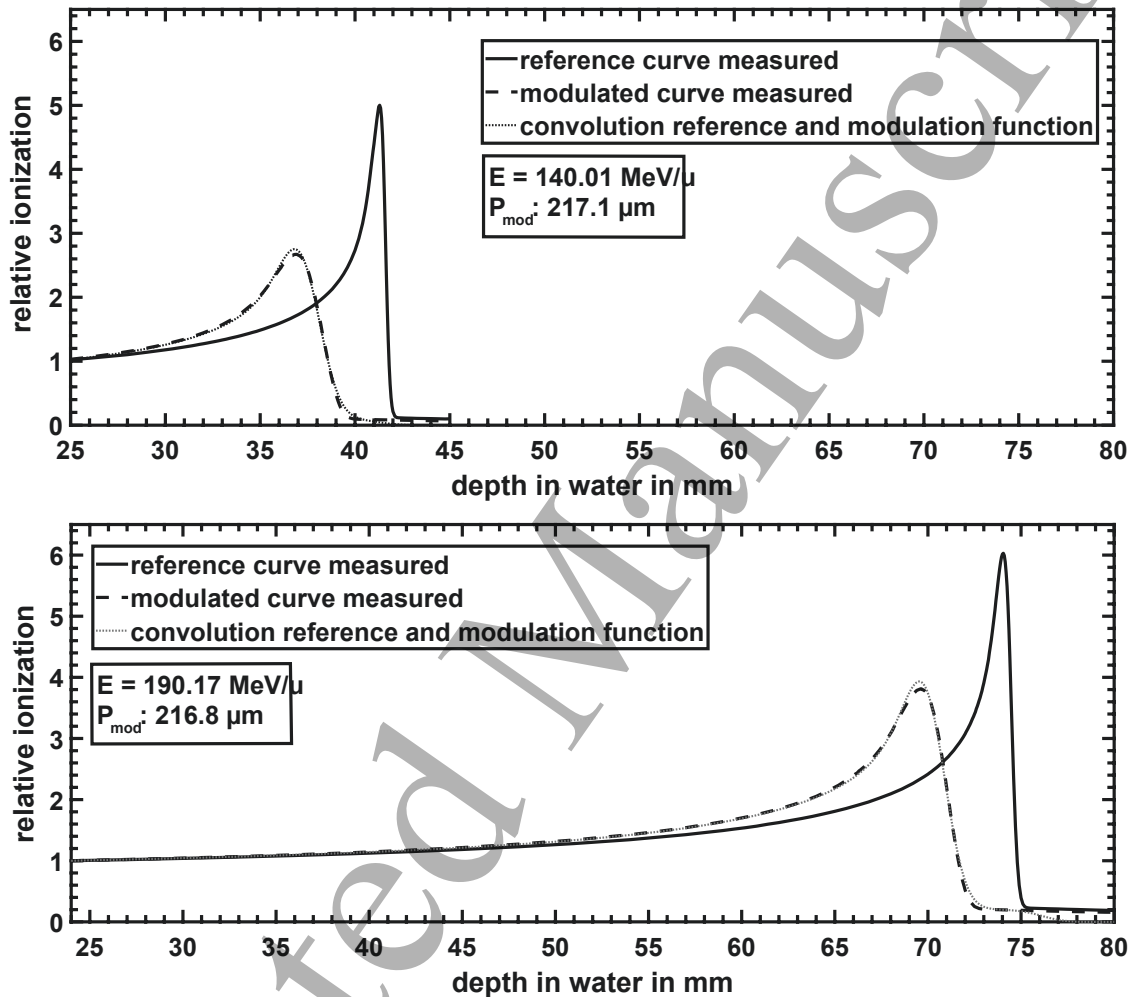
*3.4. Energy dependence of the modulation power*

To investigate if the modulation power is energy independent, lung sample No. 2 was irradiated with two different beam energies without moving it between the measurements. The modulation power was determined for both energies analogous to the other samples. The results of the measurements are shown in Figure 6. It can



1  
2  
3 *Bragg peak degradation due to lung tissue* 20

4 clearly be seen that the modulation power for both beam energies shows only minimal  
5 deviations with good coverage of the fit.  
6  
7  
8  
9



44 **Figure 6.** Measurements to verify the energy independence of  $P_{mod}$ . The same  
45 sample was irradiated at the same location first with carbon-ions with an energy of  
46 140,01 MeV/u (top) and second with 190,17 MeV/u (bottom).  
47  
48  
49  
50

#### 51 4. Discussion

52 The presented method, which uses freezing of lungs in the ventilated state to obtain  
53 samples, proved to be well applicable. With this preservation method it was possible  
54  
55  
56  
57  
58  
59  
60 to examine lung samples with both particle beam irradiation and CT imaging without

*Bragg peak degradation due to lung tissue*

21

changing the ventilation state of the samples. This stable condition can not be achieved using in-vivo lungs. Therefore, ex-vivo porcine lungs appear to be the most similar and feasible model for studying the effect of the degradation of lung tissue due to their resemblance to human lungs (Judge et al.; 2014). An influence of the residual blood volume in the lungs on the modulation power, which we assumed, could not be reliably proven in our model. The difference between physiological lung tissue and surrogates is basically that for the surrogates there is only one modulating structure size. In the lung, on the other hand, due to the physiology of the lung, there are several structures with different structural sizes that create a superposition of modulating effects in the lung. The adapted method using double Gaussian fit presented in this work is more suitable for lung tissue. It better accounts for the different modulation effects within the lung. The maximum difference we found between the two fitting methods for the samples examined was  $102 \mu\text{m}$ . Since the double Gaussian fit method works for all samples, it can always be used and produces a higher accuracy in the calculation of  $P_{mod}$  due to the more precise fit. A pre-selection of the fitting method based on structures in the sample by means of a CT image is therefore not necessary. For use in therapy planning one main outcome of this study is that lung tissue may consist of different modulation powers. In studies that have been published so far, a constant modulation power within the whole lung was regarded. Especially the solution of considering lung modulation effects during treatment planning presented by Pez et al. (2021) can only process one modulation power for each applied pencil beam. The question is, how to bypass lung samples that clearly show different modulation powers. Fitting the modulated depth dose distribution with two normal distributions gives the most precise results, however, the corresponding two modulation powers cannot be processed by the solution presented by Pez et al. (2021). In that case, calculating a total modulation power cannot reproduce

1  
2  
3 *Bragg peak degradation due to lung tissue* 22

4 the double-peak structure that can clearly be seen in the depth dose distribution, though,  
5 however, is clinically spoken more accurate than any other approach presented so far.

6  
7  
8  
9 The most accurate solution might be to use the model presented by Flatten et al. (2021)  
10 to calculate a locally resolved modulation power. Using that model, the lung can be  
11 divided into ROIs, each having a specific modulation power (corresponding to the fit  
12 with one normal distribution). This map of modulation powers could then be used to  
13  
14  
15  
16  
17  
18  
19 feed the optimization process presented by Pez et al. (2021).

20 For five lung samples and 12 beam positions measured here, we have succeeded in  
21 confirming and even narrowing down the assumptions for the modulation power in the  
22 range of 100 to approximately 1000  $\mu\text{m}$  mentioned in previous publications (Witt; 2014;  
23  
24  
25  
26  
27  
28  
29 Baumann et al.; 2017; Flatten et al.; 2019; Baumann et al.; 2019; Hranek et al.; 2020).

30 Since it was clear that sample No. 5 was not properly ventilated, this sample is not  
31 suitable as a model for physiologically ventilated lungs. Removing this sample from the  
32 data pool again significantly reduces the range for the measured  $P_{mod}$  for lung tissue to  
33  
34  
35  
36  
37  
38  
39  
40  
41  
42  
43  
44  
45  
46  
47  
48  
49  
50  
51  
52  
53  
54  
55  
56  
57  
58  
59  
60  
61  
62  
63  
64  
65  
66  
67  
68  
69  
70  
71  
72  
73  
74  
75  
76  
77  
78  
79  
80  
81  
82  
83  
84  
85  
86  
87  
88  
89  
90  
91  
92  
93  
94  
95  
96  
97  
98  
99  
100  
101  
102  
103  
104  
105  
106  
107  
108  
109  
110  
111  
112  
113  
114  
115  
116  
117  
118  
119  
120  
121  
122  
123  
124  
125  
126  
127  
128  
129  
130  
131  
132  
133  
134  
135  
136  
137  
138  
139  
140  
141  
142  
143  
144  
145  
146  
147  
148  
149  
150  
151  
152  
153  
154  
155  
156  
157  
158  
159  
160  
161  
162  
163  
164  
165  
166  
167  
168  
169  
170  
171  
172  
173  
174  
175  
176  
177  
178  
179  
180  
181  
182  
183  
184  
185  
186  
187  
188  
189  
190  
191  
192  
193  
194  
195  
196  
197  
198  
199  
200  
201  
202  
203  
204  
205  
206  
207  
208  
209  
210  
211  
212  
213  
214  
215  
216  
217  
218  
219  
220  
221  
222  
223  
224  
225  
226  
227  
228  
229  
230  
231  
232  
233  
234  
235  
236  
237  
238  
239  
240  
241  
242  
243  
244  
245  
246  
247  
248  
249  
250  
251  
252  
253  
254  
255  
256  
257  
258  
259  
260  
261  
262  
263  
264  
265  
266  
267  
268  
269  
270  
271  
272  
273  
274  
275  
276  
277  
278  
279  
280  
281  
282  
283  
284  
285  
286  
287  
288  
289  
290  
291  
292  
293  
294  
295  
296  
297  
298  
299  
300  
301  
302  
303  
304  
305  
306  
307  
308  
309  
310  
311  
312  
313  
314  
315  
316  
317  
318  
319  
320  
321  
322  
323  
324  
325  
326  
327  
328  
329  
330  
331  
332  
333  
334  
335  
336  
337  
338  
339  
340  
341  
342  
343  
344  
345  
346  
347  
348  
349  
350  
351  
352  
353  
354  
355  
356  
357  
358  
359  
360  
361  
362  
363  
364  
365  
366  
367  
368  
369  
370  
371  
372  
373  
374  
375  
376  
377  
378  
379  
380  
381  
382  
383  
384  
385  
386  
387  
388  
389  
390  
391  
392  
393  
394  
395  
396  
397  
398  
399  
400  
401  
402  
403  
404  
405  
406  
407  
408  
409  
410  
411  
412  
413  
414  
415  
416  
417  
418  
419  
420  
421  
422  
423  
424  
425  
426  
427  
428  
429  
430  
431  
432  
433  
434  
435  
436  
437  
438  
439  
440  
441  
442  
443  
444  
445  
446  
447  
448  
449  
450  
451  
452  
453  
454  
455  
456  
457  
458  
459  
460  
461  
462  
463  
464  
465  
466  
467  
468  
469  
470  
471  
472  
473  
474  
475  
476  
477  
478  
479  
480  
481  
482  
483  
484  
485  
486  
487  
488  
489  
490  
491  
492  
493  
494  
495  
496  
497  
498  
499  
500  
501  
502  
503  
504  
505  
506  
507  
508  
509  
510  
511  
512  
513  
514  
515  
516  
517  
518  
519  
520  
521  
522  
523  
524  
525  
526  
527  
528  
529  
530  
531  
532  
533  
534  
535  
536  
537  
538  
539  
540  
541  
542  
543  
544  
545  
546  
547  
548  
549  
550  
551  
552  
553  
554  
555  
556  
557  
558  
559  
560  
561  
562  
563  
564  
565  
566  
567  
568  
569  
570  
571  
572  
573  
574  
575  
576  
577  
578  
579  
580  
581  
582  
583  
584  
585  
586  
587  
588  
589  
590  
591  
592  
593  
594  
595  
596  
597  
598  
599  
600  
601  
602  
603  
604  
605  
606  
607  
608  
609  
610  
611  
612  
613  
614  
615  
616  
617  
618  
619  
620  
621  
622  
623  
624  
625  
626  
627  
628  
629  
630  
631  
632  
633  
634  
635  
636  
637  
638  
639  
640  
641  
642  
643  
644  
645  
646  
647  
648  
649  
650  
651  
652  
653  
654  
655  
656  
657  
658  
659  
660  
661  
662  
663  
664  
665  
666  
667  
668  
669  
670  
671  
672  
673  
674  
675  
676  
677  
678  
679  
680  
681  
682  
683  
684  
685  
686  
687  
688  
689  
690  
691  
692  
693  
694  
695  
696  
697  
698  
699  
700  
701  
702  
703  
704  
705  
706  
707  
708  
709  
710  
711  
712  
713  
714  
715  
716  
717  
718  
719  
720  
721  
722  
723  
724  
725  
726  
727  
728  
729  
730  
731  
732  
733  
734  
735  
736  
737  
738  
739  
740  
741  
742  
743  
744  
745  
746  
747  
748  
749  
750  
751  
752  
753  
754  
755  
756  
757  
758  
759  
760  
761  
762  
763  
764  
765  
766  
767  
768  
769  
770  
771  
772  
773  
774  
775  
776  
777  
778  
779  
780  
781  
782  
783  
784  
785  
786  
787  
788  
789  
790  
791  
792  
793  
794  
795  
796  
797  
798  
799  
800  
801  
802  
803  
804  
805  
806  
807  
808  
809  
810  
811  
812  
813  
814  
815  
816  
817  
818  
819  
820  
821  
822  
823  
824  
825  
826  
827  
828  
829  
830  
831  
832  
833  
834  
835  
836  
837  
838  
839  
840  
841  
842  
843  
844  
845  
846  
847  
848  
849  
850  
851  
852  
853  
854  
855  
856  
857  
858  
859  
860  
861  
862  
863  
864  
865  
866  
867  
868  
869  
870  
871  
872  
873  
874  
875  
876  
877  
878  
879  
880  
881  
882  
883  
884  
885  
886  
887  
888  
889  
890  
891  
892  
893  
894  
895  
896  
897  
898  
899  
900  
901  
902  
903  
904  
905  
906  
907  
908  
909  
910  
911  
912  
913  
914  
915  
916  
917  
918  
919  
920  
921  
922  
923  
924  
925  
926  
927  
928  
929  
930  
931  
932  
933  
934  
935  
936  
937  
938  
939  
940  
941  
942  
943  
944  
945  
946  
947  
948  
949  
950  
951  
952  
953  
954  
955  
956  
957  
958  
959  
960  
961  
962  
963  
964  
965  
966  
967  
968  
969  
970  
971  
972  
973  
974  
975  
976  
977  
978  
979  
980  
981  
982  
983  
984  
985  
986  
987  
988  
989  
990  
991  
992  
993  
994  
995  
996  
997  
998  
999  
1000  
1001  
1002  
1003  
1004  
1005  
1006  
1007  
1008  
1009  
1010  
1011  
1012  
1013  
1014  
1015  
1016  
1017  
1018  
1019  
1020  
1021  
1022  
1023  
1024  
1025  
1026  
1027  
1028  
1029  
1030  
1031  
1032  
1033  
1034  
1035  
1036  
1037  
1038  
1039  
1040  
1041  
1042  
1043  
1044  
1045  
1046  
1047  
1048  
1049  
1050  
1051  
1052  
1053  
1054  
1055  
1056  
1057  
1058  
1059  
1060  
1061  
1062  
1063  
1064  
1065  
1066  
1067  
1068  
1069  
1070  
1071  
1072  
1073  
1074  
1075  
1076  
1077  
1078  
1079  
1080  
1081  
1082  
1083  
1084  
1085  
1086  
1087  
1088  
1089  
1090  
1091  
1092  
1093  
1094  
1095  
1096  
1097  
1098  
1099  
1100  
1101  
1102  
1103  
1104  
1105  
1106  
1107  
1108  
1109  
1110  
1111  
1112  
1113  
1114  
1115  
1116  
1117  
1118  
1119  
1120  
1121  
1122  
1123  
1124  
1125  
1126  
1127  
1128  
1129  
1130  
1131  
1132  
1133  
1134  
1135  
1136  
1137  
1138  
1139  
1140  
1141  
1142  
1143  
1144  
1145  
1146  
1147  
1148  
1149  
1150  
1151  
1152  
1153  
1154  
1155  
1156  
1157  
1158  
1159  
1160  
1161  
1162  
1163  
1164  
1165  
1166  
1167  
1168  
1169  
1170  
1171  
1172  
1173  
1174  
1175  
1176  
1177  
1178  
1179  
1180  
1181  
1182  
1183  
1184  
1185  
1186  
1187  
1188  
1189  
1190  
1191  
1192  
1193  
1194  
1195  
1196  
1197  
1198  
1199  
1200  
1201  
1202  
1203  
1204  
1205  
1206  
1207  
1208  
1209  
1210  
1211  
1212  
1213  
1214  
1215  
1216  
1217  
1218  
1219  
1220  
1221  
1222  
1223  
1224  
1225  
1226  
1227  
1228  
1229  
1230  
1231  
1232  
1233  
1234  
1235  
1236  
1237  
1238  
1239  
1240  
1241  
1242  
1243  
1244  
1245  
1246  
1247  
1248  
1249  
1250  
1251  
1252  
1253  
1254  
1255  
1256  
1257  
1258  
1259  
1260  
1261  
1262  
1263  
1264  
1265  
1266  
1267  
1268  
1269  
1270  
1271  
1272  
1273  
1274  
1275  
1276  
1277  
1278  
1279  
1280  
1281  
1282  
1283  
1284  
1285  
1286  
1287  
1288  
1289  
1290  
1291  
1292  
1293  
1294  
1295  
1296  
1297  
1298  
1299  
1300  
1301  
1302  
1303  
1304  
1305  
1306  
1307  
1308  
1309  
1310  
1311  
1312  
1313  
1314  
1315  
1316  
1317  
1318  
1319  
1320  
1321  
1322  
1323  
1324  
1325  
1326  
1327  
1328  
1329  
1330  
1331  
1332  
1333  
1334  
1335  
1336  
1337  
1338  
1339  
1340  
1341  
1342  
1343  
1344  
1345  
1346  
1347  
1348  
1349  
1350  
1351  
1352  
1353  
1354  
1355  
1356  
1357  
1358  
1359  
1360  
1361  
1362  
1363  
1364  
1365  
1366  
1367  
1368  
1369  
1370  
1371  
1372  
1373  
1374  
1375  
1376  
1377  
1378  
1379  
1380  
1381  
1382  
1383  
1384  
1385  
1386  
1387  
1388  
1389  
1390  
1391  
1392  
1393  
1394  
1395  
1396  
1397  
1398  
1399  
1400  
1401  
1402  
1403  
1404  
1405  
1406  
1407  
1408  
1409  
1410  
1411  
1412  
1413  
1414  
1415  
1416  
1417  
1418  
1419  
1420  
1421  
1422  
1423  
1424  
1425  
1426  
1427  
1428  
1429  
1430  
1431  
1432  
1433  
1434  
1435  
1436  
1437  
1438  
1439  
1440  
1441  
1442  
1443  
1444  
1445  
1446  
1447  
1448  
1449  
1450  
1451  
1452  
1453  
1454  
1455  
1456  
1457  
1458  
1459  
1460  
1461  
1462  
1463  
1464  
1465  
1466  
1467  
1468  
1469  
1470  
1471  
1472  
1473  
1474  
1475  
1476  
1477  
1478  
1479  
1480  
1481  
1482  
1483  
1484  
1485  
1486  
1487  
1488  
1489  
1490  
1491  
1492  
1493  
1494  
1495  
1496  
1497  
1498  
1499  
1500  
1501  
1502  
1503  
1504  
1505  
1506  
1507  
1508  
1509  
1510  
1511  
1512  
1513  
1514  
1515  
1516  
1517  
1518  
1519  
1520  
1521  
1522  
1523  
1524  
1525  
1526  
1527  
1528  
1529  
1530  
1531  
1532  
1533  
1534  
1535  
1536  
1537  
1538  
1539  
1540  
1541  
1542  
1543  
1544  
1545  
1546  
1547  
1548  
1549  
1550  
1551  
1552  
1553  
1554  
1555  
1556  
1557  
1558  
1559  
1560  
1561  
1562  
1563  
1564  
1565  
1566  
1567  
1568  
1569  
1570  
1571  
1572  
1573  
1574  
1575  
1576  
1577  
1578  
1579  
1580  
1581  
1582  
1583  
1584  
1585  
1586  
1587  
1588  
1589  
1590  
1591  
1592  
1593  
1594  
1595  
1596  
1597  
1598  
1599  
1600  
1601  
1602  
1603  
1604  
1605  
1606  
1607  
1608  
1609  
1610  
1611  
1612  
1613  
1614  
1615  
1616  
1617  
1618  
1619  
1620  
1621  
1622  
1623  
1624  
1625  
1626  
1627  
1628  
1629  
1630  
1631  
1632  
1633  
1634  
1635  
1636  
1637  
1638  
1639  
1640  
1641  
1642  
1643  
1644  
1645  
1646  
1647  
1648  
1649  
1650  
1651  
1652  
1653  
1654  
1655  
1656  
1657  
1658  
1659  
1660  
1661  
1662  
1663  
1664  
1665  
1666  
1667  
1668  
1669  
1670  
1671  
1672  
1673  
1674  
1675  
1676  
1677  
1678  
1679  
1680  
1681  
1682  
1683  
1684  
1685  
1686  
1687  
1688  
1689  
1690  
1691  
1692  
1693  
1694  
1695  
1696  
1697  
1698  
1699  
1700  
1701  
1702  
1703  
1704  
1705  
1706  
1707  
1708  
1709  
1710  
1711  
1712  
1713  
1714  
1715  
1716  
1717  
1718  
1719  
1720  
1721  
1722  
1723  
1724  
1725  
1726  
1727  
1728  
1729  
1730  
1731  
1732  
1733  
1734  
1735  
1736  
1737  
1738  
1739  
1740  
1741  
1742  
1743  
1744  
1745  
1746  
1747  
1748  
1749  
1750  
1751  
1752  
1753  
1754  
1755  
1756  
1757  
1758  
1759  
1760  
1761  
1762  
1763  
1764  
1765  
1766  
1767  
1768  
1769  
1770  
1771  
1772  
1773  
1774  
1775  
1776  
1777  
1778  
1779  
1780  
1781  
1782  
1783  
1784  
1785  
1786  
1787  
1788  
1789  
1790  
1791  
1792  
1793  
1794  
1795  
1796  
1797  
1798  
1799  
1800  
1801  
1802  
1803  
1804  
1805  
1806  
1807  
1808  
1809  
1810  
1811  
1812  
1813  
1814  
1815  
1816  
1817  
1818  
1819  
1820  
1821  
1822  
1823  
1824  
1825  
1826  
1827  
1828  
1829  
1830  
1831  
1832  
1833  
1834  
1835  
1836  
1837  
1838  
1839  
1840  
1841  
1842  
1843  
1844  
1845  
1846  
1847  
1848  
1849  
1850  
1851  
1852  
1853  
1854  
1855  
1856  
1857  
1858  
1859  
1860  
1861  
1862  
1863  
1864  
1865  
1866  
1867  
1868  
1869  
1870  
1871  
1872  
1873  
1874  
1875  
1876  
1877  
1878  
1879  
1880  
1881  
1882  
1883  
1884  
1885  
1886  
1887  
1888  
1889  
1890  
1891  
1892  
1893  
1894  
1895  
1896  
1897  
1898  
1899  
1900  
1901  
1902  
1903  
1904  
1905  
1906  
1907  
1908  
1909  
1910  
1911  
1912  
1913  
1914  
1915  
1916  
1917  
1918  
1919  
1920  
1921  
1922  
1923  
1924  
1925  
1926  
1927  
1928  
1929  
1930  
1931  
1932  
1933  
1934  
1935  
1936  
1937  
1938  
1939  
1940  
1941  
1942  
1943  
1944  
1945  
1946  
1947  
1948  
1949  
1950  
1951  
1952  
1953  
1954  
1955  
1956  
1957  
1958  
1959  
1960  
1961  
1962  
1963  
1964  
1965  
1966  
1967  
1968  
1969  
1970  
1971  
1972  
1973  
1974  
1975  
1976  
1977  
1978  
1979  
1980  
1981  
1982  
1983  
1984  
1985  
1986  
1987  
1988  
1989  
1990  
1991  
1992  
1993  
1994  
1995  
1996  
1997  
1998  
1999  
2000  
2001  
2002  
2003  
2004  
2005  
2006  
2007  
2008  
2009  
2010  
2011  
2012  
2013  
2014  
2015  
2016  
2017  
2018  
2019  
2020  
2021  
2022  
2023  
2024  
2025  
2026  
2027  
2028  
2029  
2030  
2031  
2032  
2033  
2034  
2035  
2036  
2037  
2038  
2039  
2040  
2041  
2042  
2043  
2044  
2045  
2046  
2047  
2048  
2049  
2050  
2051  
2052  
2053  
2054  
2055  
2056  
2057  
2058  
2059  
2060  
2061  
2062  
2063  
2064  
2065  
2066  
2067  
2068  
2069  
2070  
2071  
2072  
2073  
2074  
2075  
2076  
2077  
2078  
2079  
2080  
2081  
2082  
2083  
2084  
2085  
2086  
2087  
2088  
2089  
2090  
2091  
2092  
2093  
2094  
2095  
2096  
2097  
2098  
2099  
2100  
2101  
2102  
2103  
2104  
2105  
2106  
2107  
2108  
2109  
2110  
2111  
2112  
2113  
2114  
2115  
2116  
2117  
2118  
2119  
2120  
2121  
2122  
2123  
2124  
2125  
2126  
2127  
2128  
2129  
2130  
2131  
2132  
2133  
2134  
2135  
2136  
2137  
2138  
2139  
2140  
2141  
2142  
2143  
2144  
2145  
2146  
2147  
2148  
2149  
2150  
2151  
2152  
2153  
2154  
2155  
2156  
2157

### *Bragg peak degradation due to lung tissue*

23

protons that a modulation power of about  $450 \mu\text{m}$  has an effect of 3% on the mean dose distribution within the tumor. This was considered to be clinically tolerable at the time of publication. For the values determined in this work, this means that the maximum measured value of the modulation power, together with a very conservative estimation of the deviation ( $367 \mu\text{m} + 110 \mu\text{m}$ ), just reaches the range for  $P_{mod}$  which is currently considered clinically tolerable for protons. The mean value of the modulation power for ventilated lung tissue measured in this study is significantly smaller (approximately  $200 \mu\text{m}$ ) and therefore not relevant in the clinical context at the moment. For the measurements regarding the energy dependence of the modulating effect, we could not measure any energy dependence of the effect in our model in the used energy range.

## **5. Conclusion**

For porcine lung tissue the modulation power could be determined in the range between  $62$  to  $367 \mu\text{m}$ . With these measurements we could generate more reliable values for  $P_{mod}$  and specify the so far published values at this point. Compared to previous publications on the determination of  $P_{mod}$  based on surrogates with modulation powers up to approximately  $1000 \mu\text{m}$  the real modulation power for lung tissue turns out to be lower and in a smaller range.

## **Acknowledgments**

The project was supported by the Federal Ministry of Education and Research within the scope of the grant “Physikalische Modellierung für die individualisierte Partikel-Strahlentherapie und Magnetresonanztomographie”, (MiPS, grant number 13FH726IX6). The experiments at MIT were supported by the Hessian state government.

## REFERENCES

24

## References

- Baumann, K.-S., Flatten, V., Weber, U., Lautenschläger, S., Eberle, F., Zink, K. and Engenhart-Cabillic, R. (2019). Effects of the Bragg peak degradation due to lung tissue in proton therapy of lung cancer patients, *Radiation Oncology* **14**(183).
- Baumann, K.-S., Witt, M., Weber, U., Engenhart-Cabillic, R. and Zink, K. (2017). An efficient method to predict and include Bragg curve degradation due to lung-equivalent materials in Monte Carlo codes by applying a density modulation, *Physics in Medicine & Biology* **62**(10): 3997–4016.
- Bichsel, H., Hiraoka, T. and Omata, K. (2000). Aspects of Fast-Ion Dosimetry, *Radiation Research* **153**(2): 208–219.
- Chang, J. Y., Zhang, X., Wang, X., Kang, Y., Riley, B., Bilton, S., Mohan, R., Komaki, R. and Cox, J. D. (2006). Significant reduction of normal tissue dose by proton radiotherapy compared with three-dimensional conformal or intensity-modulated radiation therapy in Stage I or Stage III non-small-cell lung cancer, *International Journal of Radiation Oncology Biology Physics* **65**(4): 1087–1096.
- España, S. and Paganetti, H. (2011). Uncertainties in planned dose due to the limited voxel size of the planning {CT} when treating lung tumors with proton therapy, *Physics in Medicine and Biology* **56**(13): 3843–3856.
- Flatten, V., Baumann, K.-S., Weber, U., Engenhart-Cabillic, R. and Zink, K. (2019). Quantification of the dependencies of the Bragg peak degradation due to lung tissue in proton therapy on a {CT}-based lung tumor phantom, *Physics in Medicine & Biology* **64**(15): 155005.
- Flatten, V., Michael Burg, J., Witt, M., Derksen, L., Fragoso Costa, P., Wulff, J., Baumer, C., Timmermann, B., Weber, U., Vorwerk, H., Engenhart-Cabillic, R., Zink, K. and Baumann, K. S. (2021). Estimating the modulating effect of lung tissue in

## REFERENCES

25

particle therapy using a clinical CT voxel histogram analysis, *Physics in Medicine and Biology* .

Grutters, J. P. C., Kessels, A. G. H., Pijls-Johannesma, M., Ruyscher, D. D., Joore, M. A. and Lambin, P. (2010). Comparison of the effectiveness of radiotherapy with photons, protons and carbon-ions for non-small cell lung cancer: A meta-analysis, *Radiotherapy and Oncology* **95**(1): 32–40.

Hranek, A., Resch, A. F., Georg, D. and Knäusl, B. (2020). Investigation of the Bragg peak degradation caused by homogeneous and heterogeneous lung tissue substitutes: Proton beam experiments and comparison to current clinical dose calculation, *Physics in Medicine and Biology* **65**(24).

Judge, E. P., Hughes, J. M., Egan, J. J., Maguire, M., Molloy, E. L. and O’Dea, S. (2014). Anatomy and bronchoscopy of the porcine lung: A model for translational respiratory medicine.

Kraft, G. (2000). Tumor therapy with heavy charged particles, *Progress in Particle and Nuclear Physics* **45**: S473 – S544.

Paz, A. E. S., Baumann, K., Weber, U. A., Witt, M., Zink, K., Durante, M. and Graeff, C. (2021). Compensating for beam modulation due to microscopic lung heterogeneities in carbon ion therapy treatment planning, *Medical Physics* .

Plathow, C., Ley, S., Zaporozhan, J., Schöbinger, M., Gruenig, E., Puderbach, M., Eichinger, M., Meinzer, H. P., Zuna, I. and Kauczor, H. U. (2006). Assessment of reproducibility and stability of different breath-hold manoeuvres by dynamic MRI: Comparison between healthy adults and patients with pulmonary hypertension, *European Radiology* .

Ringbæk, T. P., Simeonov, Y., Witt, M., Engenhardt-Cabillic, R., Kraft, G., Zink, K.

## REFERENCES

- and Weber, U. (2017). Modulation power of porous materials and usage as ripple filter in particle therapy, *Physics in Medicine and Biology* **62**(7): 2892–2909.
- Sawakuchi, G. O., Titt, U., Mirkovic, D. and Mohan, R. (2008). Density heterogeneities and the influence of multiple Coulomb and nuclear scatterings on the Bragg peak distal edge of proton therapy beams, *Physics in Medicine and Biology* **53**(17): 4605–4619.
- Schardt, D., Elsässer, T. and Schulz-Ertner, D. (2010). Heavy-ion tumor therapy: Physical and radiobiological benefits, *Rev. Mod. Phys.* **82**(1): 383–425.
- Schulz-Ertner, D. and Tsujii, H. (2007). Particle Radiation Therapy Using Proton and Heavier Ion Beams, *Journal of Clinical Oncology* **25**(8): 953–964.
- Sell, M., Titt, U., Perles, L., Mirkovic, D., Mohan, R., Bangert, M. and Oelfke, U. (2012). WE-E-BRB-02: Evaluation of Analytical Proton Dose Predictions with a Lung-Like Plastic Phantom, *Medical Physics* **39**(6Part27): 3956.
- Titt, U., Sell, M., Unkelbach, J., Bangert, M., Mirkovic, D., Oelfke, U. and Mohan, R. (2015). Degradation of proton depth dose distributions attributable to microstructures in lung-equivalent material, *Medical Physics* **42**(11): 6425–6432.
- Urie, M., Goitein, M., Holley, W. R. and Chen, G. T. Y. (1986). Degradation of the Bragg peak due to inhomogeneities, *Physics in Medicine and Biology* **31**(1): 1–15.
- Weber, U. and Kraft, G. (1999). Design and construction of a ripple filter for a smoothed depth dose distribution in conformal particle therapy, *Physics in Medicine and Biology* **44**(11): 2765–2775.
- Wilson, R. R. (1946). Radiological Use of Fast Protons, *Radiology* **47**(5): 487–491.
- Witt, M. (2014). Modulationseffekte von Kohlenstoffionen bei der Bestrahlung von Lungen, *Master Thesis, Technische Hochschule Mittelhessen - University of applied*

1  
2  
3 *REFERENCES*4  
5 *sciences, Giessen, Germany .*6  
7 **URL:** [https://www.thm.de/lse/images/user/KZink-105/Abschlussarbeiten/Masterarbeit\\_Matthias\\_Witt\\_27](https://www.thm.de/lse/images/user/KZink-105/Abschlussarbeiten/Masterarbeit_Matthias_Witt_27)8  
9 Witt, M., Weber, U., Simeonov, Y. and Zink, K. (2015). Range-Modulation Effects of  
10 Carbon Ion Beams in Lung Tissue, *Medical Physics* **42**(6Part23): 3491.  
11  
12  
13  
14  
15  
16  
17  
18  
19  
20  
21  
22  
23  
24  
25  
26  
27  
28  
29  
30  
31  
32  
33  
34  
35  
36  
37  
38  
39  
40  
41  
42  
43  
44  
45  
46  
47  
48  
49  
50  
51  
52  
53  
54  
55  
56  
57  
58  
59  
60



ACCEPTED MANUSCRIPT

# Estimating the modulating effect of lung tissue in particle therapy using a clinical CT voxel histogram analysis

To cite this article before publication: Veronika Flatten *et al* 2021 *Phys. Med. Biol.* in press <https://doi.org/10.1088/1361-6560/ac176e>

## Manuscript version: Accepted Manuscript

Accepted Manuscript is “the version of the article accepted for publication including all changes made as a result of the peer review process, and which may also include the addition to the article by IOP Publishing of a header, an article ID, a cover sheet and/or an ‘Accepted Manuscript’ watermark, but excluding any other editing, typesetting or other changes made by IOP Publishing and/or its licensors”

This Accepted Manuscript is © 2021 Institute of Physics and Engineering in Medicine.

During the embargo period (the 12 month period from the publication of the Version of Record of this article), the Accepted Manuscript is fully protected by copyright and cannot be reused or reposted elsewhere.

As the Version of Record of this article is going to be / has been published on a subscription basis, this Accepted Manuscript is available for reuse under a CC BY-NC-ND 3.0 licence after the 12 month embargo period.

After the embargo period, everyone is permitted to use copy and redistribute this article for non-commercial purposes only, provided that they adhere to all the terms of the licence <https://creativecommons.org/licenses/by-nc-nd/3.0>

Although reasonable endeavours have been taken to obtain all necessary permissions from third parties to include their copyrighted content within this article, their full citation and copyright line may not be present in this Accepted Manuscript version. Before using any content from this article, please refer to the Version of Record on IOPscience once published for full citation and copyright details, as permissions will likely be required. All third party content is fully copyright protected, unless specifically stated otherwise in the figure caption in the Version of Record.

View the [article online](#) for updates and enhancements.

# Estimating the modulating effect of lung tissue in particle therapy using a clinical CT voxel histogram analysis

Veronika Flatten<sup>1,2,3</sup>, Jan Michael Burg<sup>1,2</sup>, Matthias Witt<sup>1,2,3</sup>,  
Larissa Derksen<sup>2</sup>, Pedro Fragoso Costa<sup>4,5</sup>, Jörg Wulff<sup>4,5,6</sup>,  
Christian Bäumer<sup>4,5,6,7,8</sup>, Beate Timmermann<sup>4,5,6,8</sup>, Uli Weber<sup>9</sup>,  
Hilke Vorwerk<sup>1,3</sup>, Rita Engenhardt-Cabillic<sup>1,3</sup>, Klemens Zink<sup>1,2,3</sup>,  
Kilian-Simon Baumann<sup>1,2,3</sup>

<sup>1</sup>University Medical Center Giessen-Marburg, Department of Radiotherapy and Radiooncology, Marburg, Germany

<sup>2</sup>University of Applied Sciences, Institute of Medical Physics and Radiation Protection, Giessen, Germany

<sup>3</sup>Marburg Ion Beam Therapy Center, Marburg, Germany

<sup>4</sup>West German Cancer Center, Essen, Germany

<sup>5</sup>University Hospital Essen, Essen, Germany

<sup>6</sup>Westdeutsches Protonentherapiezentrum Essen, Essen, Germany

<sup>7</sup>TU Dortmund University, Faculty of Physics, Dortmund, Germany

<sup>8</sup>German Cancer Consortium (DKTK), Heidelberg, Germany

<sup>9</sup>GSI Helmholtzzentrum für Schwerionenforschung, Biophysics Division, Darmstadt, Germany

**Abstract.** To treat lung tumours with particle therapy, different additional tasks and challenges in treatment planning and application have to be addressed thoroughly. One of these tasks is the quantification and consideration of the Bragg peak degradation due to lung tissue: As lung is an heterogeneous tissue, the Bragg peak is broadened when particles traverse the microscopic alveoli. These are not fully resolved in clinical CT images and thus, the effect is not considered in the dose calculation.

In this work, a correlation between the CT histograms of heterogeneous material and the impact on the Bragg peak curve is presented. Different inorganic materials were scanned with a conventional CT scanner and additionally, the Bragg peak degradation was measured in a proton beam and was then quantified. A model is proposed that allows an estimation of the modulation power by performing a histogram analysis on the CT scan. To validate the model for organic samples, a second measurement series was performed with frozen porcine lunge samples. This allows to investigate the possible limits of the proposed model in a set-up closer to clinical conditions. For lung substitutes, the agreement between model and measurement is within  $\pm 0.05$  mm and for the organic lung samples, within  $\pm 0.15$  mm.

This work presents a novel, simple and efficient method to estimate if and how much a material or a distinct region (within the lung) is degrading the Bragg peak on the basis of a common clinical CT image. Up until now, only a direct in-beam measurement of the region or material of interest could answer this question.

## 1. Introduction

Particle therapy with protons and heavy ions is still a niche in radiation therapy but has gained more and more attention world wide. In a review article, Gjyshi and Liao (2020) described the interest and urge, as well as the challenges of proton therapy for non-small cell lung cancer (NSCLC). Due to a high mortality combined with radioinsensitiveness, lung cancer appears to be the ideal candidate for the higher biological effectiveness of particle therapy (especially carbon-ion radiotherapy) and the additional dose sparing in surrounding organs at risk (Gjyshi and Liao; 2020; Bradley et al.; 2015; Chang et al.; 2006) compared to conventional photon therapy. However, treating lung cancer with particles seems to combine several of the most challenging aspects of state-of-the-art treatment routine: From imaging over treatment planning to the particle application, the topics of movement mitigation (Bert and Durante; 2011; De Ruyscher et al.; 2015), radiobiology modelling (Sørensen et al.; 2017; Willers et al.; 2018) and the range degradation through lung tissue (Titt et al.; 2015; Urie et al.; 1986) need to be handled. Target movement is addressed by the implementation of gating (Lu et al.; 2007; Ebner et al.; 2017) or tracking (Desplanques et al.; 2013) in combination with fast rescanning or the accelerated application via passive range-modulators (Simeonov et al.; 2017), while better biological modelling is under constant discussion (Paganetti et al.; 2002; Grün et al.; 2015; McNamara et al.; 2020). The effect of the Bragg peak (BP) degradation, however, is on the verge of being accounted for in dose calculation and optimization (Winter et al.; 2020): the BP curve is degraded when particles travel through porous material like lung tissue, which was shown in measurements (Sawakuchi et al.; 2008; Titt et al.; 2015; Ringbaek et al.; 2017; Witt et al.; 2015; Hranek et al.; 2020; Burg et al.; 2021). The lung consists of microscopic, air-filled alveoli and larger bronchial structures. The resolution of the treatment planning CT, on which dose calculation is performed,

1  
2  
3  
4  
5 is not sufficient to differentiate between these micrometer scaled air cavities and the  
6 surrounding tissue. Instead it displays a homogenised density (España and Paganetti;  
7 2011). The particles of the treatment field, on the other hand, do differentiate. Thus,  
8 each particle is travelling on a slightly different path through the body and accumulates  
9 a different composition of air and tissue. Therefore, it stops at a slightly different range:  
10 the Bragg peak is degraded.  
11

12  
13  
14  
15  
16  
17  
18 Previous works (Baumann et al.; 2017; Flatten et al.; 2019; Baumann et al.; 2019) have  
19 estimated the effect on the proton dose distribution using Monte Carlo simulations.  
20 These studies show the effect and the dependencies on patient treatment plans. The  
21 assessments were recently expanded to carbon ions using an analytical dose calculation  
22 algorithm (Ringbæk et al.; 2020). However, these estimations depend strongly on the  
23 power of the modulation effect. To effectively predict and calculate the degradation  
24 effect, information on the modulation power is needed. Unfortunately, there is little  
25 published experimental data of the BP degradation when irradiating lungs (Burg et al.;  
26 2021).  
27

28  
29  
30  
31  
32  
33  
34  
35  
36  
37 Besides the implementation into treatment planning software as presented by Winter  
38 et al. (2020), a method to quantify the strength of the BP degradation is needed.  
39 Meijers et al. (2020) presented results obtained with proton radiography from which the  
40 information needed for the treatment planning could be extracted. However, although  
41 the idea of proton CTs is promising, the clinical implementation will take time. Other  
42 promising tools that compensate the information loss in clinical CT resolutions are dark  
43 field and phase-contrast CTs (Bech et al.; 2013; Braig et al.; 2020). Recent studies  
44 (Willer et al.; 2021) show that chronic obstructive pulmonary disease (COPD) patients  
45 can be staged with these novel radiography techniques, indicating a connection to the  
46 probable strength of the BP degradation. However, the available data to estimate the  
47  
48  
49  
50  
51  
52  
53  
54  
55  
56  
57  
58  
59  
60

1  
2  
3  
4  
5 modulation power of lung tissue is incomplete and can only be obtained via direct in-  
6  
7 beam measurements.

8  
9 In this study, we want to address the question of how to estimate the strength of the  
10  
11 modulating effect for a specific region in the 3D CT data set. For this reason, in-beam  
12  
13 measurements were performed to determine the modulation power of heterogeneous  
14  
15 substitutes and lung tissue samples. To allow a specific match to the CT information,  
16  
17 scans of the samples were acquired with a conventional CT scanner. Using these data, a  
18  
19 CT based histogram analysis was motivated and developed to estimate the modulation  
20  
21 power for a specific region of a clinical CT image.

22  
23  
24 The aim of this work is to present a method to use the clinical treatment planning  
25  
26 CTs to predict and analyse the lung modulation power. Thus we want to proof and  
27  
28 determine the proportionality between the CT histogram parameters and the measured  
29  
30 modulation power. This could allow to estimate a specific modulation power for a clinical  
31  
32 patient CT image. Thus, a patient-specific implementation of the BP degradation in  
33  
34 the treatment planning process is viable.  
35  
36  
37  
38

## 39 **2. Material & Methods**

### 40 41 42 *2.1. Determination of the modulation power $P_{mod}$ via in-beam measurements*

43  
44  
45 The process of estimating the modulation power from a degraded Bragg curve has been  
46  
47 described in detail by Witt et al.(2015) and Ringbaek et al.(2017). In general, for each  
48  
49 material the reference curve obtained without the degrading material in the beam line  
50  
51 was taken and convolved with a normal distribution as indicated by the blue curves in  
52  
53 figure 1.  
54  
55  
56  
57  
58  
59  
60

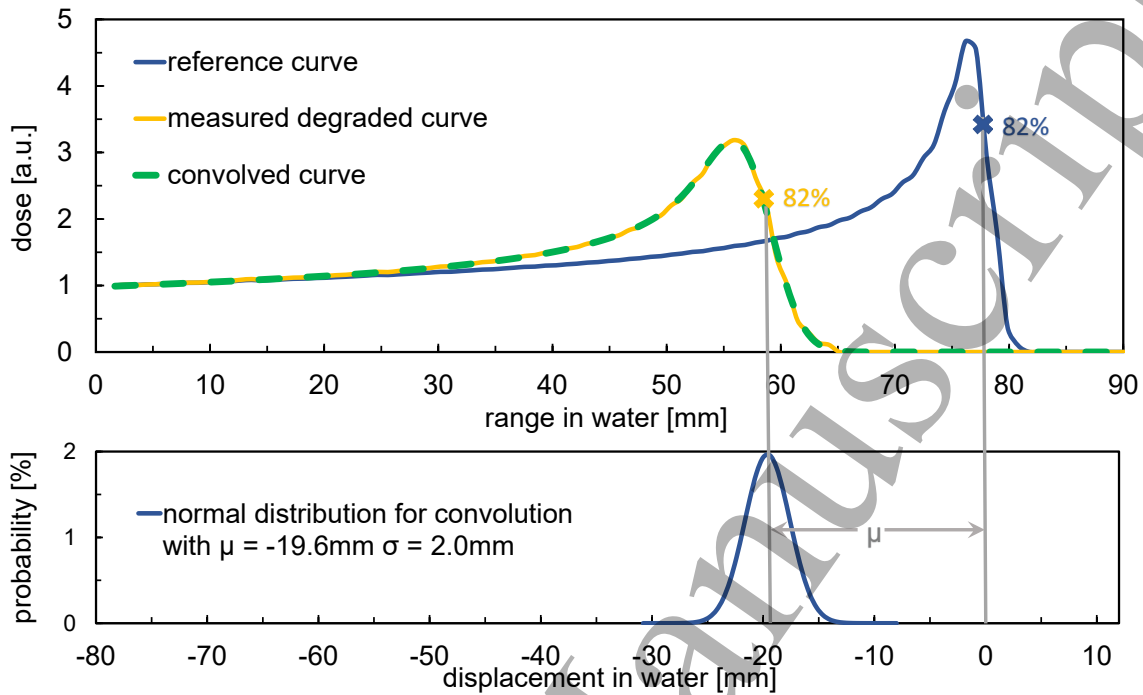


**Figure 1.** Exemplary graph showing the extraction of the modulation power from a measured degraded curve, in this case for the LN-300 material. The blue BP in the upper graph shows the reference curve without the modulating material for this specific set-up. In yellow, the measured degraded BP is shown and the green dashed curve represents the convoluted curve which was obtained by convolution of the reference curve with the normal distribution shown in the bottom graph. The mean of the normal distribution is obtained by calculating the difference of the range in water for the distal 82% dose value. At this point, the BP is minimally affected by range straggling. The width of the normal distribution is then adjusted to minimize the difference between the resulting convoluted curve and the measured degraded curve.

The modulation power is then calculated via

$$P_{\text{mod}} \equiv \frac{\sigma^2}{\mu} \quad (1)$$

## 2.2. Mathematical description of the modulating effect

In general, a substance is degrading the Bragg peak, if it consists of structured mixture of materials with different water-equivalent thicknesses on a microscopic scale. Imaging of such a modulating sample with a macroscopic resolution, leads to a loss in information about the mixture and the microscopic structure. To describe the imaging process

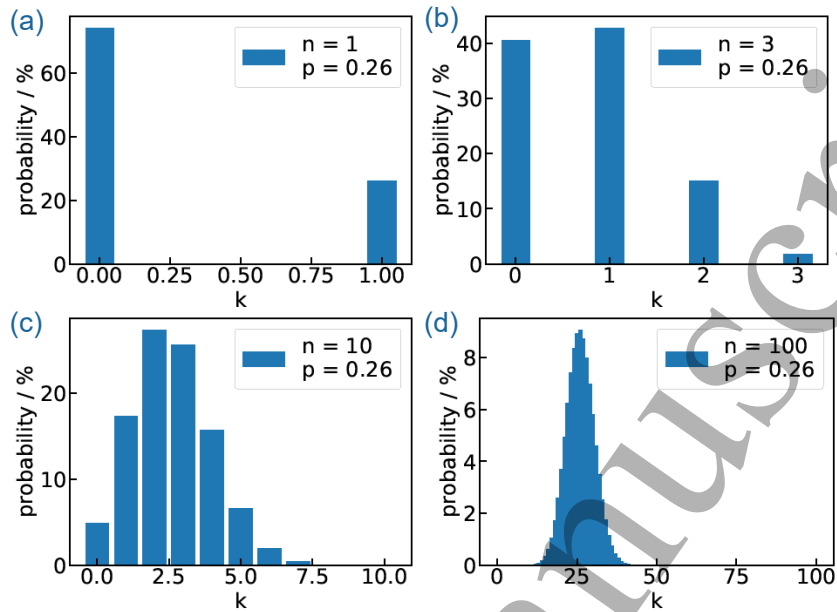


**Figure 2.** Exemplary binomial distributions for  $p = 0.26$  and increasing values of  $n$ , which indicates the number of air or tissue voxels that are merged.  $k$  counts the voxels of the  $n$  merged voxels that are tissue. (a) shows the case for  $n = 1$ : The sampled voxel is either air ( $k = 0$  with a probability of 74%) or tissue ( $k = 1$  with a probability of 26%). (b)-(d) show higher values of  $n$ : The sampled voxel is probably a mixture of air and tissue.  $k/n$  of the sampled voxel is tissue. E.g. in (b) the probability to sample a voxel with no tissue is about 40%, which is a slightly lower probability than to sample a voxel which is about a third tissue. (d) shows the case where the probability to find a purely air or tissue voxel is almost zero. And all voxel contain roughly a fourth of tissue.

mathematically, a model is proposed in the following.

In a clinical context, lung is the composite material of interest when considering the BP degradation. Hence, approximations for the mathematical model can be made:

- Only composite materials that consist of exactly two different materials are considered. This restriction is applied as the composition of lung tissue can be approximated to consist of air and tissue - as blood, vessels, fat and soft tissue have nearly the same density or Hounsfield unit (HU) value.
- For a simply computable example, air has  $-1000$  HU ( $HU_{\min}$ ) and tissue  $0$  HU ( $HU_{\max}$ ). The (inhaled) lung has a typical density of about  $0.26 \text{ g/cm}^3 \approx -740$  HU (Schneider et al.; 1996).

- For the modulating material (e.g. a porous material), we assume a constant and uniform structure size (as defined by Baumann et al. (2017)). In other words, the size of the clusters of tissue and air are the same throughout the geometry.

When sampling this approximated porous material with an infinite resolution the resulting HU histogram would consist of two bins. This is exemplarily shown in figure 2(a). In this case, the 'finest' resolution ( $r_0$ ) is defined as the resolution needed to clearly identify each voxel as either air or tissue. Every increase in resolution would not change the obtained histogram. If the resolution is not sufficient to resolve the 'finest' structures, the structures are merged and intermediate values are obtained as shown in figure 2(b) and (c). Mathematically, this can be described by a binomial distribution:

$$\text{BINOMIAL DISTRIBUTION : } B(k) = \binom{n}{k} p^k (1-p)^{n-k} \quad (2)$$

$p$  is the probability of the voxel being tissue,  $(1-p)$  the counter probability of sampling air and  $n$  is a measure for the resolution. In one dimension,  $n$  can be calculated as the ratio of the image resolution  $r$  and the 'finest' resolution  $r_0$ . Hence, it gives the number of united "finest" voxels.  $B(k)$  gives the probability that the merged voxel contains  $k$  ( $0 \leq k \leq n$ ) of the 'finest' tissue voxels.

For high values of  $n$  the discrete binomial distribution can be approximated by the differential normal distribution. This is then transferred to a continuous normal distribution, which is shown in figure 2(d). It is described by:

$$\text{NORMAL DISTRIBUTION : } F(k|\mu^*, \sigma^{*2}) = \frac{1}{\sqrt{2\pi\sigma^{*2}}} \exp\left(-\frac{(k-\mu^*)^2}{2\sigma^{*2}}\right) \quad (3)$$

So, a histogram of a macroscopic image of the lung can be described by a normal distribution with the corresponding parameters  $\mu^* = np$  and  $\sigma^{*2} = np(1-p)$  (via the



Moivre–Laplace central limit theorem).

To transfer the  $k$ -axis into HU values, a substitution has to be performed on the differential form of the normal distribution. The details are given in the appendix.

This transfer gives the new parameters:

$$\mu := \mu^* \Delta x / n = 1000 \text{HU} \cdot (p - 1) \quad (4)$$

$$\sigma^2 := \sigma^{*2} \Delta x^2 / n^2 = (1000 \text{HU})^2 \cdot p(1 - p) / n \quad (5)$$

From these equations it is clear, that the width of the normal distribution  $\sigma$  depends on the resolution ratio  $n$ , whereas the mean is independent on the resolution.

To correlate this to the modulation power, as defined by Baumann et al. (2017), the relation between the resolution ratio  $n$  and the modulation power  $P_{\text{mod}}$  has to be specified:  $n$  can be computed as the measured voxel length  $r$  divided by the 'finest' voxel length  $r_0$  in three dimensions.  $r_0$  depends on the structure size  $d$  as referred to by Baumann et al., which in turn is proportional to  $P_{\text{mod}}$ , resolving to:

$$n := \frac{r^3}{r_0^3} = c \frac{r^3}{d^3} = c' \frac{r^3}{P_{\text{mod}}^3} \quad \text{AND} \quad n \stackrel{\text{Transforming Eq. 4\&5}}{=} \frac{-1000 \text{HU} \cdot \mu - \mu^2}{\sigma^2} \quad (6)$$

where  $c$  and  $c'$  describe arbitrary proportionality factors.

Finally, the correlation that needs to be evaluated is given by:

$$P_{\text{mod}} \propto \sqrt[3]{\frac{\sigma^2}{-1000 \text{HU} \cdot \mu - \mu^2}} \equiv P_{\text{fit}} \quad (7)$$

This correlation shows that there is a mathematical relation between the parameters  $\mu$  and  $\sigma$  of a CT histogram and the modulation power  $P_{\text{mod}}$  measured in the particle beam.  $P_{\text{fit}}$  and the proportionality factor will depend on the resolution  $r$ . Aim of the study is to proof and determine the proportionality in order to directly calculate the

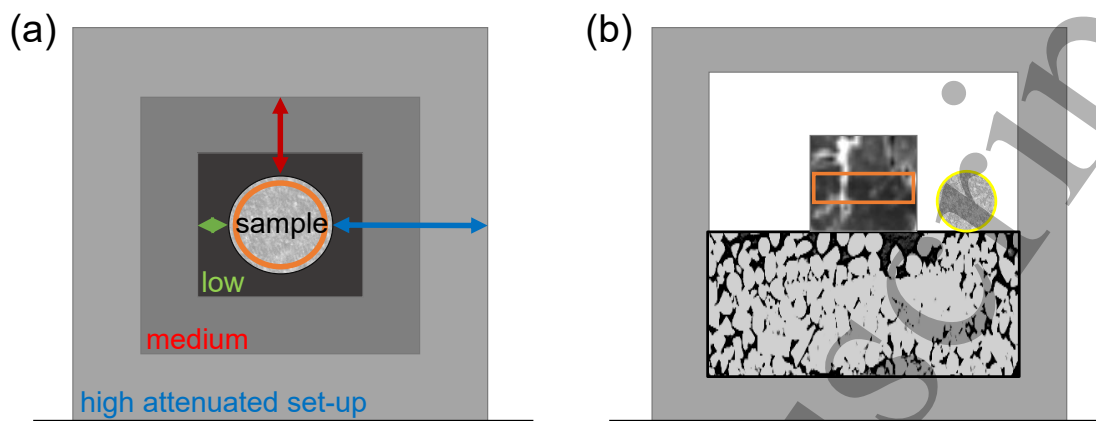


**Figure 3.** Scheme of a CT slice of measurement set-up for the CT dependencies measurement series (a) and the lung sample measurements (b). The orange marker defines the contoured region of interest. On the left panel (a), the three different PMMA thickness set-ups are indicated: The low attenuation set-up (green arrow  $\sim 2$  cm), the medium attenuation (red arrow  $\sim 4$  cm) and the high attenuation set-up (blue arrow  $\sim 8$  cm). For the measurement series of the heterogeneous surrogates, the low attenuation set-up was used. The right panel (b) shows the frozen lung sample in the center on top of the dry ice pellets. A reference material (in yellow) is added to compensate the unknown attenuation of the dry ice.

modulation power from the CT histogram.

### 2.3. CT measurement

The proposed model is based on the width of the CT histogram. Thus, it is essential to understand which measurement parameters influence the measured width.

To understand the dependencies of the CT parameters on width, a series of CT measurements was taken. The factors that primarily influence the width are described by Verdun et al. (2015). The CT configuration and the results are given in the appendix. All scans were performed with a conventional CT-Scanner (Somatom Confidence, Siemens Healthineers, Erlangen Germany) with 120 kVp and the Br43s convolution kernel. The test samples were scanned with a resolution of  $1.0 \times 1.0 \times 0.6 \text{ mm}^3$  and positioned as shown in figure 3. For low density materials the influence of the partial volume effect is minimal. To further minimize the influence, the region of interest was

1  
2  
3  
4  
5  
6  
7  
8  
9  
10  
11  
12  
13  
14  
15  
16  
17  
18  
19  
20  
21  
22  
23  
24  
25  
26  
27  
28  
29  
30  
31  
32  
33  
34  
35  
36  
37  
38  
39  
40  
41  
42  
43  
44  
45  
46  
47  
48  
49  
50  
51  
52  
53  
54  
55  
56  
57  
58  
59  
60

10  
contoured excluding material and HU boundaries (orange contour in figure 3). Then, a HU histogram was produced and a normal distribution was fitted to the data. From the optimized parameters  $\mu$  and  $\sigma$  the parameter  $P_{\text{fit}}$  (eq. 7) was calculated and compared to the modulation power  $P_{\text{mod}}$  measured in the proton beam. The porous samples were additionally scanned with a  $1.0 \times 1.0 \times 1.5 \text{ mm}^3$  resolution, as well as with a small animal CT (X-Cube, Molecubes, Gent Belgium) with a resolution of  $0.1 \times 0.1 \times 0.1 \text{ mm}^3$ .

#### 2.4. Measurement of the modulation power of heterogeneous surrogates

To determine the proportionality factor of the mathematical model in equation 7, a correlation between the in-beam measurement results and the CT histogram needs to be established. Hence, measurements of the BP degradation of various porous materials were performed at the West German Proton Therapy Center (WPE). Since 2013, the WPE features a Proteus<sup>®</sup>Plus (IBA International, Louvain-la-Neuve, Belgium) cyclotron system, where active and passive proton beam treatment with energies up to 230 MeV is offered in four clinical rooms.

Nine different materials that promise a heterogeneous composition were selected: rigid foam, polystyrene, synthetic sponge, SikaBlock PUR, black abrasive fleece, Gammex LN-300, Gammex LN-450, rubber granulate and clay granulate. For each material, the laterally integrated depth dose distributions (IDD) were measured with the "Giraffe"-type multi-layer ionization chamber (IBA Dosimetry, Schwarzenbruck Germany), while the porous material was placed directly in front of the Giraffe. Each measurement was performed with proton beam energies of 100, 130, 160, 190 and 205 MeV, respectively.

#### 2.5. Measurement of the modulation power of porcine lung samples

To further test the model, the modulation power of frozen porcine lung samples was measured by in-beam experiments. The measured modulation powers were then

1  
2  
3  
4  
5 compared to the modulation power determined via the CT histogram analysis.

6  
7 The IDD measurements of the frozen lung samples were performed at the Marburg  
8  
9 Ion Beam Therapy Center (MIT). It features a Siemens synchrotron accelerator system  
10  
11 (Siemens Healthineers, Erlangen, Germany), which offers raster-scanning proton (48-  
12  
13 221 MeV) and carbon ion (88-430 MeV/u) beam treatment to patients in four rooms.

14  
15 A detailed description of the lung sample selection and handling, the measurements and  
16  
17 evaluation is given in (Burg et al.; 2021). Five lung samples (three from domestic pigs  
18  
19 and two from a wild boar, all were slaughterhouse waste) were acquired by freezing and  
20  
21 cutting the two lungs into samples of about  $4 \times 10 \times 4 \text{ cm}^3$ . After the freezing process,  
22  
23 the samples were continuously cooled using solid carbon dioxide (dry ice pellets). The  
24  
25 lung tissue samples under investigation differed in their air filling or their localization  
26  
27 in the lung, as these factors can be expected to play a role for the BP degradation  
28  
29 effect. The samples were mounted in a retainer, allowing a distinct positioning of the  
30  
31 sample and a possibility to match the CT scan to the beam path. Again, each lung  
32  
33 sample was positioned in the beam line directly in front of the peakfinder water column  
34  
35 entrance window (PTW, Freiburg Germany) and irradiated with a 140 MeV/u carbon  
36  
37 beam. Three different measurement positions were irradiated for each sample. For  
38  
39 two positions, positioning uncertainties were evaluated by repositioning the samples, as  
40  
41 well as slightly rotating ( $\sim \pm 2^\circ$ ) and shifting ( $\pm 2 \text{ mm}$ ) the samples and repeating the  
42  
43 measurement.  
44  
45  
46  
47  
48  
49

### 50 **3. Results**

#### 51 *3.1. Evaluation of the heterogeneous surrogates*

52  
53  
54  
55  
56 Figure 4 shows the HU histograms (0.1 mm, 0.6 mm and 1.5 mm resolution) of all nine  
57  
58 porous materials that were scanned and for which the BP degradation was measured.  
59  
60

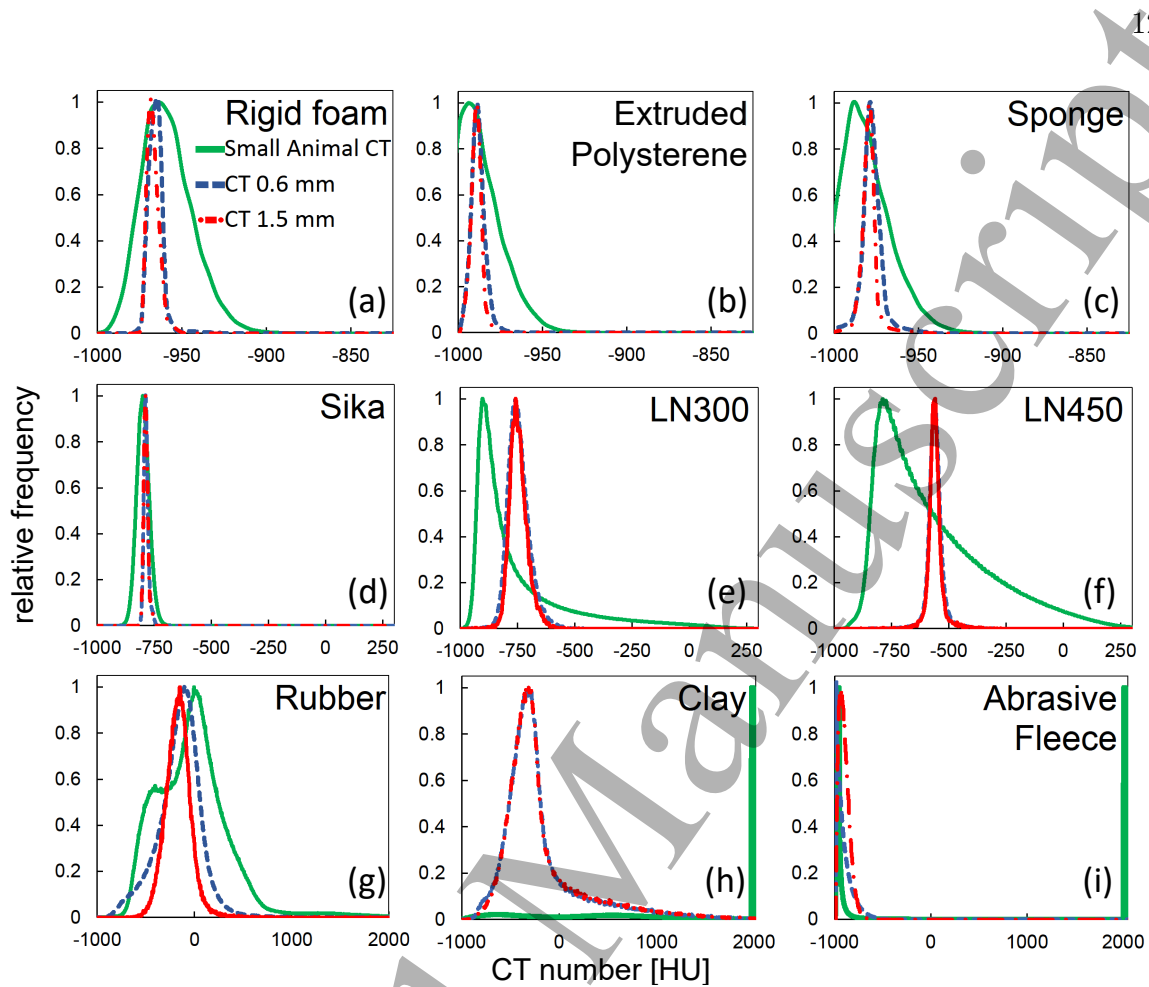


**Figure 4.** Hounsfield unit histograms for each of the nine investigated materials for three different slice thickness: 0.1 mm (small animal CT) in green, 0.6 mm in blue and 1.5 mm in red. Note the different scales on the x-axis. As the small animal CT is not calibrated, small shifts in center of gravity of the histograms can occur.

The mathematical model shows that the histogram will follow a normal distribution for increasing value of  $n$  (see figure 2 and equation 6).  $n$  is either increased by increasing the measured CT resolution  $r$  (different colours in figure 4) or by decreasing the structure size  $d$  of the material. Thus, the curve progression for each material is correlated with the structure size and therefore the modulation power. In figure 4, the first four materials (a-d) already have an almost Gaussian shape in the small animal CT, indicating, that these materials have a small structure size and hence a low modulation power. LN-300 (e) and LN-450 (f) however, show a broader HU histogram in the small animal CT but a Gaussian distribution in the clinical CT. Thus, a higher modulation power is expected.

**Table 1.** Values for  $\mu$  and  $\sigma$  obtained by the Gaussian fit for the 0.6 mm CT scan series and the 1.5 mm series, accompanied by the calculated  $P_{\text{fit}}$  (as proposed by equation 7) and values of the modulation power  $P_{\text{mod}}$  obtained via proton beam measurements.

	0.6 mm slice thickness			1.5 mm slice thickness			$P_{\text{mod}}$ BP-measurement [mm]
	$\mu_{\text{fit}}$ [HU]	$\sigma_{\text{fit}}$ [HU]	$P_{\text{fit}}$	$\mu_{\text{fit}}$ [HU]	$\sigma_{\text{fit}}$ [HU]	$P_{\text{fit}}$	
Rigid foam	58	3	0.03	57	2	0.01	0.03
Polystyrene	35	4	0.04	34	3	0.02	0.05
Sponge	46	4	0.04	44	3	0.02	0.03
Sika	237	8	0.08	236	9	0.06	0.01
LN-300	271	41	0.20	272	34	0.17	0.20
LN-450	462	22	0.11	461	19	0.10	0.13
Clay	657	208	0.65	651	161	0.48	0.69
Abrasive fleece	59	52	0.36	88	51	0.31	0.43

The histogram for rubber (g) on the other hand, shows in the small animal CT that the main modulation effect is caused by two higher density materials as the green curve distinctively indicates two peaks. Therefore, the assumptions and simplification that were made in the mathematical model can not be applied and this surrogate was not considered further in the analysis. The highest modulation power is assumed to be observed for clay granulate and the black abrasive fleece (h,i). While the small animal histogram shows a merely merged binomial distribution, the clinical CTs indicate a transition towards a normal distribution.

As the focus lies on a model for the clinical CT resolution, a normal distribution was fitted to the clinical data sets and the mean ( $\mu$ ) and width ( $\sigma$ ) was determined for each. For clay, a normal distribution was also fitted but the fit is less accurate. The uncertainty on the fit values were set to be higher.

Table 1 summarizes the values of the fitted Gaussian distribution for all materials, for both, the 0.6 mm and the 1.5 mm CT scan series. The value for  $P_{\text{fit}}$  correlates with the described relation of the CT histograms. In general, a broader distribution (large value of  $\sigma_{\text{fit}}$ ) leads to a higher  $P_{\text{fit}}$ , but it also depends on the mean  $\mu_{\text{fit}}$  as shown by the

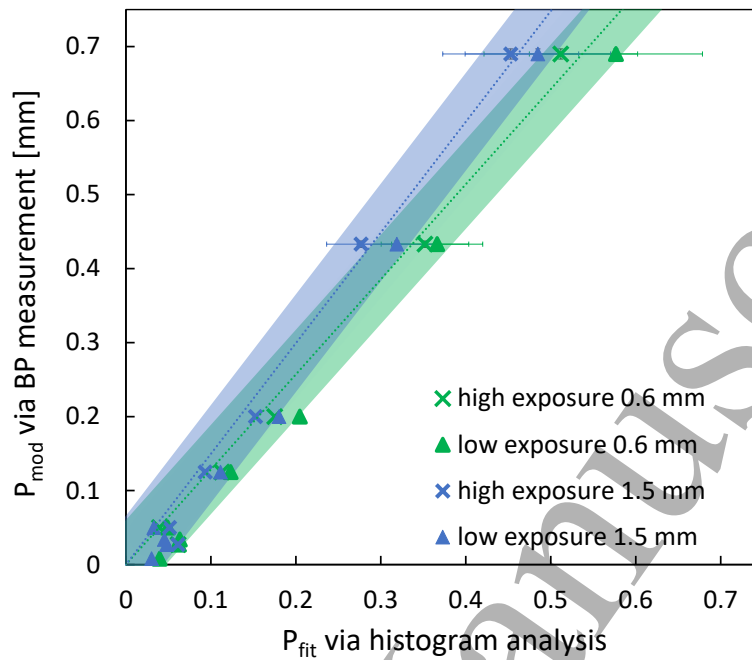


**Figure 5.** The modulation power ( $P_{\text{mod}}$ ) acquired by the proton BP measurement plotted against  $P_{\text{fit}}$  calculated with the CT histogram analysis for the 0.6 mm (in green) and 1.5 mm series (in blue). For each slice thickness, there is one curve with very high exposure (crosses) and one curve with a lower, more clinical exposure (triangles). The fitted linear regressions for the high exposure series are marked by the blue and green line, respectively. The surrounding bands indicate an agreement with the regression line within  $\pm 0.05$  mm. For each point error bars are calculated but in most cases they are smaller than the symbol size.

abrasive fleece.

The last column in table 1 gives the modulating power calculated from the proton BP-measurements for the heterogeneous surrogates.

### 3.2. Analysis of the parameters of the mathematical model

To acquire a calibration curve, the measured values for  $P_{\text{mod}}$  are plotted against  $P_{\text{fit}}$  in figure 5. For the proportionality factor (equation 7), two linear regressions were fitted to the 0.6 mm (in green) and 1.5 mm (in blue) curve. The proportionality factors are: 1.28 mm for the 0.6 mm curve and 1.50 mm for the 1.5 mm curve.

In figure 5, additional curves for each of the chosen slice thicknesses of 0.6 mm and

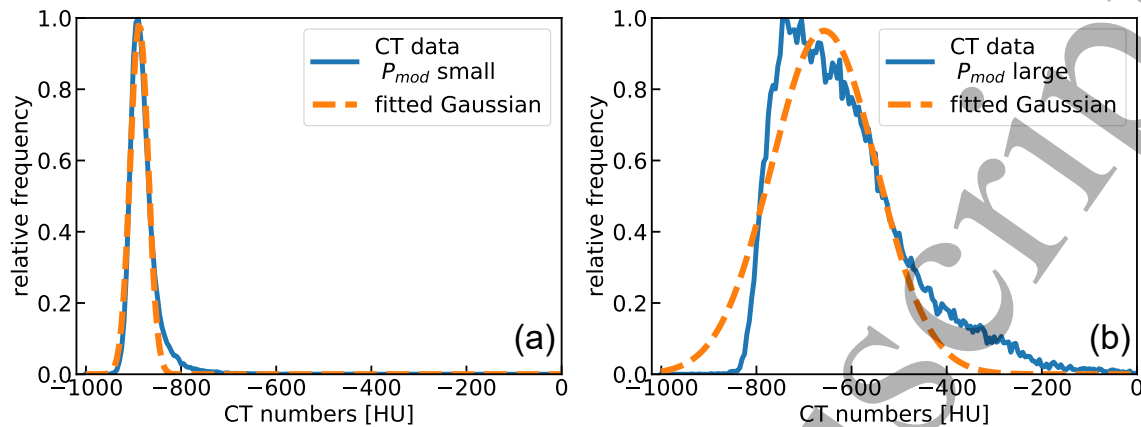


**Figure 6.** CT histograms of the porcine lung samples for a smaller (left panel) and a larger modulation power (right panel). In blue, the original data is shown and in orange the fitted Gaussian distribution.

1.5 mm are shown: Next to the analysed high exposure curve ( $E_{\text{eff}}^{-2} = 0.37 \text{ mAs}^{-2}$ ), one with a lower exposure ( $E_{\text{eff}}^{-2} = 0.64 \text{ mAs}^{-2}$  for 0.6 mm and  $E_{\text{eff}}^{-2} = 0.41 \text{ mAs}^{-2}$  for 1.5 mm, respectively) is given. The error bars indicate the nonconformity with the fitted normal distribution: the difference between the mean of the complete HU histogram and the mean of the normal distribution was taken as uncertainty. However, the band shows that all data points lie within  $\pm 0.05 \text{ mm}$  from the regression line even for the lower exposure curves.

As to be expected from the previous analysis, the normal distribution broadens with a smaller slice thickness (moving from the blue to the green curves) and with a lower exposure (moving from crosses to triangles). The increase in the width and thus  $P_{\text{fit}}$  were expected from the mathematical model, where an increasing  $n$  correlates to a smaller width (equation 5). The increased width caused by a lower exposure correlates to an increased noise in the measurement.

### 3.3. Application of the model to porcine lung samples

To apply the model in a more clinical set-up, the measured modulation powers of the porcine lung samples are compared to the ones calculated with the CT histogram



analysis.

In comparison to the technical, heterogeneous samples, which have uniform structure sizes, the lung samples show different sizes of the micro-structure (small alveoli versus larger bronchial tubes). For this reason, the CT contour was only analysed in the region where the beam traversed the sample (orange contour in figure 3b). Due to the different sized micro-structures, the CT histogram often did not feature a normal distribution. Instead, a superposition of two or more normal distributions and thus structure sizes was visible for higher values of the modulation power. Figure 6 shows the CT histogram for a smaller (a) and a larger (b) modulation power and the fitted normal distribution, which shows the discrepancy between the data and the fit, especially for higher modulation powers. The larger structures would be considered in the treatment planning system as they can be observed in the planning CT (see lung sample in figure 3b). However, as we compare the CT histogram analysis with a measured reference curve everything needs to be included and accounted for. Hence, a single Gaussian was fitted to all samples. This suggests that the modulation power calculated with the CT histogram will most likely underestimate the true degradation effect with increasing modulation power. Figure 7 shows the correspondence between the modulation power  $P_{\text{mod}}$  measured in-beam and the one based on the CT histogram analysis. The estimation of uncertainties was determined in two ways: for the uncertainty of the BP measurement (y-axis) the sample was rotated by  $2^\circ$  or shifted by 2 mm to force a positioning uncertainty. This was only evaluated at two positions but the estimated uncertainty of about 30% was applied to all measurement points. This rather large uncertainty is due to the very small beam width and sharp BP of carbon ions and is a very conservative estimation. For the histogram analysis, the dominant source of uncertainty is the defined region of interest that was evaluated. Therefore, the contour was shifted in two directions by  $\pm 2$  mm (a

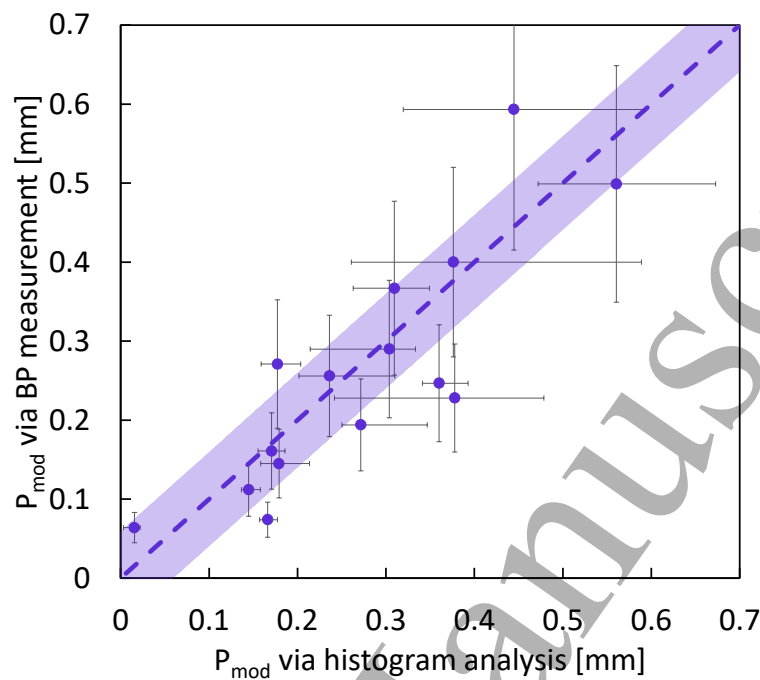


**Figure 7.** The modulation power acquired by the carbon BP measurement against the modulation power calculated with the histogram analysis for the 0.6 mm series of the porcine lung samples.  $P_{\text{fit}}$  is transferred to  $P_{\text{mod}}$  by applying the fitted calibration factor for the 0.6 mm series from figure 5. The dashed line indicates a perfect agreement between both methods and the band a range of about  $\pm 0.06$  mm. The uncertainties in  $x$  indicate the strong dependence of the contoured structure that was analysed. The uncertainties in  $y$  display the measurement and set-up uncertainty.

shift in beam direction was not performed). This was done for each measurement point.

The ends of the error bars mark the lowest and the highest calculated modulation power.

As shown in figure 7, the uncertainty of both, the measured and the calculated modulation power is rather large, especially for the high modulation power values. This, in combination with the not Gaussian CT histograms, makes an estimation of the model difficult. However, the data still shows that the calculated modulation power trends to the one measured in-beam, which is here taken as ground truth. The band in figure 7 indicates an ideal agreement within  $\pm 0.06$  mm which includes 60% of the data points.

80% lie within  $\pm 0.1$  mm and all within  $\pm 0.15$  mm with the values ranging from 0.06 mm up to 0.6 mm. Most data points agree within their uncertainty with the measured values

1  
2  
3  
4  
5 for the modulation power.  
6  
7

#### 8 **4. Discussion** 9

10  
11 In general, the results indicate that the presented model is adequate. Especially, for the  
12 inorganic heterogeneous samples, a clear correlation between a clinical CT histogram  
13 and the modulation power is visible, when the mathematical model is applied. This is an  
14 improvement to the measurement series done by Hranek et al., where no correlation was  
15 found between the width of the histogram and the modulating effect. We could validate  
16 that if only the width on the histogram is taken as measure (as shown in table 1), no clear  
17 correlation can be found. In most cases, a broader width indicates a higher modulation  
18 power, but not in all cases. As motivated by the mathematical description, the relation  
19 between the mean and the width of the CT histogram influences the calculated value of  
20 the modulation power.  
21  
22  
23  
24  
25  
26  
27  
28  
29  
30  
31  
32

33 The test of the model on the lung samples shows the limits of this model. The lung  
34 samples show a range of structure sizes that strongly depend on the specific region  
35 and filling of the lung. Thus, for small regions of interest, the CT histogram might  
36 vary depending on the exact positioning and matching of the samples. Whereas for the  
37 heterogeneous materials, no significant differences in the modulation power was observed  
38 when the contouring was altered.  
39  
40  
41  
42  
43  
44  
45

46 By adding a low density reference material as reference width in each scan of the lung  
47 samples and then correcting for the offset, we were able to analyse data with different  
48 CT measurement parameters.  
49  
50  
51  
52

53 However, even with these restrictions and high uncertainties, the model allows an  
54 estimation of the modulation power with a clinically available set-up which gives a  
55 good indication of the strength of the modulation effect. It is not as precise as e.g.  
56  
57  
58  
59  
60

proton radiography for lung as described by Meijers et al.(2020) but can easily be applied without additional dose given to patients in any clinic. From a clinical point of view, the presented high uncertainties will be drastically reduced when larger fields and thus, larger regions in the CT image will be included into the analysis. The effect of the degradation will be smoothed as all the different modulation powers level to an averaged modulation power. And even with an uncertainty of roughly 0.15 mm in mind, the studies of Baumann et al.(2019) show, that the difference of 0.15 mm in the modulation power has only a small effect (0.5% - 1% difference) on the dose distribution of the calculated patient dose distribution.

In a next step, the model can be used to analyse patient CTs and indicate the dependency of the modulation power on the breathing phase by analysing 4D-CT data sets. To further reduce the large uncertainties of the BP measurement, the model can be tested for proton fields in comparison to single BP spots as it was done in this study. An extended field would average the modulation power which could lead to a better agreement between the measured data and the calculated values.

With further investigations, the utilization of the model together with analysis of the effect of the BP degradation on patient treatment plans as done by Baumann et al.(2019) or even the incorporation of the degradation effect in the treatment planning software as proposed by Winter et al.(2020) could help estimate the effects in a worst-case scenario and allow a more robust planning.

## 5. Conclusion

In this study, a novel method to analyse the CT histograms of porous materials to derive the modulation power  $P_{\text{mod}}$ , which describes a measure of the effect of the Bragg peak degradation by porous materials is presented. The mathematical derivation of a

(CT-) measurement of a heterogeneous material with a defined resolution is combined with the definition of the modulation power. This model was then tested on eight heterogeneous materials. Although the model based on the CT histograms is very basic it gives a good indication of the modulation power with a set-up available in every clinic. For heterogeneous materials, the model correctly estimated the modulation power within  $\pm 0.05$  mm.

In a second step, the model was then transferred to frozen porcine lung samples. In this case, both, the measurement of the modulation power and the calculation via the model showed an agreement within larger uncertainties. Most points were within  $\pm 0.1$  mm of the measured value and all within  $\pm 0.15$  mm for measured modulation powers ranging from 0.06 mm up to 0.6 mm. This validates that a translation to clinical data sets can be performed, allowing in a next step the estimation of the modulation power for clinically available patient data.

In conclusion, this work allows an estimation of the modulating effect of the material or tissue in question by analysing the CT histogram obtained with a common clinical CT scanner. This is one of the uncertainties which has to be addressed for a high precision particle therapy of lung carcinomas.

### **Acknowledgement**

The project was supported by the Federal Ministry of Education and Research within the scope of the grant “Physikalische Modellierung für die individualisierte Partikel-Strahlentherapie und Magnetresonanztomographie”, (MiPS, grant number 13FH726IX6). The experiments at MIT were supported by the Hessian state government.

## REFERENCES

21

## References

- Baumann, K.-S., Flatten, V., Weber, U., Lautenschläger, S., Eberle, F., Zink, K. and Engenhart-Cabillic, R. (2019). Effects of the Bragg peak degradation due to lung tissue in proton therapy of lung cancer patients, *Radiation Oncology* **14**(1): 1–15.
- Baumann, K.-S., Witt, M., Weber, U., Engenhart-Cabillic, R. and Zink, K. (2017). An efficient method to predict and include Bragg curve degradation due to lung-equivalent materials in Monte Carlo codes by applying a density modulation, *Physics in Medicine & Biology* **62**(10): 3997.
- Bech, M., Tapfer, A., Velroyen, A., Yaroshenko, A., Pauwels, B., Hostens, J., Bruyndonckx, P., Sasov, A. and Pfeiffer, F. (2013). In-vivo dark-field and phase-contrast x-ray imaging, *Scientific reports* **3**(1): 1–3.
- Bert, C. and Durante, M. (2011). Motion in radiotherapy: particle therapy, *Physics in Medicine & Biology* **56**(16): R113.
- Bradley, J. D., Paulus, R., Komaki, R., Masters, G., Blumenschein, G., Schild, S., Bogart, J., Hu, C., Forster, K., Magliocco, A. et al. (2015). Standard-dose versus high-dose conformal radiotherapy with concurrent and consolidation carboplatin plus paclitaxel with or without cetuximab for patients with stage IIIA or IIIB non-small-cell lung cancer (RTOG 0617): a randomised, two-by-two factorial phase 3 study, *The lancet oncology* **16**(2): 187–199.
- Braig, E.-M., Pfeiffer, D., Willner, M., Sellerer, T., Taphorn, K., Petrich, C., Scholz, J., Petzold, L., Birnbacher, L., Dierolf, M. et al. (2020). Single spectrum three-material decomposition with grating-based x-ray phase-contrast CT, *Physics in Medicine & Biology* **65**(18): 185011.
- Burg, J. M., Flatten, V., Weber, U., Engenhart-Cabillic, R., Vorwerk, H., Zink, K. and

## REFERENCES

22

- Baumann, K.-S. (2021). Experimental determination of modulation power of lung tissue for particle therapy, *Submitted to Physics in Medicine & Biology* .
- Chang, J., Zhang, X., Wang, X., Kang, Y., Riley, B., Bilton, S., Mohan, R., Komaki, R. and Cox, J. (2006). Significant reduction of normal tissue dose by proton radiotherapy compared with three-dimensional conformal or intensity-modulated radiation therapy in Stage I or Stage III non-small-cell lung cancer , *International Journal of Radiation Oncology Biology Physics* **65**(4): 1087–1096.
- De Ruysscher, D., Sterpin, E., Haustermans, K. and Depuydt, T. (2015). Tumour movement in proton therapy: solutions and remaining questions: a review, *Cancers* **7**(3): 1143–1153.
- Desplanques, M., Tagaste, B., Fontana, G., Pella, A., Riboldi, M., Fattori, G., Donno, A., Baroni, G. and Orecchia, R. (2013). A comparative study between the imaging system and the optical tracking system in proton therapy at CNAO, *Journal of radiation research* **54**(suppl.1): i129–i135.
- Ebner, D. K., Tsuji, H., Yasuda, S., Yamamoto, N., Mori, S. and Kamada, T. (2017). Respiration-gated fast-rescanning carbon-ion radiotherapy, *Japanese journal of clinical oncology* **47**(1): 80–83.
- España, S. and Paganetti, H. (2011). Uncertainties in planned dose due to the limited voxel size of the planning ct when treating lung tumors with proton therapy, *Physics in Medicine & Biology* **56**(13): 3843.
- Flatten, V., Baumann, K.-S., Weber, U., Engenhardt-Cabillic, R. and Zink, K. (2019). Quantification of the dependencies of the Bragg peak degradation due to lung tissue in proton therapy on a CT-based lung tumor phantom, *Physics in Medicine & Biology* **64**(15): 155005.

## REFERENCES

23

- Gjyshi, O. and Liao, Z. (2020). Proton therapy for locally advanced non-small cell lung cancer, *The British journal of radiology* **93**(1107): 20190378.
- Grün, R., Friedrich, T., Krämer, M., Zink, K., Durante, M., Engenhart-Cabillic, R. and Scholz, M. (2015). Assessment of potential advantages of relevant ions for particle therapy: a model based study, *Medical physics* **42**(2): 1037–1047.
- Hranek, A., Resch, A. F., Georg, D. and Knaeusl, B. (2020). Investigation of the Bragg peak degradation caused by homogeneous and heterogeneous lung tissue substitutes: proton beam experiments and comparison to current clinical dose calculation, *Physics in Medicine & Biology* **65**(24): 245036.
- Lu, H.-M., Brett, R., Sharp, G., Safai, S., Jiang, S., Flanz, J. and Kooy, H. (2007). A respiratory-gated treatment system for proton therapy, *Medical physics* **34**(8): 3273–3278.
- McNamara, A., Willers, H. and Paganetti, H. (2020). Modelling variable proton relative biological effectiveness for treatment planning, *The British journal of radiology* **93**(1107): 20190334.
- Meijers, A., Seller, O. C., Free, J., Bondesson, D., Oria, C. S., Rabe, M., Parodi, K., Landry, G., Langendijk, J., Both, S. et al. (2020). Assessment of range uncertainty in lung-like tissue using a porcine lung phantom and proton radiography, *Physics in Medicine & Biology* **65**(15): 155014.
- Paganetti, H., Niemierko, A., Ancukiewicz, M., Gerweck, L. E., Goitein, M., Loeffler, J. S. and Suit, H. D. (2002). Relative biological effectiveness (RBE) values for proton beam therapy, *International Journal of Radiation Oncology\* Biology\* Physics* **53**(2): 407–421.
- Ringbæk, T. P., Santiago, A., Grzanka, L., Baumann, K., Flatten, V., Engenhart-Cabillic, R., Bassler, N., Zink, K. and Weber, U. (2020). Calculation of the beam-



## REFERENCES

- modulation effect of the lung in carbon ion and proton therapy with deterministic pencil beam algorithms, *Frontiers in Physics* **8**: 520.
- Ringbaek, T. P., Simeonov, Y., Witt, M., Engenhardt-Cabillic, R., Kraft, G., Zink, K. and Weber, U. (2017). Modulation power of porous materials and usage as ripple filter in particle therapy, *Physics in Medicine and Biology* .
- Sawakuchi, G., Titt, U., Mirkovic, D. and Mohan, R. (2008). Density heterogeneities and the influence of multiple Coulomb and nuclear scatterings on the Bragg peak distal edge of proton therapy beams, *Physics in Medicine and Biology* **53**(17): 4605–19.
- Schneider, U., Pedroni, E. and Lomax, A. (1996). The calibration of CT Hounsfield units for radiotherapy treatment planning, *Physics in Medicine and Biology* **41**(1): 111.
- Simeonov, Y., Weber, U., Penchev, P., Ringbæk, T. P., Schuy, C., Brons, S., Engenhardt-Cabillic, R., Bliedtner, J. and Zink, K. (2017). 3D range-modulator for scanned particle therapy: development, Monte Carlo simulations and experimental evaluation, *Physics in Medicine & Biology* **62**(17): 7075.
- Sørensen, B. S., Bassler, N., Nielsen, S., Horsman, M. R., Grzanka, L., Spejlborg, H., Swakoń, J., Olko, P. and Overgaard, J. (2017). Relative biological effectiveness (RBE) and distal edge effects of proton radiation on early damage in vivo, *Acta Oncologica* **56**(11): 1387–1391.
- Titt, U., Sell, M., Unkelbach, J., Bangert, M., Mirkovic, D., Oelfke, U. and Mohan, R. (2015). Degradation of proton depth dose distribution attributable to microstructures in lung-equivalent material, *Medical Physics* **42**(11): 6425.
- Urie, M., Goitein, M., Holley, W. and Chen, G. (1986). Degradation of the Bragg peak due to inhomogeneities, *Physics in Medicine and Biology* **31**(1).
- Verdun, F., Racine, D., Ott, J., Tapiovaara, M., Toroi, P., Bochud, F., Veldkamp, W., Schegerer, A., Bouwman, R., Giron, I. H., Marshall, N. and Edyvean, S. (2015).

## REFERENCES

25

- Image quality in CT: From physical measurements to model observers, *Physica Medica* **31**(8): 823 – 843.
- Willer, K., Fingerle, A., Noichl, W., De Marco, F., Frank, M., Urban, T., Schick, R., Gustschin, A., Gleich, B., Herzen, J., Koehler, T., Yaroshenko, A., Pralow, T., Zimmermann, G., Renger, B., Sauter, A., Pfeiffer, D., Makowski, M., Rummeny, E., Grenier, P. and Pfeiffer, F. (2021). X-ray Dark-Field Chest Imaging can Detect and Quantify Emphy-sema in COPD Patients, *medRxiv* .
- Willers, H., Allen, A., Grosshans, D., McMahon, S. J., von Neubeck, C., Wiese, C. and Vikram, B. (2018). Toward A variable RBE for proton beam therapy, *Radiotherapy and Oncology* **128**(1): 68–75.
- Winter, J., Ellerbrock, M., Jäkel, O., Greilich, S. and Bangert, M. (2020). Analytical modeling of depth-dose degradation in heterogeneous lung tissue for intensity-modulated proton therapy planning, *Physics and Imaging in Radiation Oncology* **14**: 32–38.
- Witt, M., Weber, U., Simeonov, Y. and Zink, K. (2015). SU-E-T-671: Range-Modulation Effects of Carbon Ion Beams in Lung Tissue, *Medical Physics* **42**(6): 3491–3491.

## REFERENCES

26

## Appendix - Mathematical Model

The following steps describe the substitution that was mentioned in the *Mathematical description of the modulating effect*, allowing to reproduce the derivation of the model without interfering the reading. Starting at equation 3, the steps to obtain equation 4 and 5 are described.

Transferring k-space to CT values is performed via a substitution on the binomial distribution or on the differential form of the normal distribution:

$$F(k|\mu^*, \sigma^{*2}) = \frac{1}{\sqrt{2\pi\sigma^{*2}}} \int_{-\infty}^k \exp\left(-\frac{1}{2}\left(\frac{t-\mu^*}{\sigma^*}\right)^2\right) dt \quad (8)$$

The substitution takes advantage of the assumptions made before ( $\Delta CT = HU_{\max} - HU_{\min} = 0 - (-1000)HU$  and  $\Delta k = k_{\max} - k_{\min} = n - 0$ ). Thus, the substitution can be defined and simplified as :

$$CT := \frac{\Delta CT}{\Delta k} \cdot k + HU_{\min} = 1000HU \frac{k}{n} - 1000HU \quad (9)$$

This gives the new substitution variable  $z$ :

$$z := \frac{1000HU \cdot t}{n} - 1000HU \rightarrow \frac{dt}{dz} dz := \frac{n}{1000HU} \quad (10)$$

Thus, the substitution is performed:

$$\begin{aligned} F(k|\mu^*, \sigma^{*2}) &= \frac{1}{\sqrt{2\pi\sigma^{*2}}} \int_{-\infty}^k \exp\left(-\frac{1}{2}\left(\frac{t-\mu^*}{\sigma^*}\right)^2\right) dt \\ &= \frac{1}{\sqrt{2\pi(1000 \cdot \sigma^*/n)^2}} \int_{-\infty}^{1000\frac{k}{n}} \exp\left(-\frac{1}{2}\left(\frac{nz/1000 - \mu^*}{\sigma^*}\right)^2\right) dz \\ &= F(CT|\mu, \sigma^2) \end{aligned} \quad (11)$$

1  
2  
3 *REFERENCES*

27

4  
5 With new parameters:

6  
7  
8 
$$\mu := 1000\text{HU} \cdot \mu^*/n - 1000\text{HU} = 1000\text{HU} \cdot (p - 1) \quad (12)$$

9  
10  
11  
12 
$$\sigma^2 := (1000\text{HU})^2 \sigma^{*2}/n^2 = (1000\text{HU})^2 \cdot p(1 - p)/n \quad (13)$$

13  
14  
15  
16 **Appendix - Impact of CT parameters on the width of the histogram**

17  
18  
19 As the model is based on the width of the CT histogram, it is essential to know what  
20  
21 influences the measured width.

22  
23 Taking a CT image of a sample is a measurement process which is associated with noise.

24  
25 The actually measured histogram width  $\sigma_{measured}$  in terms of HU is given by:

26  
27  
28  
29 
$$\sigma_{measured} = \sqrt{\sigma_{sample}^2 + \sigma_{noise}^2} \Rightarrow \sigma_{sample} = \sqrt{\sigma_{measured}^2 - \sigma_{noise}^2} \quad (14)$$

30  
31  
32  
33 as the noise of the measurement can be described by a normal distribution, too.  $\sigma_{noise}$   
34  
35 depends on the specific CT parameter set-up, especially the exposure.

36  
37 To understand the dependencies on  $\sigma_{noise}$ , a series of CT measurements was taken. The  
38  
39 factors that primarily influence the width are described by Verdun et al. (2015). Major  
40  
41 factors like the CT itself, the chosen tube voltage, the filter kernel, the x-ray beam  
42  
43 collimation and the interpolation algorithm, were kept constant as a change for these  
44  
45 parameters obviously leads to a change in the HU scale and thus the histogram width.

46  
47 Also dose sparing techniques like a modulated exposure rate or improved reconstruction  
48  
49 algorithms were not used as these would influence the width entailing a more extensive  
50  
51 analysis.  
52  
53

54  
55 The characterization scans were taken for a number of different combinations of exposure  
56  
57 (mAs), slice thickness ( $\Delta z$ ) and spatial resolution ( $\Delta x/\Delta y$ ) given in table 5. Beam  
58  
59  
60

## REFERENCES

28

Attenuation			Exposure	Number of	Slice thickness	spatial resolution	$E_{\text{eff}}$
low	med	high	$E_{\text{total}}$ [mAs]	slices $N$	$\Delta z$ [mm]	$\Delta x/\Delta y$ [mm]	[mAs]
x	x	x	50	664	0.6	1.0	0.08
x	x	x	200	664	0.6	1.0	0.30
x	x	x	574	664	0.6	1.0	0.86
x	x		722	512	0.6	1.0	1.41
x	x		722	512	0.6	1.5	1.41
x	x		722	512	0.6	0.6	1.41
x	x		700	213	1	1.0	3.29
x	x		700	142	1.5	1.0	4.93
x	x		700	142	1.5	1.0	4.93
x	x		700	71	3	1.0	9.86
x	x		700	355	0.6	1.0	1.97
x	x		700	355	0.6	1.0	1.97
x	x		700	357	0.6	1.0	1.96

**Table 2.** CT configurations for the characterization measurements. For the three different attenuation set-ups, the applied exposure  $E_{\text{total}}$ , the number of slices  $N$ , the slice thickness  $\Delta z$ , the reconstructed spatial resolution  $\Delta x/\Delta y$  and the effective exposure  $E_{\text{eff}}$  (see equation 15) are given. All measurements were performed with the Somatom Confidence and the Br43s kernel. The attenuation set-ups correspond to figure 3. The results are displayed in figure 8.

hardening was investigated by adding additional absorbing material (PMMA) around the sample, as shown in figure 3(a). In most characterization scans, water was the sample medium. However, some scans were also performed with the LN-300 lung substitute (Gammex) to validate the effects with a modulating material (Ringbaek et al.; 2017).

Figure 8 shows that width of the HU histogram is changed via three different parameters: the applied exposure ( $E_{\text{total}}$  in mAs) in combination with the length of the CT scan ( $N_{\text{slices}} \cdot \Delta z$ ) and for phantom measurements, the surrounding material. It was found that the slice thickness and the exposure in terms of the so called 'effective exposure' (Verdun et al.; 2015) had a significant effect on the width of the HU histogram for the scanned water sample. As there is no easy way to obtain a measure for the attenuating material for clinical CTs, the parameter was not included in the effective

## REFERENCES

29

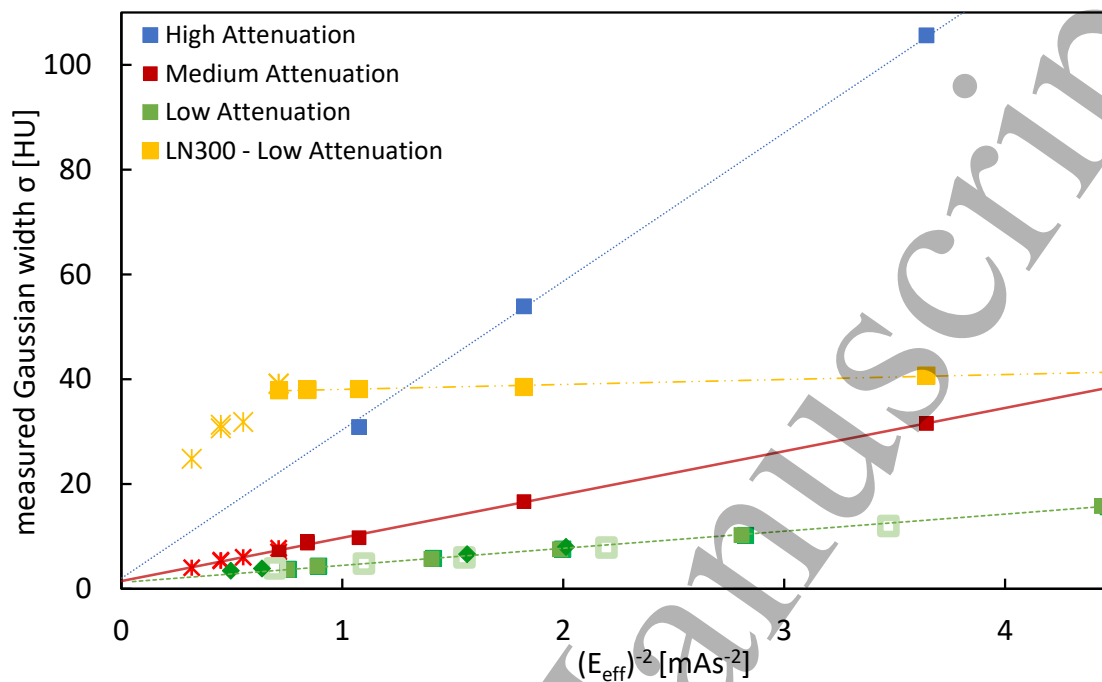


**Figure 8.** Width of the fitted normal distribution of the HU histogram for various different settings in dependency of the inverse square root of the effective exposure (relation from Verdun et al.(2015)). The data is divided into four main measurement set-ups: the high attenuated set-up with water as sample (blue), the medium (red) and the low attenuated set-up (green), both with water as sample and a series with the low attenuating set-up and LN-300 as sample (yellow) (corresponding to figure 3a). Diamond (reconstructed spatial resolution  $\Delta x = 1$  mm; slice thickness  $\Delta z = 3$  mm) and square (filled:  $\Delta x = 1$  mm;  $\Delta z = 0.6$  mm) (hollow:  $\Delta x = 0.6$  mm;  $\Delta z = 0.6$  mm) data points indicate a measurement series where the applied exposure  $E_{total}$  was changed. Crosses show series where the slice thickness was changed and the applied exposure was held constant.

exposure but analysed separately. Thus, the effective exposure  $E_{eff}$  was calculated via

$$E_{eff} = \frac{E_{total}}{N_{slices}} \quad (15)$$

Figure 8 shows a clear dependence of the widths  $\sigma$  of the histograms on the effective exposure and the attenuating material. A higher attenuation (blue squares in figure 8) leads to a lower signal measurement and thus a higher poisson noise  $\sigma_{noise}$ .

For the modulating material LN-300 (Ringbaek et al.; 2017; Hranek et al.; 2020), however, the data shows a different dependency: The effects of a change in slice thickness

*REFERENCES*

30

1  
2  
3  
4  
5 vary drastically in comparison to effects of a change in the applied exposure  $E_{\text{total}}$ . This  
6  
7 supports the mathematical model, where the proportionality factor is specific for the  
8  
9 resolution which is given by the analysed slice thickness. After the calibration,  $\sigma_{\text{noise}}$   
10  
11 is approached by including a reference material next to the sample as shown in figure  
12  
13 3(b). This enables to specifically calculate  $\sigma_{\text{noise}}$  via equation 14. All other changes in  
14  
15 parameters had only a minor effect. Thus, they were neglected in the further analysis  
16  
17 with negligible impact on the uncertainty.  
18  
19  
20  
21  
22  
23  
24  
25  
26  
27  
28  
29  
30  
31  
32  
33  
34  
35  
36  
37  
38  
39  
40  
41  
42  
43  
44  
45  
46  
47  
48  
49  
50  
51  
52  
53  
54  
55  
56  
57  
58  
59  
60

# A phantom based evaluation of the dose prediction and effects in treatment plans, when calculating on a direct density CT reconstruction

Veronika Flatten<sup>1,2</sup> | Alexandra Friedrich<sup>2,3</sup> | Rita Engenhardt-Cabillic<sup>1,4</sup> | Klemens Zink<sup>1,2,4</sup>

<sup>1</sup>Department of Radiotherapy and Radiooncology, University Medical Center Giessen-Marburg, Marburg, Germany

<sup>2</sup>Institute of Medical Physics and Radiation Protection, University of Applied Sciences, Giessen, Germany

<sup>3</sup>Department of Radiotherapy, RNS Gemeinschaftspraxis, Wiesbaden, Germany

<sup>4</sup>MIT, Marburg Ion Beam Therapy Center, Marburg, Germany

Author to whom correspondence should be addressed. Veronika Flatten  
E-Mail: flatten@staff.uni-marburg.de

## Abstract

In radiation therapy, a Computed Tomography (CT) image is needed for an accurate dose calculation. To allow such a calculation, the CT image values have to be converted into relative electron densities. Thus, standard procedure is to calibrate the CT numbers to relative electron density (RED) by using a phantom with known composition inserts. This calibration curve is energy and CT dependent, therefore most radiotherapy CT acquisitions are obtained with 120 kVp, as each tube voltage needs an additional calibration curve. The commercially available DirectDensity™ (DD) reconstruction algorithm presents a reconstruction implementation without any dependence on the tube voltage. In comparison, it allows a calibration curve that is directly proportional to the RED, reducing the need of more than one calibration curve. This could potentially optimize CT acquisitions and reducing the dose given to the patient. Three different phantoms were used to evaluate the DirectDensity™ algorithm in simple and anthropomorphic geometries, as well as setups with metal implants. Scans with the DD algorithm were performed for 80, 100, 120, and 140 kVp. As reference a scan with the standard 120 kVp scan was used. Radiotherapy photon plans were optimized and calculated on the reference image and then transferred to the DD images, where they were recalculated. The dose distributions obtained this way were compared to the reference dose. Differences were found mainly in pure air and high density materials such as bones. The difference of the mean dose was below 0.7%, in most cases below 0.4%. No indication was found that the algorithm is corrupted by metal inserts, enabling the application for all clinical cases. This algorithm offers more variability in CT parameters for radiation therapy and thus a more personalized image acquisition with a high image quality and a lower dose exposure at a robust clinical workflow.

## KEY WORDS

CT reconstruction algorithm, DirectDensity, electron density reconstruction, image reconstruction

This is an open access article under the terms of the Creative Commons Attribution License, which permits use, distribution and reproduction in any medium, provided the original work is properly cited.

© 2020 The Authors. *Journal of Applied Clinical Medical Physics* published by Wiley Periodicals, Inc. on behalf of American Association of Physicists in Medicine.



## 1 | INTRODUCTION

In radiation therapy, the Computed Tomography (CT) images provide the essential patient geometry and electron density information needed not only to delineate the tumor and organs at risk but also to calculate dose. Beforehand, a relation between CT numbers and relative electron density (RED) or mass density (MD) has to be established in the form of a calibration curve in the treatment planning system (TPS) as described by e.g., Schneider et al.<sup>1</sup>. In the common case, the CT pixel values are given in Hounsfield units (HU) and depend on the tube voltage. Thus, a calibration curve for each tube voltage is needed.<sup>1,2</sup> Some clinics feature more than the standard 120 kVp calibration curve e.g., an additional 80 kVp curve for pediatric patients. This potentially reduces the CT dose for the patient or offers a higher contrast-to-noise ratio but increases the amount of work while the workflow robustness is decreased by the additional selection of the calibration curves. Other clinics only implement the standard 120 kVp curve for all scans ignoring the potential benefit of a higher signal-to-noise ratio or a decreased dose exposure that could be achieved with an optimized tube voltage.<sup>3-5</sup>

The commercially available reconstruction algorithm ‘DirectDensity’ (DD) (Siemens Healthcare, Erlangen, Germany) promises a feasible workflow as it constructs the RED information directly from the raw CT data.<sup>6</sup> DD-CT images obtained this way are independent of the tube voltage once the calibration curve is implemented in the TPS.

Van der Heyden showed in a patient study for 33 patients that the mean dose difference between HU based dose calculated plans and those calculated on the DD image sets were found to be smaller than 1%.<sup>7</sup> In this study, the relative mean dose difference was evaluated for the planning target volume (PTV) and the organs at risk (OAR), as well as the relative difference in the volume receiving 95% of the prescribed dose were evaluated. These differences were also found to be less than 1%. These results are in agreement with the evaluation presented by Ritter.<sup>6</sup> Nevertheless, both works do not differentiate for cases that provide high uncertainties in imaging and dose calculation, such as air or metal cavities.

The present study analyzes the effect of the DD images on the dose distributions for a phantom with materials with high, medium and low density, exemplary for the density range present in the human body. As analyzing tools, a simple dose difference is accompanied by dose profiles, allowing a distinct analysis where the differences occur.

Additionally, CT scans with metal implants are compared as well as the combination of the DD algorithm with a metal reduction algorithm,<sup>8</sup> to evaluate if DD can be used in all clinical cases. Otherwise, for metal implants a standard conversion curve would be needed, revoking the easy setup and robust usability when implementing the DD algorithm.

Finally, the potential CT dose reduction benefits that could be utilized when dose acquisition parameters (e.g., the tube voltage) are optimized for image quality, are presented.

## 2 | MATERIALS AND METHODS

### 2.A | DirectDensity reconstruction

To understand the procedure behind the DirectDensity images and understand problematic setups and cases, a brief introduction of the algorithm is given. A more detailed description is given by Ritter.<sup>6</sup>

Figure 1 describes the main steps in the algorithm. First, a single energy CT image ( $I$ ) is needed for the DirectDensity reconstruction. By applying an attenuation threshold ( $I_S$ ), a bone image ( $I_B$ ) is generated. In the projection plane, a model based material decomposition is applied to the original sinogram ( $S_\mu$ ), separating all materials present in the human body into either water or bone. With an underlying physical attenuation model, the effective water thickness ( $d_W$ ) for all materials can be obtained. The combination of the effective bone thickness ( $d_B$ ) gained from the information of the bone sinogram ( $S_B$ ) and the effective water thickness ( $d_W$ ) together with the RED of water and bone gives an electron density line integral ( $S_{RED}$ ). Thus, in a final step a RED proportional image ( $I_{DD}$ ) via filtered back projection of the RED sinogram is gained.

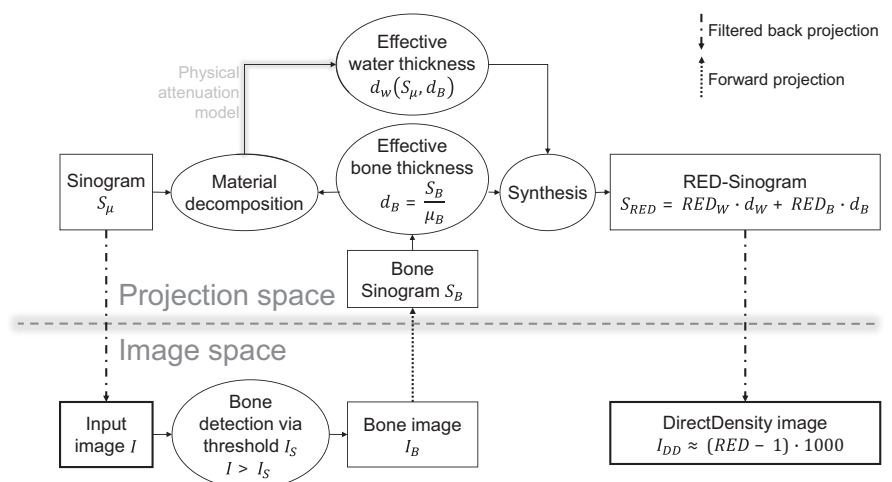


**FIG. 1.** A flowchart Ritter<sup>6</sup> that displays the main steps of the DirectDensity algorithm. The steps can be divided in the ones taking place in the image space and the ones performed in the projection space.

The connection between the image values of the final DD image and the RED is given in eq. (1).<sup>6</sup>

$$I_{DD} \approx (RED - 1) * 1000 \Rightarrow I_{DD} = \underbrace{(RED - 0.994) * 1000}_{\text{Implemented calibration in this work}} \quad (1)$$

## 2.B | Density calibration

To obtain the RED information from the CT scan, calibration curves for 80, 100, 120, and 140 kVp tube voltage were generated with the Gammex 467 Tissue Characterization Phantom (Gammex, Giesse-Allendorf, Germany) for the HU and the DD reconstruction. All scans were taken with a constant tube current of 250 mAs on the SOMATOM Confidence (Siemens Healthcare, Erlangen, Germany). The reconstruction with 3 mm slice thickness was executed with the B40s and E30s convolution filters. For the calibration, the mean CT value of each tissue mimicking insert was plotted against the RED of the material. The mean CT value for each insert was obtained in ImageJ (v1.50i, National Institutes of Health, Bethesda, USA). The CT values were averaged over a sphere of 2 cm diameter, centered in the middle of the insert. As the calibration curves in Fig. 2 show, the energy dependence vanishes when the DD reconstruction is applied. The right panel displays this implemented calibration given in eq. (1).

## 2.C | Study setup

All phantoms displayed in Fig. 3 were scanned with the SOMATOM Confidence CT. In general, images for 80, 100, 120 kVp, as well as 140 kVp were generated for the E30s (DD) kernel. The reference images (HU) were done with 120 kVp and the B40s kernel, as this represents the standard parameters in the clinical routine. The tube current was set between 140 and 300 mAs, depending on the thickness of the phantom, but held constant for each phantom. Slices of

3 mm thickness were acquired. All scans were imported into Eclipse (version 13.6, Varian Medical Systems, Palo Alto, CA, USA). The contouring was performed on the HU image and then copied to the DD images. The same procedure was followed creating the dose plans: Each plan was optimized and calculated on the 120 kVp HU image and transferred to all DD images. Then, each plan was recalculated holding all beam parameters constant.

The dose was calculated in the TPS Eclipse with the Anisotropic Analytical Algorithm (AAA) (v.13.6.23, Eclipse, Varian Medical Systems, Palo Alto, CA, USA), a 3D pencil beam superposition convolution algorithm. For this algorithm, only RED but not MD needs to be assigned to the CT voxels for a correct dose calculation.<sup>9,10</sup> Thus, the immediate relation between dose and the DD images which contain RED information is evaluated. The dose calculation grid size was chosen to be 0.125 cm.

To compare the different dose distributions, a dose difference between each plan on the DD reconstruction with the HU dose distribution as reference was created. Because the dose distributions were calculated on identically positioned phantom CT scans, which were performed without moving the phantom, the gamma criteria<sup>11</sup> which is typically used is not needed. However, passing rates for the dose differences are presented which equal a gamma analysis with 0 mm distance-to-agreement and 0.5% dose difference in the region with doses higher than 5% of the maximum dose.

Additionally, dose-volume histograms (DVH) were used to evaluate dose distributions in specific regions like the PTV and surrounding OARs as contoured in Fig. 3. For the general evaluation, dose profiles were used to further investigate the effect of high and low density materials on the dose distribution.

### 2.C.1 | Setup for the general DD evaluation

To evaluate the dose distribution in simple geometries a slightly modified version of the planar IMRT phantom Gammex 473

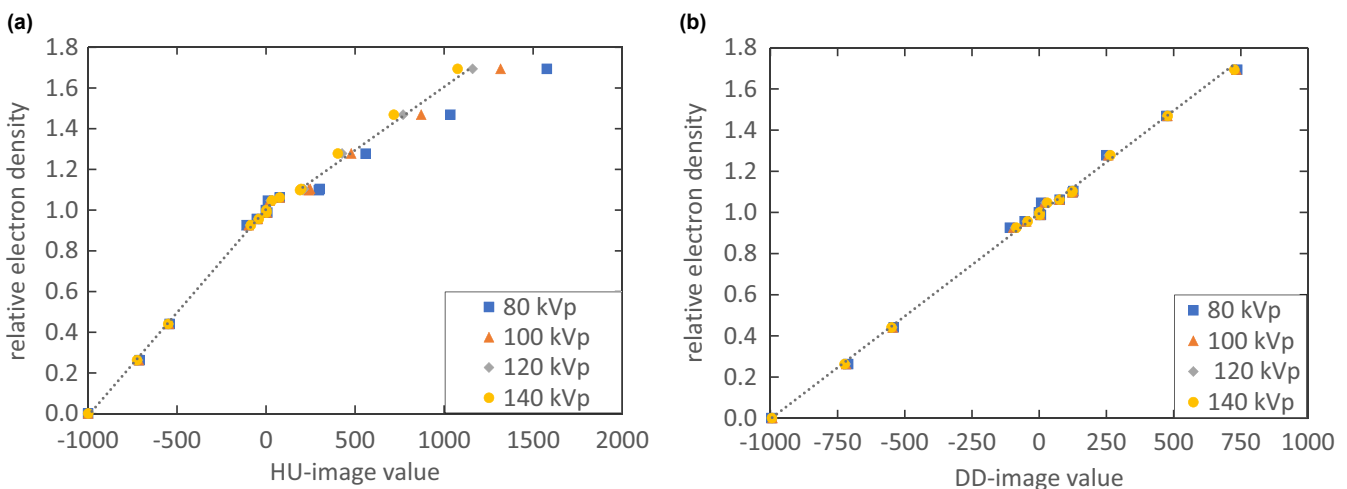


**FIG. 2.** The calibration curves to convert the CT image values into RED for the HU reconstruction (left) and the DD reconstruction (right) for all four tube voltages. The values were obtained with inserts of the Gammex 467 Tissue Characterization Phantom. The dotted linear regression was performed on the 120 kVp data points.

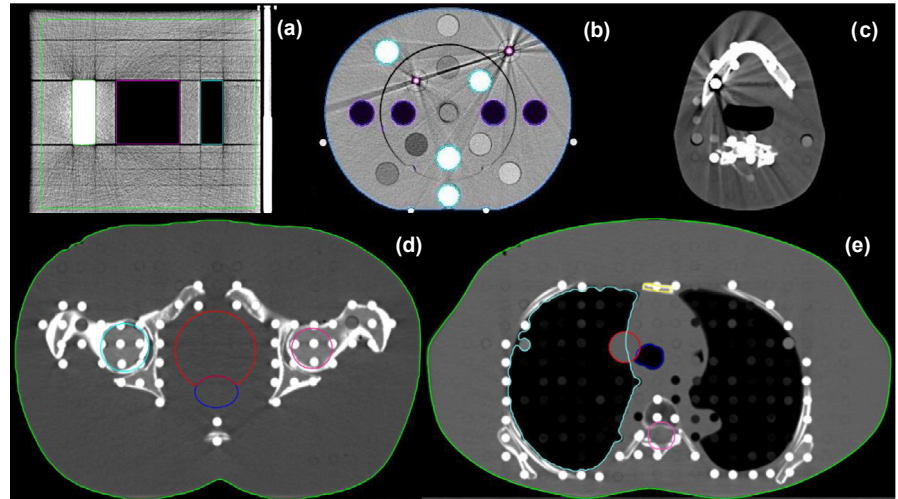


**FIG. 3.** Phantom overview: Panel (a) shows the IMRT phantom in a transverse view. Panel (b) displays the CBCT phantom with its inserts. In panel (c) the metal insert is included in the ART phantom head. Panels (d) and (e) show the ART phantom in a transverse slice in the abdominal and thoracic region.

(Gammex, Giessen-Allendorf, Germany), scanned with 250 mAs, was used. The phantom, consisting of solid water slabs, was extended by a cork as well as two plaster inserts as shown in (a) in Fig. 3. These materials were chosen because the RED of plaster is close to typical bone RED, while the cork RED matches lung density. One cavity was left unfilled to also examine effects in air.

To also evaluate a more realistic setup, the anthropomorph male Alderson Radiation Therapy (ART) Phantom (RSD Radiology Support Devices, Long Beach, USA) was additionally investigated. Scans were conducted for the pelvis (scanned with 250 mAs) and thorax region (scanned with 140 mAs) as presented in part (d) and (e) of Fig. 3.

On the IMRT phantom, a single 6 MV open field was planned in Eclipse with a TrueBeam model (Varian Medical Systems, Palo Alto, CA, USA). The plan was computed on the HU image and then copied to all DD images, whereas the assigned monitor units (MU) were held constant. For the Alderson phantom, a 3D conformal and a volumetric modulated arc therapy (VMAT) plan was optimized for a simulated prostate and lung carcinoma treatment.

**2.C.2 | Setup for metal implants**

One of the main advantages of the implementation of the DD algorithm in the clinic is the reduction from many CT calibration curves to only one. Therefore, the effect of metal implants in combination with the DD reconstruction was tested, as the DD reconstruction could define the metal as high density bone due to the applied threshold. If this is the case, an inadequate interpretation of metal

could wrongfully influence the reconstruction around these implants. For this study, a third phantom was used. The CBCT Electron Density Phantom (CIRS, Norfolk, USA), as shown in (b) in Fig. 3, which is comparable to the Gammex Tissue Characterization Phantom, was chosen. It has the possibility to insert high density materials like titanium and stainless steel next to bone, adipose and lung tissue

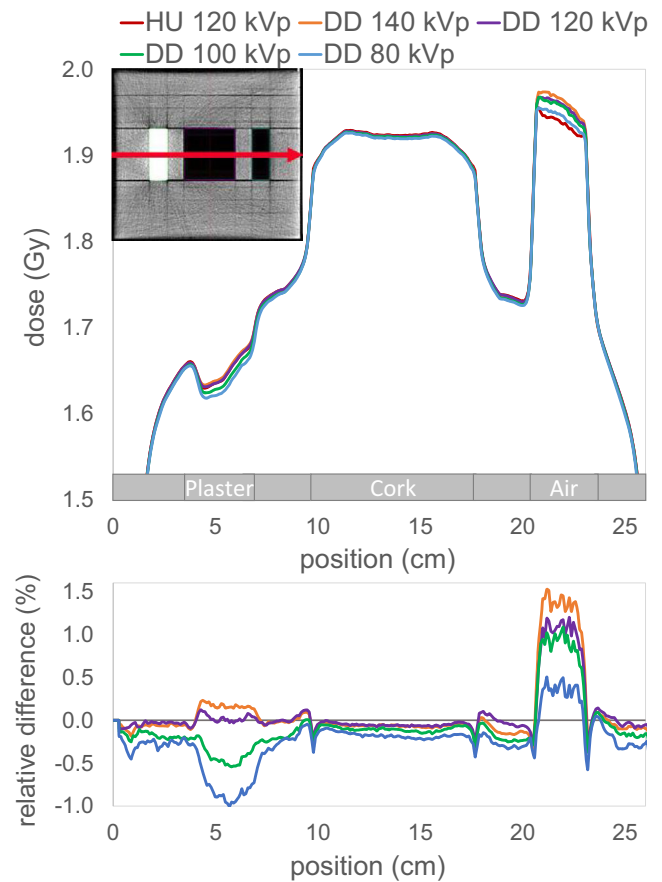


**FIG. 4.** Lateral dose profile along the red line indicated in the upper left corner for the single field irradiated from above for the HU and the four DD reconstructions. The lower plot shows the relative differences of the DD doses compared to the HU dose.

**TABLE 1** Mean RED and its standard deviation for three different materials of the IMRT phantom for all reconstructions.

CT set	RED <sub>Plaster</sub>	RED <sub>Cork</sub>	RED <sub>Air</sub>
HU <sub>120</sub>	1.37 ± 0.01	0.26 ± 0.02	0.04 ± 0.01
DD <sub>80</sub>	1.43 ± 0.06	0.27 ± 0.02	0.03 ± 0.01
DD <sub>100</sub>	1.39 ± 0.02	0.26 ± 0.02	0.03 ± 0.02
DD <sub>120</sub>	1.35 ± 0.03	0.26 ± 0.02	0.02 ± 0.01
DD <sub>140</sub>	1.35 ± 0.01	0.26 ± 0.02	0.02 ± 0.01

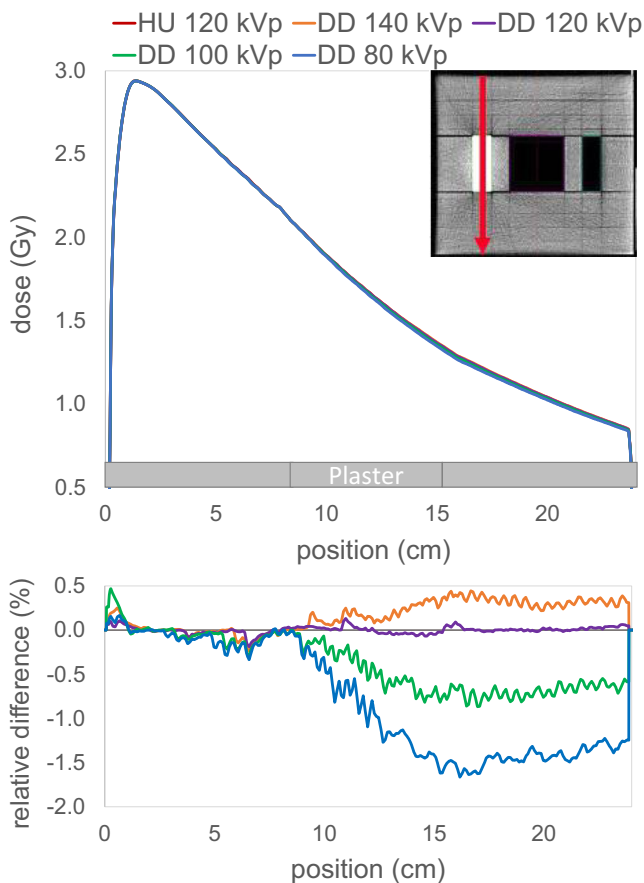


**Fig. 5.** Depth dose curve through solid water and plaster indicated by the red line in the upper right corner for the single field irradiated from above for the HU and the four DD reconstructions. The lower plot shows the relative differences of the DD doses compared to the HU dose.

equivalents. Using this phantom allows unbiased results because it was not used to produce the calibration curve. The scan was performed with 300 mAs.

For a more anthropomorphic setup, the ART head was scanned with and without a brass insert simulating a dental prosthesis at 200 mAs. As differences due to the artifacts induced by metal ought to appear, an additional reconstruction with a metal reduction algorithm (Siemens Healthcare, Erlangen, Germany) was also evaluated. The iterative Metal Artifact Reduction (iMAR) algorithm reduces the artifacts caused by metal implants via beam hardening correction, sinogram inpainting and frequency split<sup>8</sup>. As most dose calculation algorithms have large uncertainties when calculating in metal, only a RED comparison was performed.

All RED estimations were performed with the presented calibration curves limited to a maximum RED of 1.7. Thus differences for higher RED ought to appear.

### 2.C.3 | CARE dose option

To evaluate the possible dose savings when the DD algorithm is implemented, the tube-current as well as the voltage were varied.

The pelvis and thorax of the ART phantom was scanned again using CARE kV and CARE Dose4D (Siemens Healthcare, Erlangen, Germany). The CARE Dose4D algorithm modulates the tube current on the basis of a topogram<sup>12</sup> during the scan to reduce dose exposure while maintaining a high image quality without affecting CT numbers. CARE kV on the other hand suggests a probable tube voltage and regulates the tube current to deliver the same Contrast-to-Noise-Ratio. These CARE options changed the CT parameters in such a way that the patient could potentially benefit from a reduced dose exposure without reducing the image quality.

## 3 | RESULTS

### 3.A | General evaluation of the DirectDensity algorithm

#### 3.A.1 | RED comparison

First, the relative electron density of different materials in the IMRT phantom is compared. As the dose computation relies on the right mapping of the RED, differences in the mean RED will most likely result in dose differences. Table 1 gives the mean RED found in the

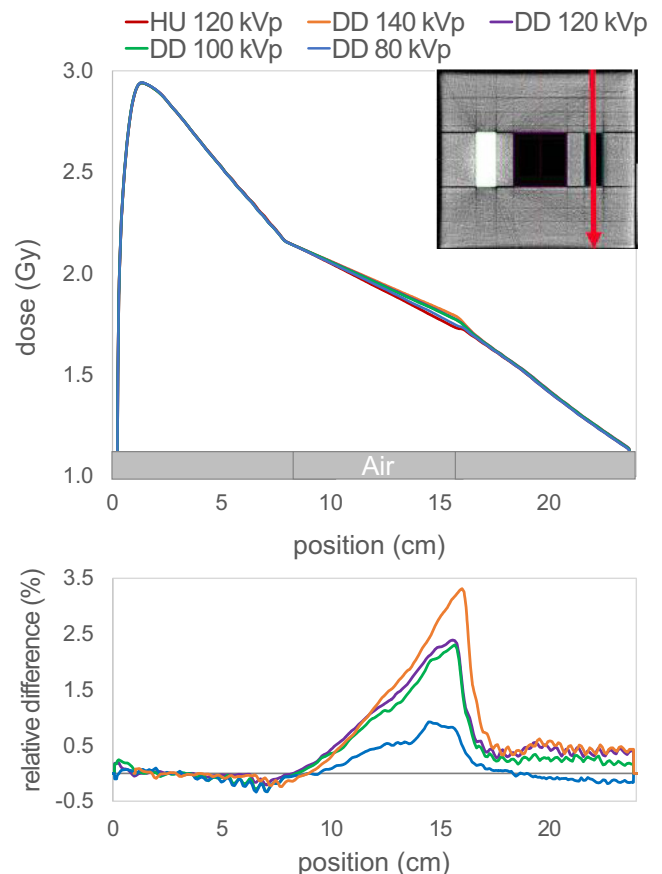


**Fig. 6.** Depth dose curve through solid water and air indicated by the red line in the upper right corner for the single field irradiated from above for the HU and the four DD reconstructions. The lower plot shows the relative differences of the DD doses compared to the HU dose.

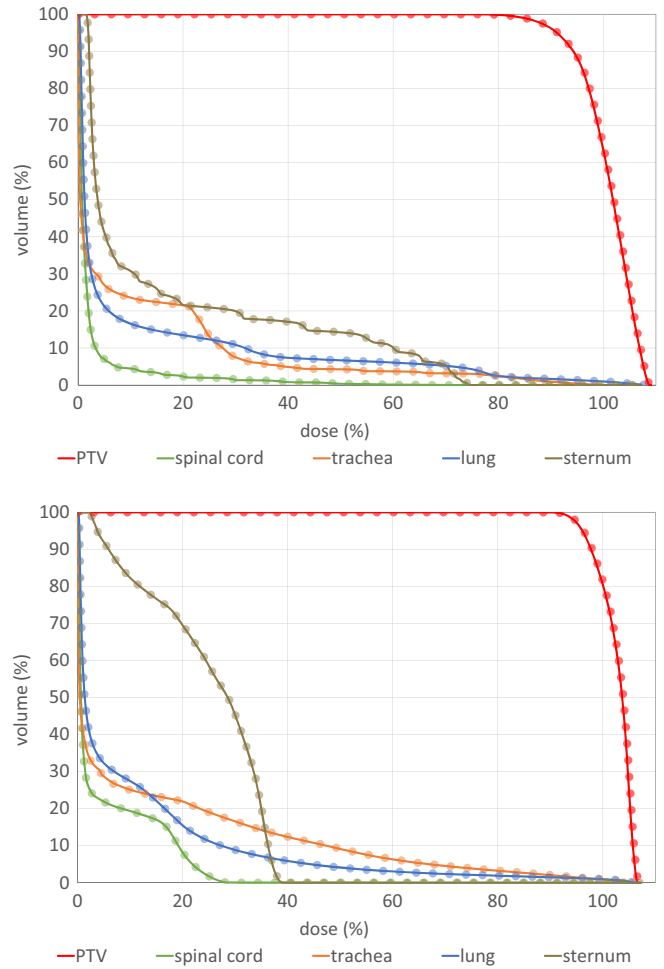
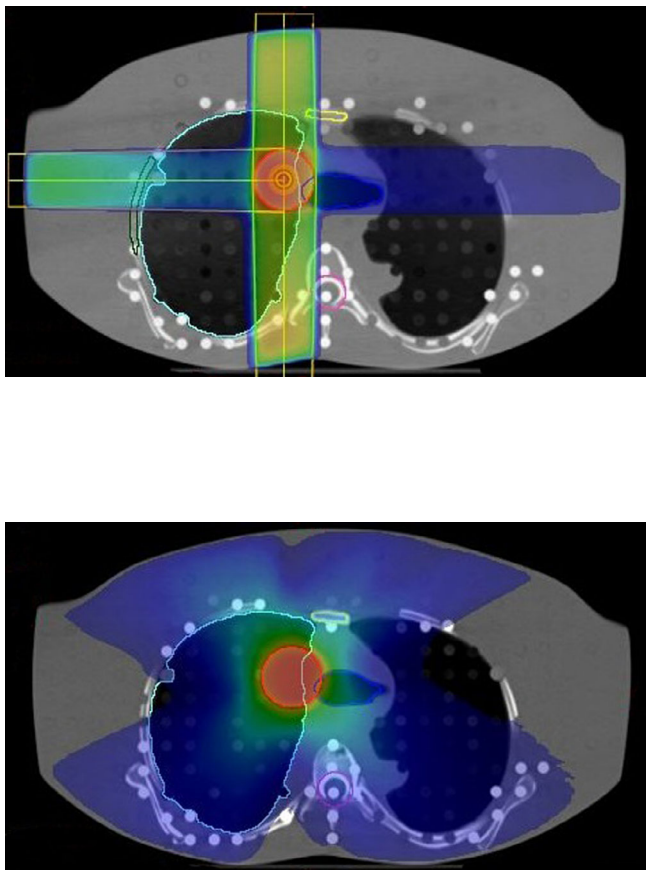


**FIG. 7.** Exemplary traversal slices of the dose distribution on the left and the DHV for the thorax 3D conformal as well as the VMAT plan on the right. The dots in the DVH mark the DD results, while the solid line the HU reference DVH.

different materials of the IMRT phantom with its standard deviation for all CT reconstructions. It can be observed that the assigned RED in the DD cases is higher the lower the tube voltage. Thus, the tube voltage dependence is not completely vanished.

### 3.A.2 | Simple geometry

Figure 4 displays a lateral profile and Figs. 5 and 6 two depth dose curves through the center of the inserts of the IMRT phantom. The maximum dose discrepancy for plaster was  $-1.7\%$  in the  $DD_{80}$  (see Fig. 5) and for air  $+3.3\%$  in the  $DD_{140}$  (see Fig. 6). The dose difference in the depth dose curves for air is resolved beyond the air insert. Whereas after the plaster insert, there is still a noticeable discrepancy in the solid water after the beam traverses the plaster insert.

Despite the differences observed in the depth dose curves, there is a good agreement between the DD dose distribution and the HU reference dose for the evaluation of the 0.5% dose difference with passing rates over 98.3%. Having a closer look at the location of the failed points, it can be noticed that for the lower tube voltages more points in the plaster regions fail, while for the higher tube voltages this shifts to the air region. Because there are two plaster inserts, far

more points for the  $DD_{80}$  fail resulting in a lower passing rate (98.3% in comparison to over 99%).

### 3.A.3 | Anthropomorphic geometry

Figures 7 and 8 show the dose distribution for the 3D conformal and VMAT plans that were optimized on the ART phantom. All DVHs for the HU and the DD dose distributions are displayed next to the transverse slice. In the DVH only minor differences can be observed, e.g., a minimal higher dose in the PTV calculated on the DD images.

The passing rates of the 0.5% dose difference for the anthropomorphic ART phantom, again, show the good agreement between the DD dose distributions when compared to the dose calculated on the HU reconstruction. The VMAT plans show an agreement of over 99.3%, while a slightly lower agreement is found in the 3D-conformal plans (all over 98%). An exception is the 3D-conformal thorax plan, where a large dose is deposited in the trachea leading to passing rates around 90% for 0.5% and over 98% for 1% dose difference.

As the DVH show no visible differences, the mean dose was the point chosen to evaluate. The results are shown in Table 2. In the

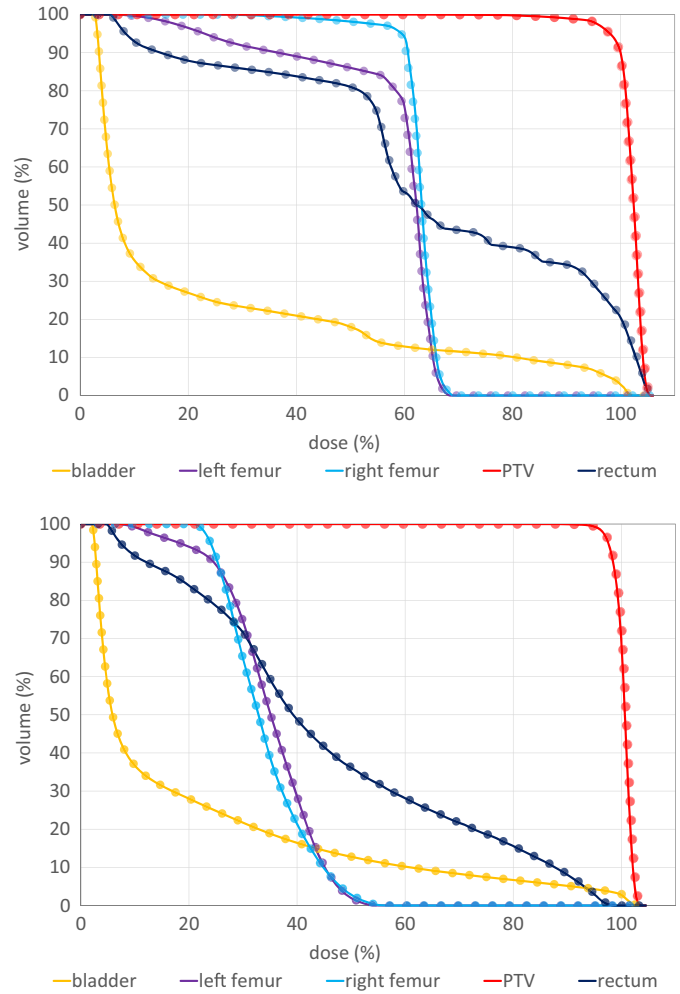
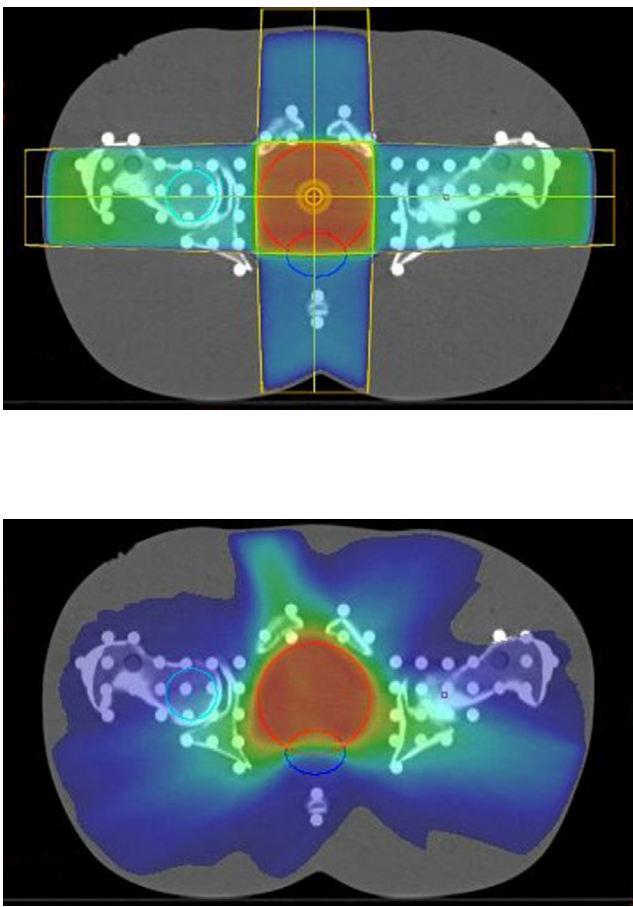


**FIG. 8.** Exemplary traversal slices of the dose distribution on the left panel and the DHV for the pelvis 4-field box as well as the VMAT plan on the right panel. The dots in the DVH mark the DD results, while the solid line the HU reference DVH.

**TABLE 2** Mean discrepancies as well as the minimum and maximum value for the mean dose of each ROI over all DD plans on the ART phantom in the form of “Mean  $\Delta D_{mean}$  [Min  $\Delta D_{mean}$ ; Max  $\Delta D_{mean}$ ]”.

	Mean $\Delta D_{mean}$ (%)	
	3D	VMAT
Thorax		
Trachea	0.7 [0.0; 1.1]	0.0 [0.0; 0.0]
Sternum	0.1 [0.0; 0.6]	0.4 [0.4; 0.4]
PTV	0.2 [0.1; 0.2]	0.3 [0.3; 0.3]
Pelvis		
Femur left	-0.1 [-0.2; 0.0]	0.2 [0.0; 0.3]
Femur right	-0.3 [-0.3; -0.2]	0.0 [0.0; 0.0]
Rectum	0.2 [0.1; 0.3]	0.2 [0.2; 0.2]
PTV	0.0 [-0.1; 0.1]	0.3 [0.2; 0.3]

PTV, planning target volume; ART, alderson radiation therapy; VMAT, volumetric modulated arc therapy.

lung as well as in the bladder, no deviation in the mean dose was found. The largest difference was observed in the trachea for the conformal thorax plan. This is due to two reasons: For one, one of

the three beams aims directly at the trachea leading to a high dose in this region and additionally, the trachea is filled with air. With the results of the IMRT air cavity in mind, a higher dose has to be expected and is observed. Nevertheless, the values in Table 2 are in an order to be negligible.

### 3.B | Effects of metal implants

Table 3 presents the mean RED values for the CBCT inserts gained with the calibration curve obtained without metal inserts (stopping at a RED value of 1.7). For both, the standard reconstruction as well as the DD reconstruction, the RED values agree with the reference given by the manufacturer for materials found in the human body and thus in the range of the calibration curve. For high density bones (or high density materials like teeth), which are not within the range of the calibration curve, a slight difference occurs and for metal, there are severe deviations. However, the differences for titanium (-25% for the HU and between -33% and -8% for the DD reconstruction) and for stainless steel (-59% HU and -64% to -50% for DD) show an equally bad RED determination of metal for all reconstructions. Figures 9 and 10 shows the same effect for the

**TABLE 3** Mean RED values and its standard deviation for the different inserts of the CBCT phantom for all reconstructions.

Insert	Reference	HU <sub>120</sub>	DD <sub>80</sub>	DD <sub>100</sub>	DD <sub>120</sub>	DD <sub>140</sub>
Lung Inhale	0.20	0.22 ± 0.02	0.23 ± 0.05	0.22 ± 0.03	0.22 ± 0.02	0.22 ± 0.02
Lung Exhale	0.50	0.50 ± 0.03	0.50 ± 0.05	0.49 ± 0.02	0.49 ± 0.02	0.49 ± 0.02
Adipose	0.95	0.94 ± 0.03	0.92 ± 0.05	0.93 ± 0.03	0.93 ± 0.02	0.93 ± 0.02
Breast	0.98	0.98 ± 0.02	0.96 ± 0.04	0.97 ± 0.03	0.97 ± 0.02	0.97 ± 0.02
Muscle	1.04	1.03 ± 0.03	1.03 ± 0.04	1.03 ± 0.03	1.04 ± 0.02	1.04 ± 0.02
Liver	1.05	1.04 ± 0.02	1.05 ± 0.04	1.05 ± 0.02	1.05 ± 0.02	1.06 ± 0.02
Bone 200	1.12	1.13 ± 0.03	1.12 ± 0.02	1.12 ± 0.02	1.11 ± 0.01	1.11 ± 0.01
Bone 800	1.46	1.49 ± 0.04	1.48 ± 0.03	1.47 ± 0.02	1.46 ± 0.02	1.46 ± 0.01
Bone 1250	1.70	1.76 ± 0.03	1.80 ± 0.04	1.77 ± 0.03	1.75 ± 0.02	1.74 ± 0.02
Titan	3.74	2.81 ± 0.01	2.51 ± 0.03	2.99 ± 0.05	3.28 ± 0.05	3.45 ± 0.06
Steel	6.92	2.81 ± 0.01	2.50 ± 0.08	2.97 ± 0.13	3.24 ± 0.16	3.41 ± 0.19

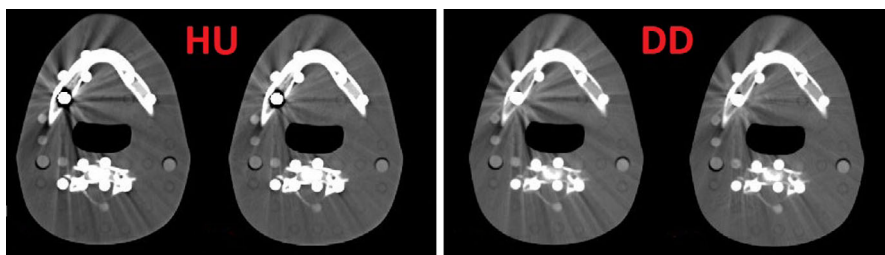


**FIG. 9.** CT images with brass inserts (left on both panels) and the iMAR algorithm (right on both panels) for the HU reconstruction (left panel) and the 120 kVp DD reconstruction (right panel).

brass insert in the ART head phantom, which should have a RED value around 7. In every case, the RED is severely underestimated. Surprisingly, the DD reconstructions show no metal shadow around the insert in comparison to the HU reconstruction. No significant difference can be found between the standard and the iMAR reconstructions.

However, a calibration for high density materials could be added, diverging from the straight line from eq. (1). If this is implemented, CTs with high density materials should only be acquired with one chosen tube voltage as the metal values are not independent of the tube voltage anymore as visible in Table 3 and Fig. 10.

### 3.C | Dose reduction with CARE dose

The use of the CARE kV and CARE Dose4D options allow the CT to acquire a high quality image with a potentially reduced dose exposure by choosing the kV and adapting the mAs to the given situation. While CARE Dose4D can be used with the conventional HU calibration, CARE kV can only be enabled in radiation therapy when the DD algorithm is implemented.

A comparison between the CT parameters estimated during the acquisition with and without the CARE options is given in Table 4. It shows a dose reduction via the reduction in the dose length product

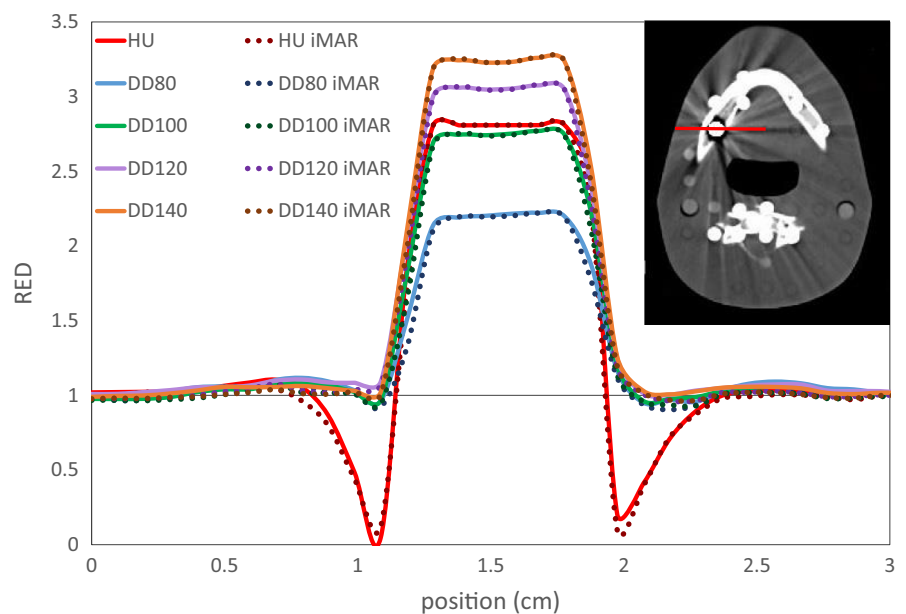


**FIG. 10.** RED line through the brass insert for all reconstructions as presented with the red line on the CT image. The underestimation of the RED values around the metal can only be observed for the HU reconstruction.

**TABLE 4** Comparison of the CT parameters before and after the CT options CARE kV and CARE Dose4D parameter optimization.

	Thorax			Pelvis		
	Routine	Care dose	Care kV	Routine	Care dose	Care kV
Tube voltage (kVp)	120	120	120	120	120	100
Current-time product (mAs)	140	104	103	250	133	223
Dose-length product (mGy-cm)	411	306	303	609	329	321
CTDIvol(32 cm)	11.3	8.4	8.4	20.0	10.8	10.5

CTDI, CT Dose Index.

of 26% for the thorax scan and 46% for the pelvis scan, for the CARE Dose4D option. The pelvis scan chooses a lower voltage when CARE kV is turned on. This does not further reduce the CT dose, however, this might in some cases result in an optimized image without a higher CT Dose Index (CTDI).

The passing rate for the dose difference between the dose calculated on these scans and the HU dose are in the same order of magnitude as all other DD scans. The image quality (see Fig. 11) was found to be sufficient.

## 4 | DISCUSSION

The Siemens DirectDensity™ algorithm was implemented and validated. With a simple phantom, the consistency of the RED conversion for the conventional HU to RED conversion and the Direct Density to RED conversion was tested. The results show small discrepancies that indicate that there will be discrepancies in the dose distributions. These were evaluated for different radiation modalities and setups as well as simple and also anthropomorphic geometries. A direct correlation was observed between an overestimated RED and an overestimation in dose and vice versa. Air was found to produce the biggest dose discrepancies. The highest RED difference in air was +3.3%. In general, dose was overestimated in the DD air regions in comparison to the HU dose distributions. In air, decreasing the x-ray tube voltage lead to a decreased RED deviation and thus to a decreased dose difference. For plaster as bone substitute, a maximum RED difference of -1.7% was noticed. Here, an increased tube voltage results in an increasing agreement.

Almost all evaluated phantoms showed a good passing rate of over 99% at 0.5% dose difference (the one exception reached 98%

at 1% dose difference). This matches the results of Ref. 13 where the passing rates for the gamma criteria of 1 mm and 1% were found to be greater than 99%. The results presented in this work suggest that the gamma criteria tool to evaluate the effects of the direct density dose gives a good indication but for a complete analysis it is not sufficient.

The differences for the mean dose (see Table 3) are in agreement with results from Ref. 7. Van der Heyden et al. identified that all dose deviations in the mean dose for the target volume and all ROIs were below 1%. In this work, the largest difference was found in the trachea with a deviation of 0.7% in the mean dose all other deviations were found to be below 0.4%.

Additionally, we showed that the DD reconstruction can also be used when metal implants are present. However, the metal density is dramatically underestimated in all cases.

It is advisable to focus on one tube voltage when metal implants are present and extend the calibration curve for this specific tube voltage. As this study is limited to the selected materials, a general statement about the correctness of materials foreign to the body is critical as other chemical compounds might have an influence. In these cases, however, the HU calibration is probable to also give a wrong output.

Two major benefits could result from the implementation of the DirectDensity™ algorithm in the clinical routine in radiotherapy departments besides a robust workflow: The first side effect that could be exploited is the comparability with other institutions as the CT characteristics are reduced. Thus, the RED curve needed for the implementation are more alike than a standard Hounsfield lookup table. A comparison to the Siemens RED curve and to the curves used by Ritter and Van der Heyden<sup>6,7,14</sup> shows that the slope of the calibration curve is the same in all cases (0.001, see section 2.2). However, the intercept differs by 0.006 in the maximum case, as Ritter and Van der Heyden used 1 and we fitted 0.994 as intercept. Changing the intercept would change our results not significantly. The deviations in air would decrease while the ones for bone would slightly increase in case of low tube voltages. Thus, CTs of other institutions with DirectDensity™ could be used with differences of less than 1% in the mean dose. If acceptable, this would benefit the patient by canceling the additional dose of another planning CT.

The second major benefit is the patient dose reduction by the implementation of DD with CARE kV and CARE Dose4D. This can reduce the dose significantly without reducing the image quality, allowing a more patient specific CT acquisition.

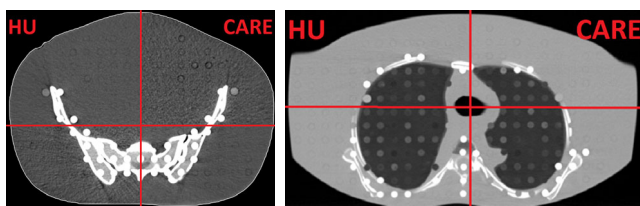


**FIG. 11.** Check view image as quality check for the dose reduction with CARE. The upper left and lower right part of each view show the HU image, while the upper right and the lower left show the CARE image.



A problem that could occur with the implementation are the danger of CT scans with an unsuitable tube voltage, resulting in an unusable scan and thus a rescan with additional dose to the patient.

## 5 | CONCLUSION

A CT reconstruction method for a direct translation between image values and relative electron density was implemented and found to provide sufficient image quality and dose calculation accuracy. The evaluated dose distributions showed only small differences between the dose calculated on the DirectDensity™ images and on the standard HU images. The results for dose distributions calculated on CT scans containing metal implants showed a larger difference but are still in good agreement, opening up the possibility to implement the direct density reconstruction algorithm for all clinical protocols. The DirectDensity™ implemented in the clinical routine allows a robust workflow while moving CT acquisition in radiotherapy to a dose optimized and thus a more personalized medicine.

## CONFLICT OF INTERESTS

We have no conflict of interest to declare.

## REFERENCES

- Schneider U, Pedroni E, Lomax A. The calibration of ct hounsfield units for radiotherapy treatment planning. *Phys Med Biol.* 1996;41:111.
- Constantinou C, Harrington JC, DeWerd LA. An electron density calibration phantom for ct-based treatment planning computers. *Med Phys.* 1992;19:325–327.
- Chen G-P, Noid G, Tai A, et al. Improving ct quality with optimized image parameters for radiation treatment planning and delivery guidance. *Phys Imaging Radiat Oncol.* 2017;4:6–11.
- Kalender WA, Wolf H, Suess C, Gies M, Greess H, Bautz WA. Dose reduction in CT by on-line tube current control: principles and validation on phantoms and cadavers. *Eur Radiol.* 1999;9:323–328.
- Seyal AR, Arslanoglu A, Abboud SF, Sahin A, Horowitz JM, Yaghmai V. CT of the abdomen with reduced tube voltage in adults: a practical approach. *Radiographics.* 2015;35:1922–1939.
- Ritter A. (2016). DirectDensity™: technical principles and implications for radiotherapy (white paper).
- Van der Heyden B, Öllers M, Ritter A, Verhaegen F, van Elmpt W. Clinical evaluation of a novel ct image reconstruction algorithm for direct dose calculations. *Phys Imaging Radiat Oncol.* 2017;2:11–16.
- Kachelriess M, Krauss A. (2016). Iterative metal artifact reduction (imar): Technical principles and clinical results in radiation therapy (white paper).
- Breitman K, Rathee S, Newcomb C, et al. Experimental validation of the eclipse aaa algorithm. *J Appl Clin Med Phys.* 2007;8:76–92.
- Tsuruta Y, Nakata M, Nakamura M, et al. Dosimetric comparison of acuros xb, aaa, and xvmc in stereotactic body radiotherapy for lung cancer. *Med Phys.* 2016;41:081715.
- Low DA, Harms WB, Mutic S, Purdy JA. A technique for the quantitative evaluation of dose distributions. *Med Phys.* 1998;25:656–661.
- Ulzheimer S, Endt H, Leidecker C. (2011). CARE kV how to optimize individualized dose (white paper).
- Zhao T, Mistry N, Ritter A, Sun B, Li H, Mutic S. (2016). Dosimetric evaluation of direct electron density computed tomography images for simplification of treatment planning workflow. *Int J Radiat Oncol Biol Phys.* 96:E674–E675. Proceedings of the American Society for Radiation Oncology.
- Siemens Healthcare GmbH. *SOMATOM Gebrauchsanweisung - Bildgebung bei RTP Version 2.* Erlangen: Siemens Healthcare; 2016.

## Verzeichnis der akademischen Lehrenden

Meine akademischen Lehrenden waren in Aachen:

- Prof. Dr. Josef Bemelmans
- Prof. Dr. Martin Erdmann
- Prof. Dr. Lutz Feld
- Prof. Dr. Uwe Klemradt
- Prof. Dr. Michael Krämer
- Prof. Dr. Andreas Lehrach
- Prof. Dr. Volker Meden
- Prof. Dr. Jörg Pretz
- Prof. Dr. Frank Arthur Raupach
- Prof. Dr. Stefan Roth
- Prof. Dr. Thomas Schäpers
- Prof. Dr. Thomas Schmitz-Rode
- Prof. Dr. Herbert Schoeller
- Prof. Dr. Achim Stahl
- Prof. Dr. Rudolf Leonhard Stens
- Prof. Dr. Christopher Wiebusch

Meine akademischen Lehrenden waren in Marburg:

- Prof. Dr. Rita Engenhardt-Cabillic
- Prof. Dr. Klemens Zink

## Danksagung

Zunächst möchte ich allen danken, die mich auf meinen Weg zur Promotion unterstützt und begleitet haben.

Mein besonderer Dank gilt Prof. Dr. Rita Engenhardt-Cabillic und Prof. Dr. Klemens Zink, die mir die Möglichkeit eröffnet haben in Marburg und Gießen diese Arbeit zu schreiben. Ich habe mich immer unterstützt gefühlt, so dass gemeinsam alle Probleme, Themen und Diskussionen angegangen werden konnten. Auch für die vielen Besuche von Konferenzen und Weiterbildungen, an denen ich teilnehmen durfte um meine Arbeit vorzustellen und diese mit Kollegen diskutieren konnte, möchte ich mich ganz herzlich bedanken.

Ein besonderer Dank gilt auch Dr. Kilian-Simon Baumann, ohne den diese Dissertation mit Sicherheit ganz anders verlaufen wäre. Die vielen sehr angeregten Diskussionen und das immer offene Ohr habe ich sehr geschätzt.

Weiterhin möchte ich mich für die ideenreichen und produktiven Kooperationen bedanken. Insbesondere bei Dr. Uli Weber von der GSI und Dr. Jörg Wulff und Dr. Christian Bäumer vom WPE.

In den letzten fünf Jahren habe ich mit sehr vielen tollen Kollegen zusammenarbeiten dürfen, welche mir vieles erklärt und beigebracht haben: Ich danke allen, die in der Strahlentherapie mit mir zusammengearbeitet haben, insbesondere der Medizinphysik, welche mich erst so richtig in die Strahlentherapie eingearbeitet hat, allen Kollegen am IMPS, den gesamten Flur, aber vor allem natürlich allen in meinem Büro für das Interesse an meiner Arbeit und zu guter Letzt allen Kollegen am MIT und auch hier insbesondere der Medizinphysik, welche mir die klinische Seite der Partikeltherapie nochmal näher gebracht haben.